Stereom differentiation in sea urchin spines under special consideration as a model for a new impact protective system

Dissertation

zur Erlangung des Grades eines Doktors der Naturwissenschaften

der Geowissenschaftlichen Fakultät der
Eberhard Karls Universität Tübingen

vorgelegt von
Jan Nils Großmann
aus Frankfurt/Main

2010

Tag der mündlichen Prüfung: 30.09.2010

Dekan: Prof. Dr. Peter Grathwohl

1. Berichterstatter: Prof. Dr. James H. Nebelsick

2. Berichterstatter: Prof. Dr. Oliver Betz

Table of contents

Overview: Aim of the project

This doctoral thesis is part of an interdisciplinary project "New materials for light, permeable impact protective systems: sea urchins as a model" in which sea urchin spines are analysed to develop a new bio-inspired (biomimetic) impact-protective-system. As shown in Figure 1, systematic studies of, for example, the sea urchins morphology and the recognition of changing material characteristics from the perspective of its evolution can lead to methods and procedures that have major implications for the potential development of new, biologically inspired outcomes.

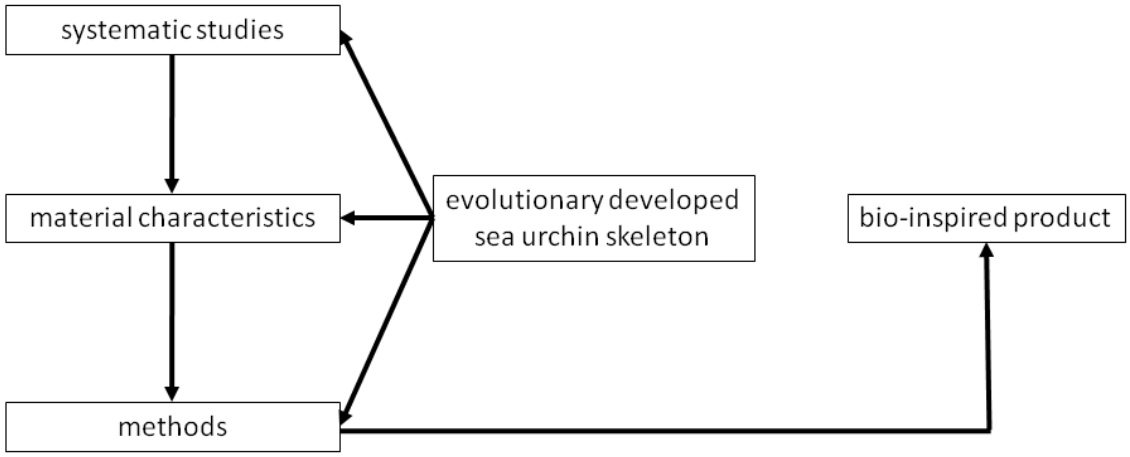

Figure 1: Analytical way from nature to a technical product

The spines of several sea urchins were analysed in order to investigate further the fundamental principles of echinoid skeleton architecture with respect to morphology, mineralogy and mechanics. An interest in echinoderm morphology is relevant and pertinent on several grounds:

- In terms of evolution, there is a significant fossil record; the earliest examples dated at about 500 million years ago (Smith 1984, 2005, Bottjer et al. 2006);
- With regard to habitat, since some sea urchins live in highly exposed areas such as the fore reef environment;
- Due to the magnesium calcite of which the sea urchins are built up and their light weight;
- Methodologically, the 'biomimetic' approach, focusing on the 3-D structure of sea urchins, suggests that there is great potential here, especially with regard for impact-protective-systems.

Generally speaking, the field of biomimetics deals with the analysis of biological phenomena and their potential transfer to technical applications (Buschan 2009). Well known examples are given by Barthlott & Neinhuis (1997) and Neinhuis & Barthlott (1997) for the application of plant surface water repulsive phenomena – the so called “Lotus-Effect” – in industrial products. One of the earliest studies, from a biomimetic perspective, can be traced as far back as Leonardo da Vinci who made conjectures about flying animals and potential technical flight machines (Videler 2006). Despite this early recognition, however, there have been relatively few studies concerning the biomimetic potential of the echinoderm skeleton, even though they seem to suggest great potential and promise in various fields of biomechanics, material sciences and nanotechnology (e.g. Addadi &Weiner 1992, Grossmann & Nebelsick 2010). The industrial potential of sea urchin spines has, however, never been investigated in detail so far.

References

Addadi, L. & Weiner, S. (1992). “Kontroll- und Designprinzipien bei der Biomineralisation”. Angewandte Chemie 104: 159-176.

Barthlott, W. & Neinhuis, C. (1997). “Purity of the sacred lotus or escape from contamination in biological surfaces.” Planta 202: 1-8.

Bottjer, D. J., Davidson, E. H., Peterson, K. J. & Cameron, R. A. (2006). “Paleogenomics of echinoderms.” Science 314: 956-960.

Bhushan, B. (2009). “Biomimetics.” Philosophical Transactions of the Royal Society of London A 367: 1443-1444.

Grossmann, N. & Nebelsick, J. H. (in review). “Stereom differentiation in spines of *Plococidaris verticillata*, *Heterocentrotus mammillatus* and other regular sea urchins.” In: Johnson, C.: Echinoderms in a changing world (Proceedings of the 13th international echinoderm conference), A. A. Balkema.

Neinhuis, C. & Barthlott, W. (1997). “Characterization and distribution of water-repellent, self-cleaning plant surfaces.” Annals of Botany 79: 667-677.

Smith, A. B. (1984). “Echinoid palaeobiology.” Harper Collins, London.

Smith, A. B. (2005). “The pre-radial history of echinoderms.” Geological Journal 40(3): 255-280.

Videler, J. J. (2006). “Avian flight.” Oxford University Press, Oxford: 5-6.

Chapter 1: The world of echinoderms

Abstract In this chapter an overview about the phylum Echinodermata is given. The history of echinoderms in general is described as well as special considerations of habitat, morphology, feeding strategy, predator-prey interaction, microstructure of the test. The properties of regular and irregular sea urchins are shown and compared. The regeneration process and growth of sea urchins, including that of the spines, is described.

1. Introduction & general features

The word “echinoderm” derives from the Greek words “echinos”, which means hedgehog or spiny, and “derma”, the membrane. The phylum Echinodermata consists of marine invertebrates which occupy almost every major marine habitat throughout the world, from the inter-tidal zone to depths of more than 5000 metres. Five classes of echinoderms exist today: sea lilies (Crinoidea), brittle stars (Ophiuroidea), sea stars (Asteroidea), sea cucumbers (Holothuroidea) and sea urchins (Echinoidea). The oldest echinoderms date to at least 545 million years ago (Ruppert et al. 2004). The fossil records for sea urchins stretch back to the Late Ordovician era, about 500 million years ago. All of the echinoderms have a primary pentamerous symmetry in the adult form, but can develop secondary bilateralism (Nichols 1969). Common to all echinoderms is the mesodermal calcite skeleton.

Since large amounts of calcite are associated with them, echinoderms (including sea urchins) are often found in the fossil record (Bottjer et al. 2006). Furthermore, the preservation of fossils is strongly dependent on the taphonomic processes affecting the organism (Nebelsick 1995a). Factors leading to preservation are the skeletal morphology, ancient environmental conditions and time related effects (Sprinkle 1980, Nebelsick 1995b).

The skeleton of the echinoderms is built up of discrete magnesium calcite plates which form the “test” or “corona”. This test can be round, elongated, flattened or have an egg-like form. The microstructure of each plate consists of porous three-dimensional meshwork of trabeculae (sometimes called “struts”), known as the “stereom”, which is anchored to other plates, thus giving most sea urchins an inflexible body. The type of stereom found in the skeleton depends on the specific architecture of the test and can vary between as well as within species, within the skeleton of simple individuals and within distinct plates of the test. The pores of the stereom are filled with the stroma, built up of a fluid and several organic components such as extracellular fibrils and connective tissue cells (Cavey & Märkel 1994).

The echinoderms have a large variety of appendices to the test including tube-feet, pedicellariae, sphaeridia and spines. The tube-feet are comprised of a soft tissue and move hydraulically since they are connected to the internal water vascular system. The major functions of these tube-feet are gaseous exchange and locomotion, insofar as they can also work as a sucker on different substrates (Ruppert et al. 2004). Pedicellaria are multifunctional as they are for defense, feeding and cleaning purposes. Sphaeridia occur in the ambulacral regions in all echinoids but are missed in the cidaroids (Cavey & Märkel 1994). Spines, the major emphasis of this thesis, are described later.

2. General development of echinoderms

All echinoderms are sexually differentiated. Therefore sperms and eggs are released from different specimens and fertilised in the water. The development of three classes of the echinoderms is shown in Figure 1. The embryo develops to a bilateral planktotrophic larval stage and then larvae metamorphose into an adult pentamerous organism which can only live on the sea floor. The number of stages associated with this process of metamorphosis from larvae to adult organisms can vary, from two (for example in echinoids) to four (for example in ophiuroids). After Smith (1997) the larval forms can be used to differentiate the taxonomic groups. The larval skeleton is built up of calcite. The process is described by Lowenstam & Weiner (1989).

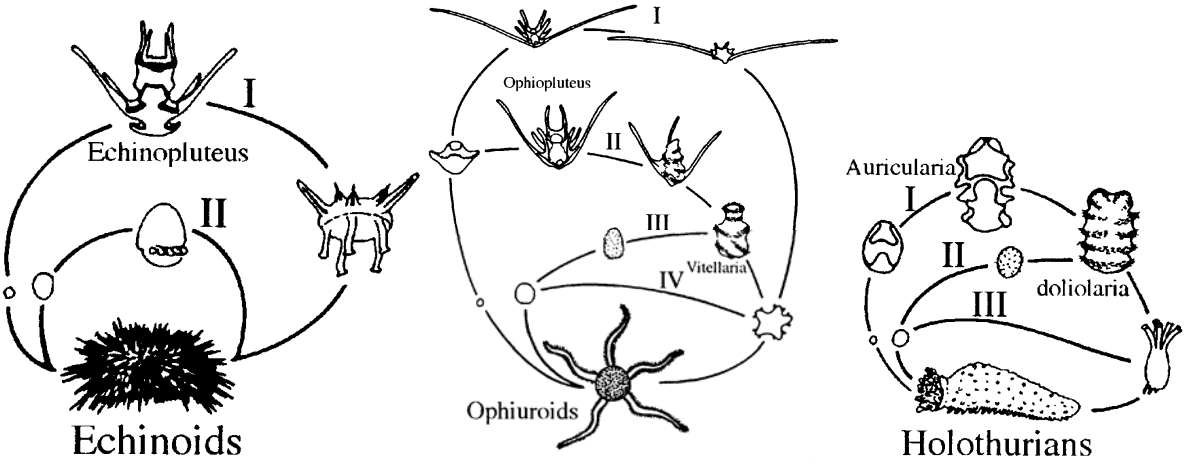

Figure 1: Echinoderms and their diverse steps from larval stages to adult organisms (after Smith 1997)

3. Defence strategy of echinoderms

Echinoderms bear a wide range of defence mechanisms including camouflage (e.g. algae), spines, autotomy and pedicellariae. The autotomy is the controlled losing or dropping of parts of the skeleton (such as internal organs or arms), as a possible way to avoid capturing by predators or other stress induced situations. Sea cucumbers for example can extrude internal organs and brittle stars are able to clip off their own arms (Fleming 2007). For both defence and cleaning, echinoderms also have so called “pedicellariae” which are small appendages attached to the test surface by a stalk. The defence function is self-evidently important since echinoderms (especially sea urchins) are preyed upon by a wide variety of animals, such as fish, sea stars, molluscs, several bird species and other vertebrates (Moore 1956, Schroeder 1962, Hughes & Hughes 1971 and 1981, Schmalfuss 1976, Estes et al. 1978, Kurz 1995, Sala & Zabala 1996, Kowalewski & Nebelsick 2003, Guidetti 2004, Guidetti & Mori 2005, Verling et al. 2005, Hori & Noda 2007, Gianguzza et al. 2009).

4. General morphology & body plan of sea urchins

In general, sea urchins can be separated by their morphology into regular and irregular forms. Regular sea urchins have a pentamerous symmetry. Irregular sea urchins, in contrast, show a secondary bilateral symmetry.

The test of sea urchins comprises ten double columns of plates (also known as ossicles), containing five ambulacral zones (ambulacralia) and five interambulacral zones (interambulacralia). Ambulacral plates have double pores corresponding to the tube feet (podia). A top view of a regular cidaroid sea urchin, where the pentamerous symmetry is well presented, is seen in Figure 2. Each interambulacral plate bears a tubercle where the primary spine is situated.

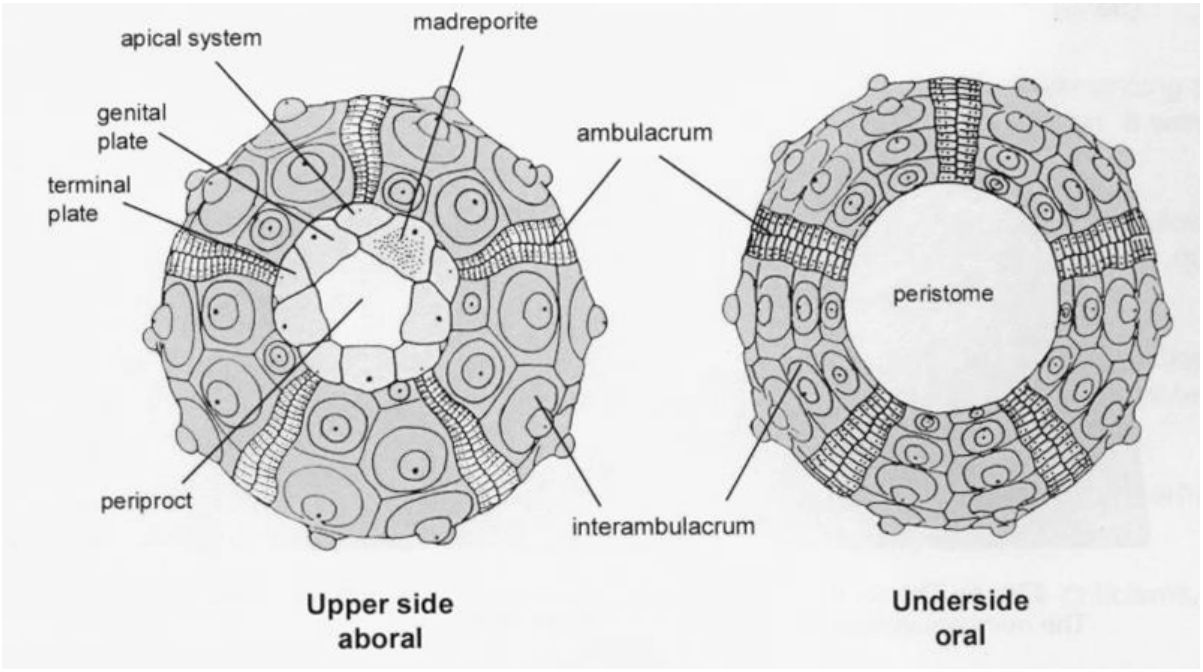

Figure 2: Test of a regular sea urchin (cidaroid) from aboral and oral (after Schultz 2006): The test comprises of several plates which are separated in those of the interambulacralia and ambulacralia. The periproct is the after, the peristome is the mouth of a sea urchin

By contrast, Figure 3 shows a typical irregular clypeasteroid sea urchin test. As mentioned before, irregular sea urchins are bilateral symmetric with the after lying outside of the apical system.

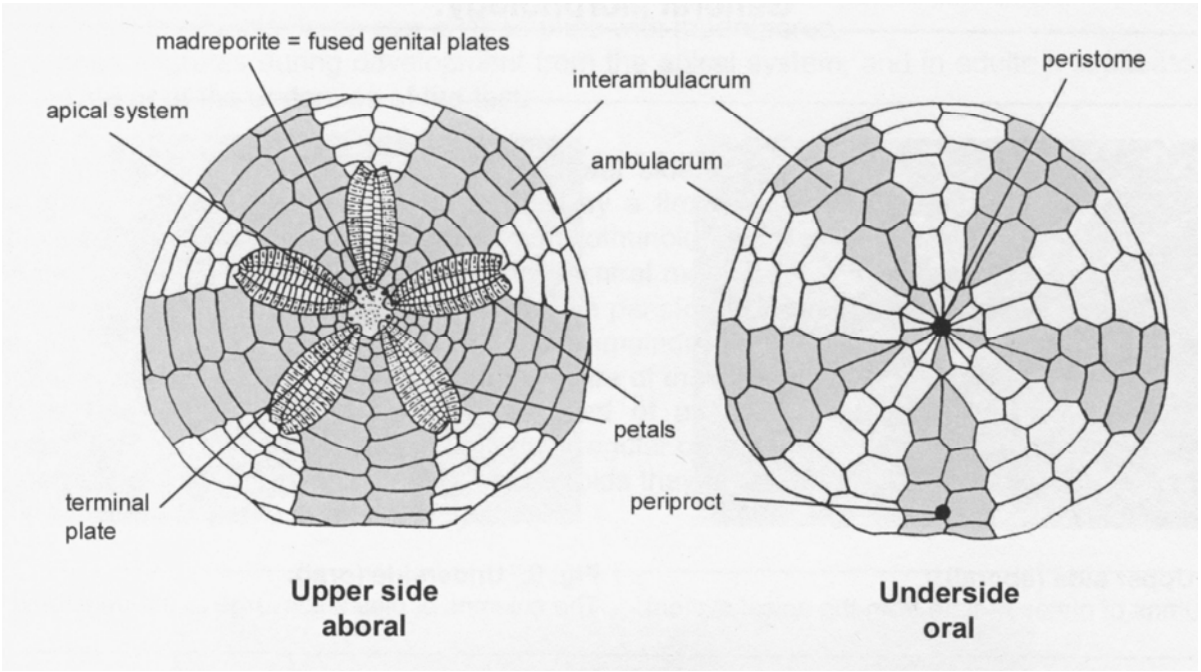

Figure 3: Test of an irregular sea urchin (clypeasteroid), showing the aboral and oral side (after Schultz 2006): The bilateral symmetry is demonstrated in this Figure. The periproct (after) and peristome (mouth) are situated on one side of the test

Morphological varieties of regular sea urchins including size of sea urchins, shape and form of the spines can be seen in Figure 4, also with regard to surface colour. Moreover, the feeding strategy and habitat differs in regular and irregular sea urchins, as regular sea urchins live mainly on the surface and feed on algae and other nutrition. Irregular sea urchins live below the surface and feed on detritus.

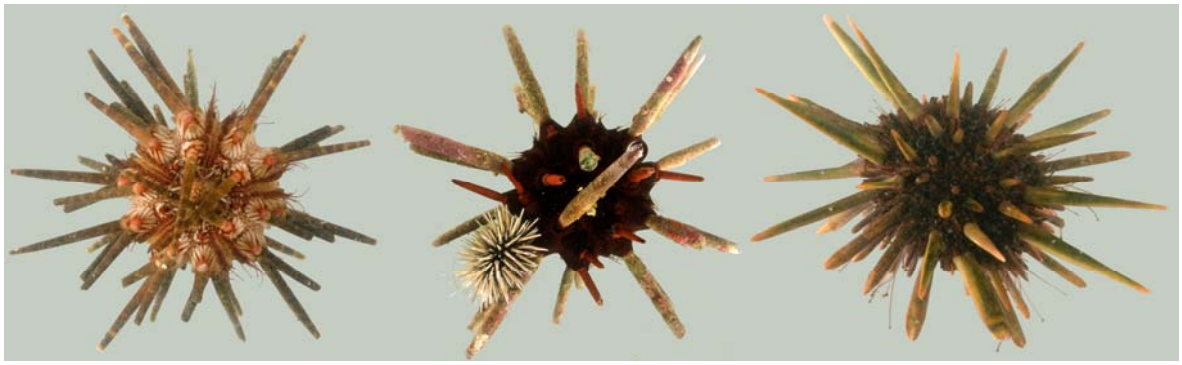

Figure 4: Morphology of regular sea urchins (from the testing aquaria): Specimen of *Eucidaris metularia* (left), *Echinometra mathaei* (centre, left side) & *Phyllacanthus imperialis* (centre, right side) and *Heterocentrotus mammillatus* (right)

In Figure 5 an example of the internal morphology for a regular sea urchin is shown. The mouth (peristome) lies on the oral side, whereas the anus (periproct) is in an aboral position. Using the internal jaws of the Aristotle's lantern they can feed on almost every substrate (detritus, sponges, mussels, algae). The digestive tract stretches from the lantern to the anus. The internal space of the sea urchin, in addition to the digestive tract, is filled with fluid and the gonads.

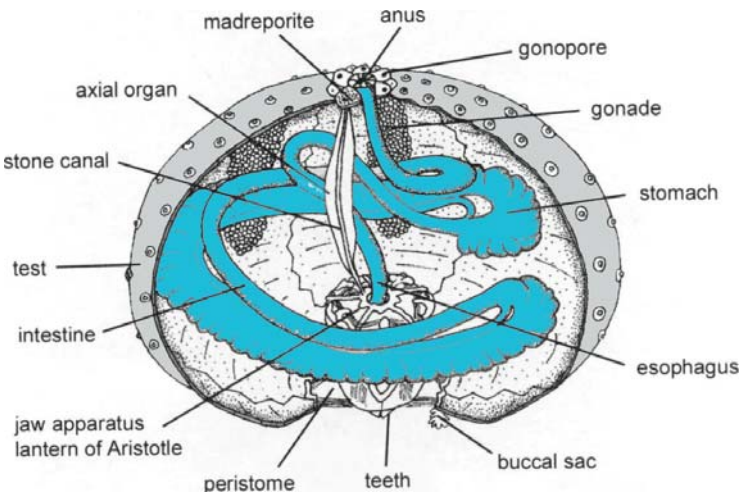

Figure 5: Internal morphology of a regular sea urchin: The test comprises the organs (digestive tract in blue). The water-vascular-system is not shown (after Schultz 2006)

5. General features of spines

Spines perform several functions, amongst them defence (spiky and since some of them are, in part, poisonous), burrowing, reducing wave energy and locomotion (e.g. Nichols 1967, Cavey & Märkel 1994). The role of echinoid spines in preventing structural damage is described by Strathmann (1981). Detailed inspection of the spine reveals that it may be separated into two sections: the base, with a perforate or imperforated acetabulum, and the shaft including neck and tip (Märkel & Röser 1983a). The boundary between the base and the shaft is an elevated area called the milled ring. The structure of spines can also be used for taxonomic differentiation since the shaft of a spine may take different forms. It can be smooth, or ornamented by thorns, granules and ribs. The primary spines are larger than the surrounding secondary spines (Figure 6) and the miliary spines (tertiary spines, which are used also to remove particles from the test surface).

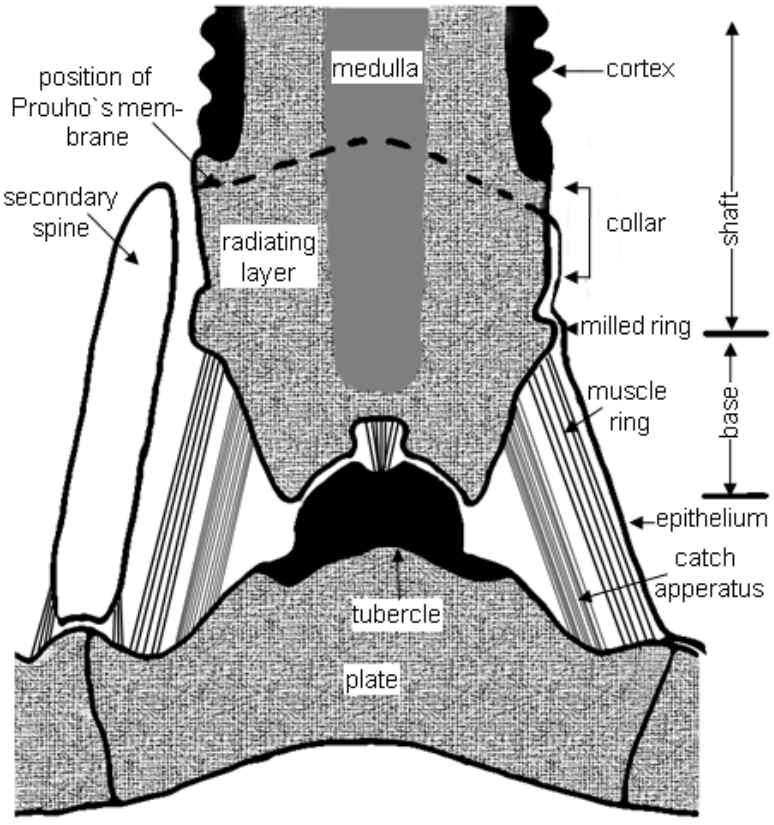

Figure 6: Longitudinal view of a cidaroid spine: The spine resides at the tubercle, attached to the test with the catch apparatus and muscle fibres. The shaft (including the tip) is not displayed in total (after Märkel & Röser 1983b; Stauber & Märkel 1988)

The spines are attached to the surface of the sea urchins skeleton, by a ball-and-socket-joint. Due to the catch apparatus (a circumferential ligament) the spine can be locked in a specific position, e.g. in case of an attack by predators, and further on a relaxation is possible. Nerves and muscles fibres (collagen bundles) are connected from the test and tubercle to the

spine such that the spine can be moved (Ruppert el al. 2004). The collagen might be arranged in bundles of 30 microns (Smith 1990). The tubercle is an elevated area of a plate of the sea urchins test (Lawrence 1984). The collar is an area between the milled ring and the cortex, without cortex layer, but with epithelium. The medulla is positioned in the centre of the spine, with a cylindrical form from the base to the tip, accompanied by the radiating layer which ends at the surrounding cortex, in cidaroids, or outer growth ring (members of the family Echinoida). Detailed analyses of the spine structures are presented in chapter 2.

On inspection of cross-sections of spines, they display a diverse morphology with respect to stereom distribution ranging from more solid forms, found in *Echinometra mathaei* (Figure 7A) to forms with hollow parts, found in *Diadema setosum* (Figure 7B). In cross-section, the internal arrangement of the spine can vary. The spine of *Echinometra mathaei* is separated in the growth rings, followed by the radiating layer and the innermost part, the medulla. In contrast, in the spines of *Diadema setosum* no medulla is present but a lumen, which is a hollow part in the middle of the spine.

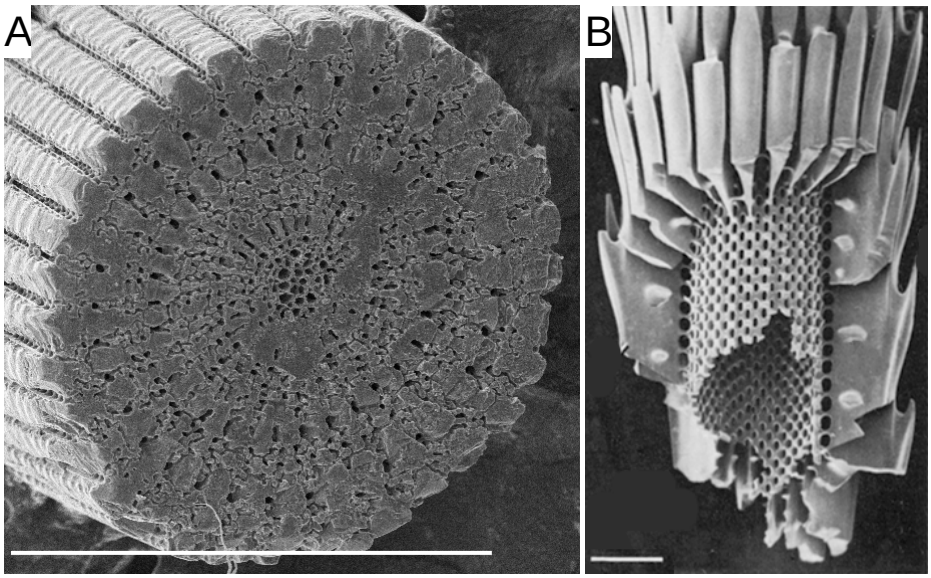

Figure 7: SEM images of a primary spine of *Echinometra mathaei* (A) and *Diadema setosum* (B) in cross-section: *Echinometra matheaei* (A) - The stereom inside the spines is shown with a regular alternation of growth rings and pores from the inner part to the surface (scale bar = 1 mm). *Diadema setosum* (B) - Lumen in the centre then follows the stereom (scale bar = 200 µm) (Figure 7B after Burkhardt et al. 1983)

In Figure 8, a large variety of spines is displayed in longitudinal views, with forms ranging from long & thin (*Echinometra mathaei* (A)) to highly ornamented (*Plococidaris verticillata* (B)) or thick ones (*Heterocentrotus mammillatus* (C) *& Phyllacanthus imperialis* (D)). Additionally, the spine surfaces of *Echinometra mathaei* (A) and *Heterocentrotus mammillatus* (C) are smooth as they are covered by an epidermis throughout life. The spines of *Phyllacanthus imperialis* (D) in contrast show intense encrustation.

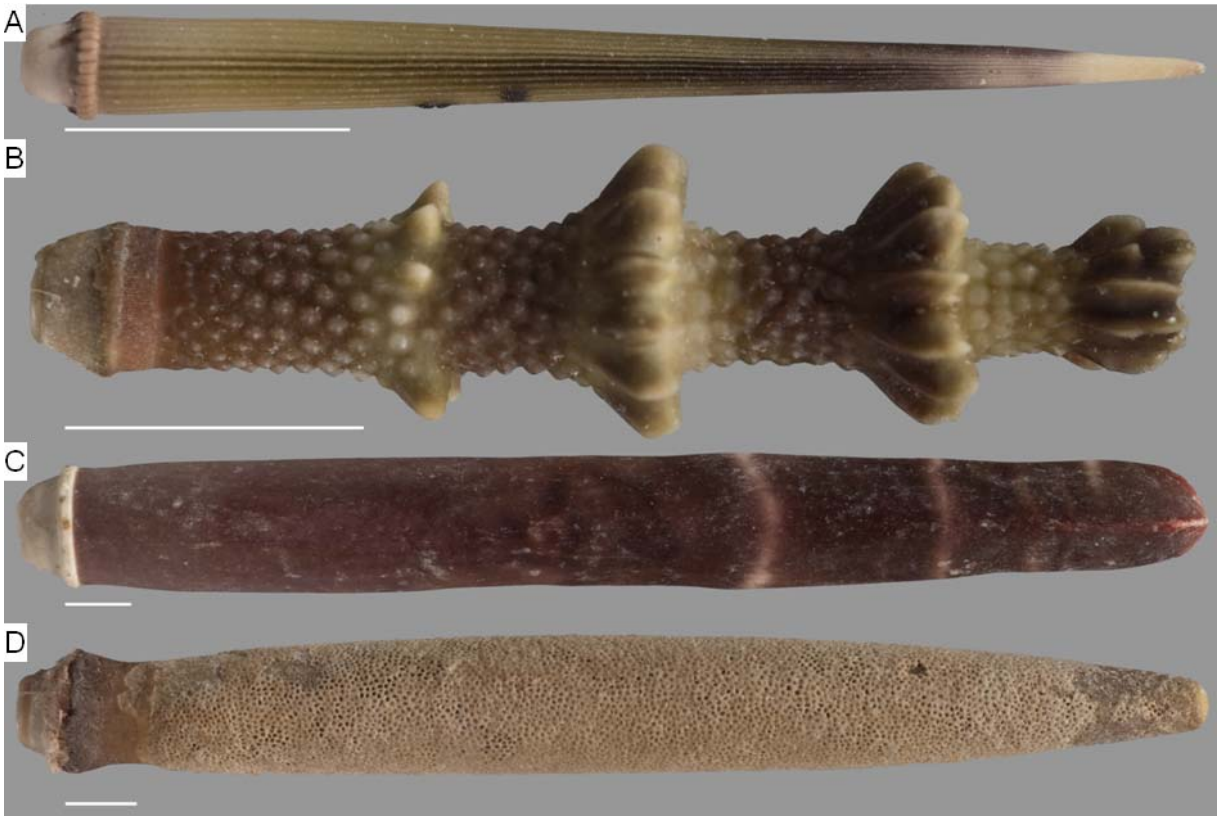

Figure 8: Images of the investigated primary spines of *Echinometra mathaei* (A), *Plococidaris verticillata* (B), *Heterocentrotus mammillatus* (C) and *Phyllacanthus imperialis* (D): The diverse ornamentation and encrustations on the surface of sea urchins are shown (scale bar = 5 mm)

6. General regeneration possibilities and growth of spines and plates

There is a significant potential for self-regeneration in echinoderms where damage or loss have occurred. In brittle stars and sea stars, small pieces of the original specimen can regenerate whole organisms. During growth in echinoids, new plates are added at the outer edge of the terminal plate on the upper side of the test. The procedure of regeneration, growth of spines and plates has been investigated and is not yet completely understood (e.g. Becher 1914, Deutler 1926, Weber 1969, Ebert 1982, Dotan & Fishelson 1985, Lowenstam & Weiner 1989, Dubois & Jangoux 1990, for sea stars see Stump & Lucas 1990). Furthermore, the regeneration is dependent on several factors, including water temperature (e.g. Davies et al. 1972, Bonasoro et al. 2004). In general, mineral compositions are deposited adjacent to the fracture of the spine or near the growth area (Mischor 1975, Dubois & Jangoux 1990, Cavey & Märkel 1994). Prouho`s membrane is seen as the area where calcite is re-absorbed for the growing process or in case of repairing, for regeneration of the damaged spines.

If the spine is completely lost, the base is regenerated and then the spine grows incrementally and thickens to its original size (Heatfield 1971, Dubois & Jangoux 1990, Dubois & Ameye 2001), during which the spine is covered by an epidermis (Prouho 1887,

Borig 1933, Märkel et al. 1971, Märkel & Röser 1983a). Significantly, the epidermis is lost once this process of regeneration has been completed and encrusting organisms can cover the spine of cidaroids. In all other echinoids, there is a continuously living epidermis that covers the spine which inhibits encrustation. In general, the spine and test contain a limited amount of organic tissue. The magnesium content changes from the base (2 %) to the tip (12 %) of a spine (Richter 1974, 1979, Lawrence & Guille 1982, Hozman 1983, Berman et al. 1988, Magdans & Gies 2004, Magdans 2005).

In the following chapters, detailed investigations on several sea urchin spines are presented including detailed analysis by scanning electron microscopy (chapter 2), computer tomography (chapter 3) and bending tests (chapter 4).

7. References

Becher, S. (1914). “Über statische Strukturen und kristalloptische Eigentümlichkeiten des Echinodermenskeletts. ” Verhandlungen der Deutschen Zoologischen Gesellschaft 24: 307-327.

Berman, A., Addadi, L. & Weiner, S. (1988). “Interactions of sea-urchin skeleton macromolecules with growing calcite crystals - a study of intracrystalline proteins.” Nature 331(11): 546-548.

Bonasoro, F., Ferro, P., Benedetto, D. di, Sugni, M., Mozzi, D. & Candia Carnevali, M. D. (2004). “Regenerative potential of echinoid test.” In: Heinzeller, T. & Nebelsick, J. H. (Eds.): Echinoderms: München, Taylor & Francis, London: 97-103.

Borig, P. (1933). “Über Wachstum und Regeneration der Stacheln einiger Seeigel.” Zoomorphology 27(4): 624-653.

Bottjer, D. J., Davidson, E. H., Peterson, K. J. & Cameron, R. A. (2006). “Paleogenomics of echinoderms.” Science 314: 956-960.

Burkhardt, A., Hansmann, W., Märkel, K. & Niemann, H.J. (1983). "Mechanical design in spines of diadematoid echinoids (echinodermata, echinoidea." Zoomorphology **102**: 189-203.

Cavey, M. J. & Märkel, K. (1994). “Echinodermata.” In: Harrison, F. W. (Ed.): Microscopic Anatomy of Invertebrates, Wiley, New York: 345-400.

Davies, T. T., Crenshaw, M. A. & Heatfield, B. M. (1972). “The effect of temperature on the chemistry and structure of the echinoid spine regeneration”. Journal of Paleontology 46(6): 874-883.

Deutler, F. (1926). “Über das Wachstum des Seeigelskeletts.” Zoologische Jahrbücher 48: 119-200.

Dotan, A. & Fishelson, L. (1985). “Morphology of spines of *Heterocentrotus mammillatus* (Echinodermata: Echinoidae) and its ecological significance.” In: Keegan, B. F. & O`Connor, B. D. S. (Eds.): Echinodermata: Proceedings of the international echinoderm conference, Galway September 24.-29.9.1984, A. A. Balkema, Rotterdam: 253-260.

Dubois, P. & Ameye, L. (2001). “Regeneration of spines and pedicellariae in echinoderms - A review.” Microscopy Research and Technique 55: 427-437.

Dubois, P. & Jangoux, M. (1990). “Stereom morphogenesis and differentiation during regeneration of adambulacral spines of *Asteria rubens* (Echinodermata, Asteroida).” Zoomorphology 109: 263-272.

Ebert, T. A. (1982). “Longevity, life history and relative body wall size in sea urchins.” Ecological Monographs 52(4): 353-394.

Estes, J. E., Smith, N. S. & Palmisano, J. F. (1978). “Sea otter predation and community organization in the western aleutian islands, Alaska.” Ecology 59(4): 822-833.

Gianguzza, P., Bonaviri, C. & Guidetti, P. (2009). “Crushing predation of the spiny star *Marthasterias glacialis* upon the sea urchin *Paracentrotus lividus*.” Marine Biology 156(5): 1083-1086.

Guidetti, P. (2004). “Consumers of sea urchins, *Paracentrotus lividus* and *Arbacia lixula*, in shallow mediterranean rocky reefs.” Helgoland Marine Research 58: 110-116.

Guidetti, P. & Mori, M. (2005). “Morpho-functional defences of mediterranean sea urchins, *Paracentrotus lividus* and *Arbacia lixula*, against fish predators.” Marine Biology 147: 797-802.

Fleming, P. A., Muller, D. & Bateman, P. W. (2007). “Leave it all behind: a taxonomic perspective of autotomy in invertebrates.” Biological Review 82: 481-510.

Heatfield, B. M. (1971). “Growth of the calcareous skeleton during regeneration of spines of the sea urchin, *Strongylocentrotus purpuratus* (Stimpson): A light and scanning electron microscopic study.” Journal of Morphology 134(1): 57-90.

Hori, M. & Noda, T. (2007). “Avian predation on wild and cultured sea urchin *Strongylocentrotus intermedius* in a rocky shore habitat.” Fisheries Science 73(2): 303-313.

Hozman, P. (1983). “Das unterschiedliche Härteverhalten biogener und anorganischer Calcitkristalle.” Bochumer Geologische und Geotechnische Arbeiten 10: 1-100.

Hughes, R. N. & Hughes, H. P. I. (1971). “A study of the gastropod *Cassis tuberosa* (L.) preying upon sea urchins.” Journal of Experimental Marine Biology and Ecology 7(3): 305-314.

Hughes, R. N. & Hughes, H. P. I. (1981). “Morphological and behavioural aspects of feeding in the Cassidae (Tonnacea, Mesogastropoda).” Malacologia 20(2): 385-402.

Kowalewski, M., & Nebelsick, J. H. (2003). “Predation and parasitism on recent and fossil echinoids”. In: Kelley, P. H., Kowalewski, M. & Hansen, T. A. (Eds.): Predator-prey interactions in the fossil record, Topics in Geobiology Series, Plenum Press/Kluwer, New York: 279-302.

Kurz, R. C. (1995). “Predator-prey interactions between gray triggerfish (*Balistes capriscus* Gmelin) and a guild of sand dollars around artificial reefs in the northeastern Gulf of Mexico.” Bulletin of Marine Science 56: 150-160.

Lawrence, L. M. & Guille, A. (1982). “Organic composition of tropical, polar and temperate-water echinoderms.” Comparative Biochemistry and Physiology 72B(2): 283-287.

Lawrence, J. M. (1987). “A functional biology of echinoderms.” John Hopkins University Press, Baltimore**.**

Lowenstam, H. A. & Weiner, S. (1989). “Chapter 8 Echinodermata.” In: Lowenstam, H. A. (Ed.): On biomineralization, Oxford University Press, Oxford: 123-134.

Magdans, U. (2005). “Mechanismen der Biomineralisation von Calcit am Beispiel von Seeigel-Stacheln: Untersuchung der Wechselwirkung zwischen Sorbat-Molekülen und Calcit-Wachstumsgrenzflächen mit Oberflächen-Röntgenbeugung und numerischen Simulationen.” PhD thesis, Faculty of Geology, Ruhr University, Bochum.

Magdans, U. & Gies, H. (2004). “Single crystal structure analysis of sea urchin spine calcites: Systematic investigations of the Ca/Mg distribution as a function of habitat of the sea urchin and the sample location in the spine.” European Journal of Mineralogy 16(2): 261 - 268.

Märkel, K. & Röser, U. (1983a). “The spine tissues in the echinoid *Eucidaris tribuloides*.” Zoomorphology 103: 25-41.

Märkel, K. & Röser, U. (1983b). “Calcite-resorption in the spine of the echinoid *Eucidaris tribuloides*.” Zoomorphology 103: 43-58.

Märkel, K., Kubanek, F. & Willgallis, A. (1971). “Polykristalliner Calcit bei Seeigeln (Echinodermata, Echinoidea).” Cell and Tissue Research 119(3): 355 - 377.

Mischor, B. (1975). “Zur Morphologie und Regeneration der Hohlstacheln von *Diadema antillarum* Philippi und *Echinothrix diadema* (L.) (Echinoidea, Diadematidae).” Zoomorphology 82: 243-258.

Moore, D. R. (1956). “Observations of predation on echinoderms by three species of Cassididae.” The Nautilus 69(3): 73-76.

Nebelsick, J. H. (1995a). “Comparative taphonomy of clypeasteroids.” Eclogae Geologicae Helvetiae 88(3): 685-693.

Nebelsick, J. H. (1995b). “Actuopaleontological investigations on echinoids: the potential for taphonomic interpretation.” In: Emson, R. H., Smith, A. B. & Campbell, A. C. (Eds.): Echinoderm Research, A. A. Balkema, Rotterdam, 209–214.

Nichols, D. (1967). “The origin of echinoderms.” Symposia of the Zoological Society of Academic Press, London.

Prouho, H. (1887). “Recherches sur le *Dorocidaris papillata* et quelques autres échinides de la Méditerranée.” Archives de zoologie expérimentale et générale 15:213-380.

Richter, D. K. (1974). “Zur subaerischen Diagenese von Echinidenskeletten und das relative Alter pleistozaener Karbonatterrassen bei Korinth, Griechenland.” Neues Jahrbuch für Geologie und Paläontologie 146: 51-77.

Richter, D. K. (1979). “Die Stufen der meteorisch-vadosen Umwandlung von Mg-Calcit in Calcit in rezenten bis pliozänen Biogenen Griechenlands.” Neues Jahrbuch für Geologie und Paläontologie 158: 277-333.

Ruppert, E. E., Fox, R. S. & Barnes, R. D. (2004). “Invertebrate Zoology. Chapter 28: Echinodermata.” Brooks/Cole, Belmont: 872-929.

Sala, E. & Zabala, M. (1996). “Fish predation and the structure of the sea urchin *Paracentrotus lividus* populations in the NW Mediterranean.” Marine Ecology Progress Series 140: 71-81.

Schmalfuss, H. (1976). “Ökologisch-funktionsmorphologische Untersuchungen an karibischen Krabben (Decapoda, Brachyura) I. *Percnon gibbesi* (H. Milne-Edwards, 1837) (Grapsidae, Plagusiinae).” Studies on Neotropical Fauna and Environment 11(4): 211 - 222.

Schroeder, R. E. (1962). “Urchin killer.” Sea Frontiers 8: 156–160.

Schultz, H. (2006): “Sea-urchins, a guide to worldwide shallow water species”, Scientific Publications, Hemdingen.

Smith, A. B. (1984). “Classification of the Echinodermata.” Palaeontology 27(3): 431-459.

Smith, A. B. (1990). “Biomineralization in echinoderms.” In: Carter, J. G. (Ed.): Skeletal Biomineralization: patterns, process and evolutionary trends, Van Nostrand Rheinhold, New York: 413-443.

Smith, A. B. (1997). “Echinoderm larvae & phylogeny.” Annual Review of Ecology and Systematics 28: 219-241.

Sprinkle, J. (1980). “An overview of the fossil record.” In: Broadhead, T. W. & Waters, J. A. (Eds.): Echinoderms - notes for a short course, Knoxville University of Tennessee: 15-26.

Strathmann, R. R. (1981). “The role of spines in preventing structural damage to echinoid tests.” Paleobiology 7(3): 400-406.

Stauber, M. & Märkel, K. (1988). “Comparative morphology of muscle-skeleton attachments in the Echinodermata.” Zoomorphology 108: 137-148.

Stump, R. J. W. & Lucas, J. S. (1990). “Linear growth in spines from *Acanthaster planci* (L.) involving growth lines and periodic pigment bands.” Coral Reefs 9: 149-154.

Verling, E., Barnes, D. K. A. & Crook, A. C. (2005). “Smashing tests? Patterns and mechanisms of adult mortality in a declining echinoid population.” Marine Biology 147: 509-515.

Weber, J. N. (1969). “Origin of concentric banding in the spines of the tropical echinoid *Heterocentrotus*.” Pacific Science 23: 452-466.

Chapter 2: Morphological differentiations in sea urchin spines

Abstract In this chapter, several tropical regular sea urchin spines, including those of *Plococidaris verticillata*, *Phyllacanthus imperialis*, *Eucidaris metularia*, *Prionocidaris baculosa*, *Heterocentrotus mammillatus* and *Echinometra mathaei*, are analyzed by scanning electron microscopy and critical point drying technique. The specimens were kept in several fully equipped aquaria, with marine conditions, over the whole period of the investigation. These sea urchins were chosen, due to their habitat and partly large and thick spines. Afterwards, the microstructure inside the spines, the stereom, was analyzed by measuring and comparing morphological aspects including pore size, pore diameter and trabeculae diameter. The spine medulla of the investigated species was always of a laminar arrangement. The radiating layer differed between the species. The stereom of the radiating layer and the growth rings is of a microperforate structure. A difference also occurred between juvenile and fully grown spines, as well as between oral and aboral spines.

1. Introduction

1.1 Bionically inspired material based on the echinoderm skeleton

There are a large number of tools available for describing natural objects. These methods for analyzing natural objects comprise scanning electron microscopy (SEM) as well as critical point drying. SEM is a common method used to describe microstructures of specimens in a bionic context (actual up to magnification to 0.1 nm), e.g. the adhesive devices in insects (Betz et al. 2003, Sukontason et al. 2006).

The microstructure of echinoderms has been of interest to scientists for centuries (e.g. Müller 1854, Stewart 1871, Hesse 1900, Mortensen 1909, Becher 1914, Deutler 1926, Borig 1933, Macurda 1973, Mischor 1975, Smith 1980 & 1990, Carnevali et al. 1991, Birenheide & Motokawa 1997, Wilkie 2001, Mannaerts 2007). Recent results deal with the mechanical relations of spines of *Paracentrotus lividus* (Moureaux et al. 2010). Considerations regarding the role of the microstructure of spines in influencing ectosymbiotic attachment of cidaroid spines have been discussed by David et al. (2009). Further investigations focus on the possible implementation of these nature-inspired structures into the technical field, for example implants (Vecchio 2007). Other applications deal with the replication of the galleried stereom structure of plates to construct a sandwich-like polymer - macroporous copper (Lai et al. 2007). This investigation revealed that incorporating the sea urchin plate structure into a

copper material improved it. Other application ideas have been already published by the project partners (Nickel et al. 2009a).

Sea urchin spines and plates are of a special interest for biomimetic research because of their lightweight material properties in combination with their inherent stability (Weber et al. 1971, Hiratzka et al. 1979, Hasenpusch 2000, Oaki & Imai 2006, Lai et al. 2007, Meldrum 2007). Hieratzka et al. (1979) focused on the stereom structure of *Heterocentrotus mammillatus* spines for new prosthesis materials. Hasenpusch (2000) postulated that the sea urchin skeleton can, for example, provide insights into new architectural approaches. Further applications deal with the production of crystals based on the regular morphology of the stereom (Oaki & Imai 2006, Meldrum 2007). Further possibilities of using the stereom structure as a base for bionically inspired material pursued within the project in which this dissertation was conducted, include for example in automotive production processes or in material needed in impact protection (e. g. bicycle helmets) (Nickel et al. 2009a, b, Presser et al. 2009). The use of computer aided optimization (CAD) or finite element analysis (FEA) as adequate methods to simulate and optimize objects, such as the stereom structure is in preparation for publication by the project partners (for other objects see Rayfield et al. 2001, Rayfield 2007 and Widak & Norajitra 2009).

1.2 Sea urchins skeletal morphology

The spines and also the test (= corona) of sea urchins are built out of high magnesium calcite. The skeleton of sea urchins is mesodermal, the test of the sea urchins are built out of plates. The relation of magnesium to calcium is different throughout a single individual and inside the skeletal element (Richter 1974 & 1979, Hozman 1983, Smith 1990, Magdans & Gies 2004, Magdans 2005). The calcium carbonate in echinoderms gives the test and the spines unusually high strength properties with a minimum of amount of material (Weber et al. 1969).

Higher magnesium concentrations are due to the different mechanical stress situations (e.g. teeth, spines) (Richter 1984). The higher the magnesium content, the less the shearing effects of the materials. Enrichment of magnesium in the lowest part of the base of spines, for example, assists the strengthening of spines and prevents breakage at the base. Magnesium incorporated in spines range from 2 - 12 mol% (Magdans 2005). In general, the Mg/Ca ratio in the skeleton of marine invertebrates (e.g. echinoids and crabs) is proportionally to the amount in the available seawater in which they are growing (Ries 2004).

The microstructure of the test and the spines, is called stereom and has a porous three dimensional arrangement built out of trabeculae (= struts). The pore space (stroma) is filled

by fluid, connective tissue cells and extracellular fibrils (Cavey & Märkel 1994). Märkel & Röser (1983) classified the cells that may be involved in the mineralization process of the cortex. Most of the cells in the stereom are sclerocytes which are responsible for producing the skeleton. The histology of spines and plates of sea urchin is investigated in detail by Cavey & Märkel (1994). The stereom differentiation in echinoids was extensively studied by Smith (1980) in which the stereom of plates was separated into various categories such as galleried or imperforate (Figure 1). An imperforate stereom is solid and shows no pores (A). A microperforate stereom is a structure with irregular perforation of the calcite layer and upright canals (B), regular perforate refers to canals in different directions towards the outer surface (C). The galleried form describes long parallel galleries, which are connected by struts with a regular arrangement of pores (D). Labyrinthic stereom is present as a structure with irregular struts where the pore size varies (E). The laminar stereom is built up of several layers which are loosely connected (F).

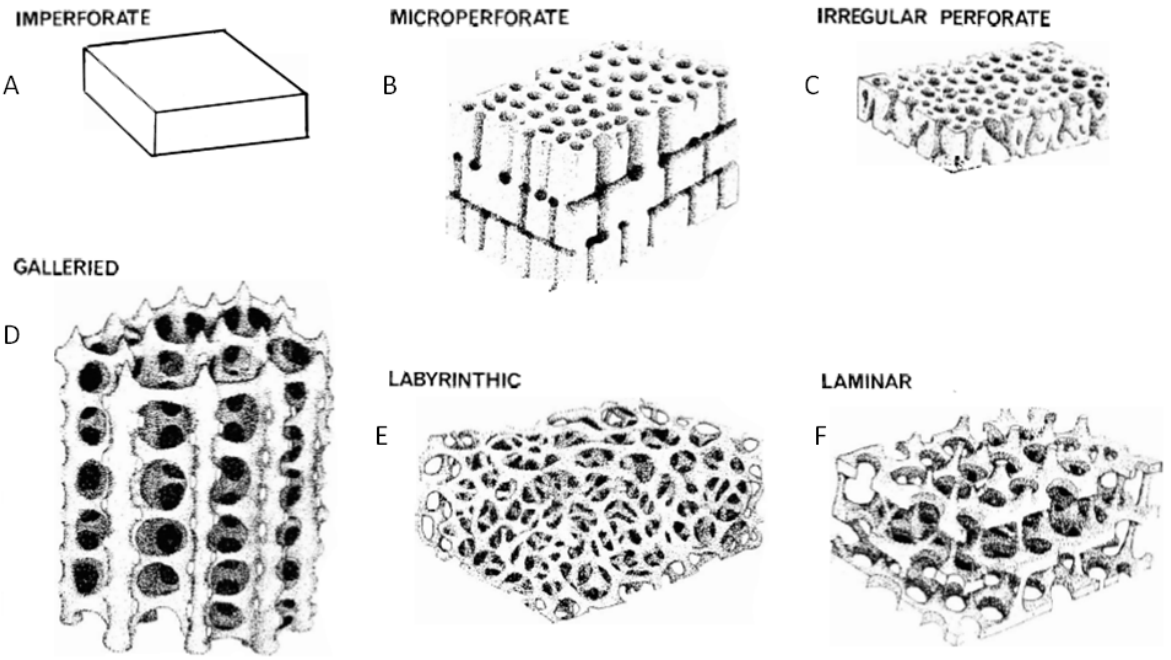

Figure 1: Stereom differentiations in sea urchins (after Smith 1980)

1.2.1 Stereom in spines

The terminology used by Smith (1980) can also be applied to the stereom of spines. The arrangement of the stereom inside a spine is shown in Figure 2. The cross-section of a *Prionocidaris* spine shows different stereom types within a single spine. The outer cortex is microperforate with only a few canals. The stereom of the radiating layer is galleried, whereas the medulla is laminar.

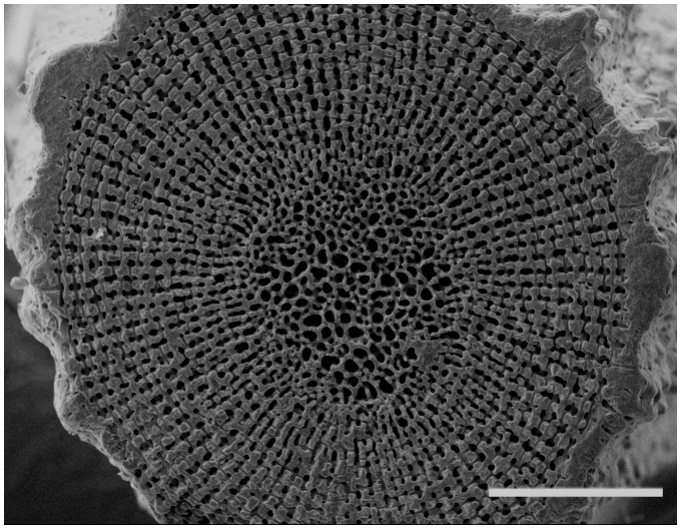

Figure 2: Typical example of the stereom arrangement in a cross-section of a spine: SEM image of a *Prionocidaris baculosa* spine: The innermost part (medulla) is followed by the radiating layer and by the thick outer cortex (scale bar = 300 µm)

The structural arrangement of a labyrinthic stereom in a *Heterocentrotus mammillatus* spine is shown in Figure 3. The pore sizes may vary and a disorganised arrangement of pores occurs in this type of stereom.

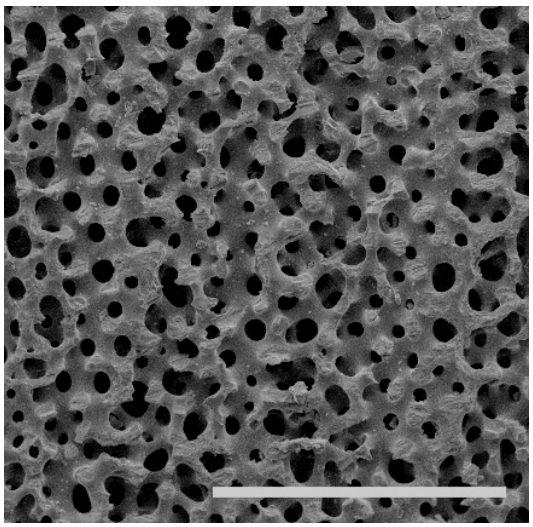

Figure 3: Typical arrangement of the stereom in longitudinal section: SEM image of the stereom in a spine of *Heterocentrotus mammillatus* (scale bar = 300 µm)

1.2.2 Morphology of the spine

In general, the primary spine of echinoids can be subdivided into several sections (base, shaft including the tip) among different taxa, for example the cidaroids and those of the Echinoida which are both studied in this dissertation (Figure 4). The differences are due to the fact that cidaroids loose the epidermal covering while Echinoida retain this features. Differences occur also between oral and aboral spines in a single specimen. In general, surface sculpturing and the influence of epibionts are important for organisms and also the costs and benefits of the host organism have to be regarded (David et al. 2009, Olabarria 2000, for extinct species see Schneider 2003). The benefits include covering, for example by algae in order to reduce the recognition by predators. The epibionthic attatchment may reduce the mobility of the organisms and may so attract predators. The spine base is attached to the sea urchin plate surface by a ball and socket joint (including muscle fibres). With the catch apparatus and its mutable connective tissue sea urchins are able to lock the spine in a specific position. The spine can be moved by myocytes to an angle of almost 100° from the upright position (Cavey & Märkel 1994, Ruppert et al. 2004).

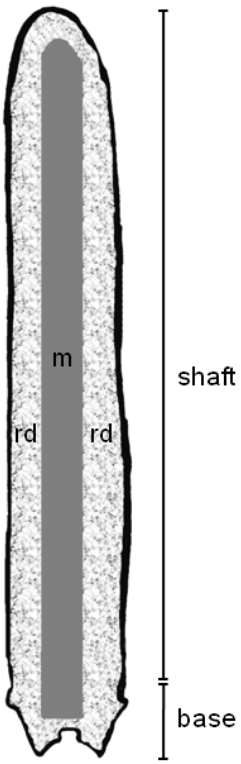

Figure 4: Schematic view of a sea urchin spine (not to scale): Spine is separated into the base and the shaft; the base is connected to the plate of the test. The stereom in the spines is different, depending on the position in the spines. Cidaroid spines have an outer cortex (dark line), spines of the Echinoida have an epidermis (dark line). Medulla (m) is surrounded by the radiating layer (rd)

2. Materials & Methods

2.1 Aquaria & technical equipment

Several equipped aquaria with fully marine conditions were used in the investigations (Figure 5 and Table 1). The further equipment of each aquarium consists of a large amount of green algae (e.g. *Caulerpa* sp.) and living stones from the Indo-Pacific. Several other invertebrates, including crabs, shrimps, fishes and hermit crabs were used to balance the fragile ecosystem in the aquaria. The following properties were generated and gradually stabilised for four aquaria with a capacity of 60 L to 400 L: daylight 10 h, salinity 36 ‰, temperature 25 °C, pH 8 - 9, nitrite 0 - 0.5 mg. The aquaria and technical systems were obtained from a local supply company (Korallenriff Shop, Rottenburg). Due to the rarity of the required specimens several shops had to be contacted, including Histoires D`eaux (Belgium), Meerwasseraquaristik Richter (Germany), Zoo Koelle (Germany), Aquaristik-Service Meyer (Germany) and Marine Fauna (Philippines). The intake phase for attaining a stable ecosystem (e.g. stable amount of nitrate, ammonium, phosphate and salinity) took less than 140 days, partly due to the favourable water conditions (for more photos regarding the assembling of the aquaria, see supplement). In contrast, Dakin (1997), Baumeister (1998), and Sander (1998) suggested about 180 days for the stabilisation phase. Chemical factors (e.g. nitrate, ammonium, calcium, carbonate concentration) and salinity were monitored on a weekly basis. A 10 to 20 % water exchange was carried out every four weeks.

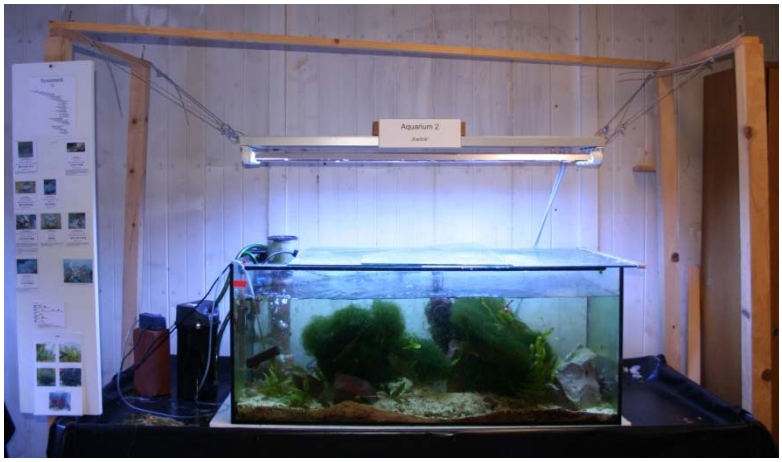

Figure 5: Fully equipped aquarium in the lab

Table 1: Technical equipment used for the aquaria

technical equipment	number per aquaria
protein skimmer (Turboflotor 750)	1
stream pump (Tunze stream 6060)	1
heater (Visitherm Taucherhitzer)	1
filter system (Eheim classic Außenfilter 2213)	1
fluorescent lamps (type T5 54 W)	4

Additionally, dead sea urchins and spine material was ordered from supply companies such as Alexandre Import Nature (France), Shell Horizons (USA) and Pacific Shells (Germany). Dried Wakame Algae as food for sea urchins was bought from different local shops and fed twice a week. The sea urchins used in this investigation are listed in Table 2 and shown in Figure 6 and 7. These species differ in morphology, spine differentiation and habitat.

Table 2: Investigated species and their habitat (after Schultz 2006)

species name	habitat	depths
Heterocentrotus mammillatus Linneus 1758	Indo-Pacific	5 - 25 m
Prionocidaris baculosa Lamarck 1816	Indo-Pacific	< 200 m
Echinometra mathaei Blainville 1825	Indo-Pacific	< 30 m
Eucidaris metularia Lamarck 1816	Indo-Pacific	5 - 570 m
Phyllacanthus imperialis Lamarck 1816	Indo-Pacific	5 - 70 m
Plococidaris verticillata Lamarck 1816	Indo-Pacific	< 50 m

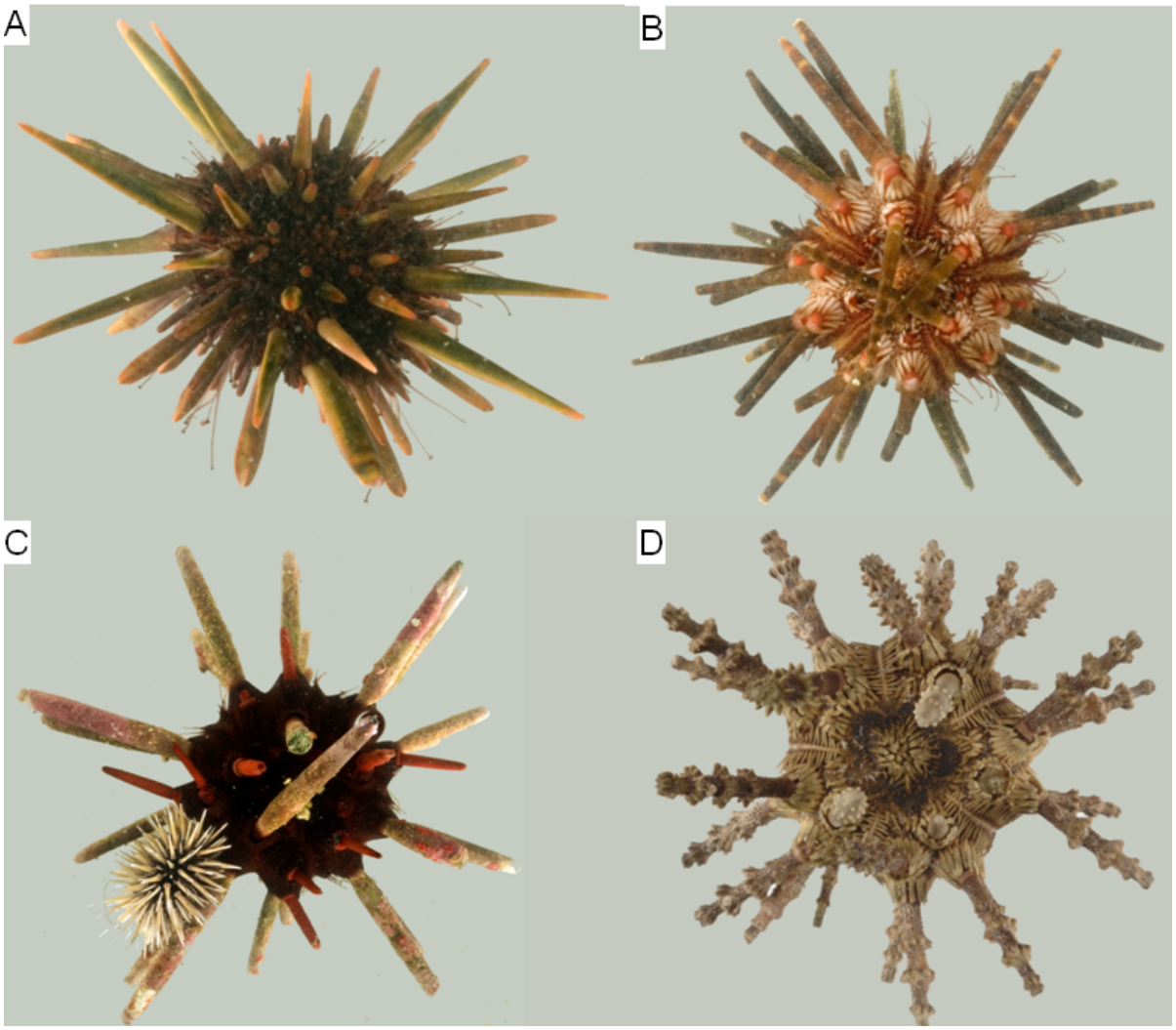

Figure 6: Images of the investigated sea urchins from the aquaria: A) *Heterocentrotus mammillatus*, B) *Eucidaris metularia*, C) *Phyllacanthus imperialis* with *Echinometra mathaei*, D) *Plococidaris verticillata*

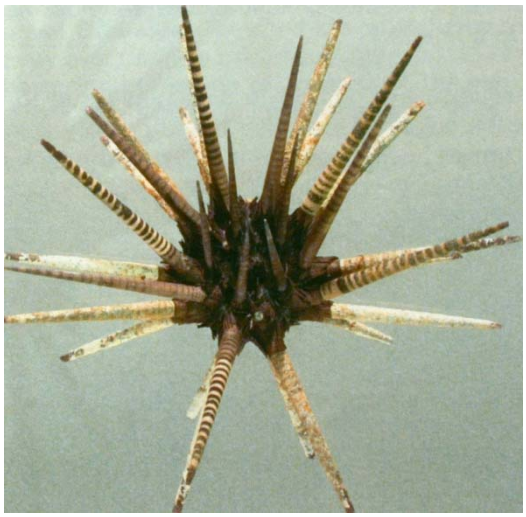

Figure 7: Single specimen of *Prionocidaris baculosa* (after Schultz 2006)

2.2 Sample preparation

Several spines were separated from the tests of living sea urchins. Spines were dried for up to two days then cut in the required form (for later SEM) and cleaned with an ultrasonic bath (model Bandelin Sonorex Super RK255H) for about 20 minutes. Then a solution of H_20_2 (40 %) was used to remove the soft tissue and the samples were again cleaned in the ultrasonic bath. After drying, for up to two days, the samples were prepared for SEM, sputtered (with a Sputter Coater BAL-TEC Model SCD 005/CEA 035) either with gold or platinum for 90 s (Robinson et al. 1985).

2.3 SEM

Scanning electron microscopy was carried out using a LEO-1450VP (OXFORD INCA Energy 200) at the Institute of Geosciences of the University of Tübingen (Figure 8). The images were taken at distances of 10 to 15 mm with an energy level of 10 to 20 kV and saved as tiff-files with a resolution of 1024 x 768 pixels (Figure 9).

Figure 8: SEM - Laboratory: The SEM (model Leo - 1450VP) at the Institute of Geosciences, Tübingen

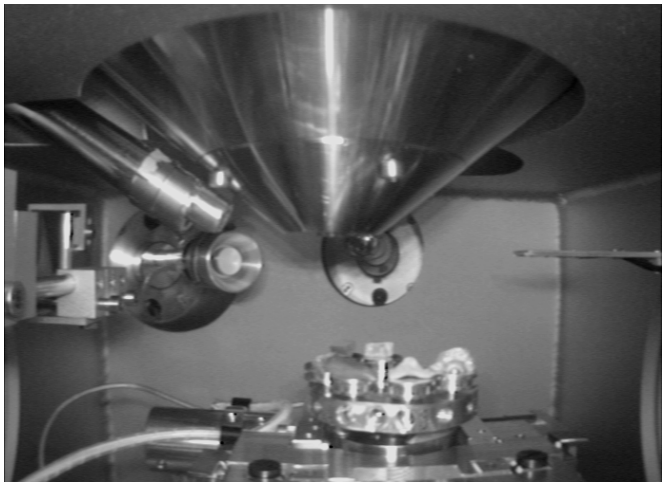

Figure 9: The chamber of the SEM at the beginning of the investigations: The prepared samples are screwed onto a plate with is positioned on a mobile table, which is movable in all directions

Later image analysis and measurements were carried out using Adobe Photoshop Extended and Microsoft Excel 2007. SEM after the critical point drying was carried out with a Hitachi S 800 under the supervision of Jürgen Berger at the Max-Planck-Institute for Development Biology in Tübingen.

2.4 Critical point drying

For the critical point drying, complete spines were dissected from a living sea urchin inside the aquaria. The samples were put in 2.5 % glutardialdehyde and PBS (phosphate buffered saline) immediately to stabilize the proteins inside the samples and left for several hours. Subsequently, the samples were then put in 1 % osmiumtetroxide for 1 h (interaction with lipids). The samples, in the solution were then broken into two pieces. Afterwards, the samples were dehydrated in an ascending concentration of ethanol (substitution of water). The ethanol was exchanged by liquid CO_2 in a locked chamber (55 bar; 25 °C). After reaching the critical point of CO_2 (73.8 bar; 31 °C) the pressure was reduced to normal conditions and the chamber opened (Robinson et al. 1985). The standard procedure for preparing specimens for SEM was then followed.

2.5 Measurement of stereom morphology

For the statistical investigation of a given stereom morphology randomly chosen areas of 200 * 200 µm of SEM images were taken. This size was chosen to minimize the impact of structural disturbances which can occur. Where it was not possible to use the selected areas because of the magnification of the object, the number of individual measurements was increased and, in some cases, results from more than one image were combined. This also depends on the size of the stereom features (e.g. Smith 1980). The following parameters were measured: pore sizes, maximum diameter of pores and minimum diameter of trabeculae (Smith 1980). For the measurements, Adobe Photoshop Extended was used and the pore space was selected by the selection tool within this software (Figure 10). Damaged areas inside the spine were avoided. In case of damaged areas inside the image, pore size was estimated. Statistical tests were carried out using the program package of SPSS 17.0.2.

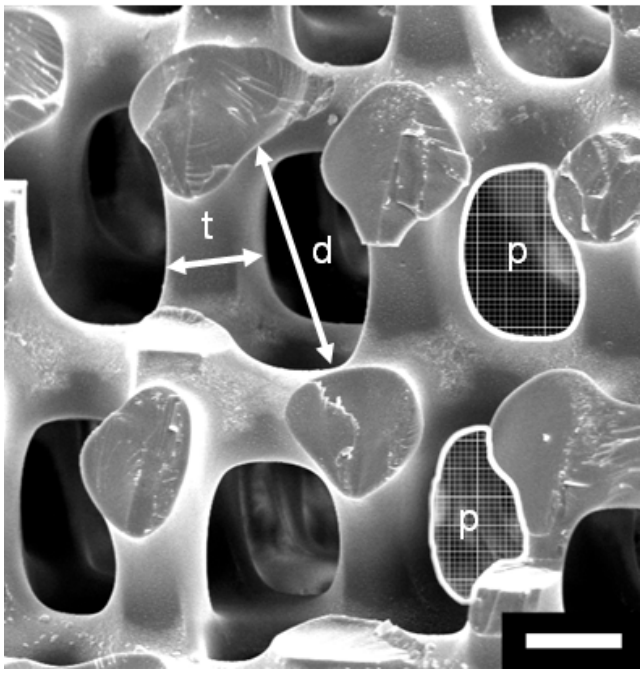

Figure 10: Diameter and size measurements in a selected stereom: Measurements were done in Adobe Photoshop Extended (d = pore diameter; t = trabeculae diameter and p = pore size. All pores in the image were measured for pore size. More than 50 measurements for pore and trabeculae diameter were carried out if possible (scale bar = 10 µm)

The results are presented in form of box plots or histograms, including minimum and maximum values for a specific position inside the spine, marked by a number later in the figures (Figure 11). Outliers, meaning values that are numerically distant from the rest of the data set, are indicated by a star and marked by a number which represents the line number inside the software. A box-plot provides an easy summary for the distribution of data with their minimum and maximum values. The box stretches from the lower hinge (the 25 % percentile) to the upper hinge (the 75 % percentile) and contains about 50 % of the values. The median is shown as a line across the box, meaning that 50 % of values are smaller or equal of this value. Other statistical data was presented using Microsoft Excel 2007.

The histogram (Figure 11 right) is used for a graphical display of frequencies, shown as upright bars in the Figure. The Gaussian distribution can be added, displayed as a black line. With the SPSS software also the skewness coefficient and the kurtosis were measured. The skewness coefficient gives information about the symmetry of the investigated data sets around the mean value (Untersteiner 2007).

Skewness = 0 = symmetric, normal distribution

Skewness = < 0 = negative skewness, long tail in the negative direction (to the left)

Skewness = > 0 = positive skewness, long tail in the positive direction (to the right)

The kurtosis gives information about the peakedness of flatness of a distribution compared to the normal distribution.

Kurtosis = 0 = normal distribution (mesokurtic)

Kurtosis = < 0 = tends to be more on a plateau, lighter tails (platykurtic)

Kurtosis = > 0 = relative peaked distribution, higher tails (leptokurtic)

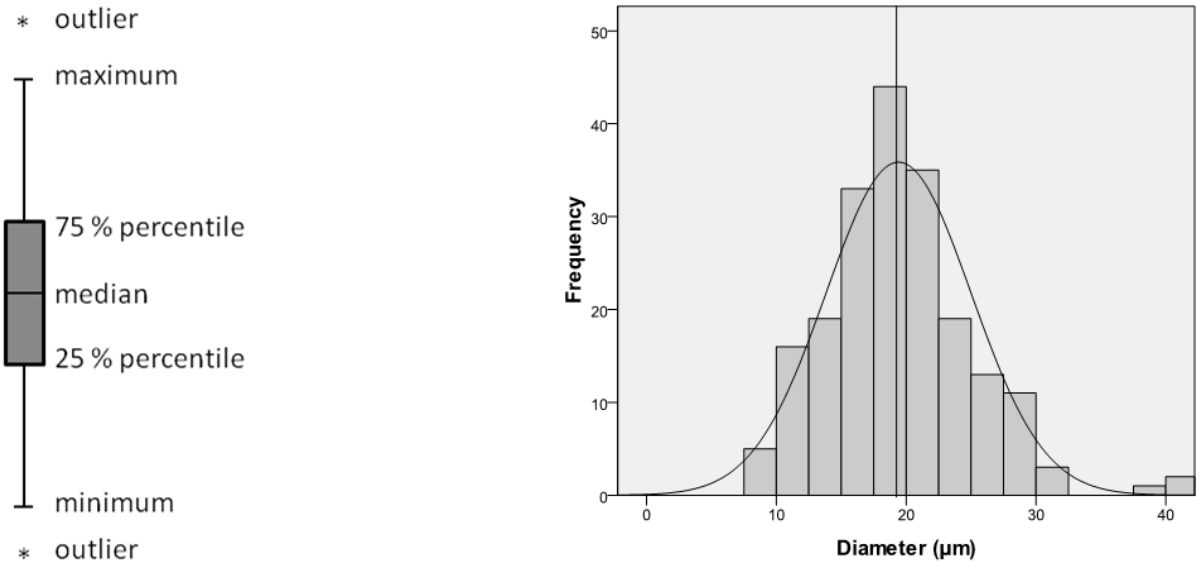

Figure 11: A box plot (left side) and a histogram (right side) used in the SPSS program: The box plot includes the median, minimum and maximum values of the data set and the outliers, as well as the area where 25% and 75% of the values are lying. The histogram includes the frequencies, and the distribution curve as well as the mean value (dark line vertical to the x-axis)

3. Results

Primary spines of six sea urchin species were thoroughly investigated (*Plococidaris verticillata*, *Phyllacanthus imperialis*, *Eucidaris metularia*, *Prionocidaris baculosa*, *Heterocentrotus mammillatus* and *Echinometra mathaei*) (Table 3).

Table 3: Classification of the investigated sea urchin species (based on Schultz 2006)

Tribe Echinodermata

Subphylum Eleutherozoa
Superclass Cryptosyringida

Class Echinoidea
- Subclass Euechinoidea
- Superorder Echinacea
- Order Echinoida
  - Family Echinometridae
  - Genus *Echinometra*
    - *E. mathaei*
  - Genus *Heterocentrotus*
    - *H. mammillatus*

- Subclass Perischoechinoidea
- Order Cidaroida
  - Family Cidaridae
    - Genus *Eucidaris*
      - *E. metularia*
    - Genus *Prionocidaris*
      - *P. baculosa*
    - Genus *Plococidaris*
      - *P. verticillata*
    - Genus *Phyllacanthus*
      - *P. imperialis*

3.1 Cidaroid spines: Surface morphology

The cortex in cidaroid spines may have different surface structures, for example perforations, nodules and pores (Figure 12). A surface sculpturing with flattened nodules is found in primary spines of *Plococidaris verticillata* (12A). Porous nodules are present in *Phyllacanthus imperialis* (12B). *Prionocidaris baculosa* has a crenulated structure in rows (12C). These crenulations themselves have thorny outgrowths. *Eucidaris metularia* has nodules arranged in distinct rows, with pores surrounding the nodules (12D).

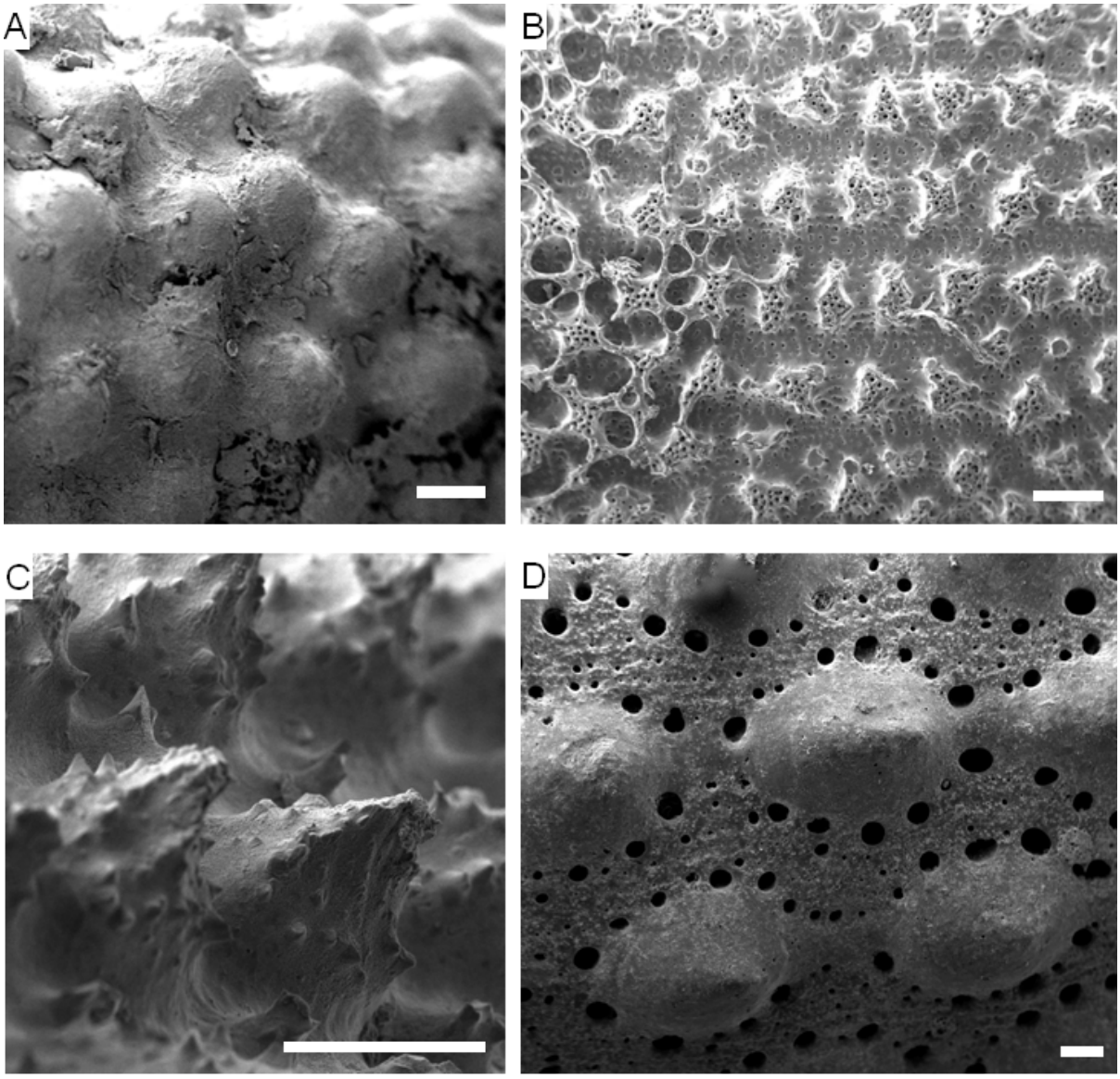

Figure 12: Surface sculpturing of several primary spines: A) *Plococidaris verticillata*, B) *Phyllacanthus imperialis*, C) *Prionocidaris baculosa* and D) *Eucidaris metularia* (scale bar = 1 mm)

3.1.1 *Plococidaris verticillata*

Primary spines of *Plococidaris verticillata* can grow up to 20 mm, the test diameter of the sea urchin is about 30 mm. Distributed around the Indo-Pacific, these sea urchins live mostly in reef systems but can also occupy sandy substrates. The successive whorls (up to four) with sharp ridges are characteristic for the spines. Randomly arranged smaller thorns are distributed between the sharp ridges. The spine culminates in a crown like structure at the tip (Figure 13). The spines from the oral side of the test lack whorls.

Figure 13: Primary spine *of Plococidaris verticillata* (scale bar = 5 mm)

A spine of *Plococidaris verticillata* is shown in longitudinal section with several areas in detail (Figure 14). The cortex present as a thick outermost layer is microperforate with small canals (diameter 10 µm) which extent to the exterior. The thickness of the cortex ranges from ~ 80 µm at the base, 60 to 70 µm on the flanks and at the tip ~ 80 µm. Figure 14A & B show the medulla and part of the cortex at the tip. In Figure 14C & D the regular arrangement of the pores of the radiating layer is visible. Figure 14E & F show the medulla with a regular arrangement of the stereom at the beginning of the shaft. The radiating layer of *Plococidaris verticillata* consists of galleried stereom (long parallel galleries connected to one another). The galleries are inclined to the medulla with a degree of around 45°. More images of the stereom of *Plococidaris verticillata* in the supplement (Plate 2).

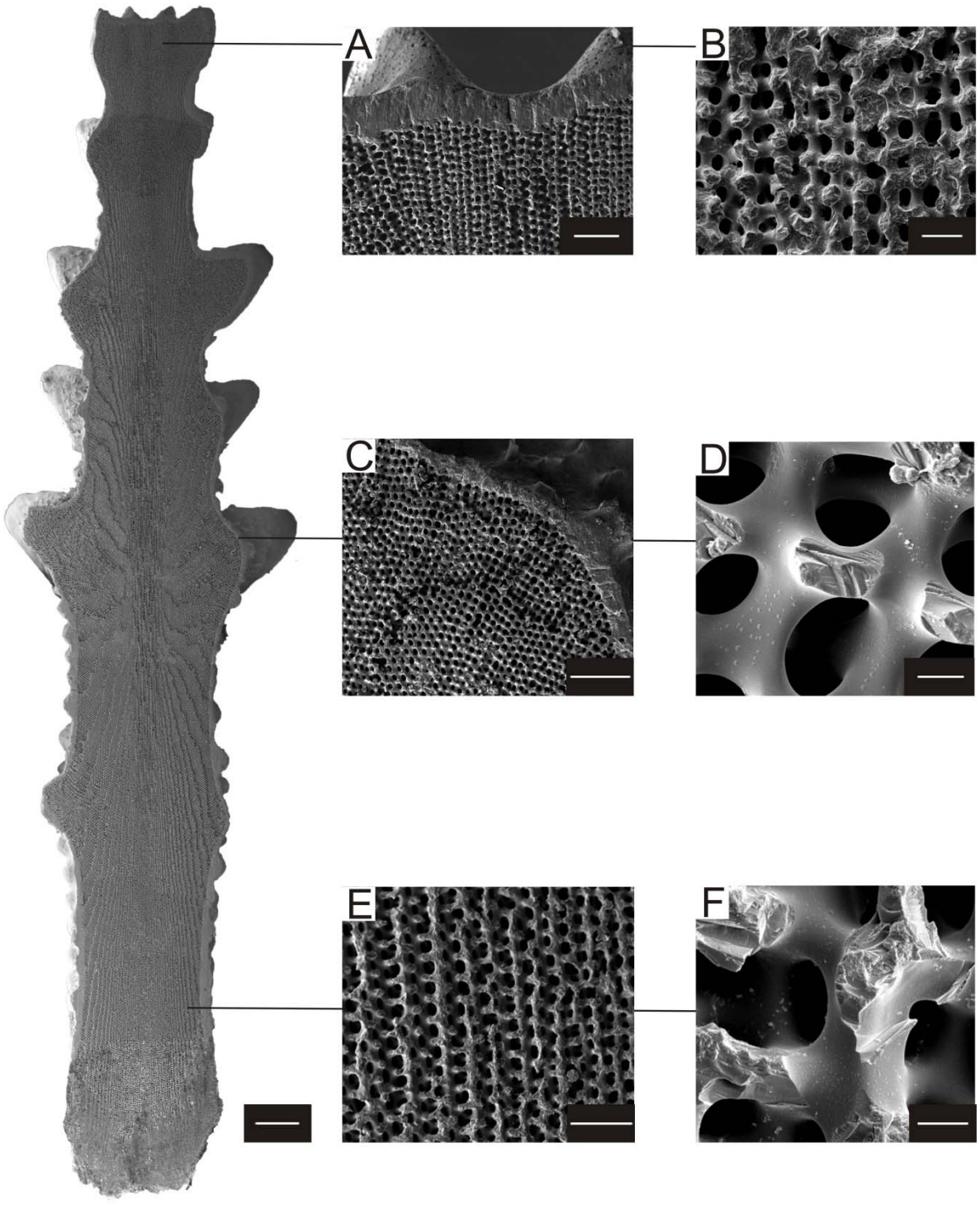

Figure 14: Compiled SEM image of a longitudinal section of a primary spine of *Plococidaris verticillata* (length 25 mm) including detailed stereom views: A = uppermost part of the medulla, finalised by the cortex, beside the medulla is the radiating layer, B = detailed view of the medulla, C = radiating layer finalised by the cortex, D = detailed view of the radiating layer, E = Medulla and F = detailed view of the medulla (scale bars: spine = 600 µm; A = 100 µm; B = 20 µm; C = 200 µm; D = 10 µm; E = 200 µm; F = 10 µm)

3.1.2 *Plococidaris verticillata*: Medulla

First, the pore size were measured and displayed by a box-plot. The Figure also includes a frontal view of the investigated spine to display the positions were the measurements have been carried out (Figure 15). The mean pore size in the medulla is 109.3 µm². The pore size decreases from 187.8 µm² at the base (1), followed by lower values at position 2 & 3, increasing to 116.5 µm² at position (4), ending with 57.8 µm² at the tip (5) of a spine. Several outliers appear in the box-plot.

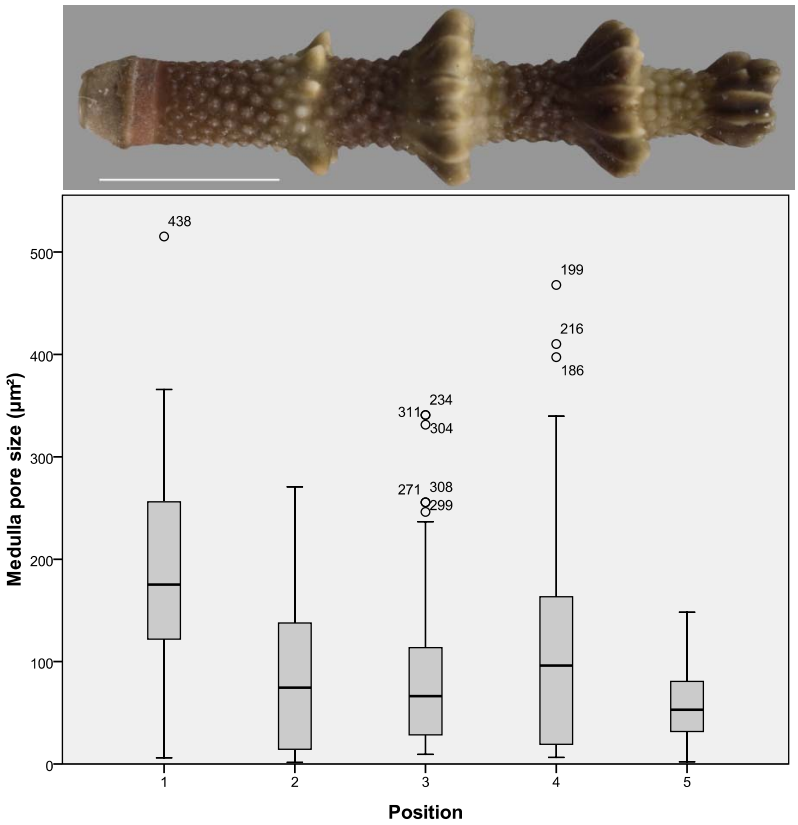

Figure 15: Box-plot of the pore size in the medulla of *Plococidaris verticillata*

In Figure 16 the values of the pore diameter of the medulla from different positions, e.g. the base (1), shaft (2 - 4) and tip (5) are shown. 120 pores of a spine of *Plococidaris verticillata* were investigated. A mean pore diameter of 17.7 ± 6.0 µm is observed in the medulla. The pore diameter at the base (Figure 16, position 1) is 22.7 µm, following 21.1 µm and then decreases to the tip (position 5) to 9.7 µm. Only a few outliers are observed, due to the box-plot. The largest range of values is found in the middle of the shaft (position 2 - 4).

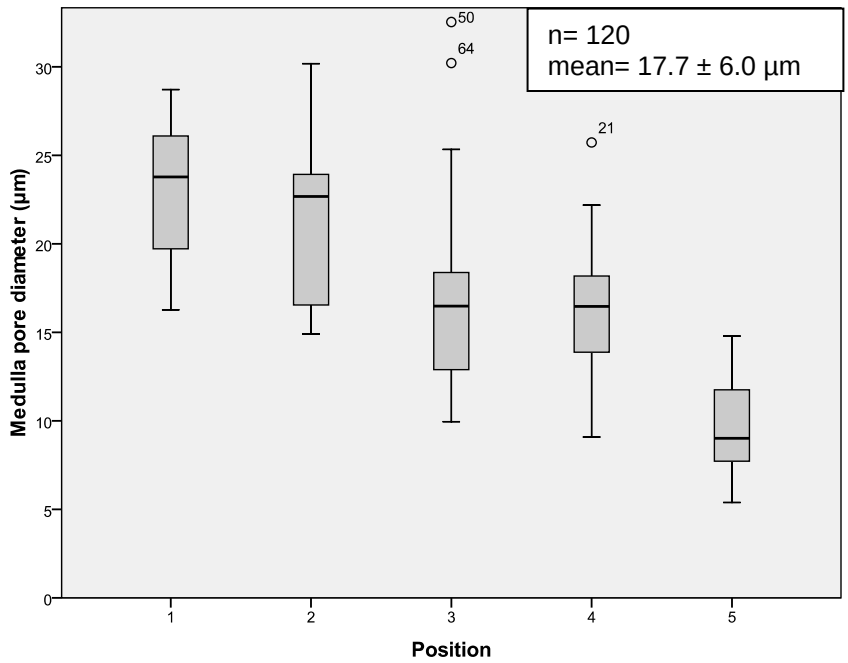

Figure 16: Box-plot of the pore diameter in the medulla of *Plococidaris verticillata*

The histogram shows the distribution curve and frequencies of the values (Figure 17). The values are distributed between 5 and 33 µm. The curve shape is bell-shaped. The skewness is positive at 0.171. A negative kurtosis is observed (- 0.618), meaning that distribution is platykurtic. The most frequent (17) pore size is around 17 µm.

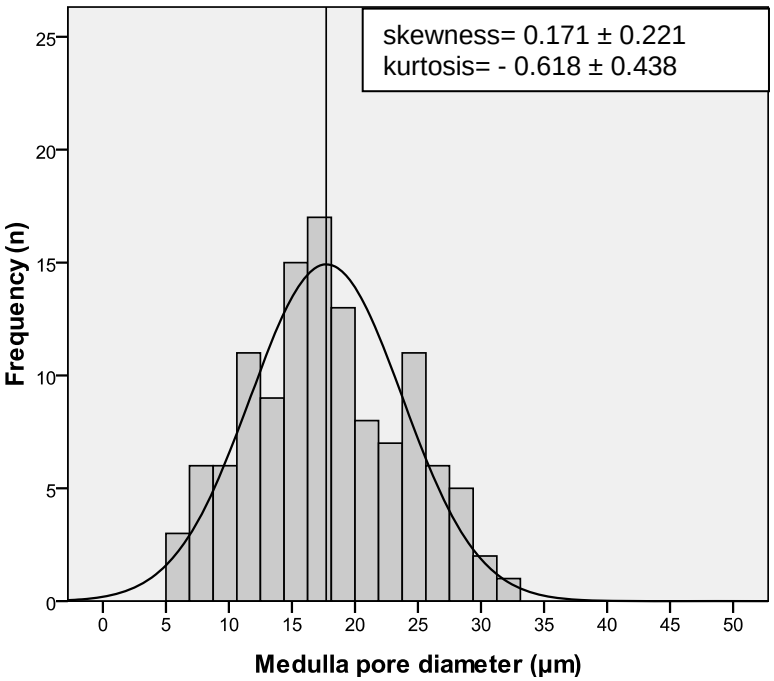

Figure 17: Histogram of the pore diameter in the medulla of *Prionocidaris verticillata*

A mean trabeculae diameter in *Plococidaris verticillata* spines of 14.9 ± 4.4 µm is observed in the medulla (n = 120), begining with 11.7 µm (1) and staying more or less in that amount, ending at the tip (5) with 12.4 µm (Figure 18). The trabeculae diameter is always lower than that of the pore diameter (except on position 4 & 5).

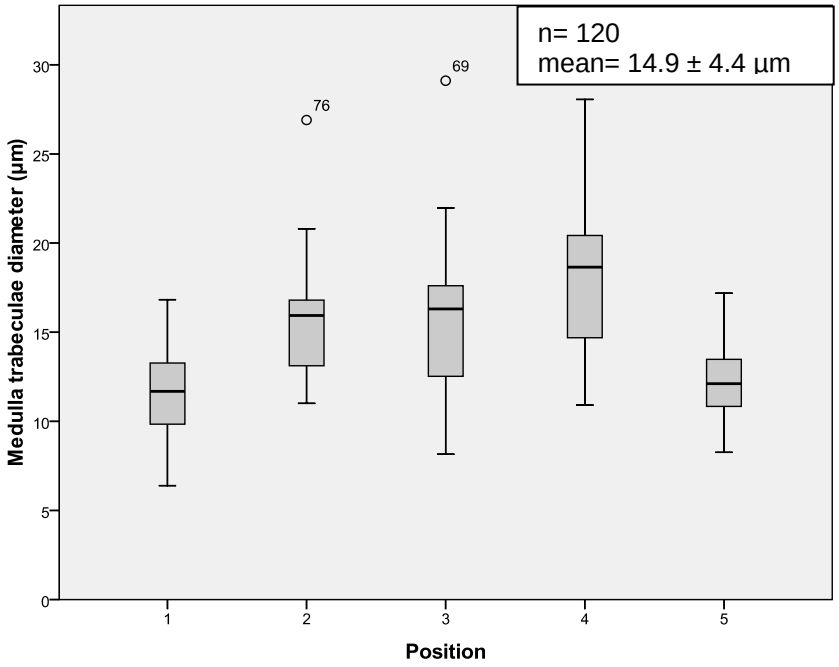

Figure 18: Box-plot of the trabeculae diameter in the medulla of *Plococidaris verticillata*

The histogram shows the distribution curve and frequencies of the values, ranging from 5 to 30 µm (Figure 19) with the most common ones at a frequency of 23. A skewness of 0.867 is observed, the curve is steep bell-shaped. The leptokurtic kurtosis is 1.014.

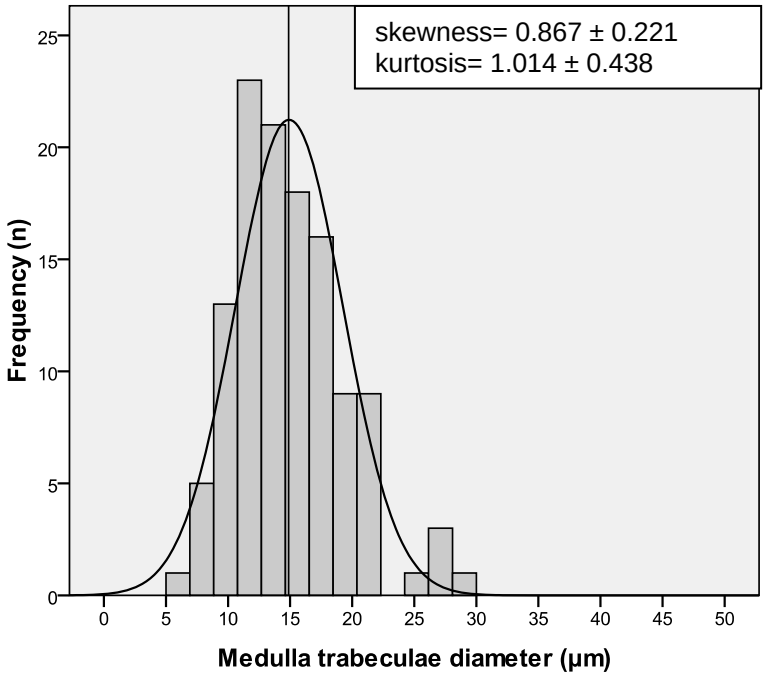

Figure 19: Histogram of the trabeculae diameter in the medulla of *Plococidaris verticillata*

3.1.3 *Plococidaris verticillata*: Radiating layer

The mean pore size in the radiating layer is 79.0 µm², beside some outlier (Figure 20). The pore size decreases from the base (1) with 183.3 µm² to the tip (5) with 67.1 µm².

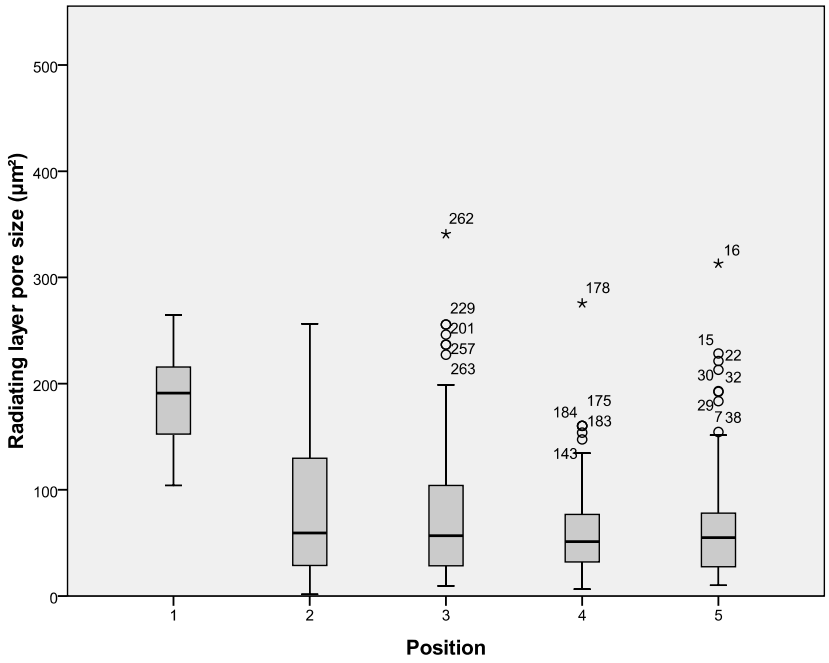

Figure 20: Box-plot of the pore size in the radiating layer of *Plococidaris verticillata*

A mean pore diameter of 17.7 ± 5.3 µm is observed in the radiating layer of *Plococidaris verticillata* spines (n = 127) (Figure 21). The pore diameter at the base (1) is 19.8 µm, followed by 18.8 µm then decreases to the tip (5) to 11.1µm.

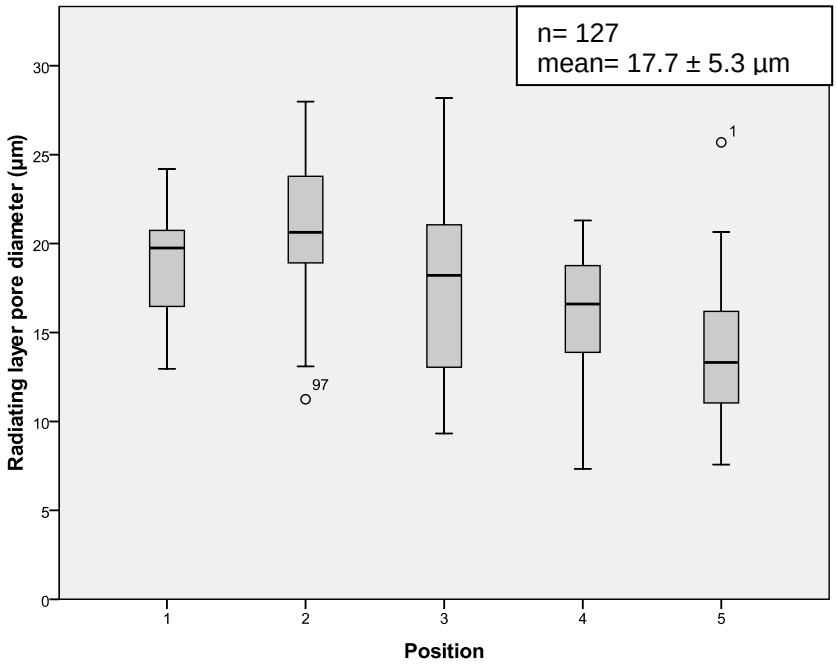

Figure 21: Box-plot of the pore diameter in the radiating layer of *Plococidaris verticillata*

The values of the pore diameter range from around 6 to 30 µm, the most common diameter (= 17 µm) with a frequency of 23 (Figure 22). A skewness of 0.802 is observed as well as a kurtosis of 2.292. The curve is bell-shaped with leptokurtic distribution.

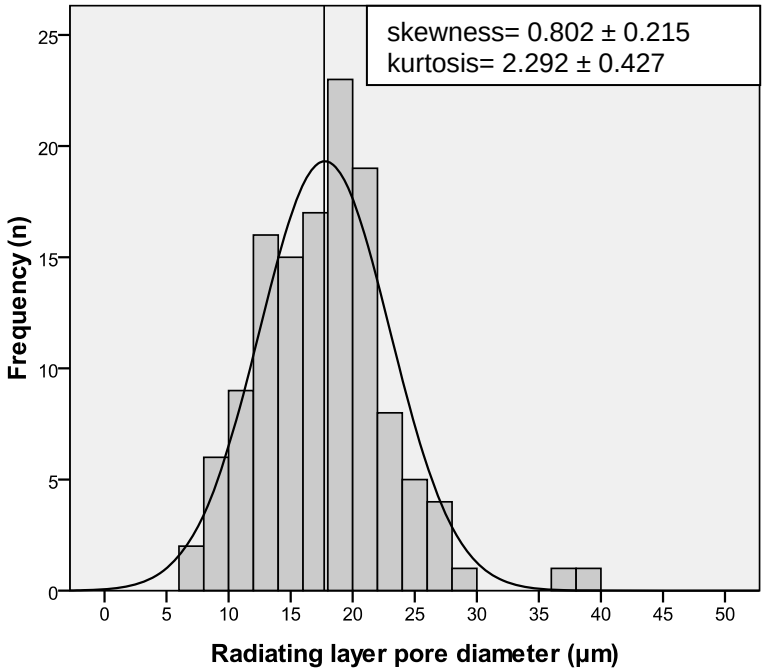

Figure 22: Histogram of the pore diameter in the radiating layer of *Plococidaris verticillata*

The trabeculae diameter (n = 127; mean pore diameter 14.2 ± 4.5 µm) begins with 20.9 µm at the base (1) and stays more or less in that concentration, ending at the tip (5) with 14.2 µm (Figure 23).

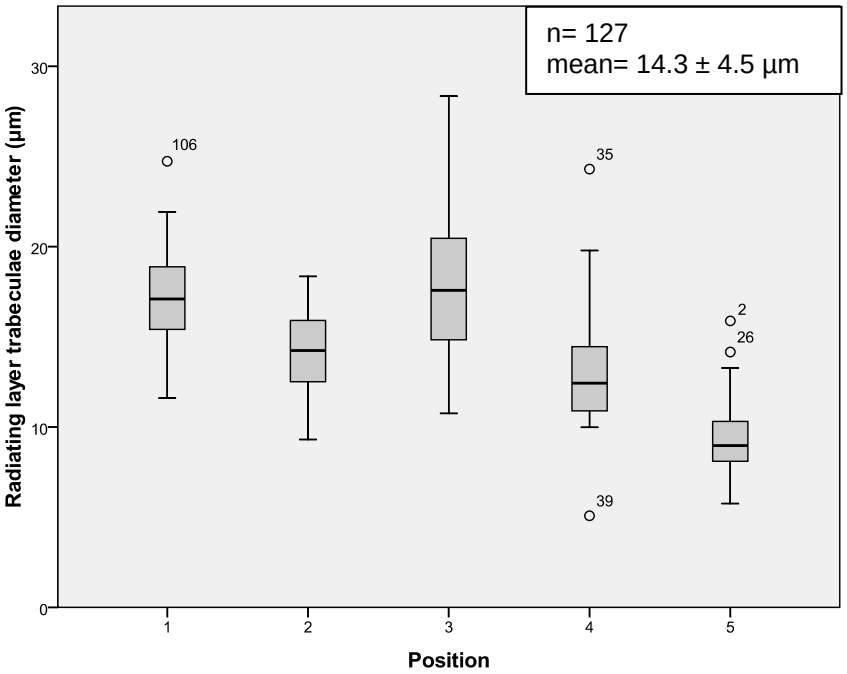

Figure 23: Box-plot of the trabeculae diameter in the radiating layer of *Plococidaris verticillata*

The frequencies of the trabeculae diameter are shown in Figure 24 with values distributed between 5 to 30 µm the curve is bell-shaped but steep. The most common diameter with ~ 10 µm has a frequency of almost 25. A skewness of 0.361 with a leptokurtic kurtosis of 0.111 is observed.

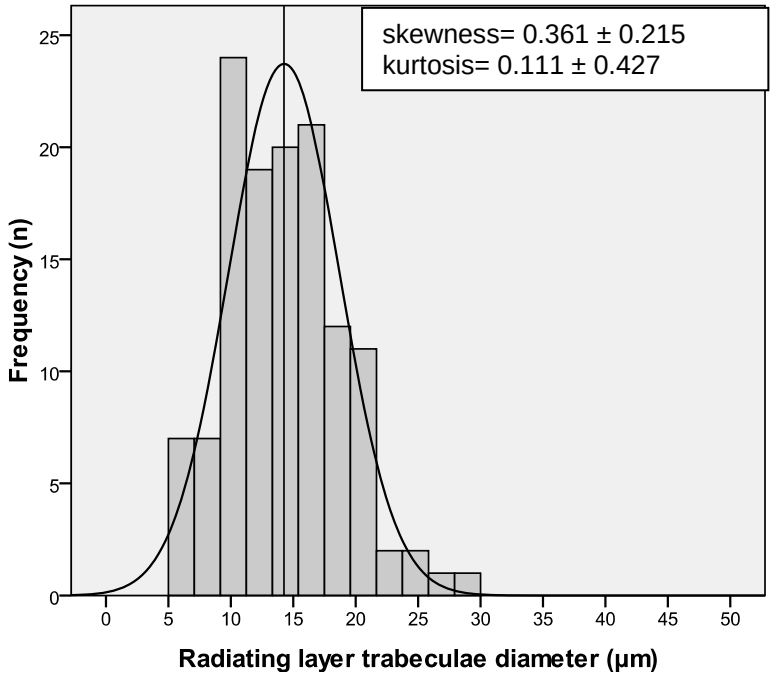

Figure 24: Histogram of the trabeculae diameter in the radiating layer of *Plococidaris verticillata*

3.2 *Phyllacanthus imperialis*

Primary spines of *Phyllacanthus imperialis* are thick, cylindrical and about as long as the diameter of the test (wide 80 mm) (Figure 25). It inhabits littoral zones in the Indo-Pacific in depths of up to 70 m.

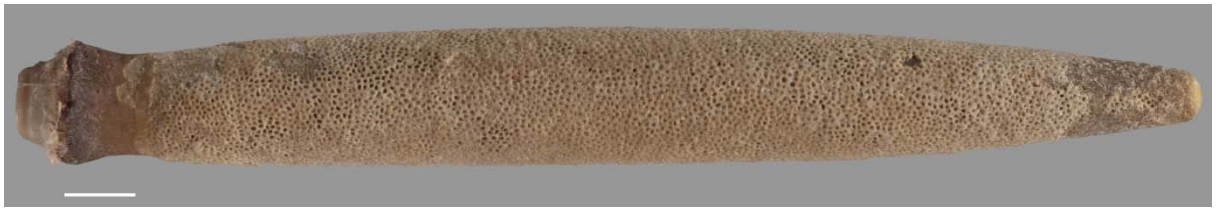

Figure 25: Encrusted primary spine of *Phyllacanthus imperialis* (scale bar = 5 mm)

3.2.1 *Phyllacanthus imperialis*: Oral spines

Figure 26 shows an oral spine in longitudinal section with some detailed views of the stereom (26A – C). Figure 26A displays the medulla in the upper part of the shaft near the tip. Figure 26B shows the galleried stereom of the radiating layer. The base is also galleried which is also present in the different layered structure in Figure 26C. The cortex thickness of an oral spine begins with 129.2 µm, and increases up until the tip to about 200.6 µm. More images of the stereom of *Phyllacanthus imperialis* in the supplement (Plate 3).

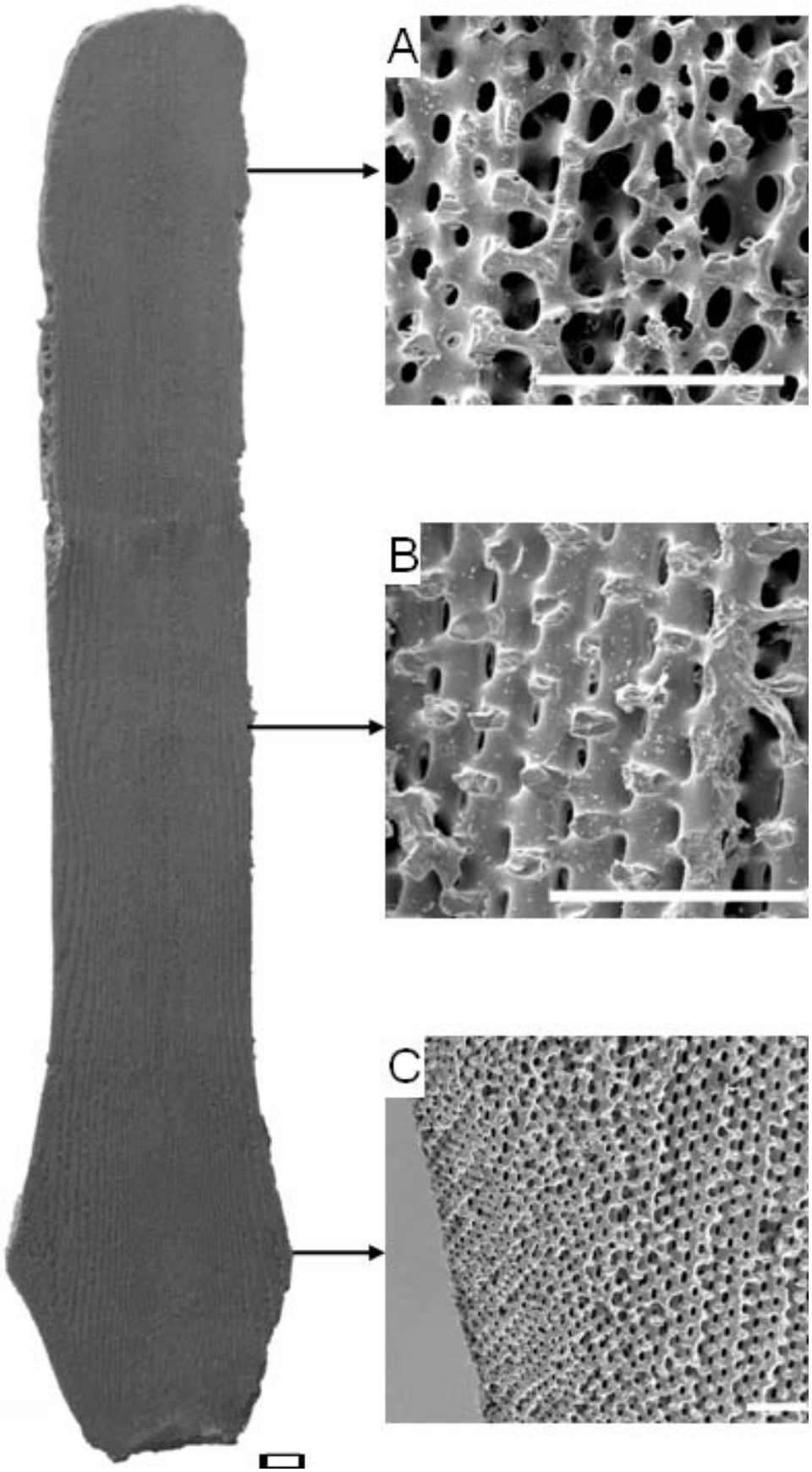

Figure 26: Compiled SEM image of longitudinal section of an oral primary spine of *Phyllacanthus imperialis* with detailed stereom: A= medulla near the tip; B = radiating layer, C = base with radiating layer (spine scale bar = 500 µm & detail scale bars = 100 µm)

3.2.2 *Phyllacanthus imperialis*: Medulla

The distribution of the pore size throughout the spine is seen in Figure 27. The mean pore size is 128.4 µm². The pore size decreases from the base (202.4 µm²) to the tip (101.5 µm²). A large number of outliers is present.

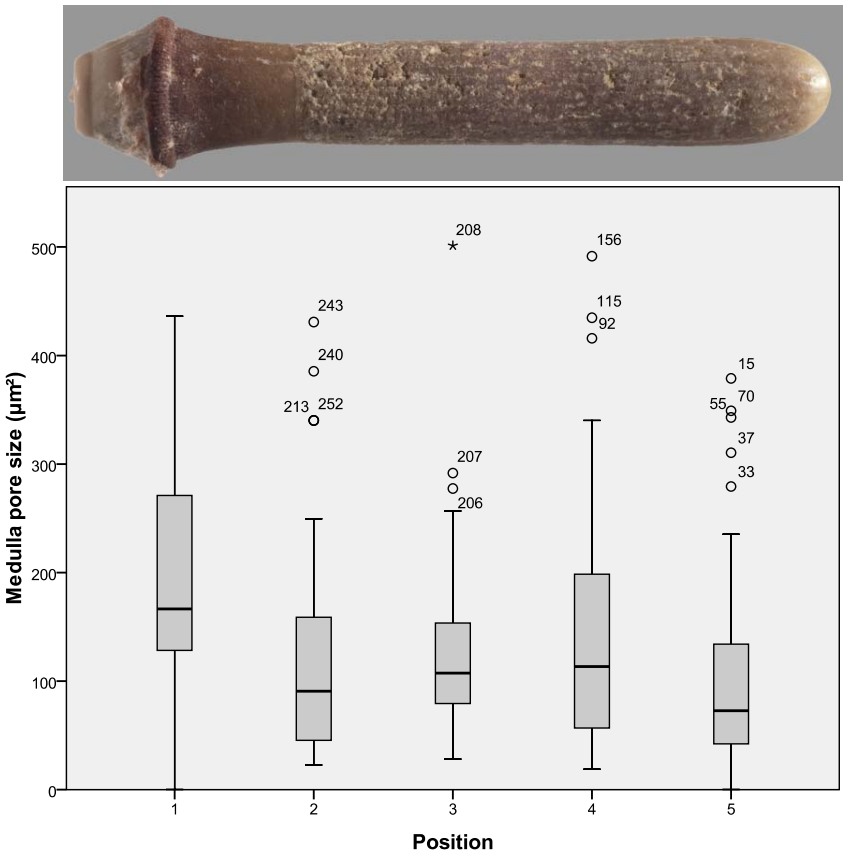

Figure 27: Box-plot of the pore size in the medulla of *Phyllacanthus imperialis*

The results of the pore diameter measurements (n = 127) of the medulla in oral spines of *Phyllacanthus imperialis* is shown in Figure 28. A mean pore diameter of 18.6 ± 5.0 is observed, with values ranging from 19.7 µm at the base (1), decreasing to 15.7 µm at the shaft (3), to the tip (5) with 15.9 µm.

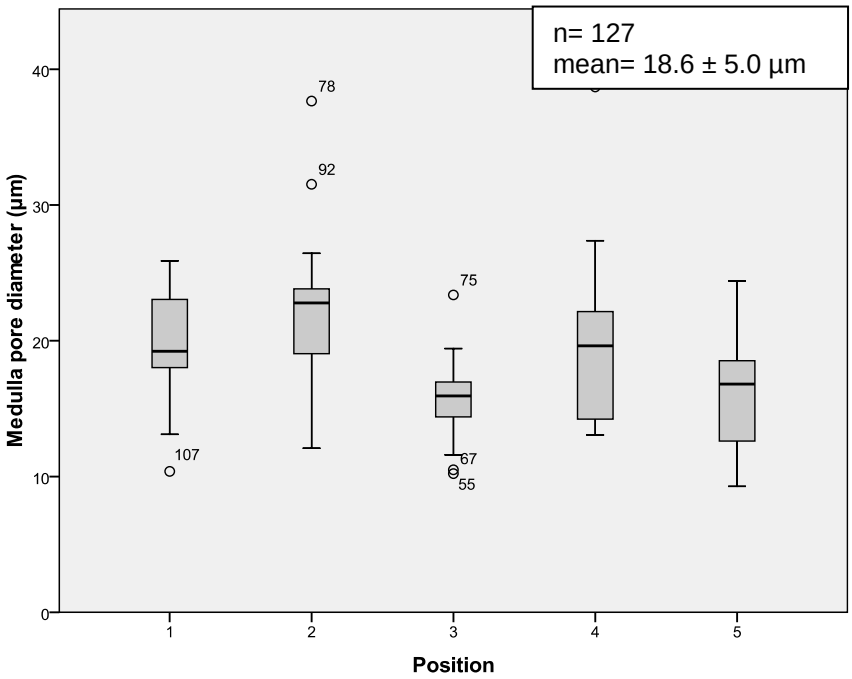

Figure 28: Box-plot of the pore diameter in the medulla of *Phyllacanthus imperialis*

The frequencies of the pore diameter, displayed in Figure 29, reach values up to 25. The most common diameter with its highest frequency is observed near 20 µm. The pore diameters range from 7 to 40 µm. A skewness of 0.908 is observed with a kurtosis of 2.2. This results in a bell-shaped curve with a leptokurtic distribution.

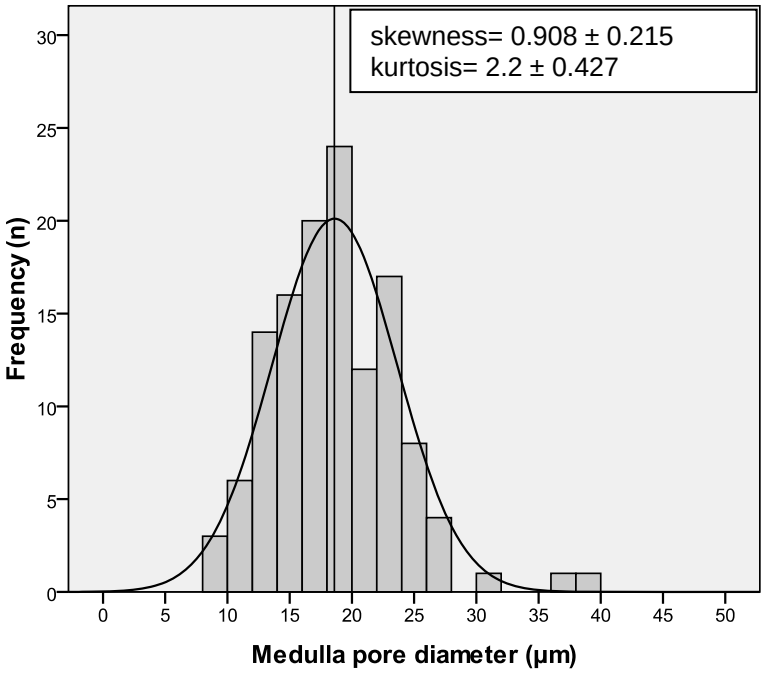

Figure 29: Histogram of the pore diameter in the medulla of *Phyllacanthus imperialis*

The values (n = 127) of the trabeculae diameter of the medulla of *Phyllacanthus imperialis* have a mean diameter of 13.6 ± 3.9 µm (Figure 30). The trabeculae diameter in the medulla are close together, beginning at the base (1) with 14.3 µm, then 15.4 µm (2), lowering to 11.9 µm (3), 15.1 µm (4) and ending with 11.0 µm at the tip (5).

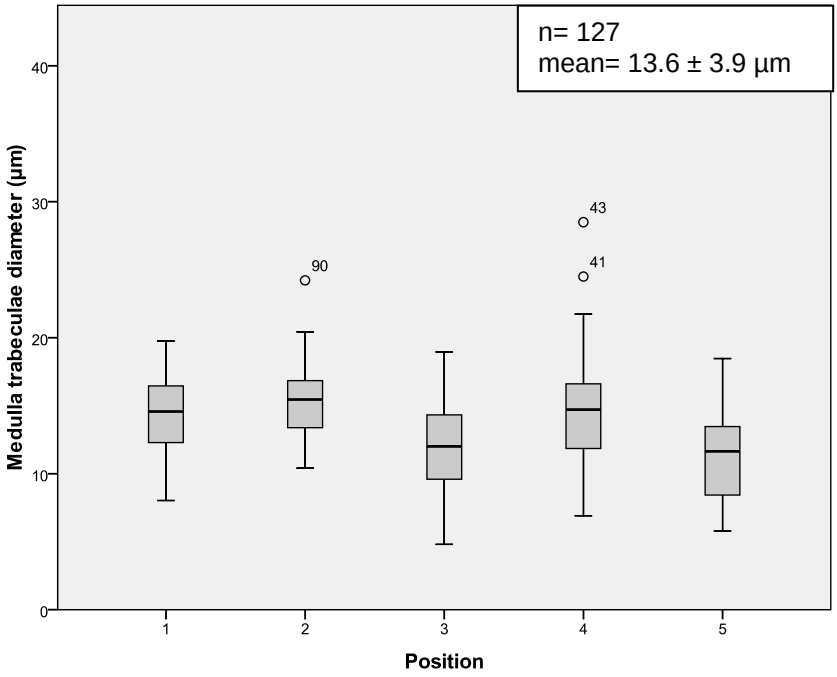

Figure 30: Box-plot of the trabeculae diameter in the medulla of *Phyllacanthus imperialis*

Figure 31 shows the frequencies of the trabeculae diameter with values range from 5 to 30 µm, the most common diameter has a frequency of 27. A skewness of 0.585 is observed with a leptokurtic kurtosis of 1.071, resulting in a bell-shaped curve.

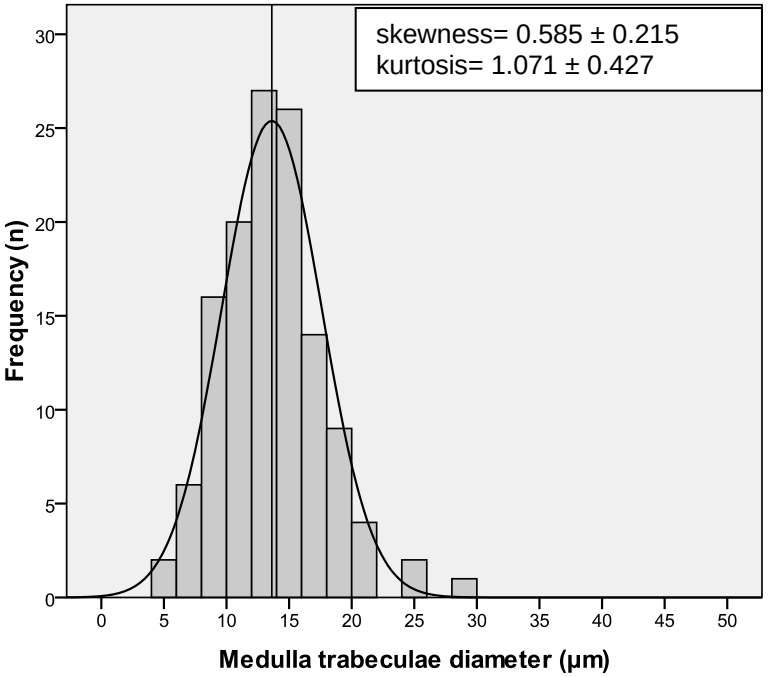

Figure 31: Box-plot of the trabeculae diameter in the medulla of *Phyllacanthus imperialis*

3.2.3 *Phyllacanthus imperialis*: Radiating layer

The radiating layer of *Phyllacanthus imperialis* has a mean pore size of 104.1 µm², beginning with 133.1 µm² at the base (Figure 32, position 1) and ending with 66.8 µm² at the tip (Figure 32, position 5). Positions 1 and 3 have the largest distribution of values. Several outliers occur for each position.

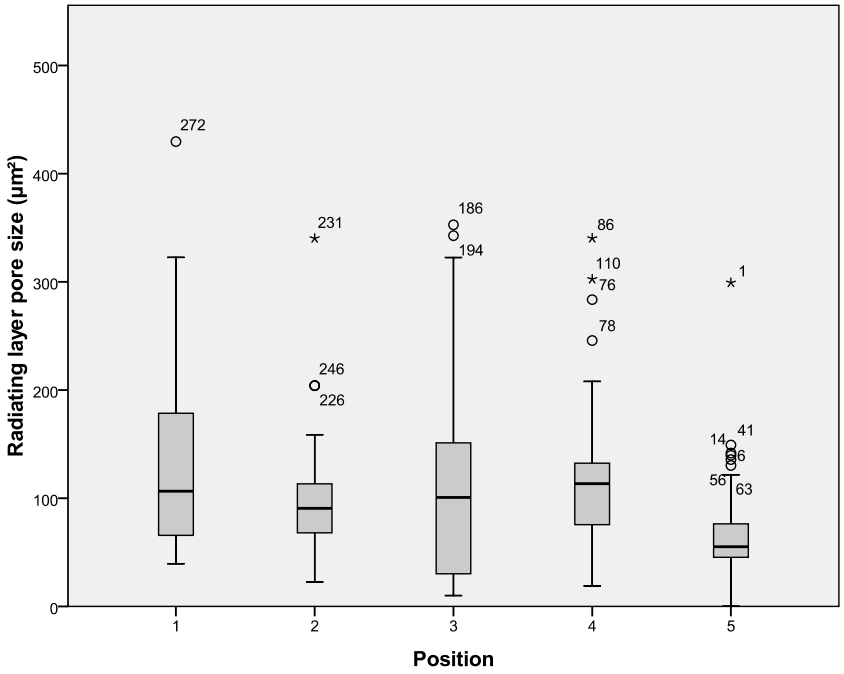

Figure 32: Box-plot of the pore size in the radiating layer of *Phyllacanthus imperialis*

The course of the pore diameter in the radiating layer, as shown in Figure 33, has a mean of 16.0 ± 3.6 µm. The values of pore diameter for the positions in the spine are close together (n= 124), beginning with 16.7 µm at the base (1), then 17.9 µm (2), over 17.1 µm (3) and 13.0 µm (4) to the tip (5) with 15.8 µm.

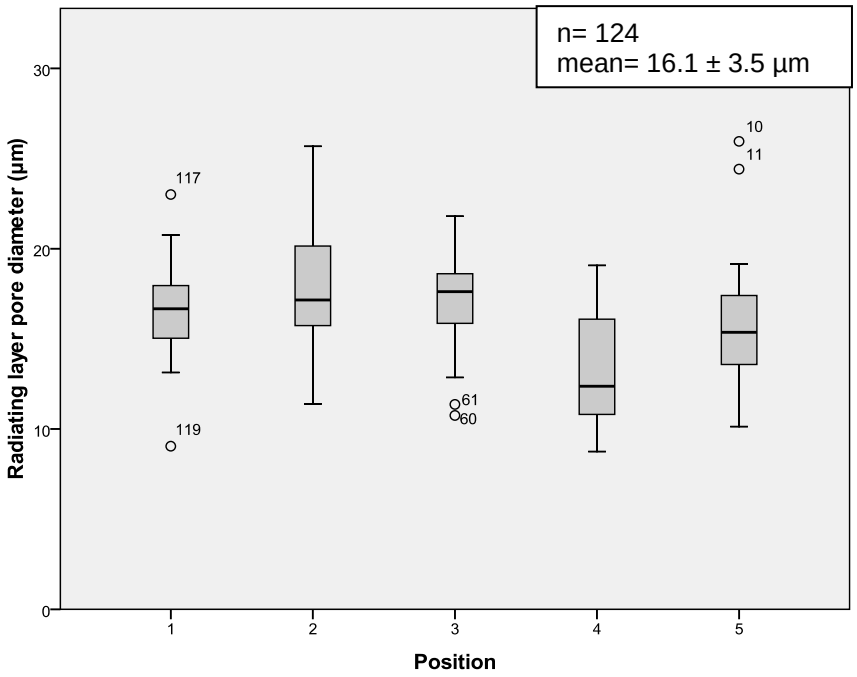

Figure 33: Box-plot of the pore diameter in the radiating layer of *Phyllacanthus imperialis*

The frequencies of the pore diameter, displayed in Figure 34, reach values up to 30. The values of the pore diameter in the radiating layer range from 8 to 26 µm. The skewness is 0.189 with a platykurtic kurtosis of -0.084. This results in a bell-shaped curve.

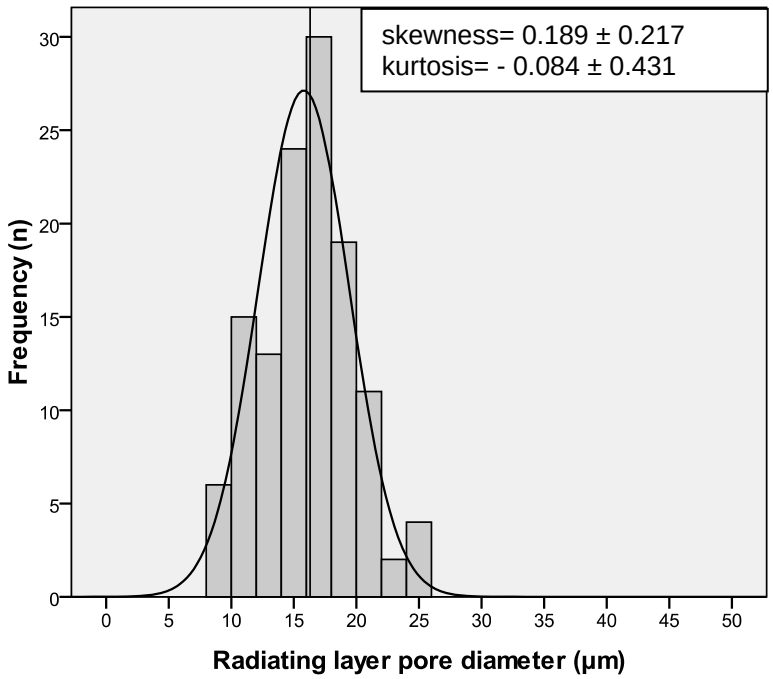

Figure 34: Histogram of the pore diameter in the radiating layer of *Phyllacanthus imperialis*

The mean diameter of the trabeculae diameter of *Phyllacanthus imperialis* is 16.6 ± 3.9 µm (Figure 35, n= 124). The trabeculae diameter begins with 17.8 µm at the base (1), followed by 17.9 µm (2), 19.3 µm (3), 14.5 µm (4) and at the tip of the spine 13.6 µm (5).

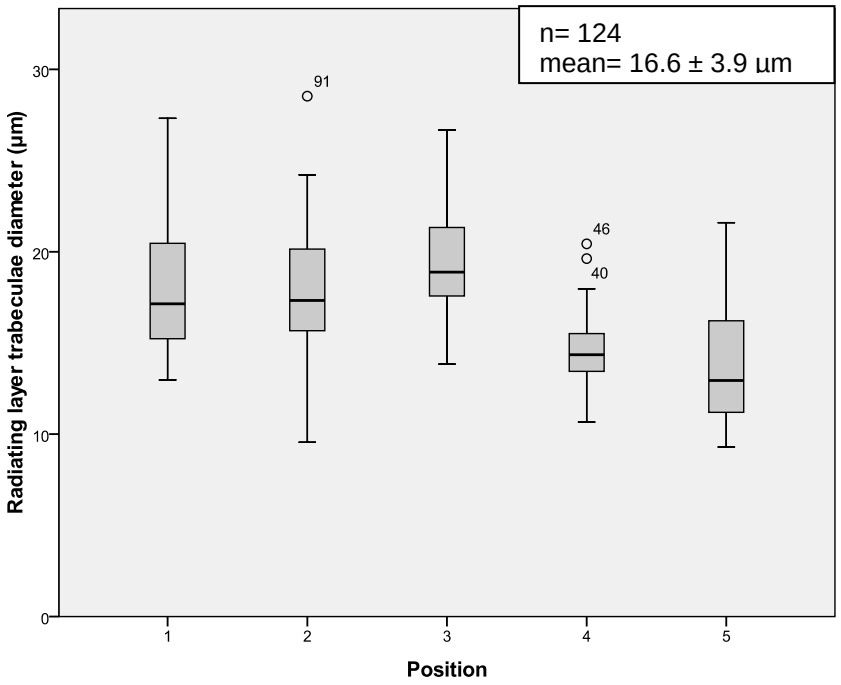

Figure 35: Box-plot of the trabeculae diameter in the radiating layer of *Phyllacanthus imperialis*

The histogram of the radiating layer of *Phyllacanthus imperialis* shows the most common diameter with a frequency of about 20 (Figure 36). The skewness is 0.450 with a kurtosis of 0.004. The curve is bell-shaped with almost mesokurtic distribution of the data.

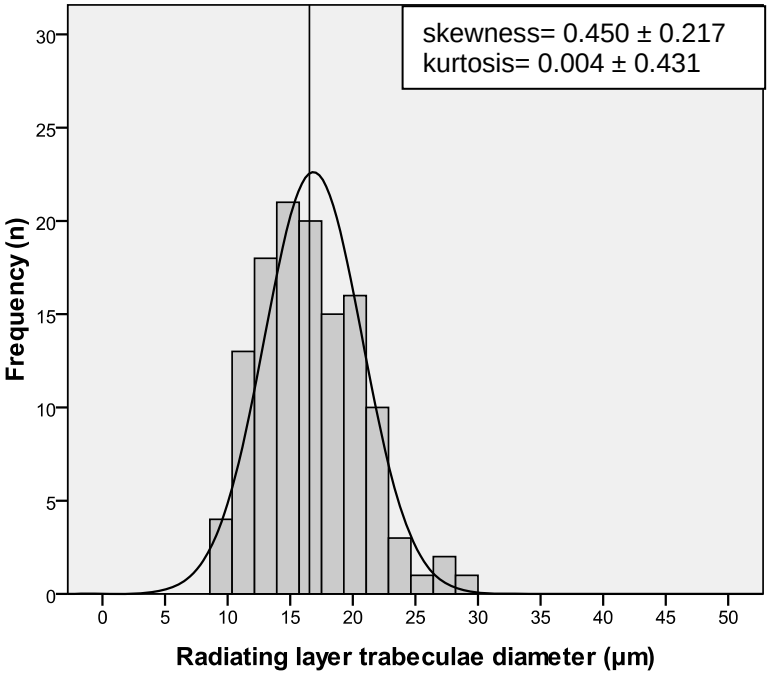

Figure 36: Histogram of the trabeculae diameter in the radiating layer of *Phyllacanthus imperialis*

3.2.4 *Phyllacanthus imperialis* spines (aboral): Medulla

The cortex thickness was measured in aboral spines of *Phyllacanthus imperialis*, beginning with 257.9 µm and increasing to 458.8 µm at the tip. The box-plot for the pore size in the medulla of aboral *Phyllacanthus imperialis* spines shows a mean pore size of 343.9 µm² (Figure 37). The values range from 151.9 µm² at the base (position 1) to 135.1 µm² at the tip (position 10) with some outlier near the upper shaft.

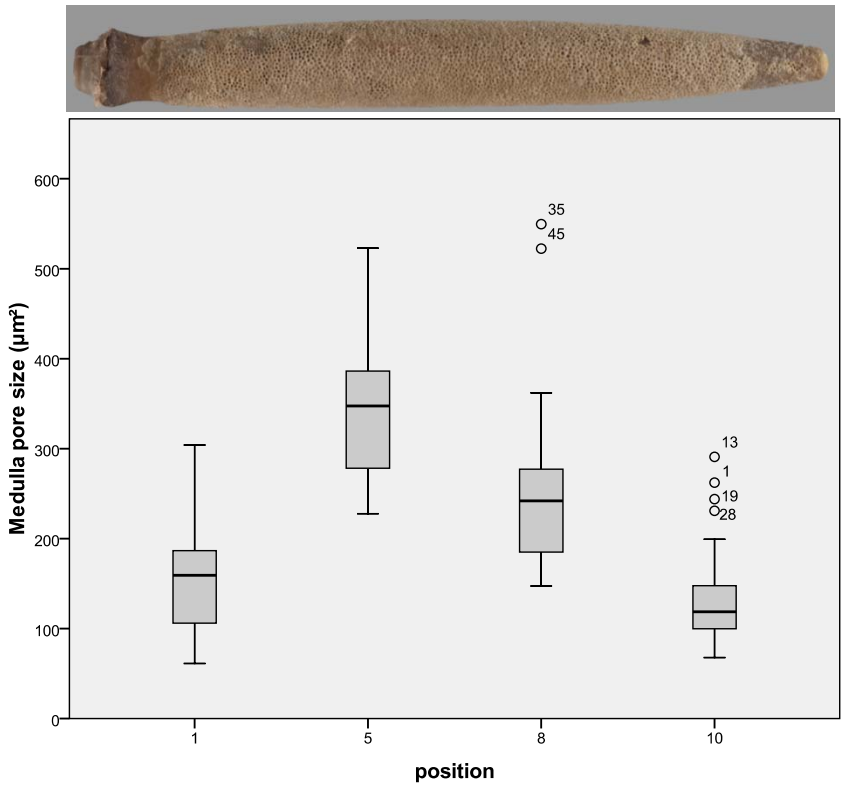

Figure 37: Box-plot of the pore size in the medulla of *Phyllacanthus imperialis*

The pore diameters in the medulla of *Phyllacanthus imperialis* (position 1-10) have a mean pore diameter of 18.6 ± 4.7 µm (Figure 38, n= 117). The values change from the base (1) from 17.6 µm, over around 20.5 µm (5 & 8) to 14.1 µm at the tip (10).

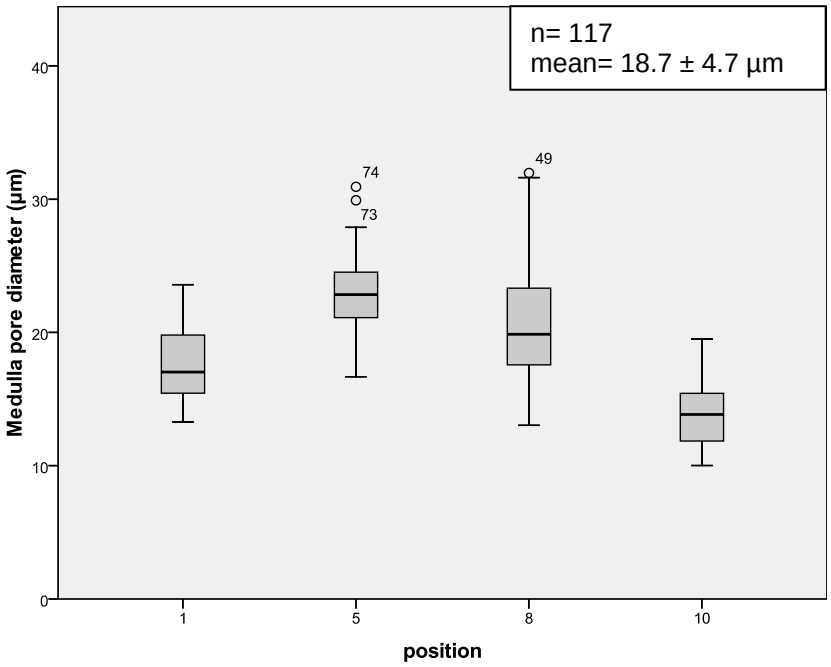

Figure 38: Box-plot of the pore diameter in the medulla of *Phyllacanthus imperialis*

With reference to the histogram (Figure 39) the values are distributed from 10 to 35 µm having the most common one in a frequency of 33. A skewness of 0.466 is observed with a kurtosis of – 0.043, these results in a bell-shaped curve with a platykurtic distribution.

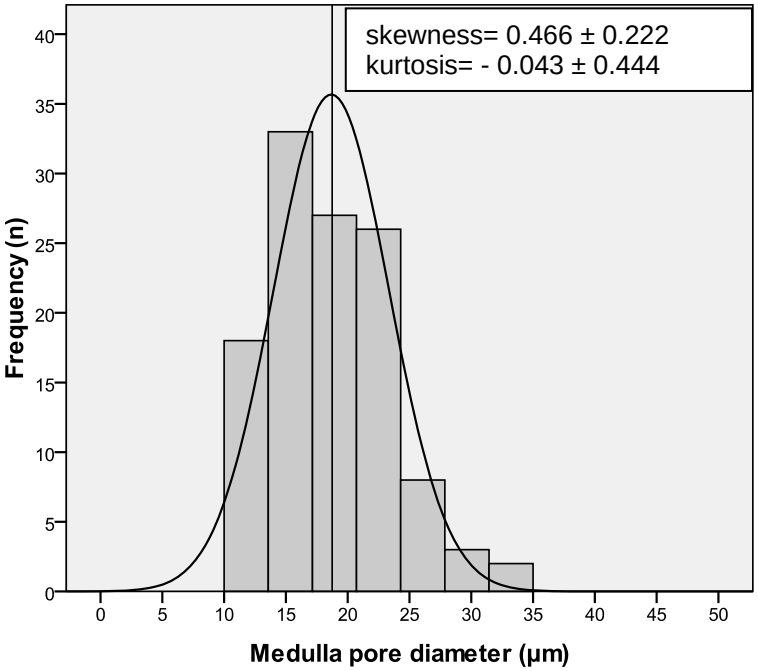

Figure 39: Histogram of the pore diameter in the medulla of *Phyllacanthus imperialis*

The trabeculae diameters in Figure 40 (position 1 - 10) have a mean value of 18.6 ± 5.7 µm (n= 117). The values change from the base (1) beginning with 17.1 µm over around 20.2 µm (5 & 8) to 14.5 µm at the tip (10), meaning the tip has smaller pores than the base.

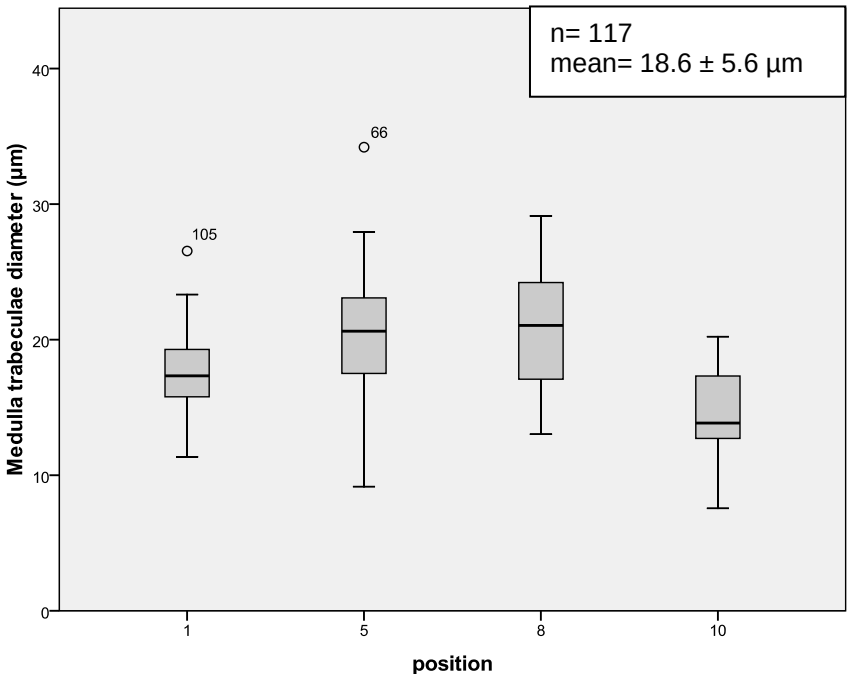

Figure 40: Box-plot of the trabeculae diameter in the medulla of *Phyllacanthus imperialis*

The histogram of the trabeculae diameter of the medulla of *Phyllacanthus imperialis* shows the most common diameters with a frequency of 34 (Figure 41). The values are distributed between 6 and 35 µm. The skewness is 2.174, with a kurtosis of 11.246. The curve is bell-shaped with leptokurtic distribution.

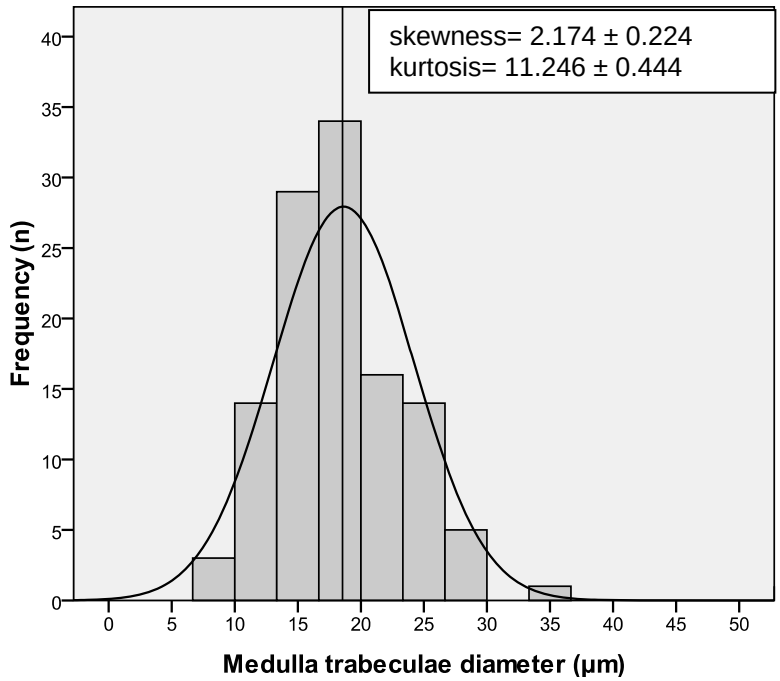

Figure 41: Histogram of the trabeculae diameter in the medulla of *Phyllacanthus imperialis*

3.2.5 *Phyllacanthus imperialis spines* (aboral): Radiating Layer

The pore size in the stereom of the medulla in aboral primary spine ranges from 172.6 µm² at the base (1) to 230.7 µm² at the tip (10), with a mean pore size of 337.0 µm² (Figure 42). A large variation of values occurs in the middle of the spine at position 5.

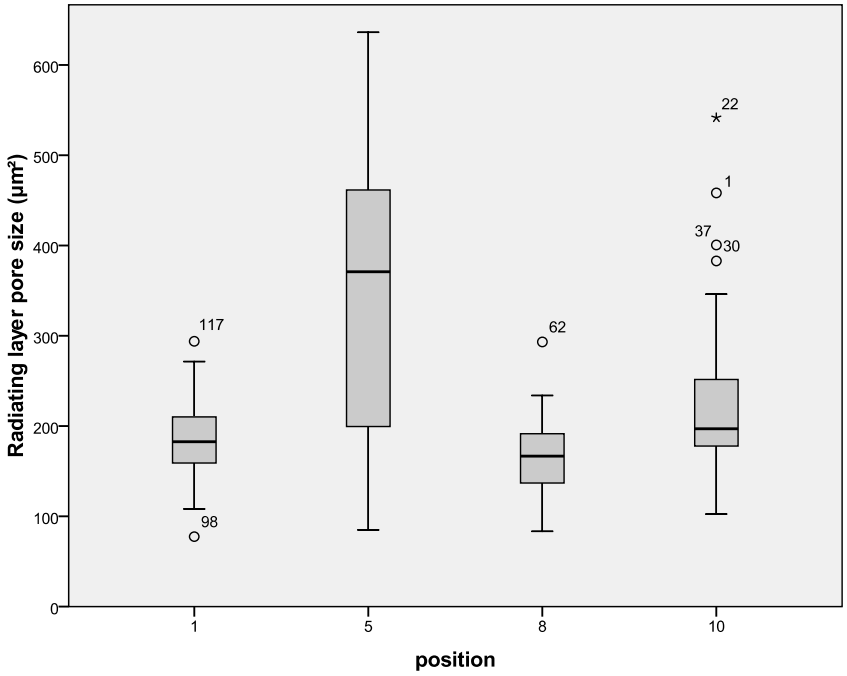

Figure 42: Box-plot of the pore size in the radiating layer of *Phyllacanthus imperialis*

The radiating layer of *Phyllacanthus imperialis* spines in Figure 43 (position 1 - 10) has a mean pore diameter of 20.2 ± 4.7 µm. The values (n = 121) change from the base (1) from 16.8 µm, over around 23.5 µm (5 & 8) to 19.2 µm at the tip (10).

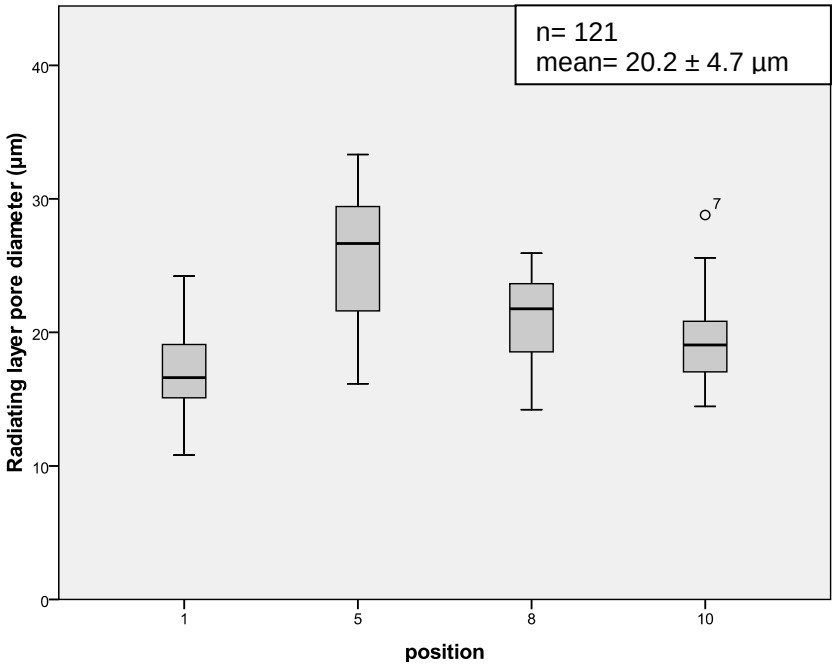

Figure 43: Box-plot of the pore diameter in the radiating layer of *Phyllacanthus imperialis*

The maximum frequencies for the pore diameter in the radiating layer of *Phyllacanthus imperialis* are shown in Figure 44. The most common diameter has a frequency of 21. The values are distributed between 10 and 35 µm. The skewness is 0.595 with a leptokurtic kurtosis of 0.139, resulting in a bell-shaped curve.

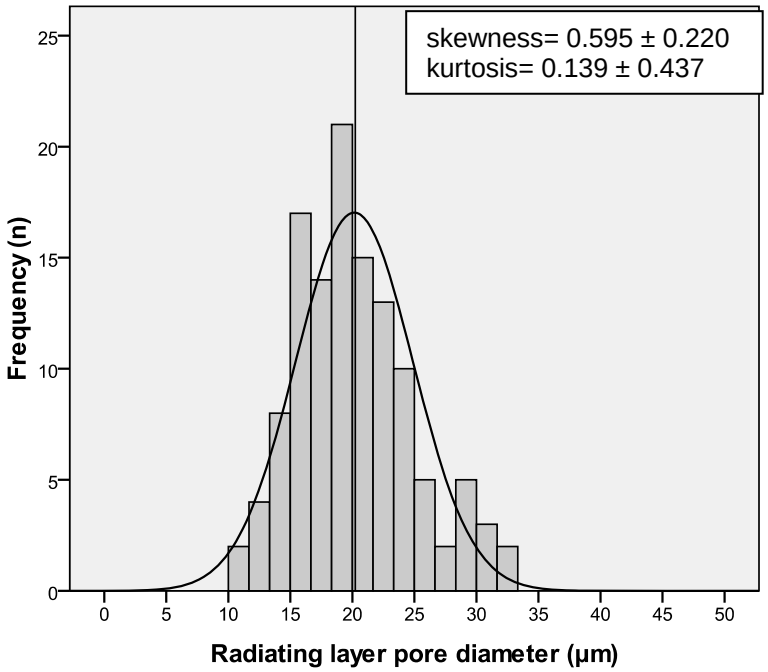

Figure 44: Histogram of the pore diameter in the radiating layer of *Phyllacanthus imperialis*

The trabeculae diameter in the radiating layer of *Phyllacanthus imperialis* (position 1-10) has a mean value of 17.9 ± 4.4 µm (Figure 45). The values (n = 121) change from the base (1) from 14.8 µm, over around 20.5 µm (position 5 & 8) to 17.1 µm at the tip (10).

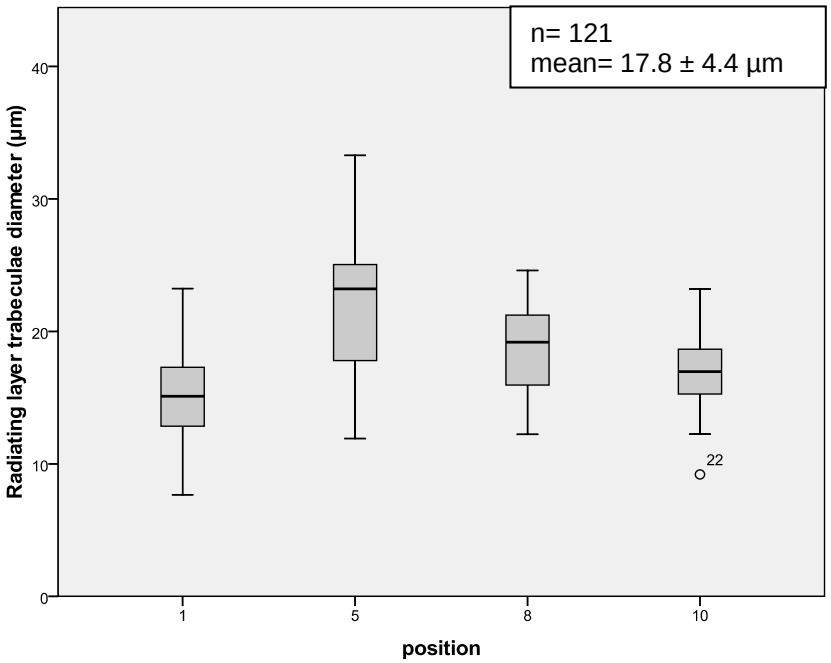

Figure 45: Box-plot of the trabeculae diameter in the radiating layer of *Phyllacanthus imperialis*

Figure 46 shows the histogram for the trabeculae diameter of the radiating layer of *Phyllacanthus imperialis* with values ranging from 7 to 34 µm. The most common diameter has a frequency of 25. As the skewness and the kurtosis have positive values the curve is bell-shaped with a leptokurtic distribution of values.

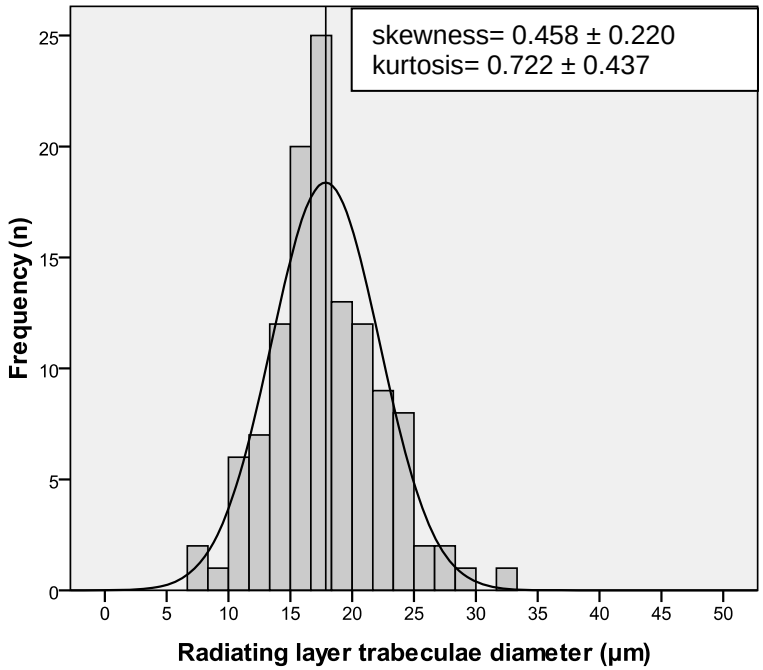

Figure 46: Histogram of the trabeculae diameter in the radiating layer of *Phyllacanthus imperialis*

3.3 *Eucidaris metularia*

Primary spines of *Eucidaris metularia* are cylindrical and shorter than the diameter of the test (Figure 47). The test of the sea urchin has a width of about 30 mm. Specimen are distributed in littoral zones in depths of up to 570 m in the Indo-Pacific.

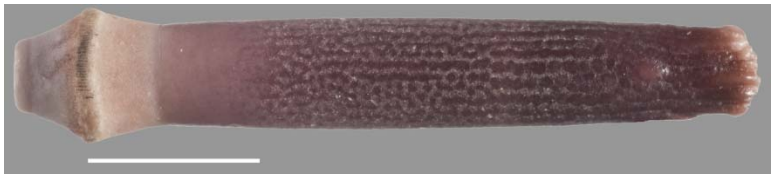

Figure 47*:* *Eucidaris metularia* spine (scale bar = 5 mm)

The medulla of *Eucidaris metularia* spines consists of laminar (= tube-like) structures with equally arranged pores (Figure 48A). The radiating layer is almost galleried showing equally distributed pores in several layers (Figure 48B). The cortex thickness has a mean value of ~ 150 µm. From the base to the tip it changes from 128 µm to 152 µm. More images of the stereom of *Eucidaris metularia* are shown in the supplement (Plate 4).

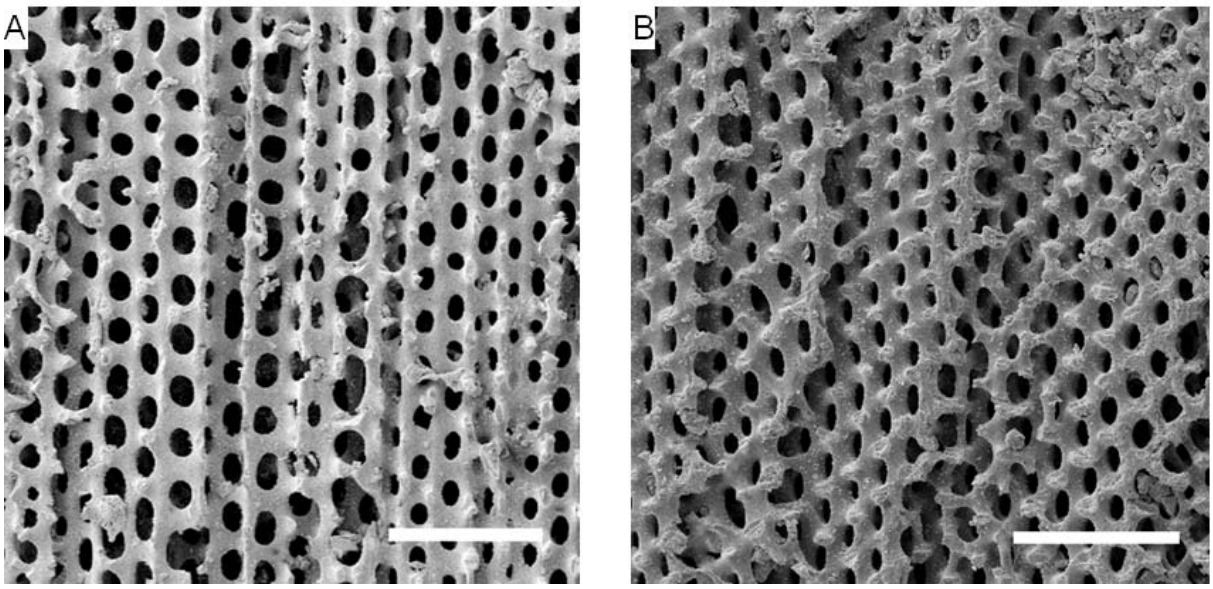

Figure 48: Typical arrangement of the medulla (A) and the radiating layer (B) in *Eucidaris metularia*: The medulla is laminar (tube-like) and the radiating layer is galleried (scale bar = 100 µm)

3.3.1 Eucidaris *metularia*: Medulla

The mean pore size in the medulla of *Eucidaris metularia* spines is 170.3 µm² (Figure 49). The pore sizes from the base to the tip range from ~180 µm² at the base (position 0) to ~160 µm² at the tip (position 4).

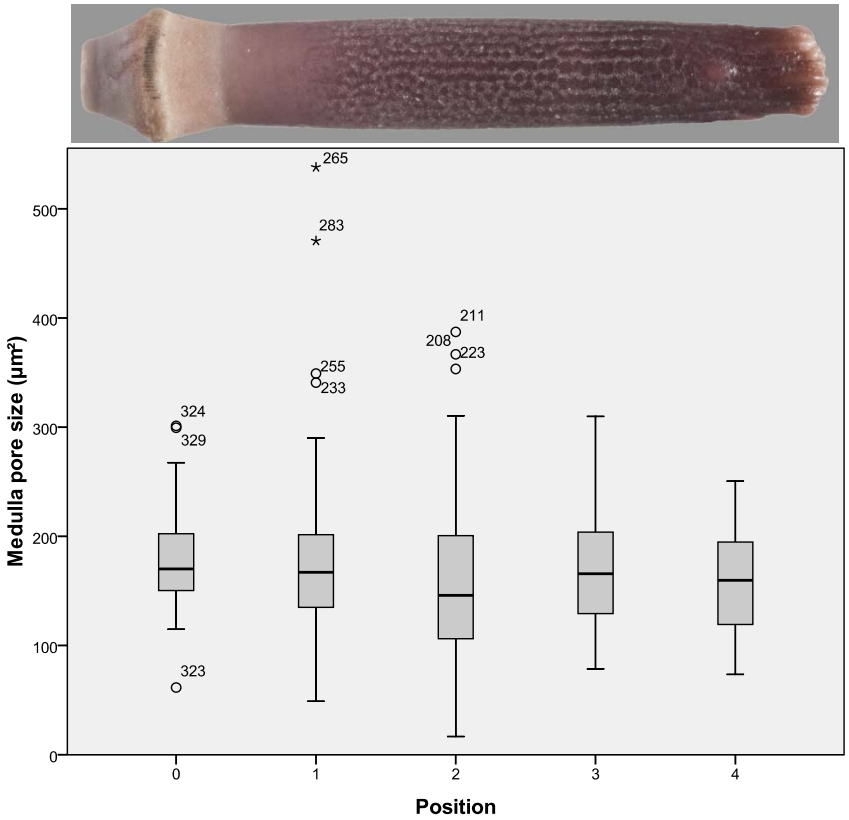

Figure 49: Box-plot of the pore size in the medulla of *Eucidaris metularia*

The values (n = 264) of the pore diameter in the medulla of *Eucidaris metularia* spines have a mean value of 15.7 ± 4.4 µm (Figure 50), beginning with 14.1 µm at the base (0), moving up to 17 µm (1 - 3) and ending with 14.4 µm (position 4). Some outlier occurred in the lower part of the spine.

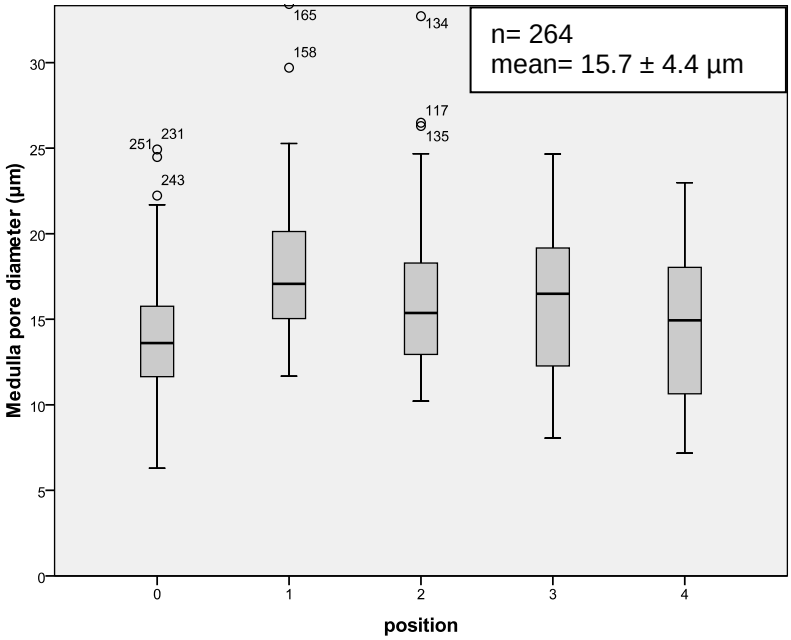

Figure 50: Box-plot of the pore diameter in the medulla of *Eucidaris metularia*

The histogram shows the most common diameters with frequencies around 45 (Figure 51). The values observed range from 5 to 35 µm. The skewness is 0.663 with a kurtosis of 1.109, resulting in a bell-shaped curve with a leptokurtic distribution.

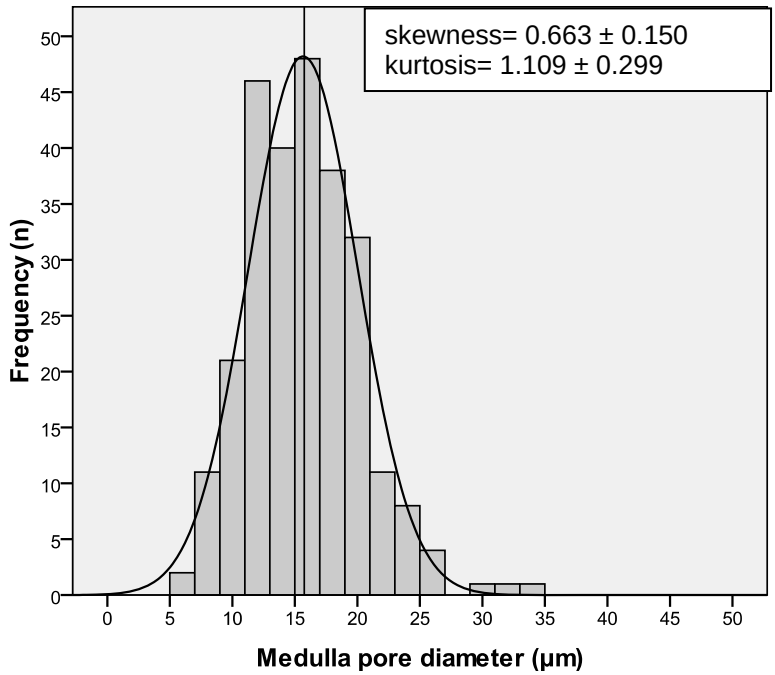

Figure 51: Histogram of the pore diameter in the medulla of *Eucidaris metularia*

The values (n = 264) of the trabeculae diameters of the medulla have a mean diameter of 15.5 ± 4.3 µm (Figure 52). The medulla in spines of *Eucidaris metularia* shows trabeculae diameters of around 16.1 µm at the base (0), decreasing to 12.6 µm (1-3) and ending at the tip at 13.1 µm (4). Most of the outliers were only observed at the base.

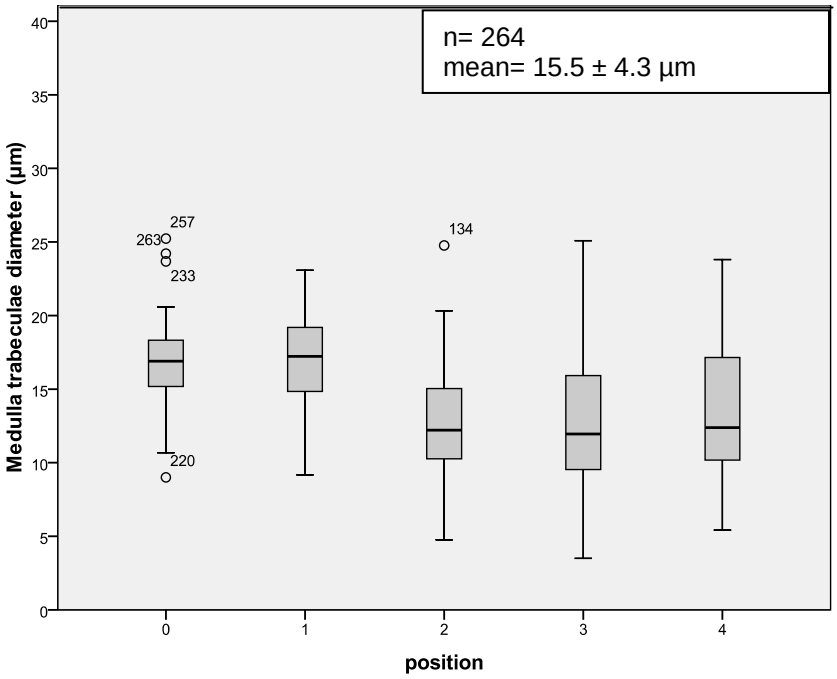

Figure 52: Box-plot of the trabeculae diameter in the medulla of *Eucidaris metularia*

The values of the trabeculae diameter range from 3 to 25 µm, with the most common ones with a frequency of 45 (Figure 53). The skewness is negative (-0.049), also the platykurtic kurtosis (-0.316), resulting in a slightly right sided curve.

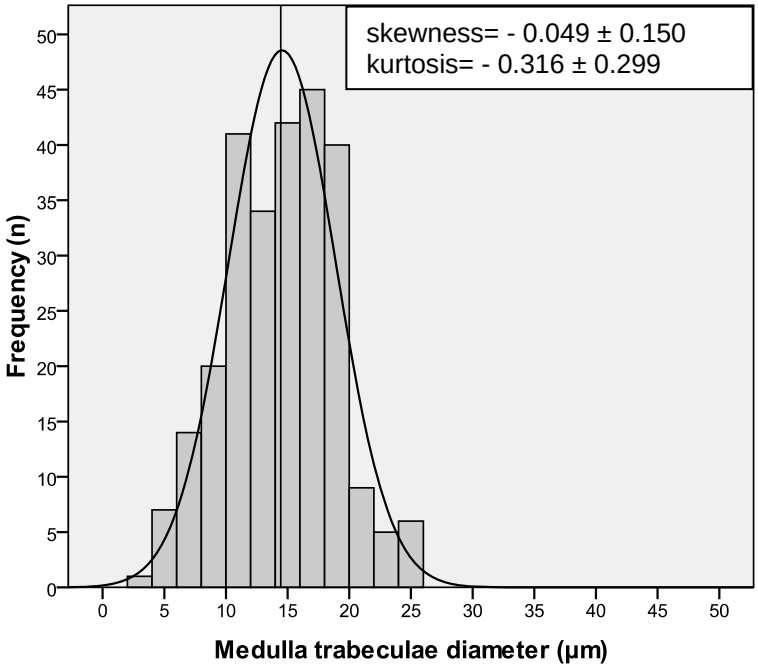

Figure 53: Histogram of the trabeculae diameter in the medulla of *Eucidaris metularia*

3.3.2 *Eucidaris metularia*: Radiating layer

The pore size in the radiating layer of *Eucidaris metularia* spines ranges from 101.6 µm² at the base(0) to 132.1 µm² at the tip (4), with a mean of 127.2 µm² (Figure 54). The highest values are observed in the upper part of the spine (position 3, 4).

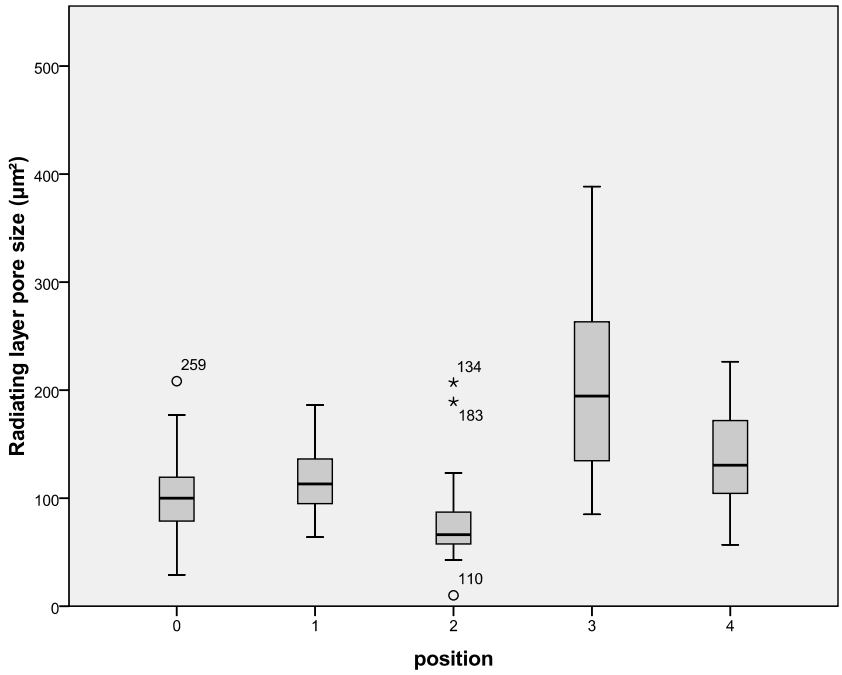

Figure 54: Box-plot of the pore size in the radiating layer of *Eucidaris metularia*

The mean pore diameter in the radiating layer of *Eucidaris metularia* spines is 14.7 ± 3.8 µm (Figure 55). The values (n = 250) of the pore diameter changes from the base (0) with 14.4 µm to 13.1 µm at the tip (4).

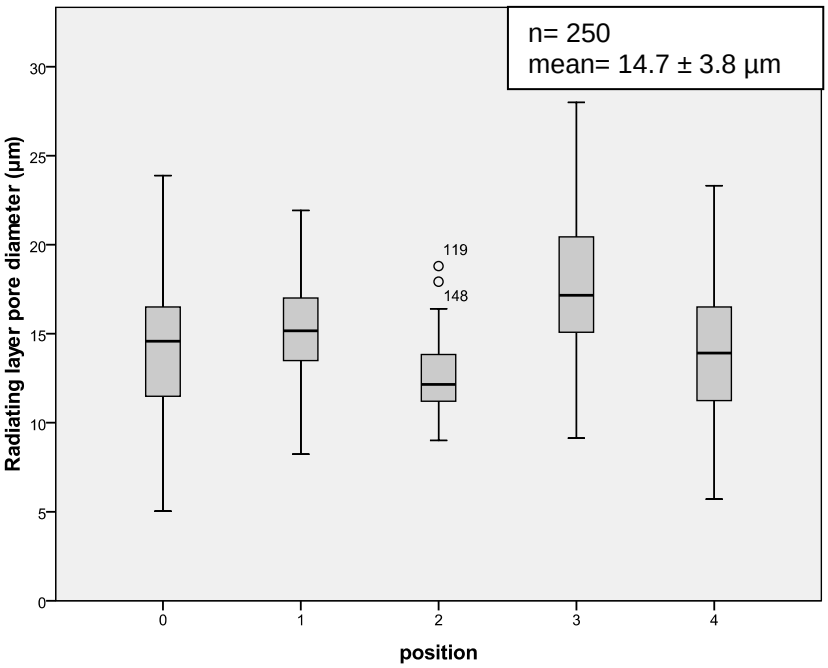

Figure 55: Box-plot of the pore diameter in the radiating layer of *Eucidaris metularia*

A frequency of more than 60 is observed for pore diameters with values around 14 µm (Figure 56). The values range from 5 to 30 µm. A skewness of 0.434 is observed with a kurtosis of 0.396, resulting in a bell-shaped curve with a leptokurtic distribution.

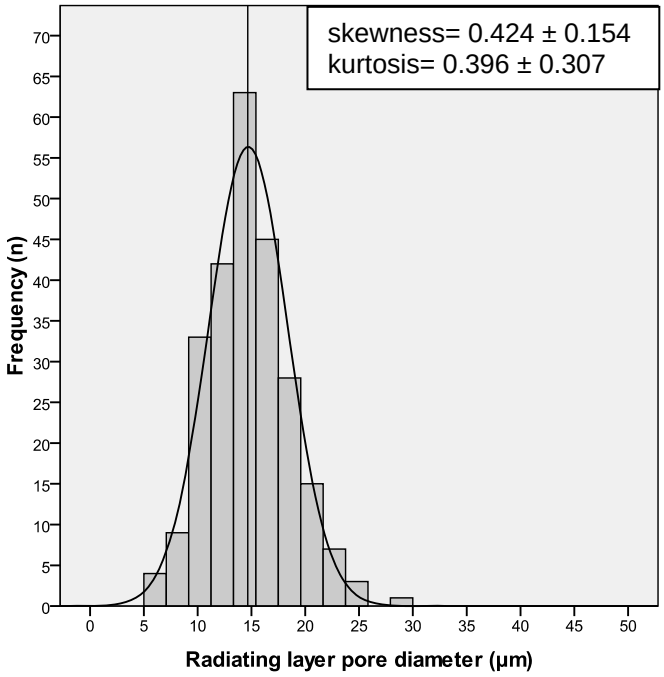

Figure 56: Histogram of the pore diameter in the radiating layer of *Eucidaris metularia*

The values (n = 250) of the trabeculae diameter in the radiating layer of *Eucidaris metularia* spines vary from the base to the tip, ranging 17.3 µm at the base (0) to 12.3 µm at the tip (4) (Figure 57). The mean trabeculae diameter is 15.4 ± 5.2 µm. Outliers occur throughout the spines measurements.

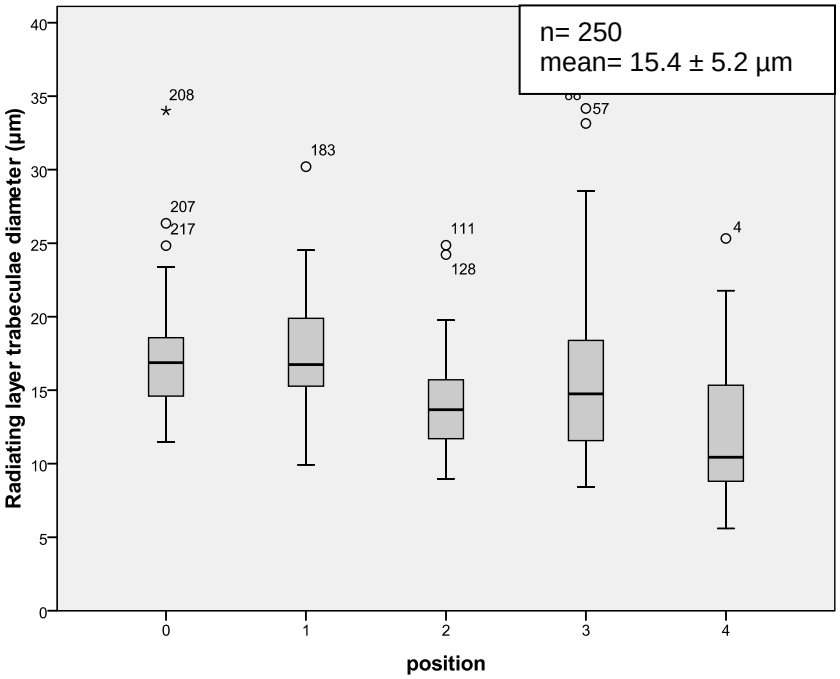

Figure 57: Box-plot of the trabeculae diameter in the radiating layer of *Eucidaris metularia*

The values of the trabeculae diameter have a wide range from 5 to 45 µm, including the most common ones with a frequency of 40 (Figure 58). The skewness is 1.538 with a kurtosis of 5.004, resulting in a bell-shaped curve with a leptokurtic distribution.

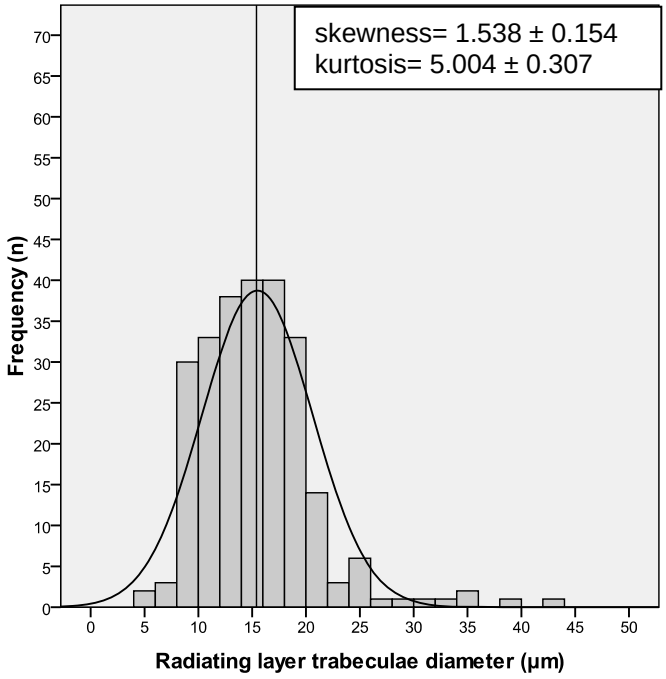

Figure 58: Histogram of the trabeculae diameter in the radiating layer of *Eucidaris metularia*

3.4 *Prionocidaris baculosa*

Primary spines of *Prionocidaris baculosa* are large (up to a size of 140 mm) with a width of the test of more than 80 mm (Figure 59). They are distributed around the Indo-Pacific to maximum depths of 200 m. The cortex thickness in *Prionocidaris baculosa* spines ranges from 65 µm at the base, 75 µm on the flanks and ending at the tip with 90 µm. The measurements of *Prionocidaris baculosa* were made in cross-sections to confirm the previous measurements in longitudinal section. More images of the stereom of *Prionocidaris baculosa* in the supplement (Plate 5).

Figure 59: Spine of *Prionocidaris baculosa* (scale bar = 5 mm)

3.4.1 *Prionocidaris baculosa*: Medulla

The pore size decreases from 257.3 µm² at the base (position 1) to 128.8 µm² at the tip (position 3) with a mean pore size of 185.9 µm² (Figure 60). The values have a wide range, including some outliers at the tip.

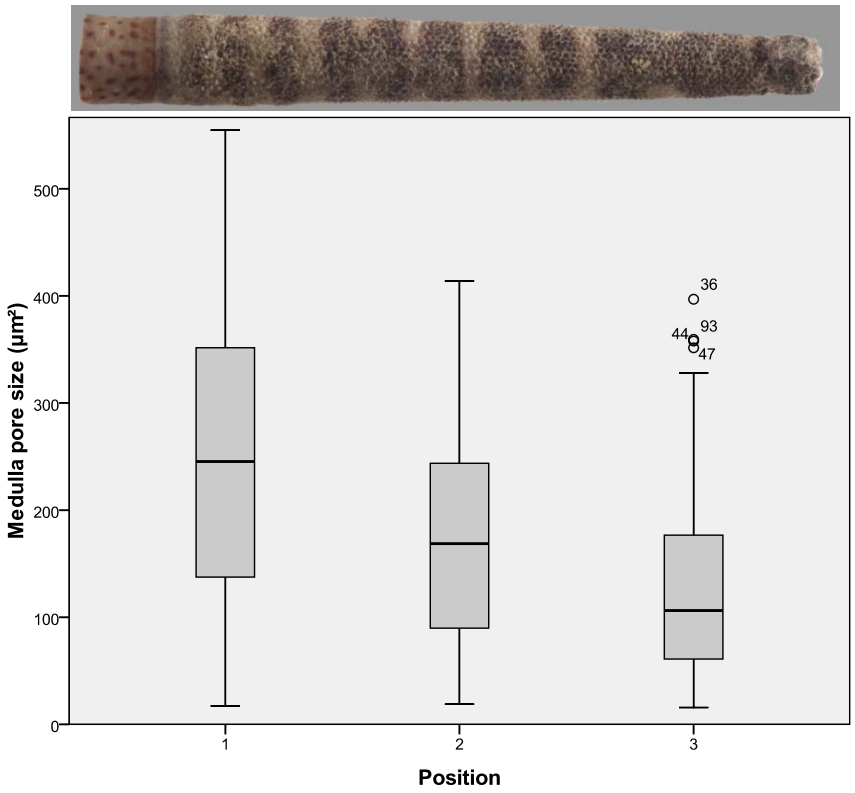

Figure 60: Box-plot of the pore size in the medulla of *Prionocidaris baculosa*

The values of pore diameter in the medulla of *Prionocidaris baculosa* range from 22.2 µm at the base (1), over 21.5 µm in the middle of the shaft (2), to the tip (3) with 18.1 µm (Figure 61). A mean of diameter of 20.6 ± 5.1 µm is observed (n = 75).

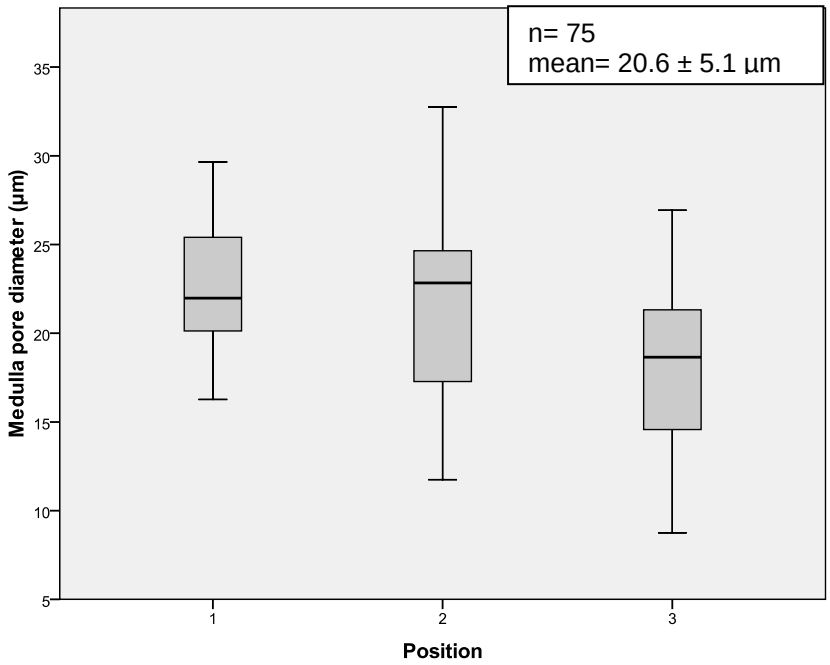

Figure 61: Box-plot of the pore diameter in the medulla of *Prionocidaris baculosa*

The frequencies of the pore diameter in the medulla of *Prionocidaris baculosa* spines have their maximum at 15, with values ranging from 7 to 35 µm (Figure 62). The skewness is negative (-0.187), also the platykurtic kurtosis (-0.264) with a slightly right-wing curve.

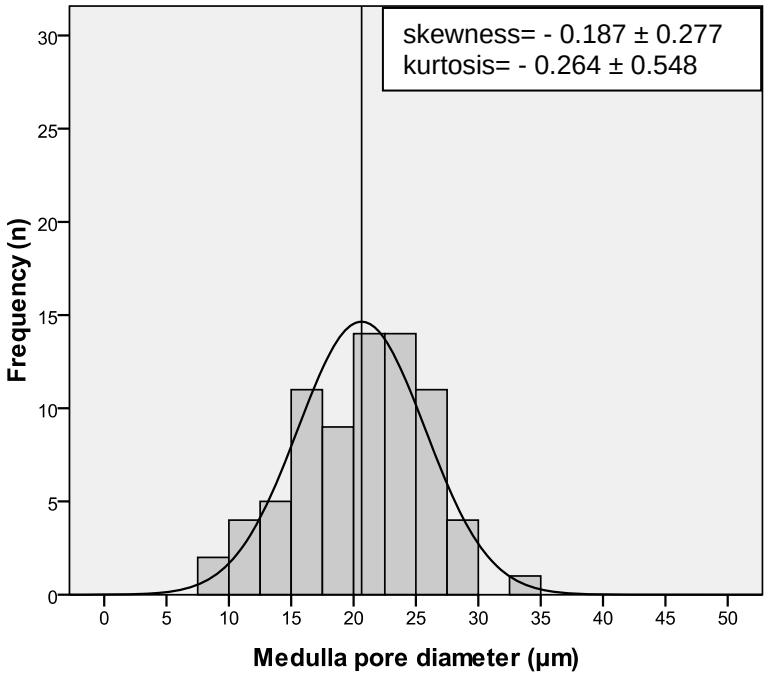

Figure 62: Histogram of the pore diameter in the medulla of *Prionocidaris baculosa*

The trabeculae measurements (n = 75) showed a mean trabeculae diameter of 9.5 ± 3.1 µm (Figure 63). The values range from 11.2 µm at the base (1), 9.2 µm (2) to 8.1 µm at the tip (3), with only a few outliers observed.

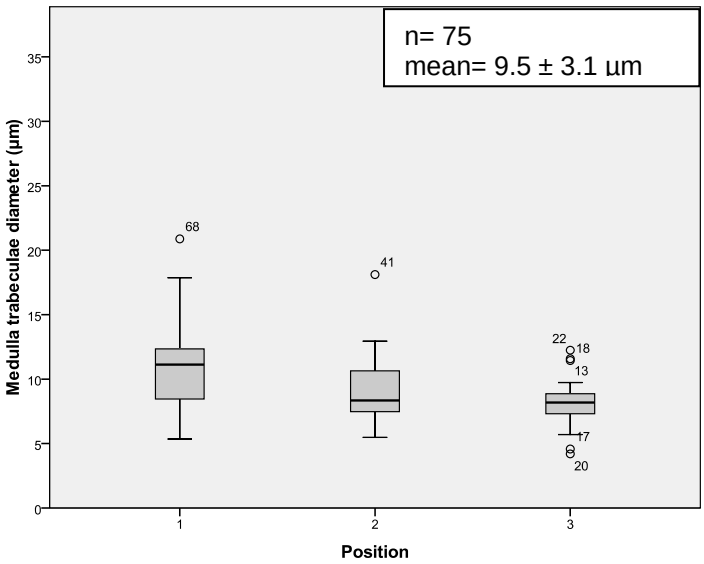

Figure 63: Box-plot of the trabeculae diameter in the medulla of *Prionocidaris baculosa*

The values of the trabeculae diameters are distributed between 3 and 20 µm (Figure 64). Maximum frequencies with around 30 are noted for diameters of ~ 9 µm. A skewness of 1.318 and a kurtosis of 2.373 are observed. This results in a bell-shaped curve with a leptokurtic distribution.

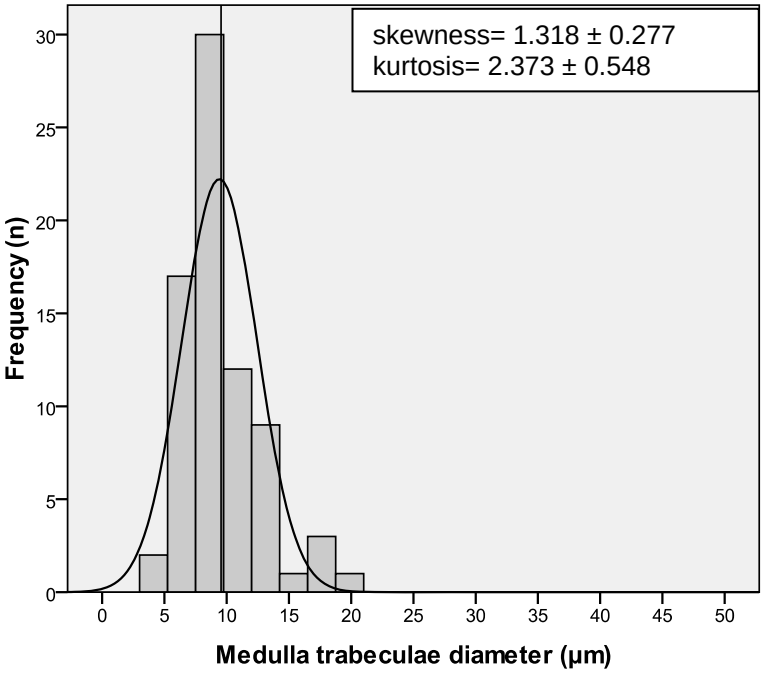

Figure 64: Histogram of the trabeculae diameter in the medulla of *Prionocidaris baculosa*

3.4.2 *Prionocidaris baculosa*: Radiating layer

The mean pore size of the radiating layer in *Prionocidaris baculosa* spines is 141.0 µm² (Figure 65). The highest values are found at the base (1) with 179.3 µm², followed by 134.8 µm² (2), decreasing towards the tip (3) with 109.1 µm², including some outliers.

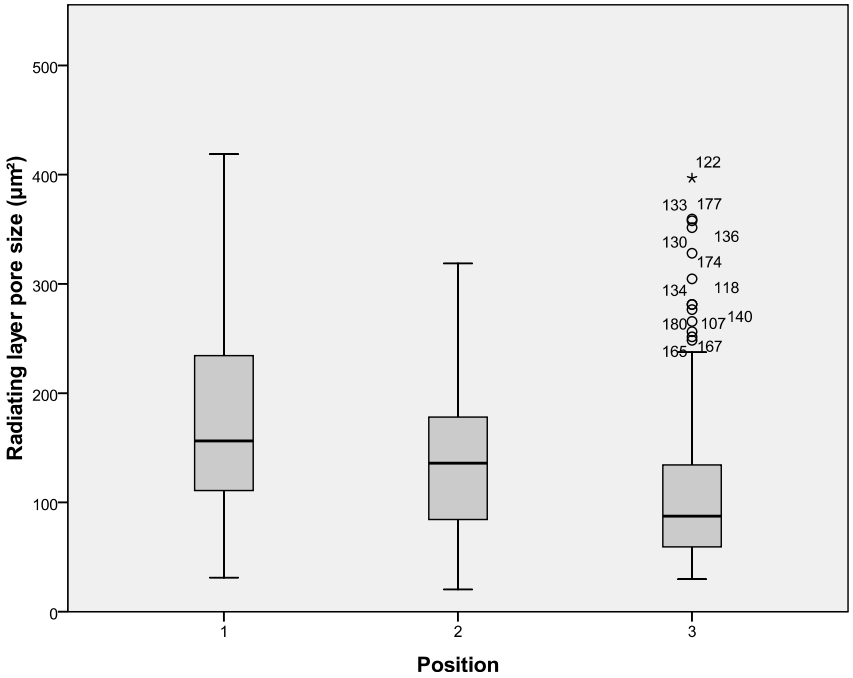

Figure 65: Box-plot of the pore size in the medulla of *Prionocidaris baculosa*

The values (n = 126) of the pore diameter in the medulla of *Prionocidaris baculosa* have a mean diameter of 14.1 ± 4.8 µm (Figure 66). The pore diameter at the base (16.1 µm) is higher than that at the tip (10.5 µm). Some outliers occurred during the measurements.

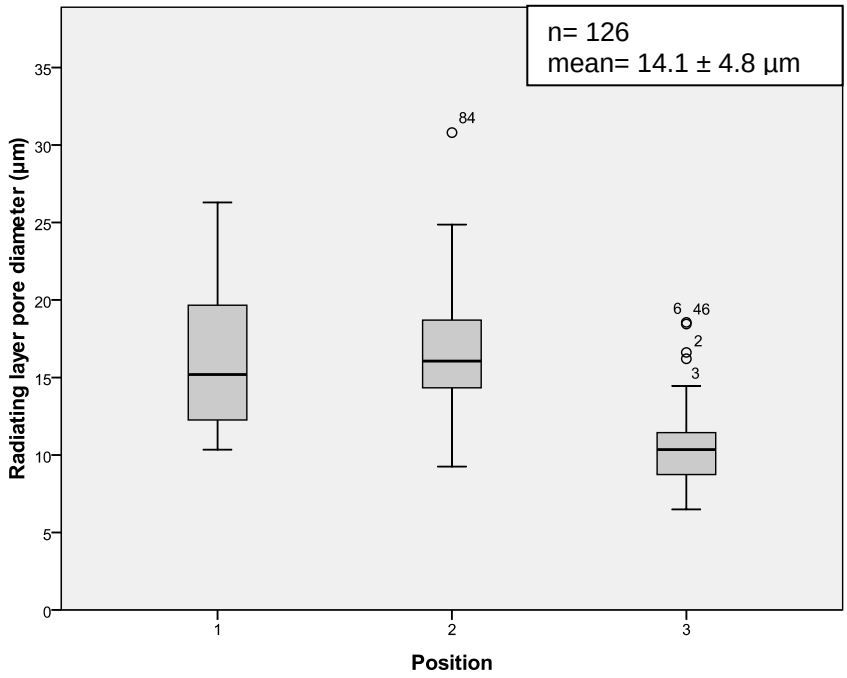

Figure 66: Box-plot of the pore diameter in the radiating layer of *Prionocidaris baculosa*

The values of the pore diameter in the histogram, as shown in Figure 67, display their maximum frequencies with almost 35. The values range from 5 to 33 µm. As the skewness (0.814) and the kurtosis (0.527) are positive, the curve is bell-shaped with a leptokurtic distribution.

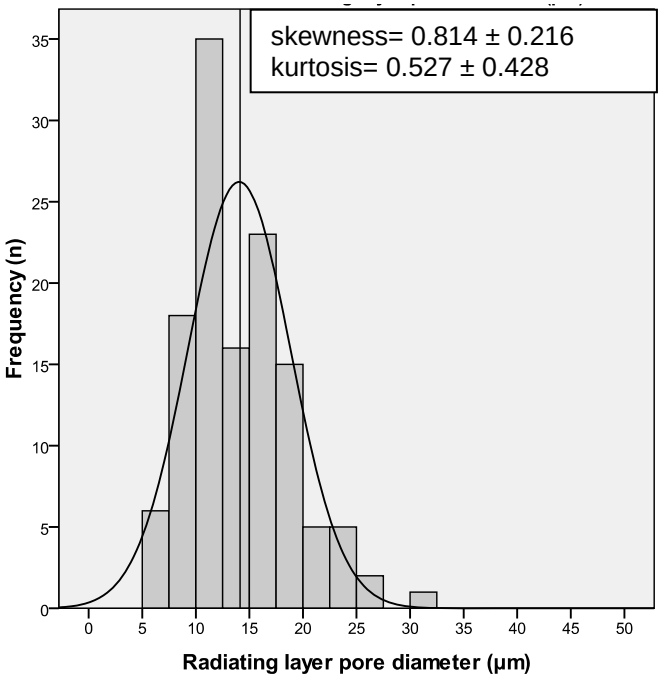

Figure 67: Histogram of the pore diameter in the radiating layer of *Prionocidaris baculosa*

The values (n = 126) of trabeculae diameter in the radiating layer of *Prionocidaris bac*ulosa have a mean diameter of 12.4 ± 4.0 µm (Figure 68). The lowest diameter is at the base (1) with 10.3 µm, followed by 15.1 µm (2), ending at the tip with 11.5 µm.

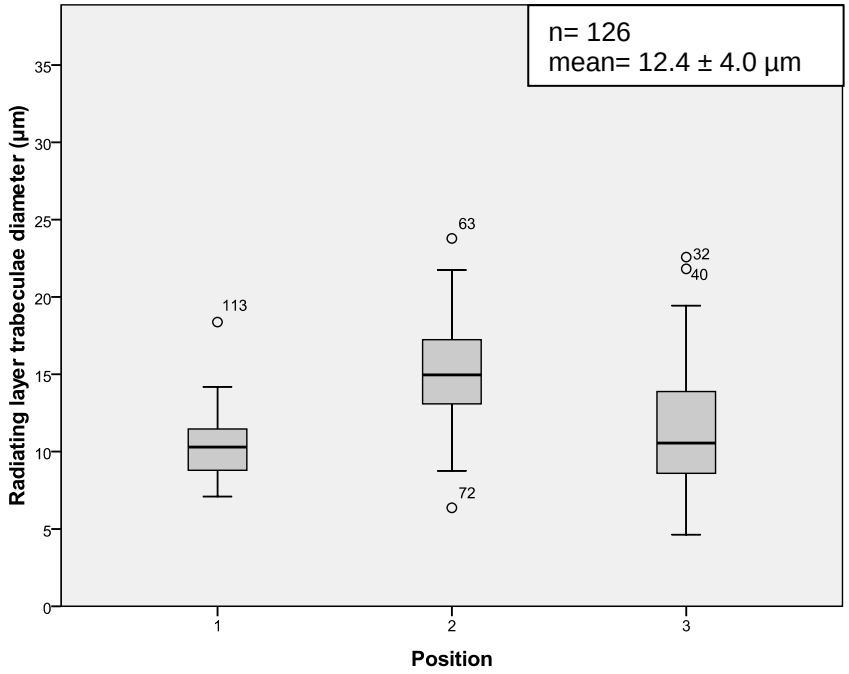

Figure 68: Box-plot of the trabeculae diameter in the radiating layer of *Prionocidaris baculosa*

The values of the trabeculae diameter in Figure 69 range from 5 to 25 µm with their maximum frequencies around 33. A skewness of 0.631 is observed and a negative kurtosis (-0.114). This results in a bell-shaped curve with a platykurtic distribution.

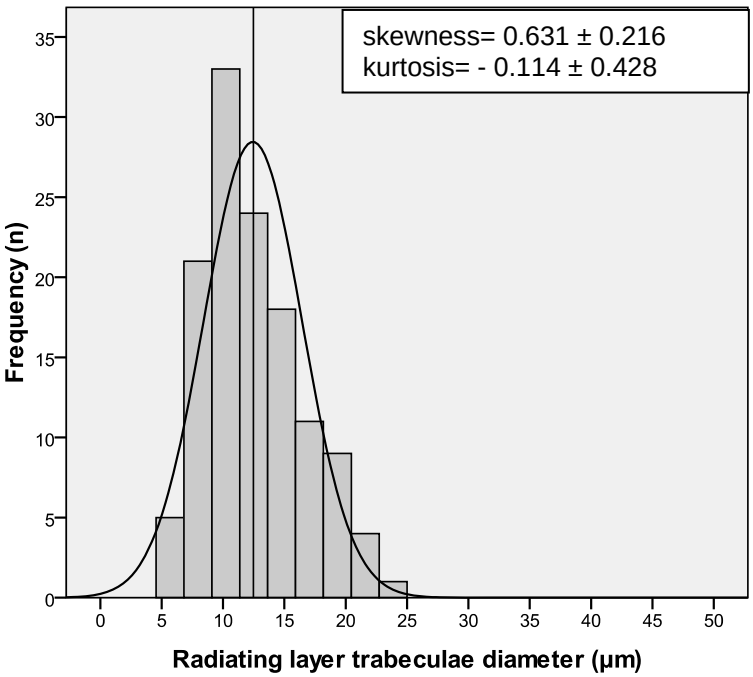

Figure 69: Histogram of the trabeculae diameter in the radiating layer of *Prionocidaris baculosa*

3.5 Spines of Echinoida: Surface morphology

The spines of Echinoida lack a cortex but are covered by an epithelium which inhibits incrustation. In contrast to cidaroids, the spines of the Echinoida have growth rings, also called in the literature growth lines or growth zones. These growth rings are then present in the investigated species *Heterocentrotus mammillatus* and *Echinometra mathaei*.

In SEM images, the surface of *Heterocentrotus mammillatus* spines shows a parallel arrangement of distinct struts (width ca. 100 µm) 10 to 30 µm apart (Figure 70A). A closer examination of the struts reveals a wedge shaped structure. They have fine transverse striations on the outer side, on the otherwise smooth surface. The surface structure of *Echinometra mathaei* spines is similar (Figure 70B). More images of the stereom of *Echinometra mathaei* in the supplement (Plate 6).

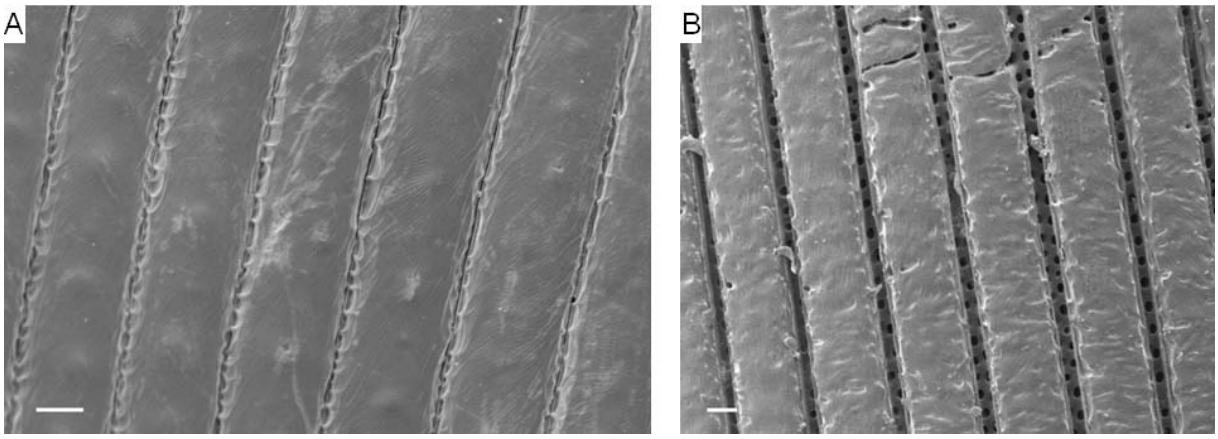

Figure 70: Surface structure of spines of *Heterocentrotus mammillatus* (A) and *Echinometra mathaei* (B) (scale bar = 40 µm)

3.5.1 *Heterocentrotus mammillatus*

Primary spines of *Heterocentrotus mammillatus* are large, robust, and can reach lengths up to 100 mm with a test width of about 90 mm (Figure 71). Distributed around the Indo-Pacific, these sea urchins live mostly at the fore-reef where strong currents and wave energies are evident; they are uncommon on sandy substrates.

Figure 71: Primary spine of *Heterocentrotus mammillatus* (scale bar = 5 mm)

3.5.2 *Heterocentrotus mammillatus*: Juvenile spine

In Figure 72, a juvenile primary spine of *Heterocentrotus mammillatus* in longitudinal section is shown in detail. From the base to the outermost tip the spine is separated into the medulla (the inner cylinder) and the radiating layer (see chapter 1 for further information). The base (E & F) ranges from a very dense imperforate structure at the outer side of the spine to a more coarsely open labyrinthic form, thereafter the radiating layer is labyrinthic towards the medulla. The medulla is of laminar structure (C & D) and the radiating layer labyrinthic, interrupted by growth rings (dense imperforate). Towards each tip of the growth ring of the medulla ends in a fountain-like structure (A). The growth rings vary in their thickness from 80 µm (lower shaft), 30 µm (shaft) to 40 µm at the tip. More images of the stereom of *Heterocentrotus mammillatus* are shown in the supplement (Plate 7).

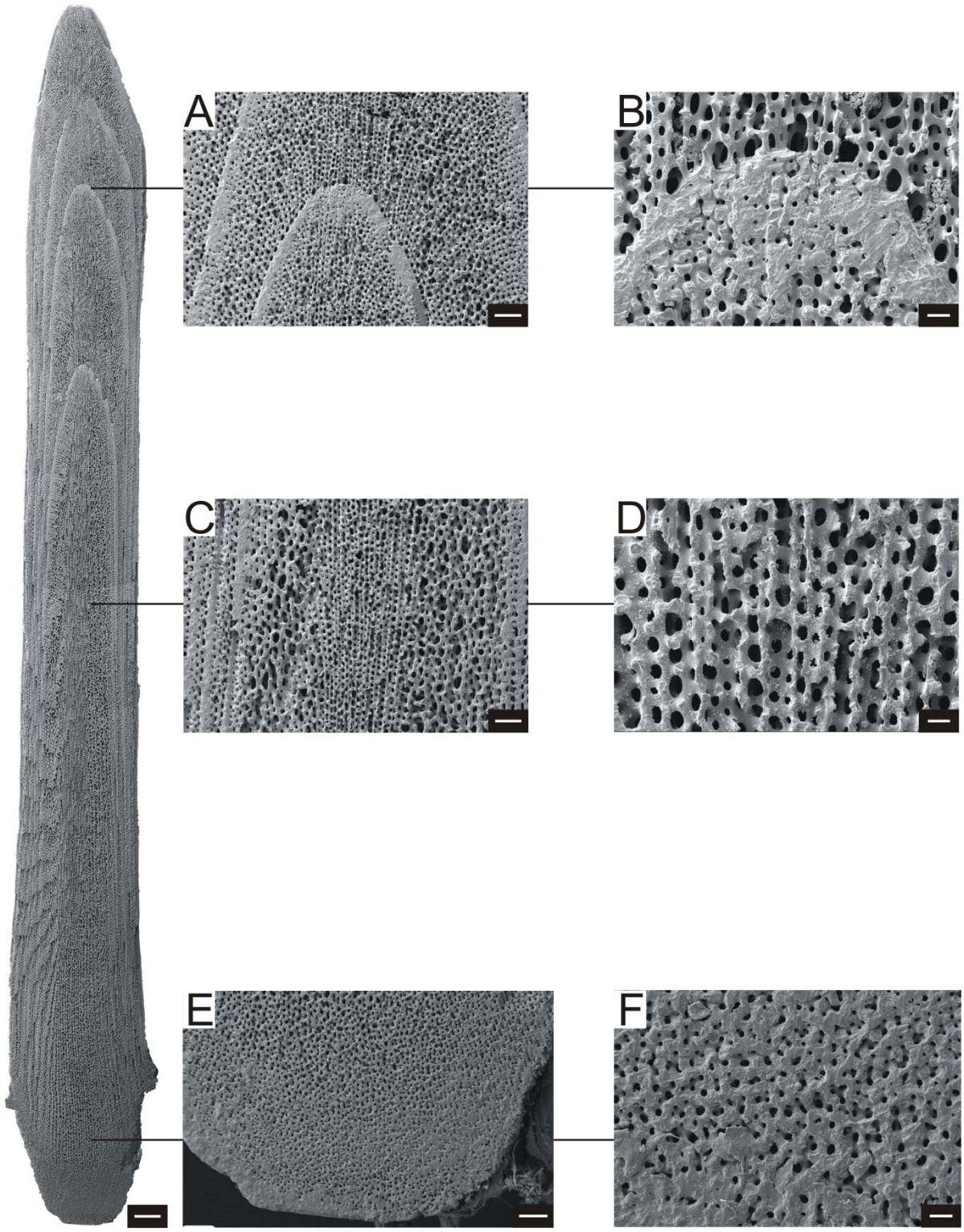

Figure 72: Stereom distribution in a longitudinal section of a juvenile primary spine of *Heterocentrotus mammillatus*: Spine length = 20 mm. Medulla = laminar; Radiating layer = labyrinthic, growth rings = microperforate A = medulla at the tip with growth rings and radiating layer; B = detailed medulla; C = middle shaft with medulla, growth rings and radiating layer; D = detailed medulla; E = base with dense and open stereom ; F = detailed base. Scale bars: spine = 300 µm; A, C, E = 100 µm; B, D, F = 20 µm

3.5.3 *Heterocentrotus mammillatus spines* (juvenile): Medulla

The mean pore size in the medulla of juvenile *Heterocentrotus mammillatus* spines is 82.7 µm² (Figure 73). The pore sizes are very low for each position, beginning at 62.5 µm² (position 1), 83.2 µm² (position 2), 125.7 µm² (position 3), 89.6 µm² (position 4), 81.3 µm² (position 5), 64.5 µm² (position 6) and ending at 68.9 µm² (position 7). Lots of outliers are observed throughout the spine.

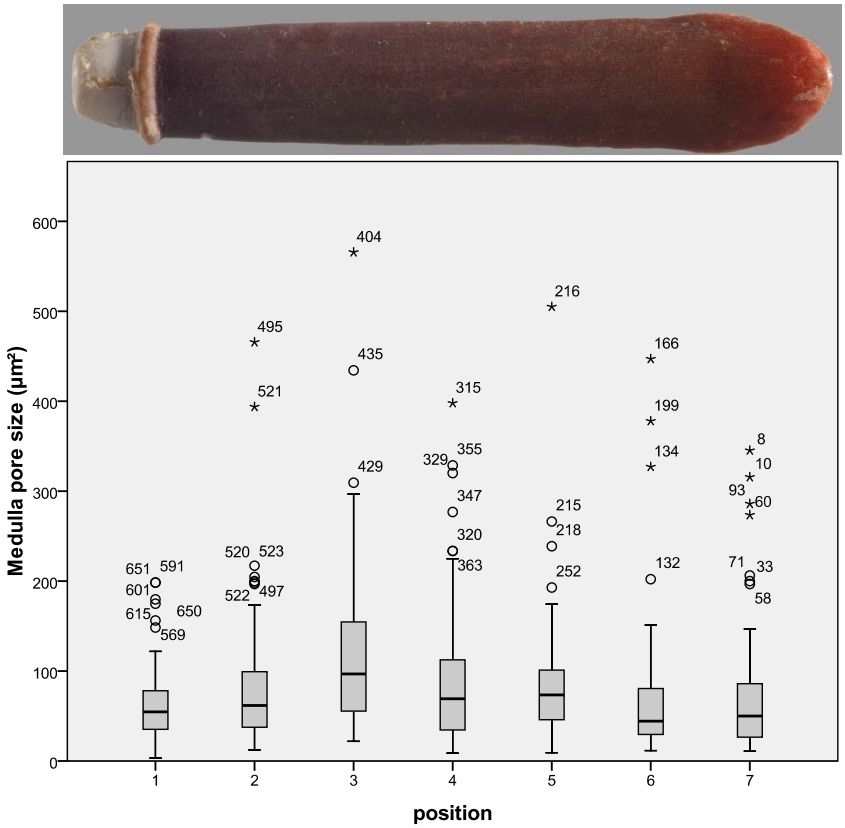

Figure 73: Box-plot of the pore size in the medulla of *Heterocentrotus mammillatus*

The values (n = 326) of the pore diameter of the medulla in *Heterocentrotus mammillatus* spines show a mean diameter of 12.9 ± 4.6 µm (Figure 74). Besides the outliers the pore diameter begins with 12.5 µm at the base (1) and is ending at the tip (7) with 13.1 µm, showing overall short pore diameters.

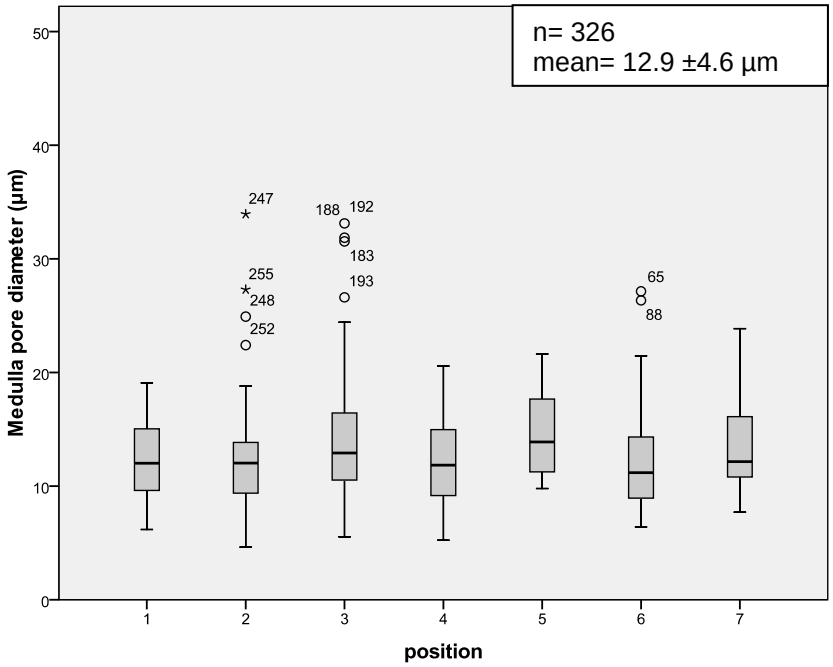

Figure 74: Box-plot of the pore diameter in the medulla of *Heterocentrotus mammillatus*

The maximum frequencies with around 55 are observed for the diameters around 12 µm (Figure 75). The range of the values is between 5 and 35 µm. The calculated skewness is 1.439 with a kurtosis of 3.433, which results in a bell-shaped curve with leptokurtic distribution.

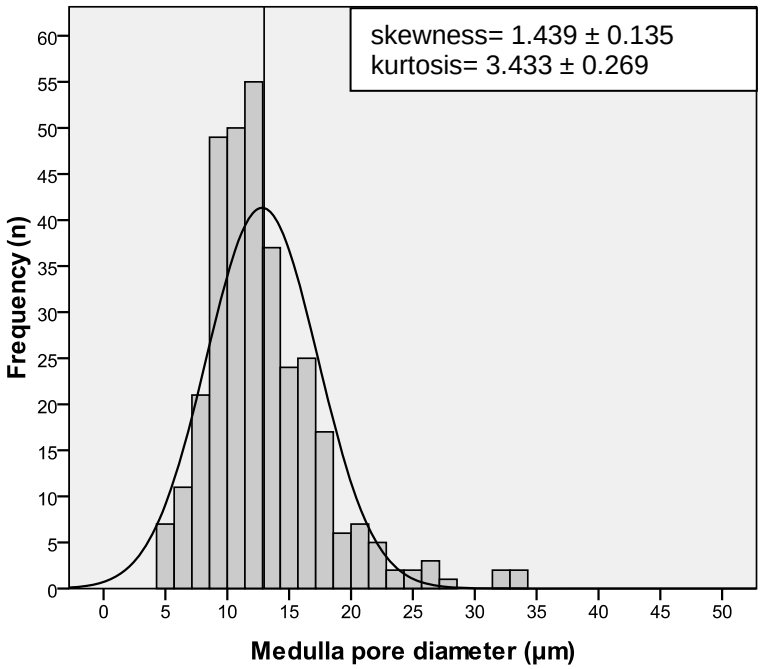

Figure 75: Histogram of the pore diameter in the medulla of *Heterocentrotus mammillatus*

A mean diameter of 12.8 ± 4.9 µm is characterized for the trabeculae diameter in the medulla of *Heterocentrotus mammillatus* (n = 326) (Figure 76). The pore diameter begins with 11.7 µm at the base (1), increases to 14.6 µm (2), decreasing to ~ 11 µm (3-5) and ending at the tip (7) at 12.7 µm.

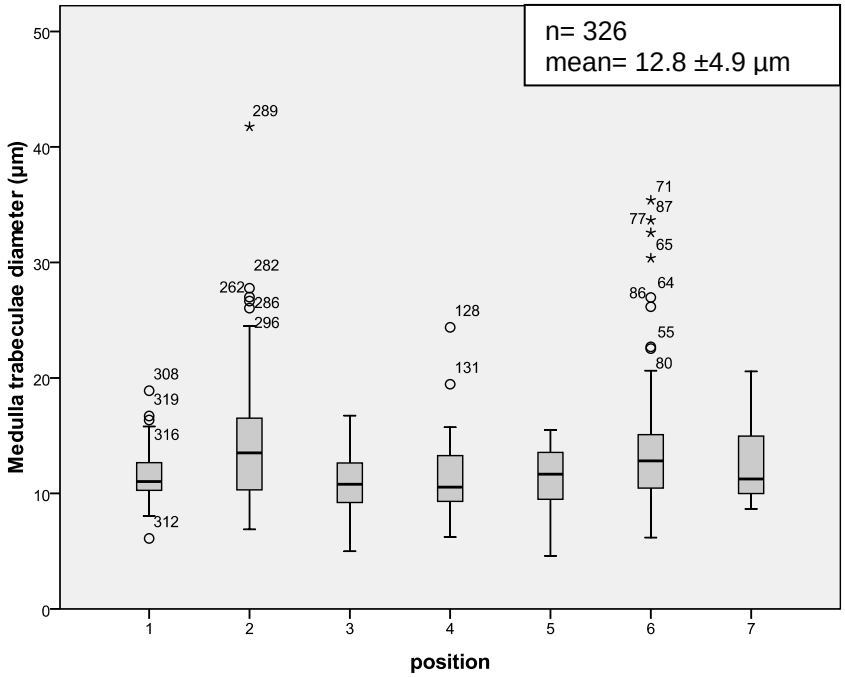

Figure 76: Box-plot of the trabeculae diameter in the medulla of *Heterocentrotus mammillatus*

The most common trabeculae diameters have a frequency of 75, ranging from 5 to 42 µm (Figure 77). A skewness of 2.081 with a leptokurtic kurtosis of 6.592 is observed. This results in a bell-shaped curve.

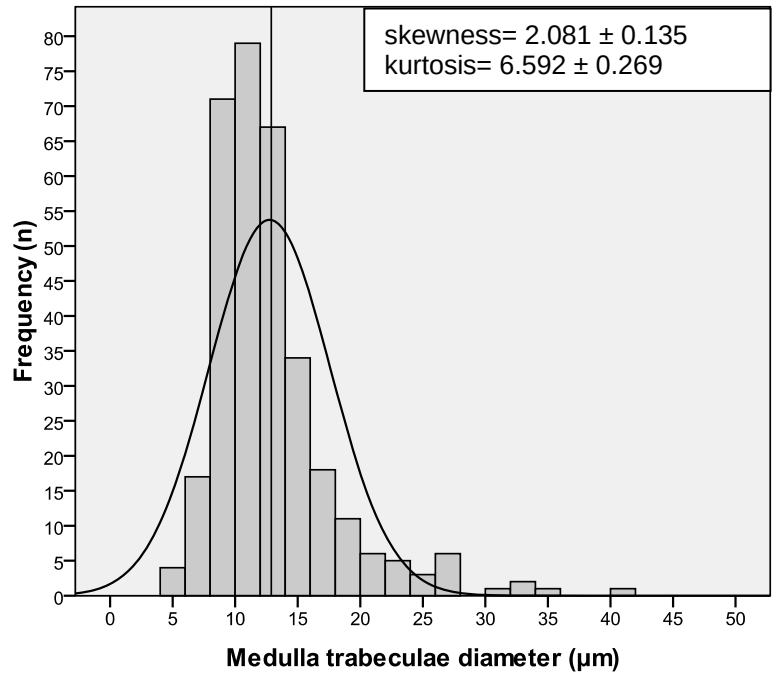

Figure 77: Histogram of the trabeculae diameter in the medulla of *Heterocentrotus mammillatus*

3.5.4 *Heterocentrotus mammillatus* spines (juvenile): Radiating Layer

The values of the pore sizes of the radiating layer are the lowest at the base (1) 30.6 µm² and the tip (7) 68.8 µm², having a mean value of 136.5 µm² (Figure 78).

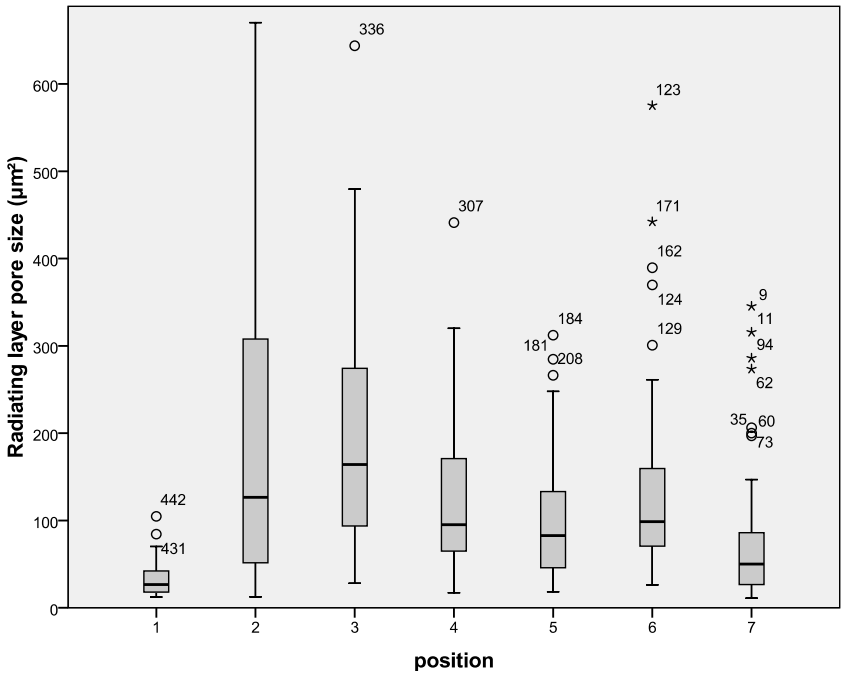

Figure 78: Box-plot of the pore size in the radiating layer of *Heterocentrotus mammillatus*

A mean value of 14.2 ± 6.1 µm is characterized for the pore diameter in the radiating layer of *Heterocentrotus mammillatus* spines (n= 266) (Figure 79). Small mean diameters are observed for each position in the radiating layer, beginning with 8.9 µm (1) and ending with 12.6 µm at the tip (7).

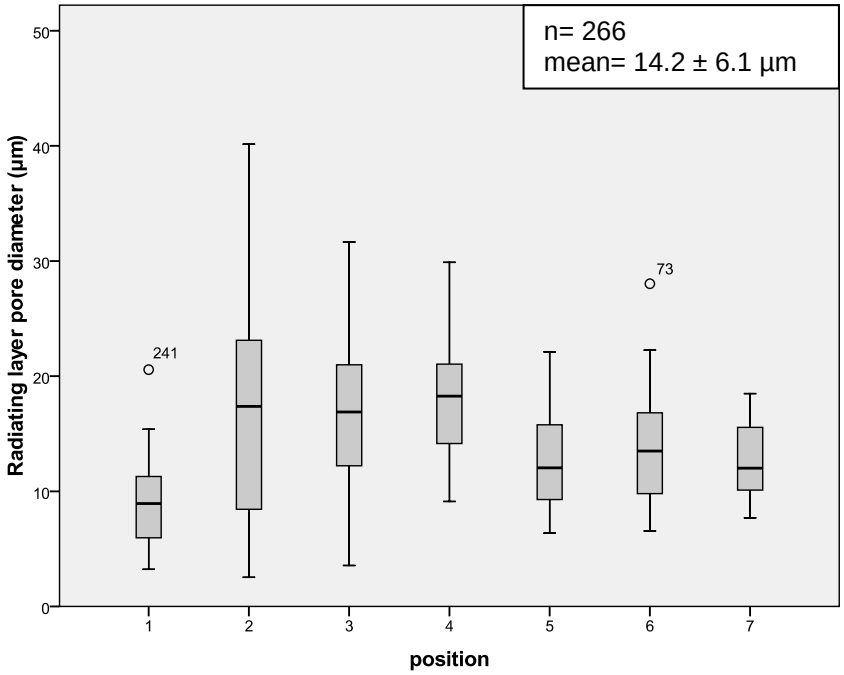

Figure 79: Box-plot of the pore diameter in the radiating layer of *Heterocentrotus mammillatus*

The highest frequencies are observed with around 40, for pore diameters of 7 to 10 µm (Figure 80). The values range from 3 to 42 µm. The skewness is 0.840 with a kurtosis of 0.885 which results in a bell-shaped curve and a leptokurtic distribution.

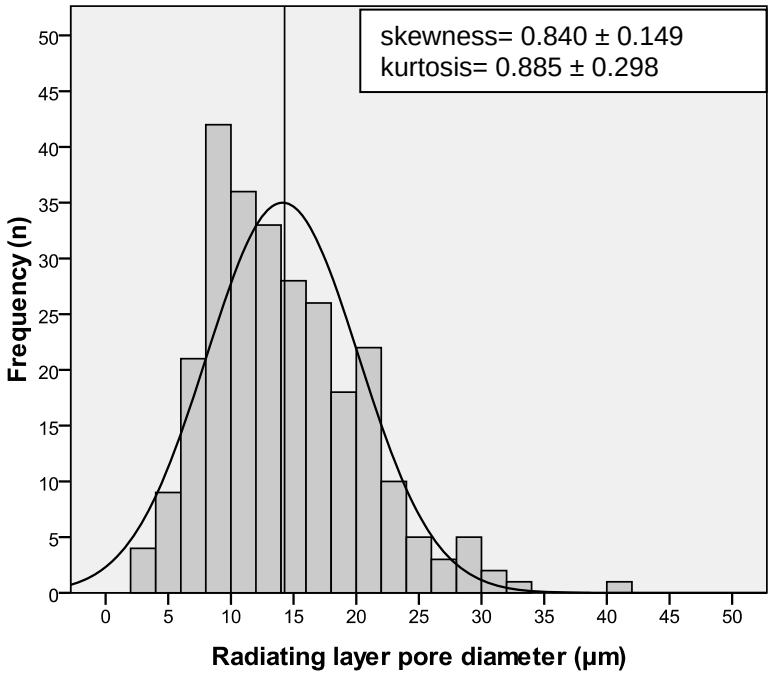

Figure 80: Histogram of the pore diameter in the radiating layer of *Heterocentrotus mammillatus*

The values (n = 247) of the trabeculae diameter are somehow larger than those of the pores with an overall mean of 16.8 ± 9.2 µm (Figure 81). The diameter of the trabeculae begins at 9.2 µm (1) and increases to 25.6 µm (3) and decreases to 13.4 µm at the tip (7), including some outliers.

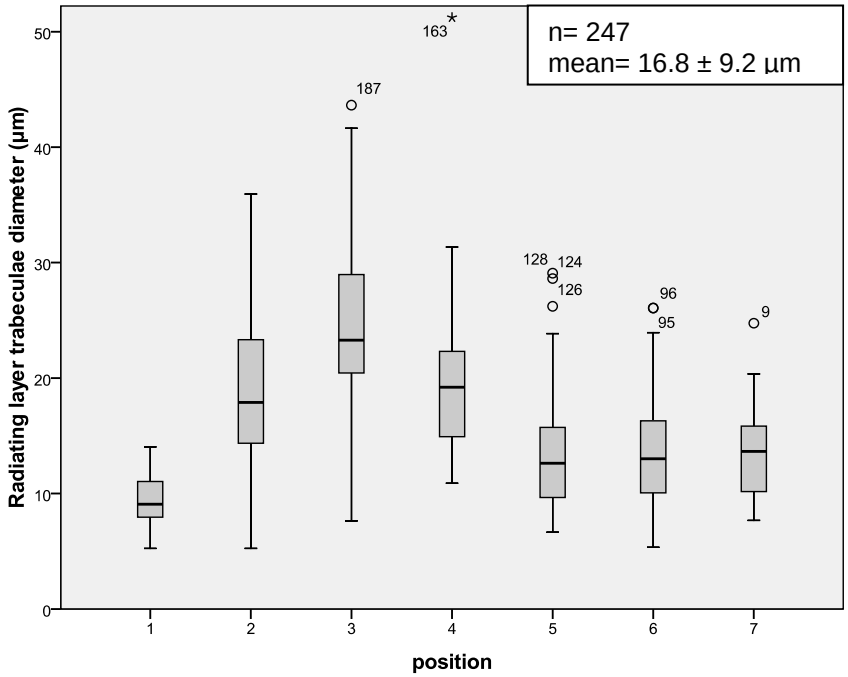

Figure 81: Box-plot of the trabeculae diameter in the radiating layer of *Heterocentrotus mammillatus*

The highest frequencies are observed with around 33, for pore diameters of 10 to 15 µm (Figure 82). The values range from 5 to 51 µm. The most frequent diameters are between 10 to 15 µm. A skewness of 2.762 with a kurtosis of 12.497 is observed. The bell-shaped curve is flattened but with leptokurtic distribution.

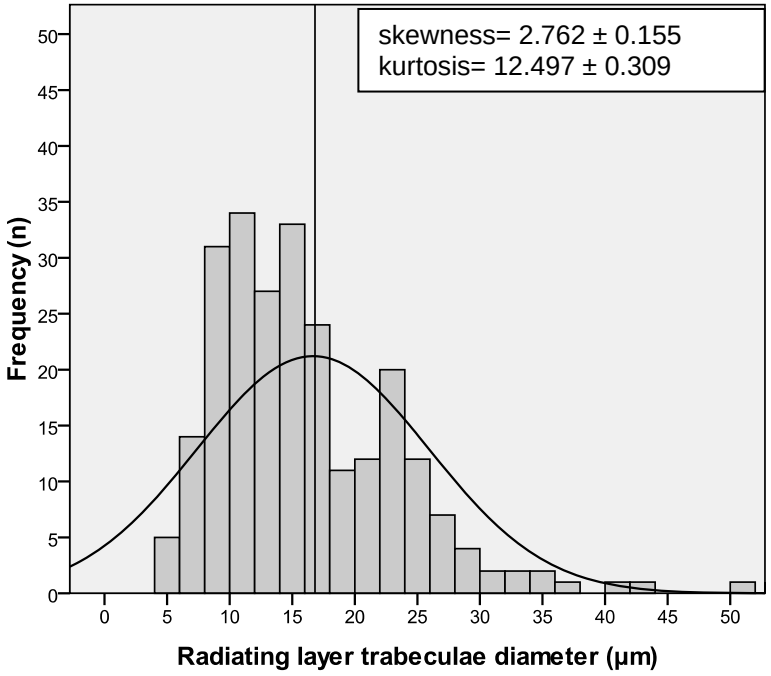

Figure 82: Histogram of the trabeculae diameter in the radiating layer of *Heterocentrotus mammillatus*

3.5.5 *Heterocentrotus mammillatus* spines (fully grown): Medulla

The values of the pore size in the medulla of aboral *Heterocentrotus mammillatus* spines have a mean pore size of 274.9 µm² (Figure 83). The values range from around 273.5 µm² at the base (1), changing to 276.1 µm² (3) and 272.0 µm² (5), ending at the tip at 277.6 µm² (7). Outliers are noted at every position throughout the spine.

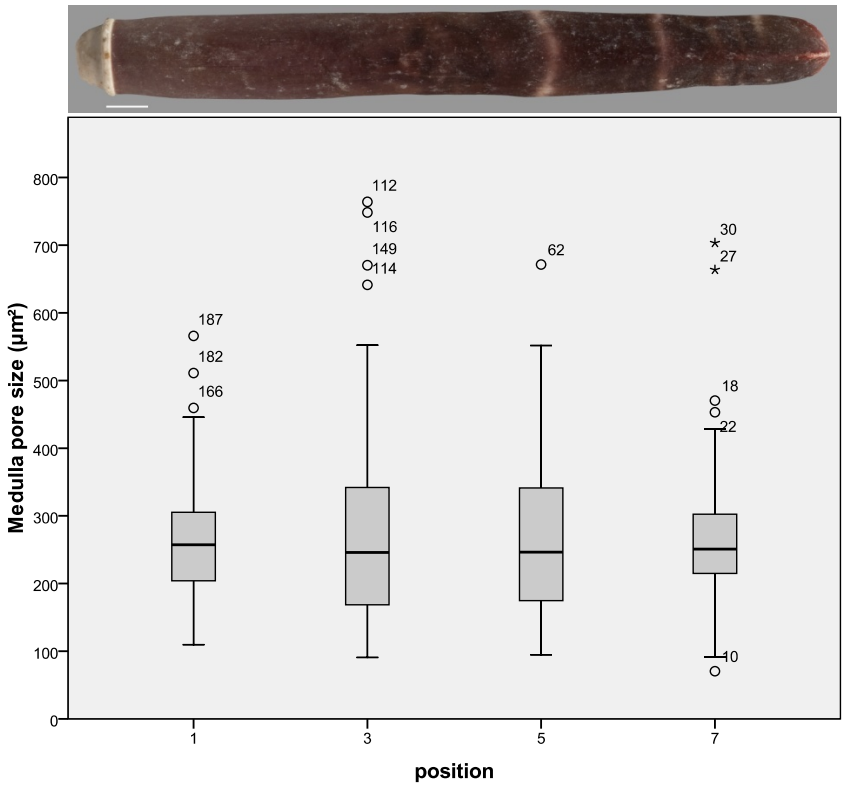

Figure 83: Box-plot of the pore size in the medulla of *Heterocentrotus mammillatus*

The values (n = 201) of the pore diameter of the medulla have their mean at 19.3 ± 5.6 µm (Figure 84). The variation is shown in the pore diameter, beginning from 19.2 µm at the base (1) to 19.3 µm at the tip (7). The outliers are observed in measurements of position 3 and at the tip.

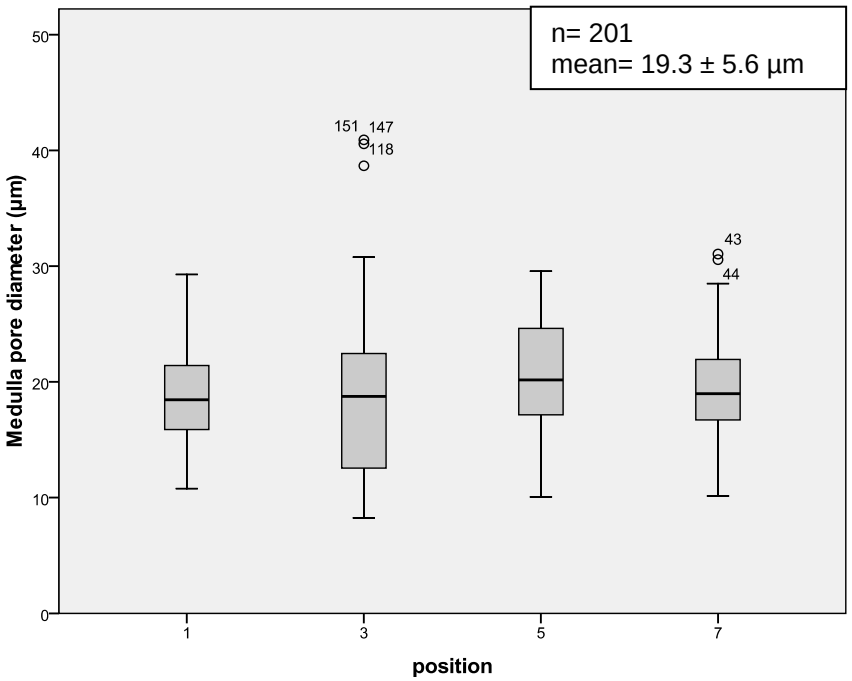

Figure 84: Box-plot of the pore diameter in the medulla of *Heterocentrotus mammillatus*

The highest frequencies are observed with around 45, for pore diameters of 17 to 20 µm (Figure 85). The values range from 7 to 42 µm. The skewness is 0.772 with a kurtosis of 1.521, which means a bell-shaped curve with a leptokurtic distribution.

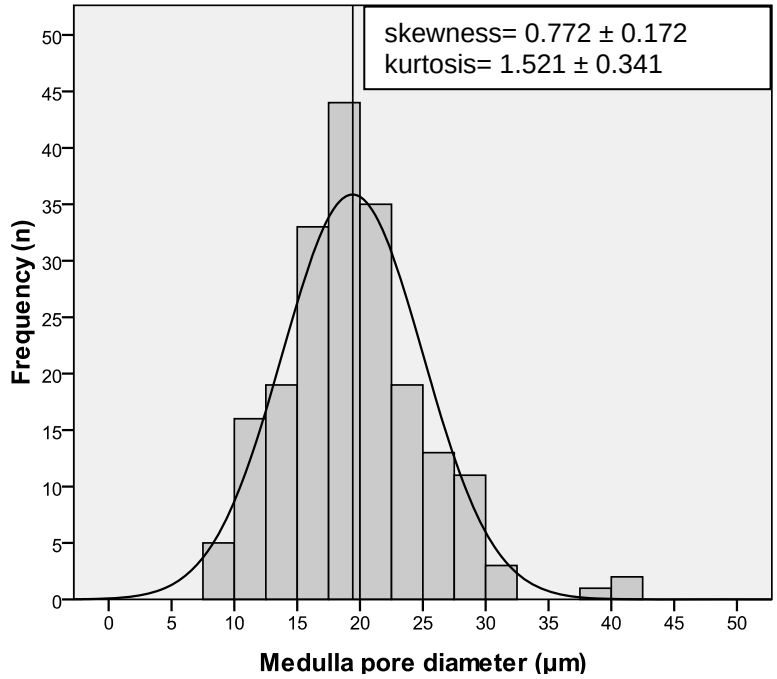

Figure 85: Histogram of the pore diameter in the medulla of *Heterocentrotus mammillatus*

The values (n = 201) of the medulla shows a mean trabeculae diameter of 17.8 ± 6.2 µm (Figure 86). The trabeculae diameter begins with 20.7 µm at the base (1), decreasing to 14.3 µm (3 & 5) and ending at the tip with 21.5 µm (7).

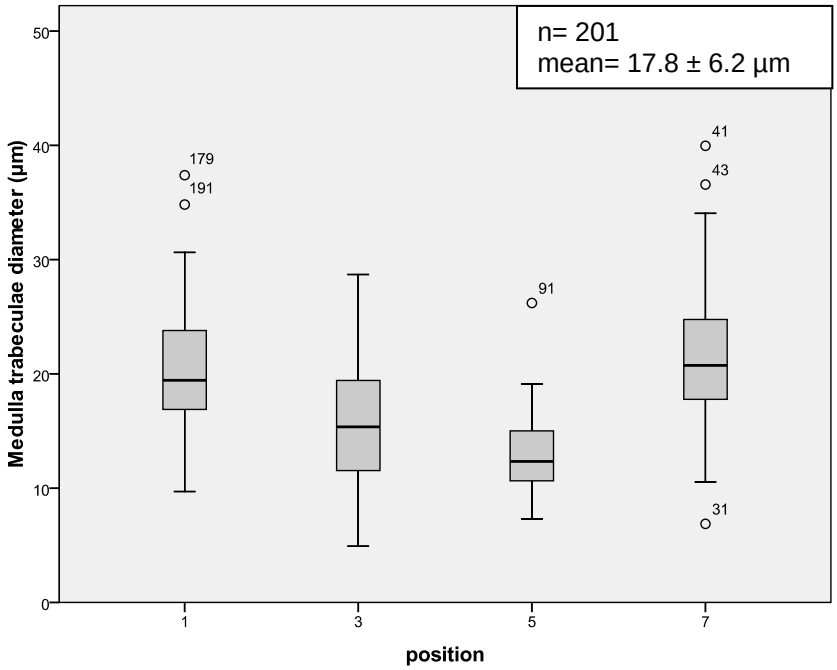

Figure 86: Box-plot of the trabeculae diameter in the medulla of *Heterocentrotus mammillatus*

The highest frequencies are observed around 35, for pore diameters of 10 to 15 µm (Figure 87). The values range from 3 to 40 µm. The skewness is 0.738 with a kurtosis of 0.576, which means a bell-shaped curve with a leptokurtic distribution.

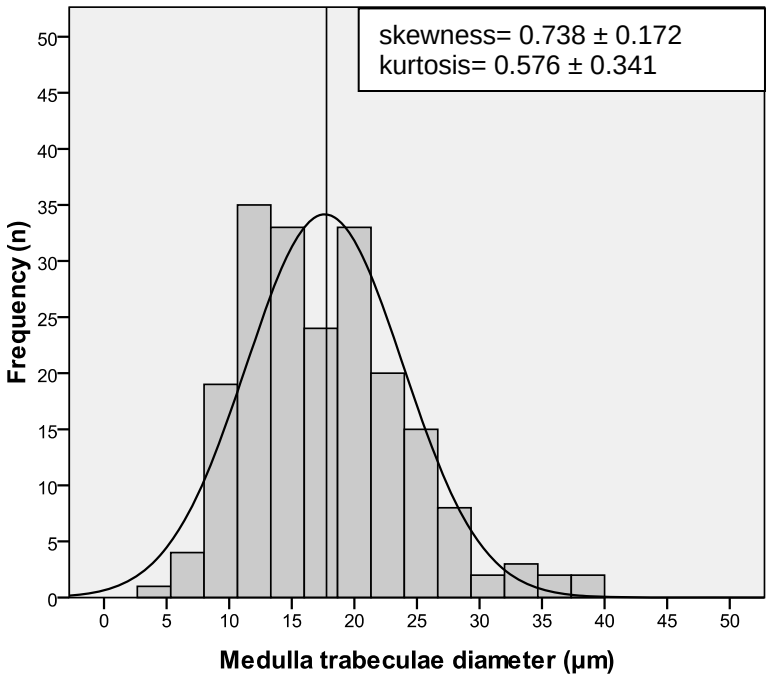

Figure 87: Histogram of the trabeculae diameter in the radiating layer of *Heterocentrotus mammillatus*

3.5.6 *Heterocentrotus mammillatus* spines (fully grown): Radiating layer

The mean pore size in the radiating layer of *Heterocentrotus mammillatus* spines is 342.6 µm² (Figure 88). The pore size changes from 248.4 µm² at the base, over 336.1 µm² (3) and 461.5 µm² (5) to 324.3 µm² at the tip (7), including some outliers at the base and the tip.

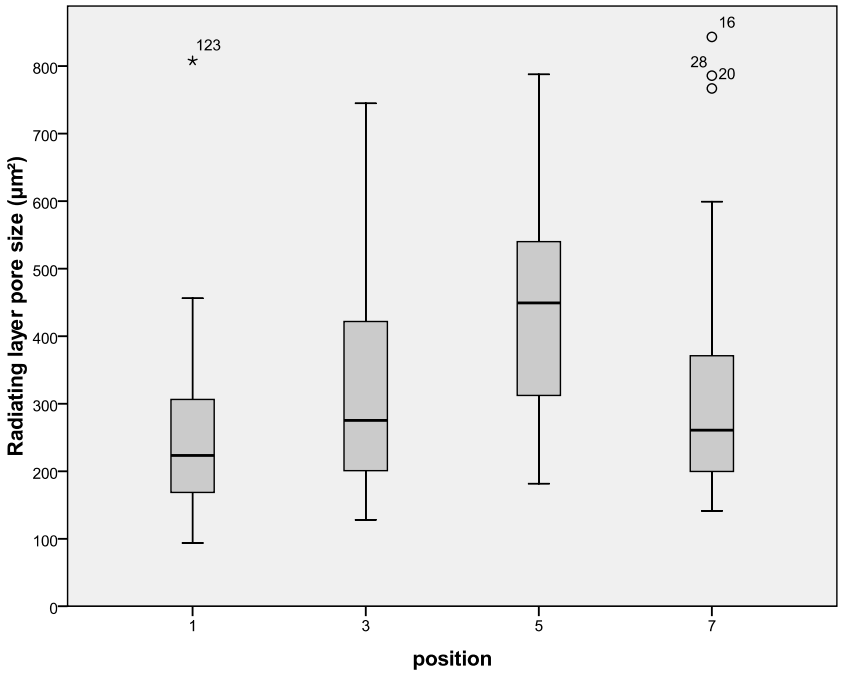

Figure 88: Box-plot of the pore size in the radiating layer of *Heterocentrotus mammillatus*

A mean pore diameter in the radiating layer of 22.2 ± 7.1 µm, as shown in Figure 89, is characterized (n = 170). Besides some outliers the pore diameter begins with 20.5 µm (1) raising up to 26.4 µm (5) and ending at the tip (7) with 21.5 µm.

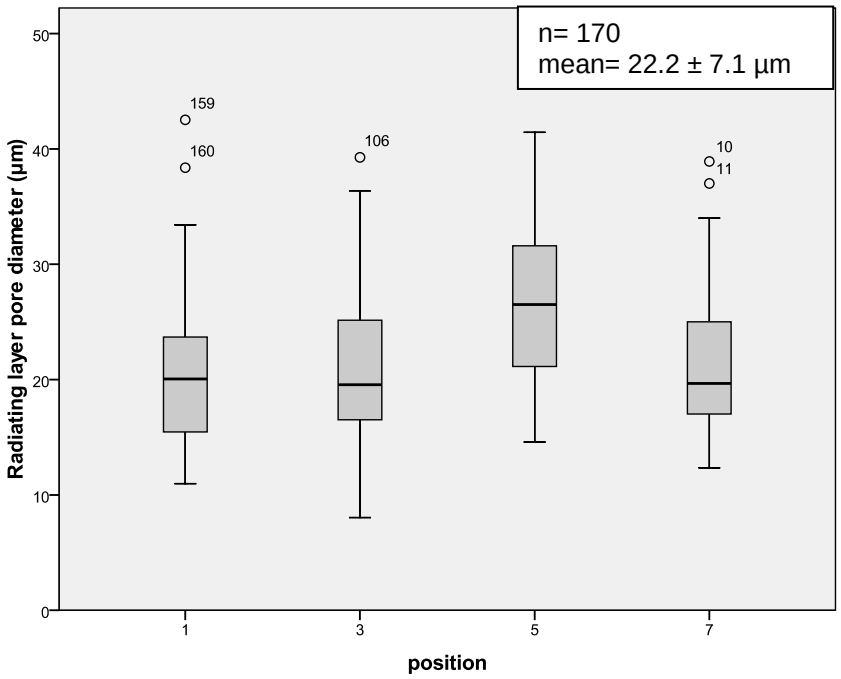

Figure 89: Box-plot of the pore diameter in the radiating layer of *Heterocentrotus mammillatus*

The highest frequencies are observed with 27, for pore diameters of 17 to 20 µm (Figure 90). The values of the pore diameter range from 7 to 45 µm. The pore diameter in the radiating layer is leptokurtic distributed with a bell-shaped curve (skewness= 0.739; kurtosis= 0.029).

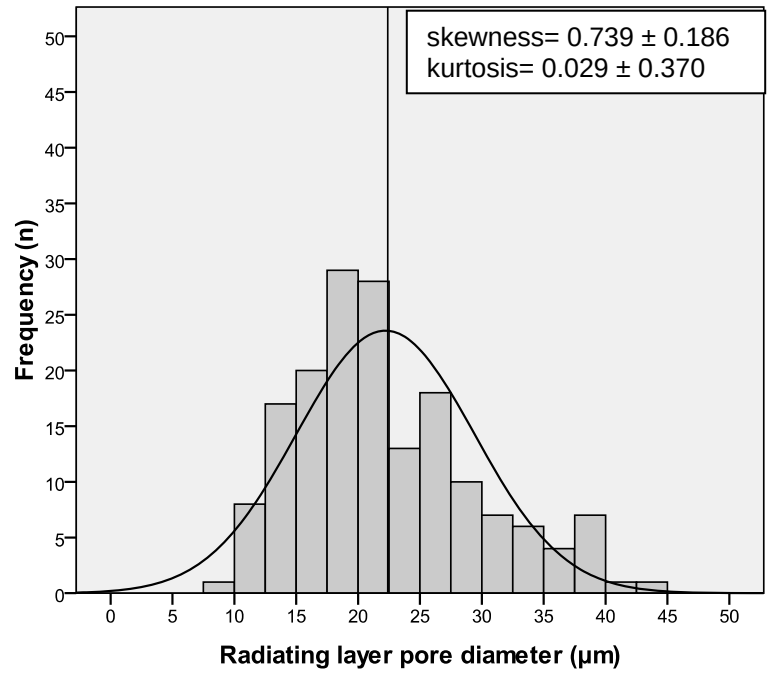

Figure 90: Histogram of the pore diameter in the radiating layer of *Heterocentrotus mammillatus*

The values (n = 170) of the box-plot in Figure 91 show a mean trabeculae diameter of 19.6 ± 6.0 µm in the radiating layer of *Heterocentrotus mammilla*tus. The trabeculae diameter

follows values not more than 20 µm, beginning with 19.8 µm (1), 19.6 µm (3), 20.6 µm (5) and ending (7) with 17.7 µm.

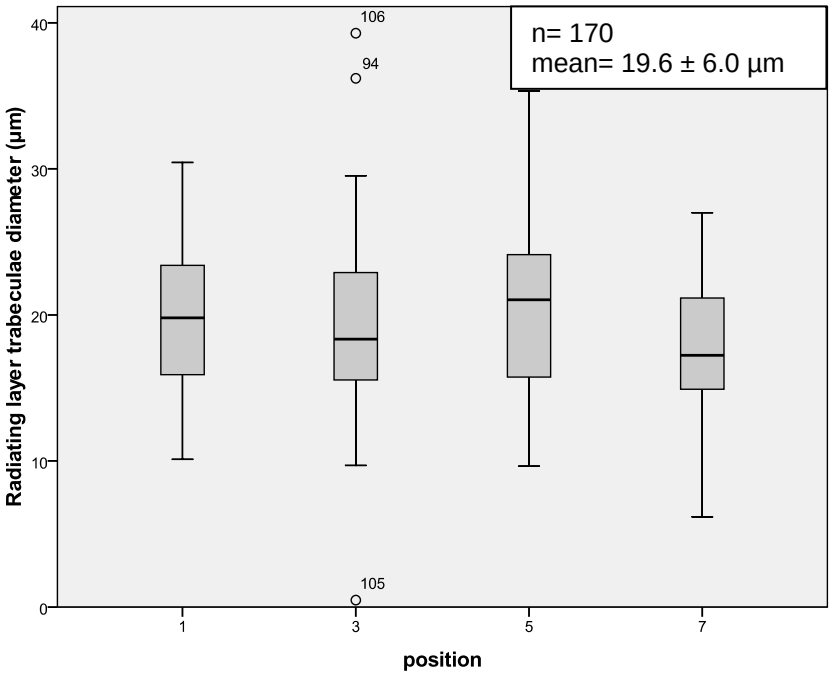

Figure 91: Box-plot of the trabeculae diameter in the radiating of *Heterocentrotus mammillatus*

The highest frequencies are observed with 30, for pore diameters of 15 to 20 µm (Figure 92). The values of the trabeculae diameter range from almost 1 to 42 µm. As the skewness (0.547) and the kurtosis (1.214) are positive, the curve is bell-shaped with a leptokurtic distribution

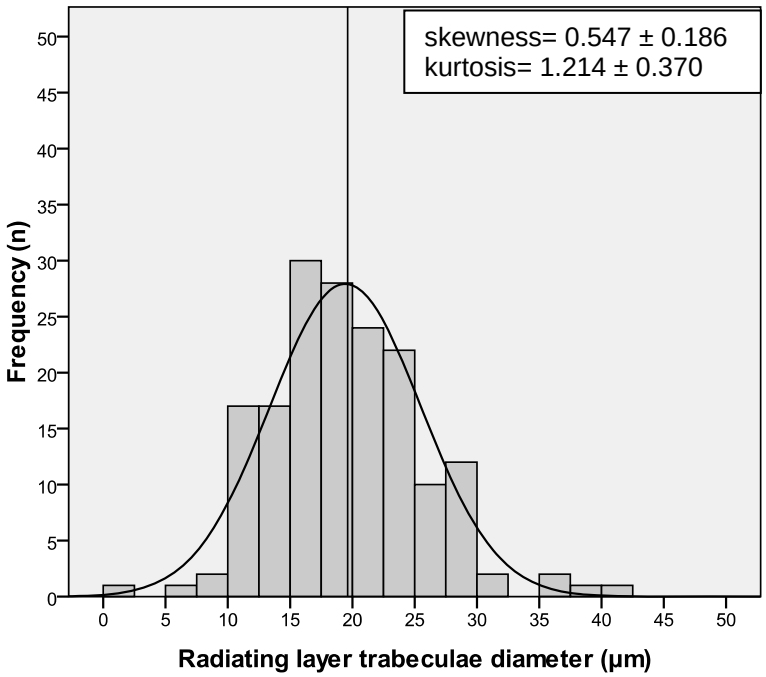

Figure 92: Histogram of the trabeculae diameter in the radiating layer of *Heterocentrotus mammillatus*

3.6 Stereom types and morphology

Table 4 gives an overview of the stereom types of the medulla, the radiating layer and the cortex (where present) of the investigated spines. This table shows that the radiating layer is mostly of a regular galleried stereom. The medulla is laminar in all spines regardless age and position of spines.

Table 4: Types of stereom in primary sea urchin spines

Species	Medulla	Radiating layer	Cortex
Plococidaris verticillata	laminar	galleried	microperforate
Phyllacanthus imperialis (aboral)	laminar	galleried	microperforate
Phyllacanthus imperialis (oral)	laminar	galleried	microperforate
Eucidaris metularia	laminar	galleried	microperforate
Prionocidaris baculosa	laminar	galleried	microperforate
Heterocentrotus mammillatus (fully grown)	laminar	labyrinthic	
Heterocentrotus mammillatus (juvenile)	laminar	labyrinthic	
Echinometra mathaei	laminar	labyrinthic	

Table 5 gives an overview of the earlier presented results of the stereom pore diameter in medulla and radiating layer in the investigated spines. The values, shown in Table 5, represent the results for the longitudinal sections of the selected spines. *Heterocentrotus mammillatus* shows a difference between juvenile and fully grown spines. This difference did not occur in spines of *Phyllacanthus imperialis*. The standard deviation was less than seven in all spines investigated. In the medulla more pore diameters lower than 20 µm occurred as in the radiating layer.

Table 5: Comparison of the pore diameter in medulla and radiating layer of several spines:
juv. = juvenile, f. g. = fully grown, pl. = platykurtic, lp. = leptokurtic

Species	Medulla	Kurtosis	Radiating layer	Kurtosis
Plococidaris verticillata	17.7 ± 4.7 µm	pl.	17.7 ± 6.0 µm	lp.
Phyllacanthus imperialis (aboral)	18.6 ± 4.7 µm	pl.	20.2 ± 4.7 µm	lp.
Phyllacanthus imperialis (oral)	18.6 ± 5.0 µm	lp.	16.1 ± 3.9 µm	pl.
Eucidaris metularia	15.7 ± 4.4 µm	lp.	14.6 ± 3.7 µm	lp
Heterocentrotus mammillatus (f. g.)	19.4 ± 5.5 µm	lp.	22.3 ± 7.2 µm	lp.
Heterocentrotus mammillatus (juv.)	12.9 ± 4.6 µm	lp.	14.2 ± 6.1 µm	lp.
Prionocidaris baculosa	20.6 ± 5.1 µm	pl.	14.1 ± 4.8 µm	lp.

3.7 Critical point drying

Several spines of *Heterocentrotus mammillatus*, *Prionocidaris baculosa* and *Phyllacanthus imperialis* were subjected to the critical point drying technique in order to recognize the organic compositions in sea urchin spines and to confirm earlier investigations made by Märkel & Röser (1983), Ameye (1999), Magdans & Gies (2004) and Magdans (2005) and to support larger investigations made by Schwartz & Reddi (1979), Marie et al. (1983), Serre et al. (1998) and Lombardi et al. (2008).

Details of the organic compositions are shown in Figure 93, for spines of *Prionocidaris baculosa* (A) and *Phyllacanthus imperialis* (B). Different cells and fibres penetrated into the pore space. The sectioning of the spines may have caused the rough surface structure (different layer) of the trabeculae.

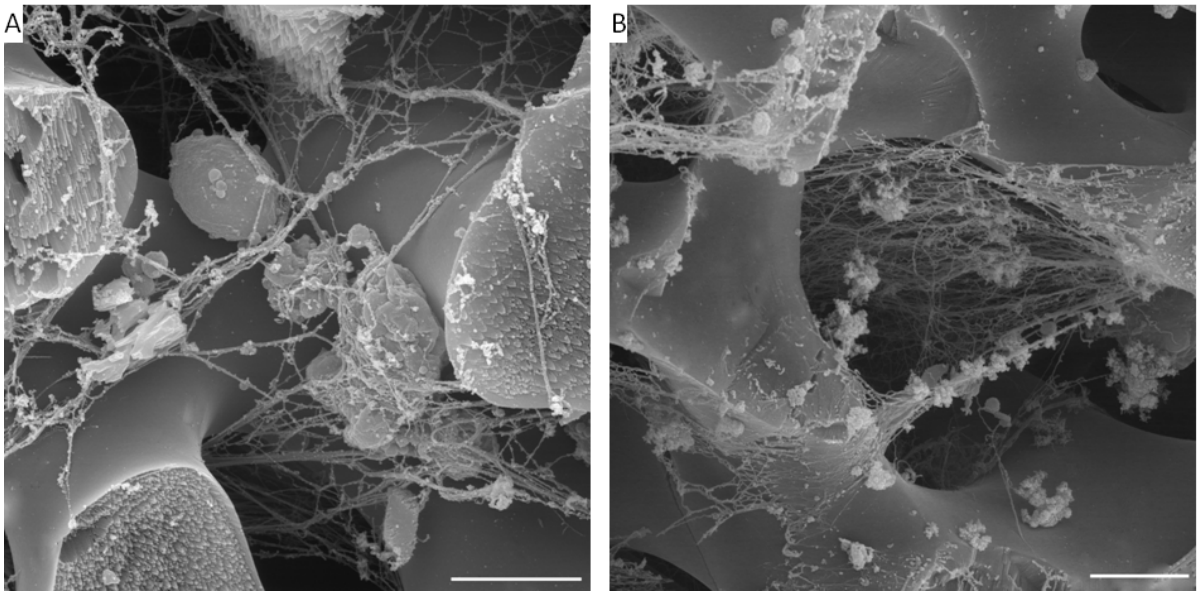

Figure 93: Detailed SEM- image of spines of *Prionocidaris baculosa* (A) and *Phyllacanthus imperialis* (B): Nerve fibres and cells are visible. The sharp fronts are the results of the earlier breakage of the spine (scale bar = 5 µm)

The detailed view of the cortex of a *Phyllacanthus imperialis* spine in cross-section is shown in Figure 94. The canals which range from the inner spine to the outer surface are surrounded by a thin organic layer, which are only a few micrometers thick. The rough structure of the cortex results either because of the earlier breakage or is due to chemical treatment that interfere with the calcite. Detailed histological investigations to describe the cell types have been carried out by Cavey & Märkel (1994).

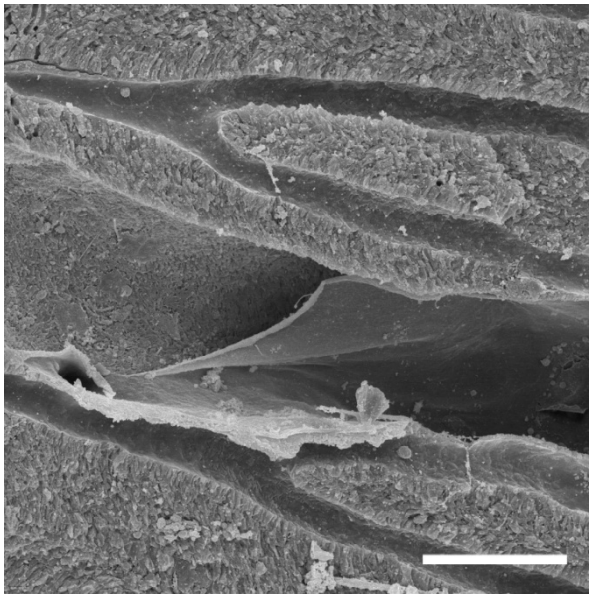

Figure 94: SEM-image of the cortex in a P*hyllacanthus imperialis* spine: The spine was broken in cross-section before the critical point drying. The stereom is microperforate with canals that range from the inside to the outer surface of the spine (scale bar = 30 µm)

In Plate 1 an overview of the spines inner and outer parts is given. Several organisms cover the surface of a *Prionocidaris baculosa* spine (A). The occurrence of fibres and cells is shown in Plate 1B. A detailed view of a cell is seen in Plate 1C. The trabeculae show a rough surface which may be due to the earlier chemical treatment, in contrast to the inner smooth pore area. The canals of the cortex, which can range from the inner to the outer side of the spine, are shown in Plate 1D. A large amount of fibres is visible in the pore spaces of a *Phyllacanthus imperialis* spine (Plate 1E). A closer examination of the stereom structure of a *Heterocentrotus mammillatus* spine shows that the surface of the pores is covered by small cells and for example crystal-like particles that might be remaining from the sea water from which they had been taken.

Plate 1: SEM images of the stereom of spines after critical point drying: *Prionocidaris baculosa*: (A) cortex and encrustation (scale bar = 100 µm), (B) medulla (scale bar = 10 µm), (C) inner stereom scale bar = 10 µm); *Phyllacanthus imperialis*: (D) cortex (scale bar = 100 µm), (E) inner stereom (scale bar = 10 µm); *Heterocentrotus mammillatus*: (F) inner stereom (scale bar = 10 µm)

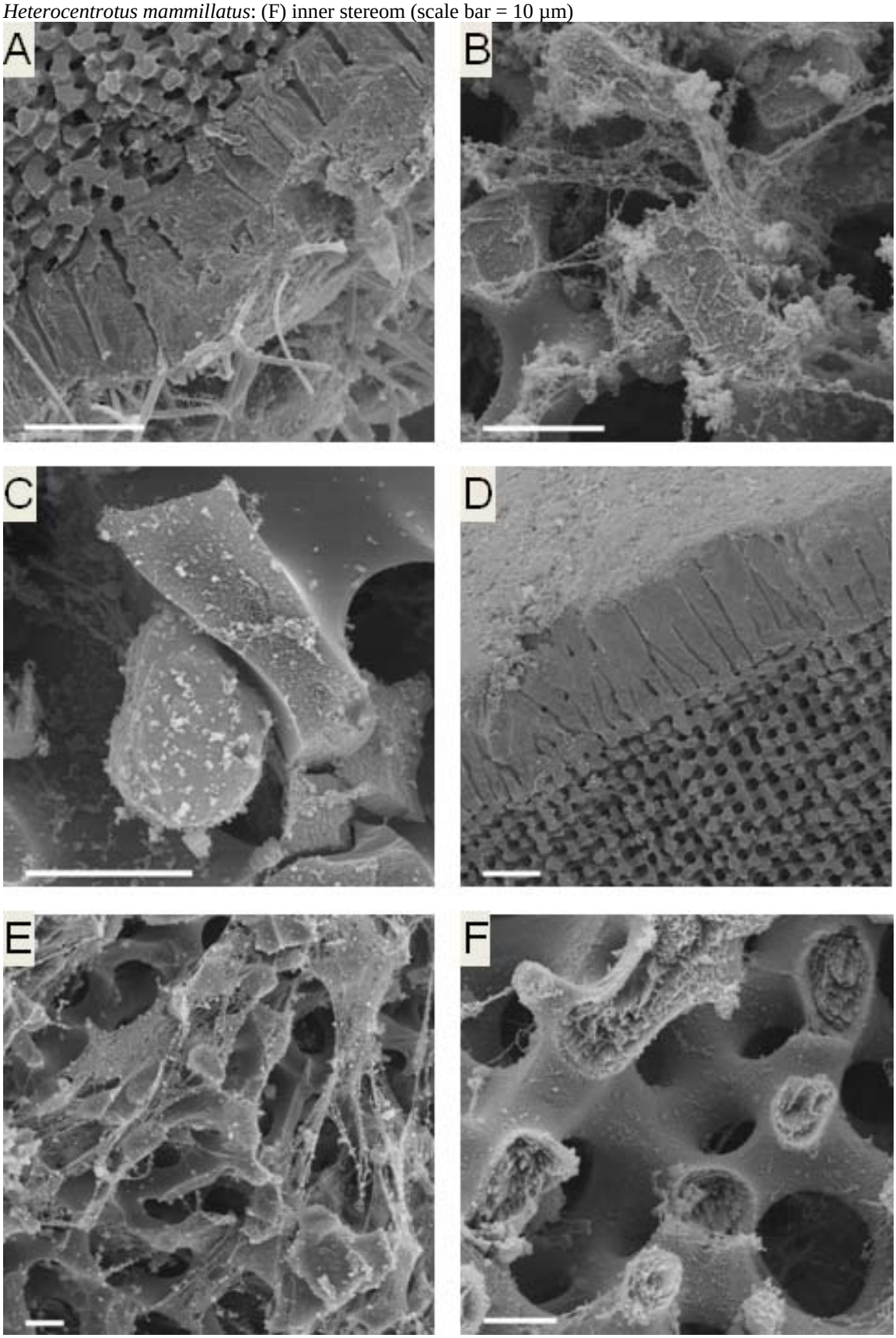

4. Discussion

For the first time, the whole length of spines and the distribution of the stereom inside the spines has been taken into account. The analyses of the stereom in spines of different sea urchins showed a large variation of values (e.g. pore diameter and pore sizes) within single spines, between younger (= smaller) to older (= larger) examples and between oral (= smaller) to aboral (= larger) spines. The stereom definitions of Smith (1980) for plates could be applied to those found in spines, e.g. galleried, microperforate and labyrinthic, but not all of the stereom types are present in spines. In general, large variations of values for each position can be noted due to the natural variation in biological objects. The reason for the outliers in almost every figure might also be due to several factors such as enlarged pores (e. g. caused by broken trabeculae) and general measurement failures.

Apart from the fact that oral spines are smaller in length than aboral spines, almost the same pore diameter occurred in the spines of *Phyllacanthus imperialis* (around 18 µm). This seems to be the most common diameter for this species and so might be the most evolutionary successful structure. This supports postulations made by Baumeister & Leinfelder (1998) and Baumeister (1999) that this is due to the primary function (daily locomotion) of spines. It could be speculated that these are adaptations (e. g. faster regeneration) to the possible higher mechanical stress on the oral side of a sea urchin. Table 1 shows that the most common structure is galleried in the radiating layer and laminar in the medulla. Due to these observations, the idea that these are the most successful structure for these positions can be postulated. Both arrangements use low amount of material, and are rather delicate (see Figure 73), compared to the growth rings or the cortex of spines, where the stereom is more or less microperforate (solid form of the stereom). This will be verified by CT scans in chapter 3. One exception is shown in the labyrinthic stereom of the radiating layer of *Heterocentrotus mammillatus*, regardless the age or position of the spine. Perforate stereom (microperforate) occurred on the outer surface of spines (e.g. in the cortex, see Plate 3). This was also found to be the case in outer surfaces of plates by Smith (1990).

The pore diameter compared in young (= smaller) and fully grown (= larger) spine differs in those of *Heterocentrotus mammillatus* but not in the oral (= smaller) and aboral (= larger) spines of *Phyllacanthus imperialis*. The SEM images, as well as the pore and trabeculae measurements, showed differences in density and trabecular thickness within the stereom types in all spines, for example that the stereom at the base of the spines is denser than in the rest of the spine (e.g. seen in *Heterocentrotus mammillatus*). This may be a

structural adaptation to the muscle fibres and the catch apparatus which penetrate the spine in that area. In all investigated *Heterocentrotus mammillatus* spines fountain-like endings near the tips occurred, which may be due to growth processes or to mechanical factors to spread impact forces. For *Heterocentrotus mammillatus* the difference between young and old spines are visible in the pore sizes. Young spines had lower pore sizes with maximum values below 100 µm². In contrast to the young spines, the old ones had pore sizes of several hundred square micrometers, also the pore and trabeculae diameters differ. The pore and trabeculae diameter in young spines is less than half that of the old ones. The pore diameter in the medulla of an old spine was lower than that of the radiating layer. The pore diameter was never more than 25 µm in all spines independent of the species. The pore diameter within young and old spines of *Heterocentrotus mammillatus* was similar at each position, but in the old ones the mean diameter was larger. The pore diameter in the radiating layer increased from the base to the tip. These results have to be seen in the context of mechanical stability. It seems that this arrangement and sizes are the best for the positions in the spines. The pore diameter in juvenile *Heterocentrotus mammillatus* spines had very low variations from the base to the tip.

The occurrence of growth rings, as a microperforate form of the stereom, could influence the mechanical behaviour of spines when compressed (see Presser et al. 2009). But the mechanical behaviour has to be seen in context with other factors, such as the muscle fibres and the catch apparatus as these are the first parts which would fail when a sea urchin is bended or compressed. The debate, whether or not the growth rings are caused by stress or can act as age markers has continued for decades (e.g. Ebert 1967, 1985, Weber 1969, Régis 1983 and Dotan & Fishelson 1985). In some sea urchins, such as *Heterocentrotus mammillatus*, the growth rate can potentially be calculated by growth rings of the spine when present (Dotan 1990).

The differences in pore size and diameter in spines of sea urchins have to be seen in the context of factors that might influence the morphology of spines such as mechanical aspects (e.g. predator impact and wave energy). Smith (1990) already mentioned that the morphology of the stereom in plates depends on several intrinsic factors such as calcite secretion, phylogeny and extrinsic factors, e.g. mechanical impacts. The innermost part of an object is the area with the least amount of material, compared to the other parts. For the spines, the thickest parts are the outer areas of the spine, e. g. cortex or the growth rings, when present. This should result in a medulla with the less amount of material compared, e. g. to the

radiating layer. This will also be discussed within the results of the CT in chapter 3and the bending tests in chapter 4.

After Smith (1990) the different stereom types can be, at least in echinoderm plates, correlated with several areas or may be associated with different functions. Laminar stereom is found in areas where low amount of material is present. This was the case in the medulla of spines. The different perforated stereom types (microperforate) may be associated with articulation surfaces (e. g. boss, mamelon or tubercle). The microperforate stereom was reported in this survey here for the cortex and the growth rings in spines. After Smith (1990) the labyrinthic and galleried stereom is associated with connective tissue or collagen fibres as the construction stereom. In the investigated spines, these types are found near the base and the milled ring, where the muscle fibres and the catch apparatus penetrate into a spine. This is also verified by critical point drying in spines of several sea urchin species, where filamentary structures and cells were reported.

5. Conclusion

- The pore measurements of the spine showed a difference from juvenile to fully grown spines. Based on the results, the juvenile spines are more compact than fully grown spines.

- The stereom type of the medulla was always of a laminar arrangement among all species, supporting the idea that this is evolutionary the most successful. The stereom types might be associated with different functions and positions in the spine of a sea urchin.

- The stereom in the radiating layer had always larger pore diameters than the medulla.

- The cortex of fully grown spines is thicker than that of the juvenile ones supporting the idea that the fully grown ones are more stabile.

- The growth rings might influence the mechanical behaviour of the spines, as already investigated by Presser et al. (2009), but it will also depend on different habitats, feeding strategy and functions of the spines.

6. References

Ameye, L. (1999). “Ultrastrucural localization of proteins involved in sea urchin biomineralization.” Journal of Histochemistry & Cytochemistry 47(9): 1189-1200.

Baumeister, W, (1998). “Meeresaquaristik.” Ulmer, Stuttgart.

Baumeister, J. G. & Leinfelder, R. R. (1998). "Constructional morphology of three Upper Jurassic echinoids." Palaeontology 41: 203-219.

Baumeister, J. (1999). "Vergleich der Funktionsmorphologie und Paläoökologie zweier Rhabdocidariden (Echinodermata: Cidaridae)." Paläontologische Zeitschrift 73(3): 319-326.

Becher, S. (1914). “Über statische Strukturen und kristalloptische Eigentümlichkeiten des Echinodermenskeletts.” Verhandlungen der Deutschen Zoologischen Gesellschaft 24: 307-327.

Betz, O., Thayer, M. K. & Newton, A. F. (2003). “Comparative morphology and evolutionary pathways of the mouthparts in spore-feeding Staphylinoidea (Coleoptera).” Acta Zoologica 84(3): 179-238.

Bhushan, B. (2009). “Biomimetics.” Philosophical Transactions of the Royal Society of London A 367: 1443-1444.

Birenheide, R. & Motokawa, T. (1997). “Morphology of skeletal cortex in the arms of crinoids (Echinodermata: Crinoidea).” Zoological Science 14(5): 753-761.

Borig, P. (1933). “Über Wachstum und Regeneration der Stacheln einiger Seeigel.” Zoomorphology 27(4): 624-653.

Carnevali, M. D. C., Bonasoro, F. & Melone, G. (1991). “Microstructure and mechanical design in the lantern ossicles of the regular sea-urchin *Paracentrotus lividus*: a scanning electron microscope study.” Bolletino di zoologia 58(1): 1 - 42.

Cavey, M. J. & Märkel, K. (1994). “Echinodermata.” In: Harrison, F. W. (Ed.): Microscopic Anatomy of Invertebrates, Wiley, New York: 345-400.

Dakin, N. (1997). “Das Meerwasseraquarium: Einrichtung, Technik und Tiere.” BLV, München

David, B., Stock, S. R., de Carlo, F., Hétérier, V. & de Ridder, C. (2009). “Microstructures of antarctic cidaroid spines: diversity of shapes and ectosymbiont attachments.” Marine Biology 156: 1559-1572.

Deutler, F. (1926). “Über das Wachstum des Seeigelskeletts.” Zoologische Jahrbücher 48: 119-200.

Dotan, A. & Fishelson, L. (1985). “Morphology of spines of *Heterocentrotus mammillatus* (Echinodermata: Echinoidae) and its ecological significance.” In: Keegan, B. F. & O`Connor, B. D. S. (Eds.): Echinodermata: Proceedings of the international echinoderm conference, Galway September 24.-29.9.1984, Rotterdam, A. A. Balkema: 253-260.

Dotan, A. (1990). “Population structure of the echinoid *Heterocentrotus mammillatus* (L.) along the littoral zone of south-eastern Sinai.” Coral Reefs 9: 75-80.

Ebert, T. A. (1967). “Growth and repair of spines in the sea urchin *Strongylocentrotus purpuratus* (Stimpson).” Biological Bulletin 133: 141-149.

Ebert, T. A. (1985). “The non-periodic nature of growth rings in echinoid spines.” In: Keegan, B. F. & O`Connor, B. D. S. (Eds.): Echinodermata: Proceedings of the international echinoderm conference, Galway September 24.-29.9.1984, Rotterdam, A. A. Balkema: 261-267.

Hasenpusch, W. (2000). "Die Stachel der Griffelseeigel." Mikrokosmos 89(1): 23 - 27.

Hesse, E. (1900). “Die Mikrostruktur der fossilen Echinoideenstachel und deren systematische Bedeutung.” Neues Jahrbuch für Mineralogie, Geologie und Palaeontologie 13: 185-264.

Hiratzka, L. F., Goeken, J. A., White, R. A. & Whright, C. B. (1979). “In vivo comparison of replamineform, silastic and bioelectric polyurethane arterial grafts.” Archives of Surgery 114(6): 698-702.

Hozman, P. (1983). “Das unterschiedliche Härteverhalten biogener und anorganischer Calcitkristalle.” Bochumer Geologische und Geotechnische Arbeiten 10: 1-100.

Lai, M., Kulak, A. N., Law, D., Zhang, Z., Meldrum, F. C. & Riley, D. J. (2007). “Profiting from nature: macroporous copper with superior mechanical properties.” Chemical Communications 34: 3547-3549.

Lombardi, C., Cocito, S., Hiscock, K., Occhipinti-Ambrogi, A., Setti, M. & Taylor, P. (2008). “Influence of seawater temperature on growth bands, mineralogy and carbonate production in a bioconstructional bryozoan.” Facies 54(3): 333-342.

Magdans, U. & Gies, H. (2004). “Single crystal structure analysis of sea urchin spine calcites: Systematic investigations of the ca/mg distribution as a function of habitat of the sea urchin and the sample location in the spine.” European Journal of Mineralogy 16(2): 261 - 268.

Magdans, U. (2005). “Mechanismen der Biomineralisation von Calcit am Beispiel von Seeigel-Stacheln: Untersuchung der Wechselwirkung zwischen Sorbat-Molekülen und Calcit-Wachstumsgrenzflächen mit Oberflächen-Röntgenbeugung und numerischen Simulationen.” PhD thesis, Faculty of Geology, Ruhr University. Bochum.

Macurda, D. B. J. (1973). “The stereomic microstructure of the blastoid endoskeleton.” Contributions from the Museum of Paleontology, University of Michigan 24(8): 69-83.

Mannaerts, G. (2007). “Effets des métaux lourds sur la morphologie et la mécanique des piquants de l’échinide *Echinus acutus*.” Diploma thesis, Faculty of Science, Université libre de Bruxelles.

Marie, P. J., Travers, R. & Delvin, E. E. (1983). “Influence of magnesium supplementation on bone turnover in the normal young mouse.” Calcified Tissue International 35(1): 755-761.

Märkel, K. Röser, U. (1983). “The spine tissues in the echinoid *Eucidaris tribuloides*.” Zoomorphology 103: 25-41.

Meldrum, F. C. (2007). “Bio-Casting: biomineralized skeletons as templates for macroporous structures.” In: Behren, P. & Bäuerlein, E. (Eds.): Handbook of Biomineralization, Wiley, Weinheim: 289-309.

Mischor, B. (1975). “Zur Morphologie und Regeneration der Hohlstacheln von *Diadema antillarum* Philippi und *Echinothrix diadema* (L.) (Echinoidea, Diadematidae).” Zoomorphology 82: 243-258.

Müller, J. (1854). “Über den Bau der Echinodermen.” Abhandlungen der preußischen Akademie der Wissenschaft 44: 123-219.

Mortensen, Th. (1909). “Die Echinoiden.” In: Drygalskie, E. von (Ed.): Deutsche Südpolarexpedition 1901-1903, Georg Reimer, Berlin. XI.Band Zoologie Band III: 1-114.

Moureaux, C., Pérez-Huerta, A., Compère, P. Zhu, W., Leloup, T. & Dubois, P. (2010). “Structure, composition and mechanical relations to function in sea urchin spine.” Journal of Structural Biology 170(1): 41-49.

Nickel, K. G., Presser, V., Schultheiß, S., Berthold, C. (2009a). “Meeresfrucht mit Köpfchen.” Labor & More 9 (4): 54 - 56.

Nickel, K.G., Presser, V., Schultheiß, S., Berthold, C., Kohler, C., Nebelsick, J. H., Grossmann, N., Stegmaier, T., Finckh, H. & Vohrer, A. (2009b). “Seeigelstachel als Modell für stoffdurchlässige Einschlagschutzsysteme.” In: Kesel, A. B. & Zehren, D. (Eds.): Bionik-Patente aus der Natur, Bionik-Innovations-Centrum Bremen, Bremen: 26-36.

Oaki, Y. & Imai, H. (2006). “Nanoengineering in echinoderms: The emergence of morphology from nanobricks.” Small 2(1): 66-70.

Olabarria, O. (2000). “Epibiont molluscs on neogastropod shells from sandy bottoms, pacific coast of mexico.” Journal of the Marine Biological Association of the United Kingdom 80: 291-298.

Presser, V., Schultheiß, S., Berthold, C., Nickel, K. G. (2009). “Sea urchin spines as a model-system for permeable, light-weight ceramics with graceful failure behavior. Part I. Mechanical behavior of sea urchin spines under compression.” Journal of Bionic Engineering 6(3): 203 - 213.

Qin, L.-R., Zhao, J.-W., Zhang, L.-D. & Zou, X.-W. (2007). “Fabrication and photoluminescence of urchin-like ZnO/MgO hierarchical structures.” Chemistry Letters 36(5): 598 - 599.

Rayfield, E. J., Norman, D. B., Horner, C. C., Horner, J. R., Smith, P. M., Thomason, J. J. & Upchurch, P. (2001). “Cranial design and function in a large theropod dinosaur.” Nature 409(22): 1033-1037.

Rayfield, E. J. (2007). “Finite element analysis and understanding the biomechanics and evolution of living and fossil organisms.” Annual Review of Earth and Planetary Sciences 35: 541-576.

Régis, M. B. & Thomassin, B. A. (1983). “Anomalies de structure des radioles de *Heterocentrotus mammillatus* (Echinodermata: Echinoidea) en microcosme in vitro.” Marine Biology 75: 89-98.

Richter, D. K. (1974). “Zur subaerischen Diagenese von Echinidenskeletten und das relative Alter pleistozaener Karbonatterrassen bei Korinth, Griechenland.” Neues Jahrbuch für Geologie und Paläontologie 146(1): 51-77.

Richter, D. K. (1979). “Die Stufen der meteorisch-vadosen Umwandlung von Mg-Calcit in Calcit in rezenten bis pliozänen Biogenen Griechenlands.” Neues Jahrbuch für Geologie und Paläontologie 158(3): 277-333.

Richter, D. K. (1984). “Zur Zusammensetzung und Diagenese natürlicher Mg-Calcite.” Bochumer Geologische und Geotechnische Arbeiten 15: 1-310.

Ries, J. B. (2004). “Effect of ambient Mg/Ca ratio on Mg fractionation in calcareous marine invertebrates: A record of the oceanic Mg/Ca ratio over the phanerozoic.” Geology 32(11): 981-984.

Robinson, D. G., Ehlers, U., Herken, R., Herrmann, B., Mayer, F. & Schürmann, F.-W. (1985). “Präparationsmethodik in der Elektronenmikroskopie.” Springer, Heidelberg.

Ruppert, E. E., Fox, R. S. & Barnes, R. D. (2004). “Invertebrate Zoology. Chapter 28: Echinodermata.” Brooks/Cole, Belmont: 872-929.

Sander, M. (1998). “Aquarientechnik in Süß-und Seewasser.” Ulmer, Stuttgart.

Schultz, H. (2006): “Sea-urchins, a guide to worldwide shallow water species”, Scientific Publications, Hemdingen.

Schwartz, R. & Reddi, A. (1979). “Influence of magnesium depletion on matrix-induced endochondral bone formation.” Calcified Tissue International 29(1): 15-20.

Serre, C. M., Papillard, M., Chavassieux, P., Voegel, J. C. & Boivin, G. (1998). “Influence of magnesium substitution on a collagen-apatite biomaterial on the production of a calcifying matrix by human osteoblasts.” Journal of Biomedical Materials Research 42(4): 626-633.

Schneider, C. L. (2003). “Hitchhiking on pennsylvanian echinoids: epibionts on *Archaeocidaris*.” Palaios 18: 435-444.

Smith, A. B. (1980). “Stereom microstructure of the echinoid test.” Special Papers in Palaeontology 25: 1-83.

Smith, A. B. (1990). “Biomineralization in echinoderms.” In Carter, J. G. (Ed.): Skeletal Biomineralization: patterns, process and evolutionary trends, Van Nostrand Rheinhold, New York: 413-443.

Stewart, C. (1871). “On the minute structure of certain hard parts of the genus *Cidaris*.” Quarterly Journal of Microscopical Science s2-11(41): 51-55.

Sukontason, K., Bunchu, N., Methanitikorn, R., Chaiwong, T. & Kuntalue, B. (2006). “Ultrastructure of adhesive device in fly in families calliphoridae, muscidae and sarcophagidae, and their implication as mechanical carriers of pathogens.” Parasitology Research 98(5): 477-481.

Untersteiner, H. (2007). “Statistik - Datenauswertung mit Excel und SPSS: für Naturwissenschaftler und Mediziner.” UTB, Wien.

Vecchio, K. S., Zhang, X., Massie, J. B., Wang, M. & Kim, C. W. (2007). “Conversion of sea urchin spines to Mg-substituted tricalcium phosphate for bone impants.” Acta Biomaterialia 3: 785-793.

Weber, J. N. (1969). “Origin of concentric banding in the spines of the tropical echinoid *Heterocentrotus*.“ Pacific Science 23: 452-466.

Weber, J. N., White, E. W. & Lebiedzik, J. (1971). “New porous biomaterials by replication of echinoderm skeletal microstructures.” Nature 233: 337-339.

Weber, J. N., Greer, R., Voight, B., White, E. & Roy, R. (1969). “Unusual strength properties of echinoderm calcite related structure.” Journal of Ultrastructure Research 26: 355-366.

Widak, V. & Norajitra, P. (2009). “Optimization of He-cooled divertor cooling fingers using a CAD-FEM method.” Fusion Engineering and Design 84 (7-11): 1973-1978.

Wilkie, I. C. (2001). “Autotomy as a prelude to regeneration in echinoderms.” Microscopy Research and Technique 55.

7. Supplement

7.1 Aquaria assemblage

The mounting of the aquaria took place on robust wooden tables (Figure 95 & 96). The technical equipment was installed near the aquaria.

Figure 95: The assembling of two aquaria in the lab of the Institute

Figure 95: Aquaria after the complete installation of the technical equipment

The growth process inside the aquaria until the finishing of the intake phase after 140 days is shown in Figure 97 to 99. The development of the ecosystem took several months. After placing a few algae and a sea urchin inside the aquarium the first brown algae occur (Figure 98).

Figure 97: The aquaria after an intake phase of three weeks

Figure 98: Aquarium after 2 months, algae beginning to grow

Figure 99: Fully equipped aquaria after six months

7.2 Scanning electron microscopy images

Several hundred scanning electron microscopy images have been taken during the investigation of the sea urchins spines. The following plates give an additional overview of the stereom structure in spines

Plate 2: *Plococidaris verticillata* spine : A) top view of a whorl, including radiating layer and cortex (scale bar = 100 µm); B) detailed view of the galleried radiating layer of a whorl (scale bar = 10 µm); C) top view near the base (scale bar = 500 µm); D) medulla near the base (scale bar = 100 µm); E) tip of a spine including, medulla, radiating layer and cortex (scale bar = 500 µm); F) detailed view at the base including medulla and radiating layer (scale bar = 500 µm)

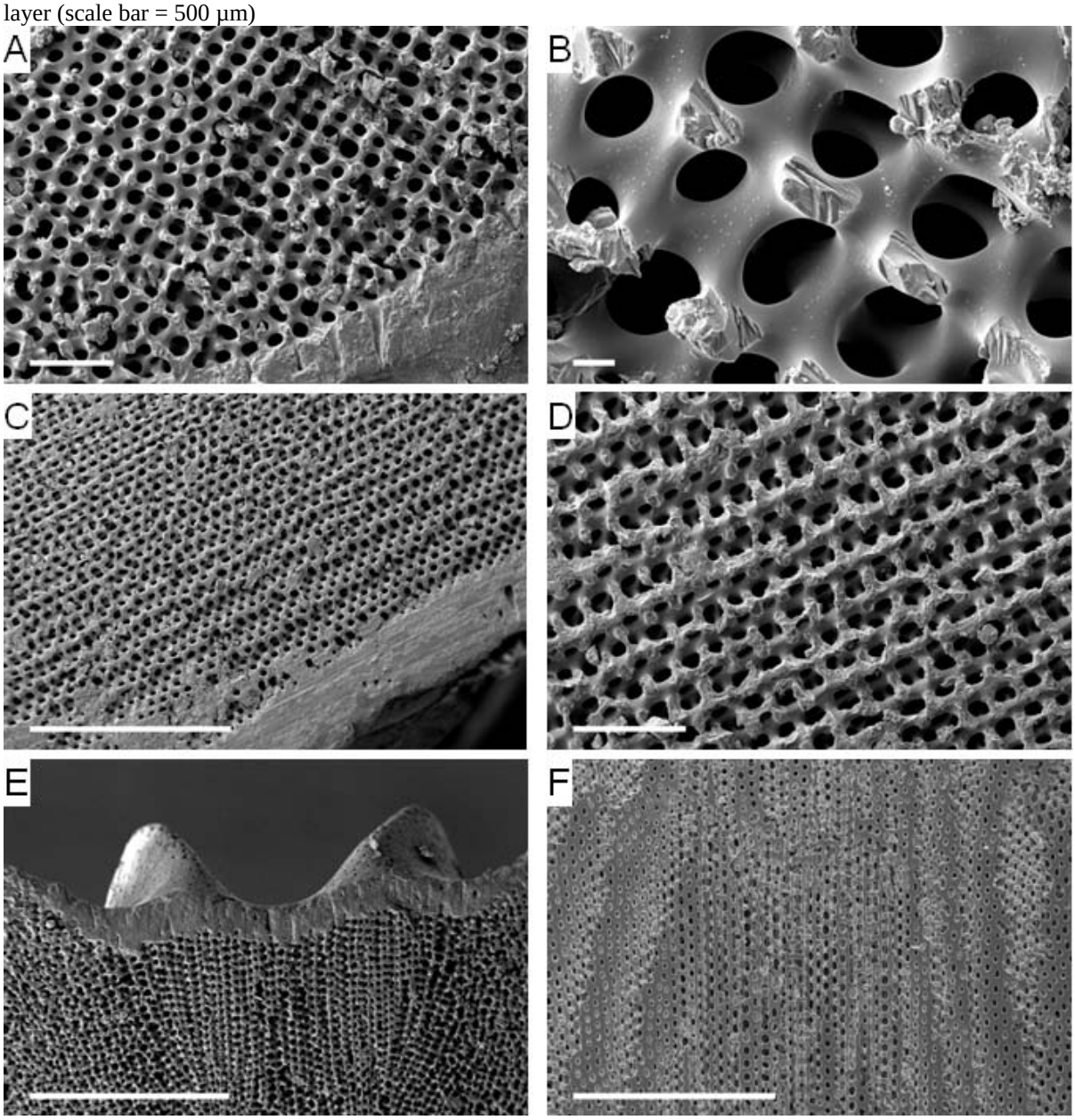

Plate 3: *Phyllacanthus imperialis* spine: A) The tip of a spine including medulla, radiating layer and the cortex (scale bar = 500 µm); B) detailed view of the medulla, followed by the radiating layer (scale bar = 500 µm); C) detailed view of the microperforate cortex (scale bar = 100 µm); D) radiating layer (scale bar = 100 µm); E) radiating layer near the base (scale bar = 100 µm); F) radiating layer in the middle of the shaft (scale bar = 100 µm)

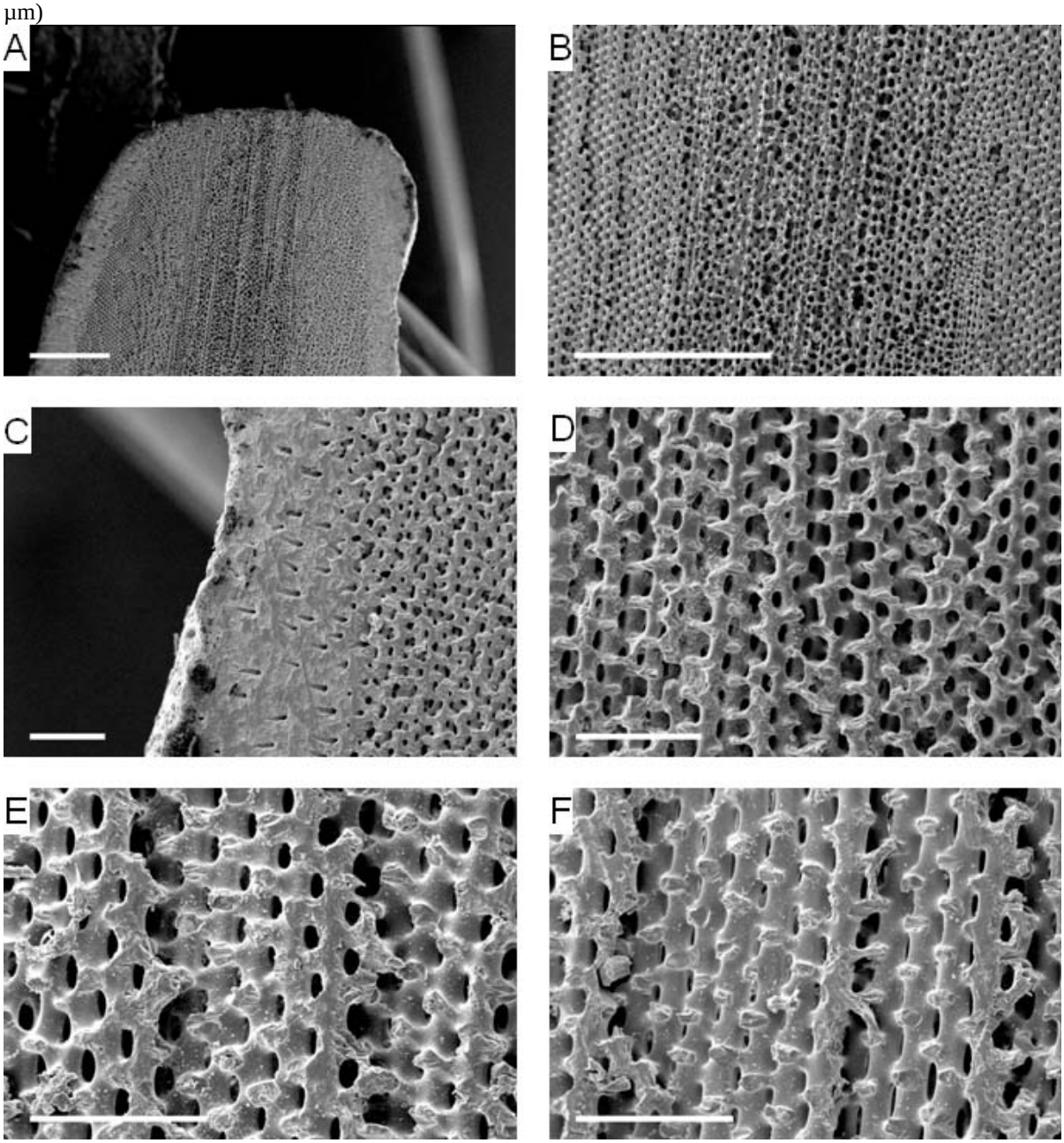

Plate 4: *Eucidaris metularia* spine: A) Longitudinal view of the medulla in the centre near the milled ring followed by the radiating layer (scale bar = 500 µm); B) detailed view of the galleried radiating layer (scale bar = 100 µm); C) longitudinal view of the shaft (scale bar = 100 µm); D) detailed view of a canal in the cortex (scale bar = 10 µm); E) longitudinal view of the radiating layer and the cortex (scale bar = 500 µm); F) detailed view of the medulla (scale bar = 100 µm)

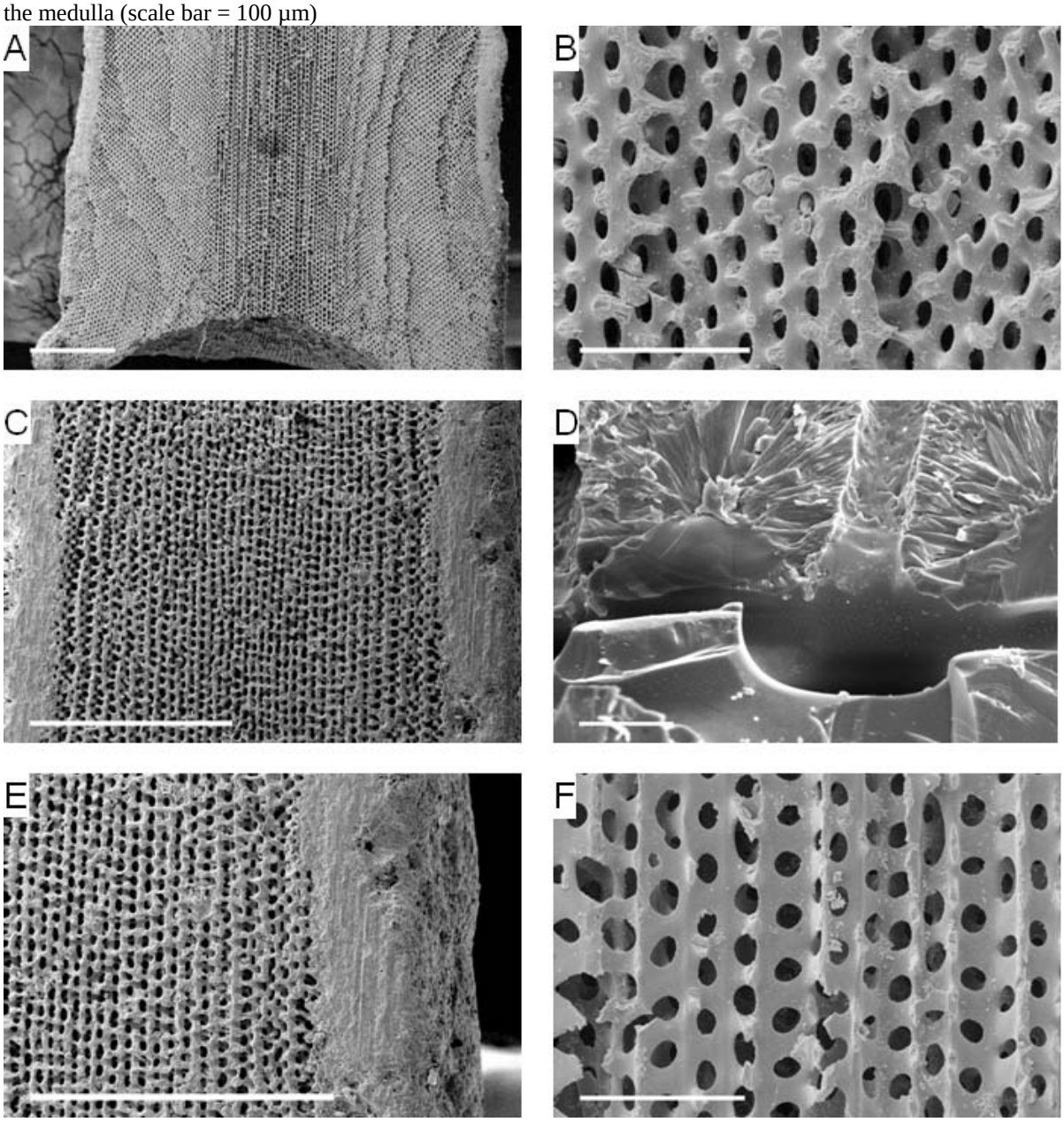

Plate 5: *Prionocidaris baculosa* spine: A) longitudinal surface view including equally spaced nodules (scale bar = 500 µm); B) stereom of the base (scale bar = 500 µm); C) detailed view of the base (scale bar = 500 µm); D) galleried stereom of the radiating layer (scale bar = 100 µm); E) cortex and radiating layer (scale bar = 100 µm); F) galleried stereom in cross-section (scale bar = 100 µm)

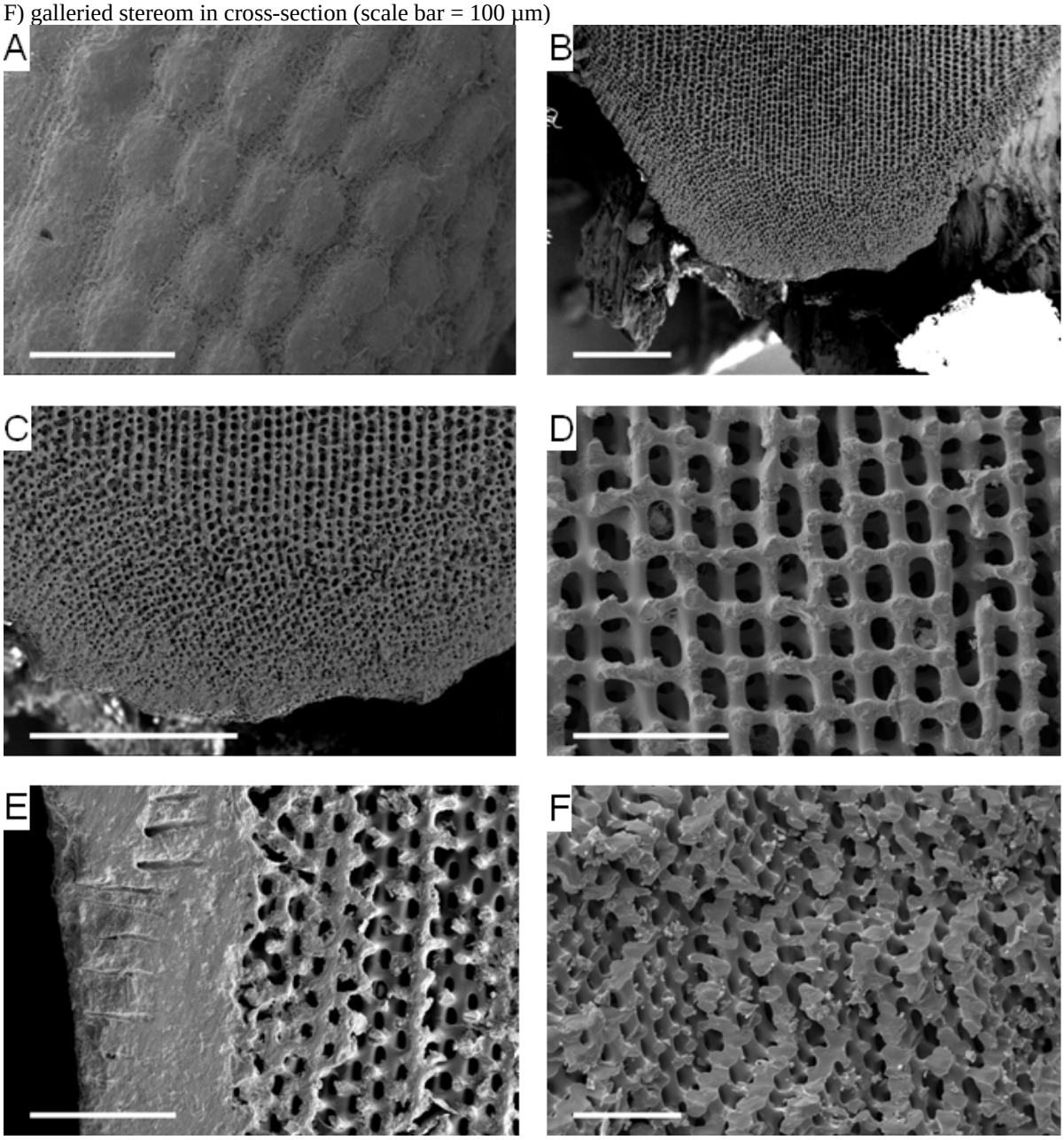

Plate 6: *Echinometra mathaei* spine: A) longitudinal surface view including the equally spaced struts (scale bar = 500 µm); B) cross-section near the base, including part of the medulla, radiating layer and the growth rings (scale bar = 100 µm); C) & D) cross-sections in the middle of the shaft (scale bar = 100 µm); E) longitudinal view of the base and lower shaft, including growth rings (scale bar 500 µm);; F) cross-section of the spine near the tip (scale bar = 100 µm)

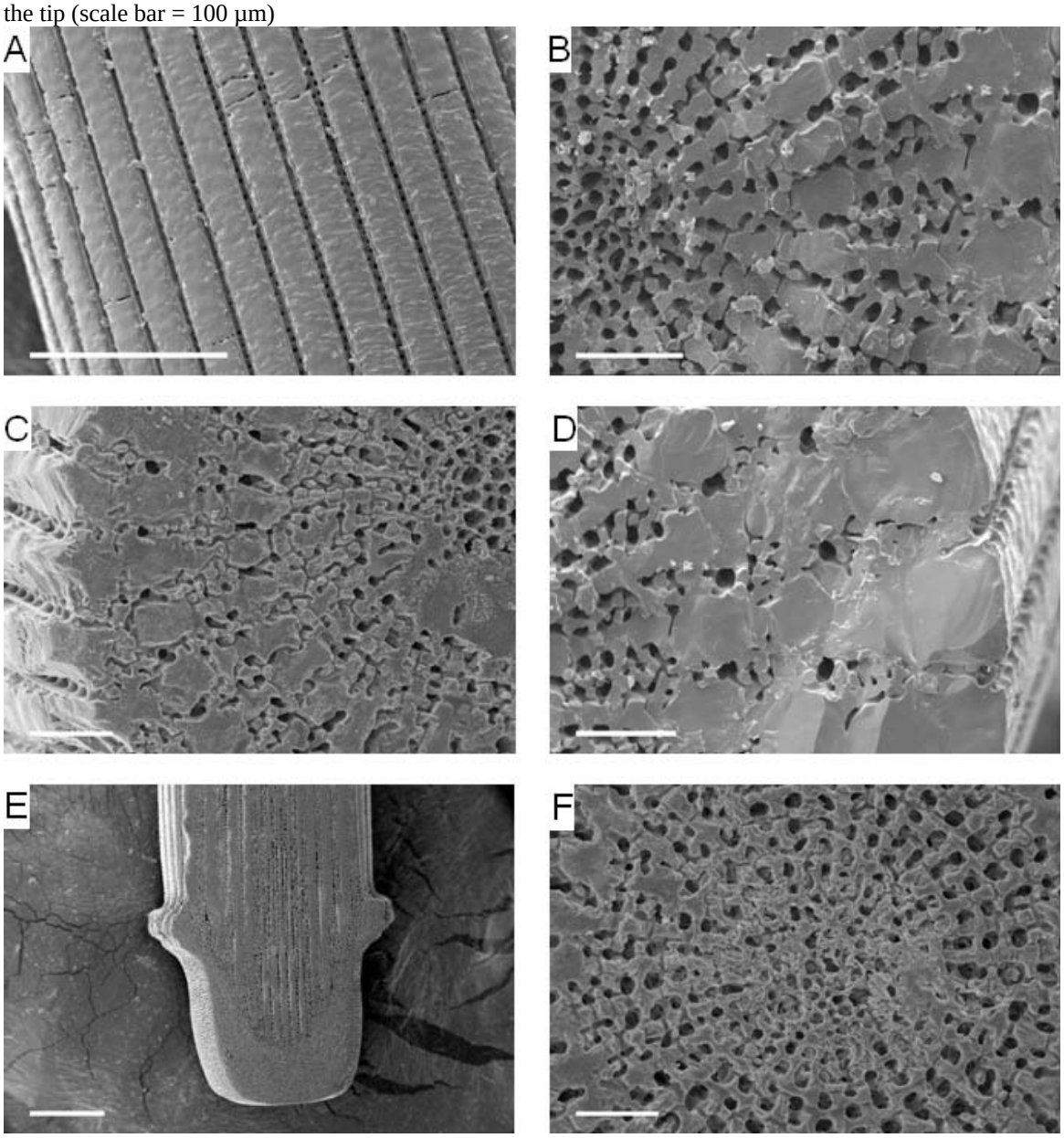

Plate 7: *Heterocentrotus mammillatus* spine: A) stereom of the base (scale bar = 500 µm); B) detailed view of the lower shaft including growth rings (scale bar = 500 µm); C) cross-section of a spine, regular disruption of the radiating layer by the growth rings (scale bar = 500 µm); D) detailed view of growth rings (scale bar = 500 µm); E) detailed view of the labyrinthic radiating layer (scale bar = 100 µm); F) middle shaft including medulla and radiating layer with growth rings (scale bar = 500 µm)

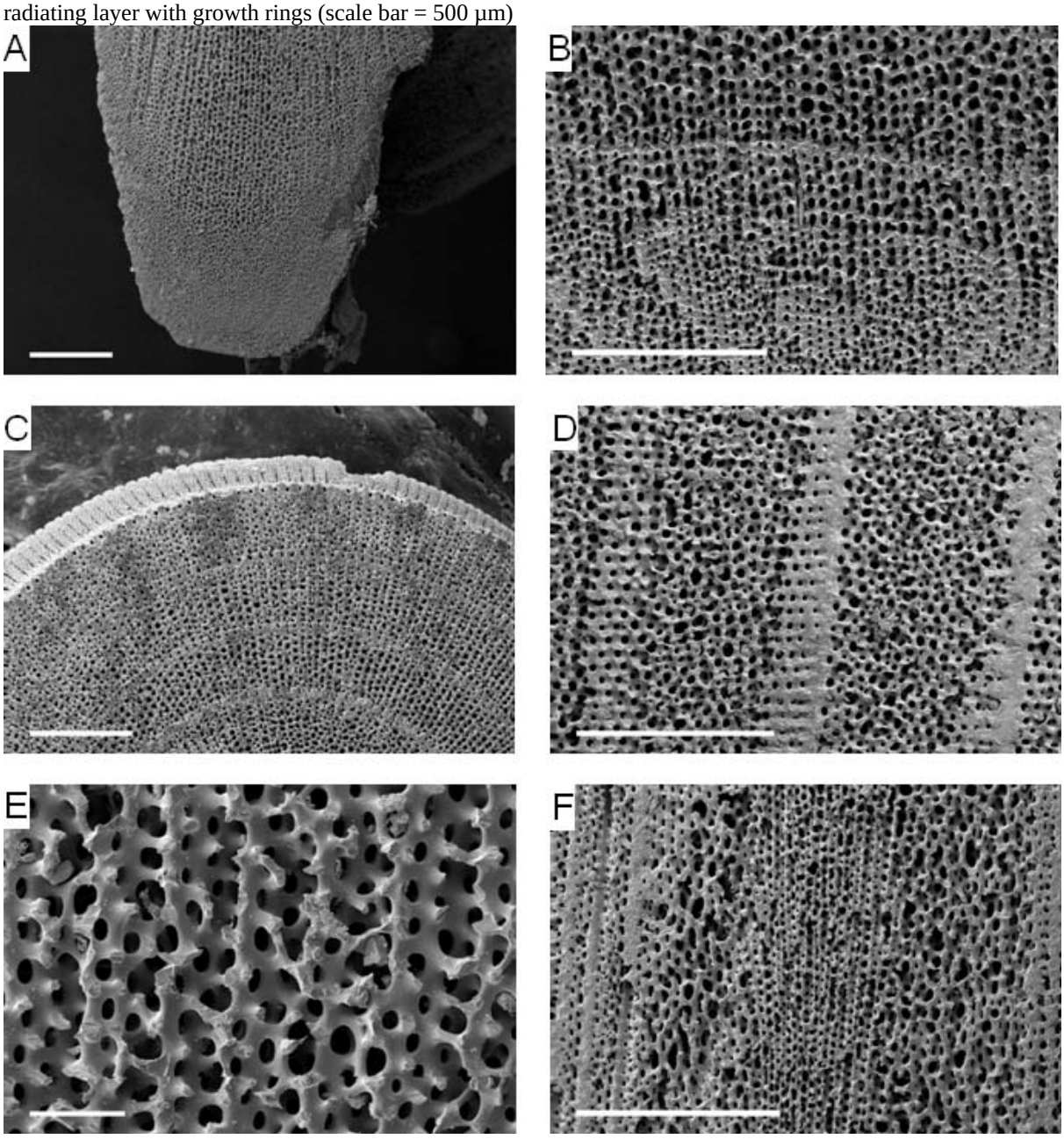

Chapter 3: X-ray Computer Tomography of sea urchin spines

Abstract The history of computer tomography in general and with respect to echinoderm research is described. Investigations regarding the internal structure of several sea urchin spines (including *Heterocentrotus mammillatus*, *Phyllacanthus imperialis* and *Prionocidaris baculosa*) were carried out. For *Heterocentrotus mammillatus* and *Phyllacanthus imperialis*, both aboral and oral spines are compared. Special focus lies on the growth rings and different densities of the stereom in the investigated spines. The growth rings are denser than the surrounding stereom. The medulla and the radiating layer differ in the amount of material. Computer tomography as a method to describe the internal structure of an object is compared to that of the scanning electron microscopy technique.

1. Introduction

Computer Tomography (CT) is a non-invasive (non-destructive) method for obtaining structural and functional information about objects and their anatomy by computer processing. The word "tomography" derives from the Greek words "tomos" which means to cut and "graphein" to write. Numerous x-ray images are taken from an object in order to generate a 3D image. In biological studies CT is used where only a few specimens are available, e.g. in fossil studies (Sutton 2008) or for interpretations of cultural history (Ebinger-Rist et al. 2009). CT scanning has the potential to generate predictions regarding the mechanics of several materials, such as polymer foam, e.g. to display structural characteristics during formation of polymer foams (Elmoutaouakkil et al. 2003, Fischer et al. 2009 & Rack et al. 2009). Data and hypotheses generated by CT scans are helpful in the determination of structural densities of objects.

Historically, CT was developed for diagnosis in humans. Analyses of the torso and organs are now common and relatively routine in many cases (cancer and heart diagnoses stand as examples), thus providing a key means for detection and treatment of disease (e.g. Kim et al. 1999, Flohr 2008, Schuetz et al. 2010). Beginning with the invention techniques in standard computer tomography date from the late 1970s and by the 1990s it was possible to develop images from CT scans with fewer impediments (Crawford & King 1990, Kalender et al. 1990 & Kalendar 2006). More recently, techniques use synchrotron x-ray phase-contrast microtomography and nanotomography (Attwood 2006, Betz et al. 2007). At first, the x-ray beam is attenuated in different amounts depending on structure, material and object (e.g.

organs, muscles, other materials). The different signals are picked up by a detector and sent electronically to a computer. This procedure is repeated from different directions and subsequently two dimensional CT images can be analysed. These two dimensional images can be transformed to 3D objects, which is of interest in medical and biological sciences (Maisey 2001, Gravante & Giordano 2008).

The TomoScope used in this survey, is a special x-ray in-vivo scanner mostly used to analyse technical components such as construction material, polymer foams or load bearing structures. With a turntable it is possible to turn objects by 360° during a CT scan (for further information see Stach 2006). Secondly, in echinoderm research detailed CT image analyses are common for structural description (David et al. 2009), e. g. for mapping material distribution during growth in sea urchin teeth (Stock et al. 2002a, 2002b, 2004 & Stock & Veis 2003) or for analyzing material in specimens & their spines (Berman et al. 1990, Su et al. 2000). Rahman et al. (2009) used the computed tomography to display former non visible areas in echinoderm fossils. The newest method, magnetic resonance imaging (MRI) has been used to analyse recent or fossil echinoderms (Ziegler 2008) and other species such as belemnites (Mietchen et al. 2005 & 2008) or the material distribution in echinoderms (Holland & Ghiselin 2009, Ziegler et al. 2008 & 2009).

Most recent studies have been undertaken by David et al. (2009) with the use of μCT to describe ectosymbiotic attachment in antarctic cidaroids. Most notable, however, is the work of Xiao et al. (2007), who used cross-section images of spines in different CT methods to display error estimation in their analyses. Here the questions addressed were, firstly, whether or not the standard CT, used in medicine and clinical applications, could contribute to the classification of the stereom structure, in addition to SEM images: and, secondly, if this method was found to be appropriate, to generate predictions regarding the mechanical behaviour of objects could stimulate further research.

2. Materials & Methods

2.1 Materials

The following sea urchin species were kept in several fully equipped aquaria (including other invertebrates): *Heterocentrotus mammillatus*, *Phyllacanthus imperialis* and *Prionocidaris baculosa*. For further information about the aquaria and the equipment see chapter 2. *Heterocentrotus mammillatus* is found throughout the whole Indo-Pacific area in depths of up to 25 m. It is notable for its very thick & large primary spines (diameter 1 cm, length 10 cm) and also for its growth rings. A major habitat is the reef system, and they are not often found on open sandy areas (Dotan 1990a, b). After Dotan & Fishelson (1985) it is difficult in oral spines to count the rings (as growth marks) at the base, as these rings may also occur in young spines (less than one year old) where growth rings cannot be present. *Phyllacanthus imperialis* is a common sea urchin in the Indo-Pacific area in depths of 5 to 70 m and characterized by thick & large primary spines (diameter 1 cm, length 8 cm) corrugated at their tips. Like other species *Phyllacanthus imperialis* is able to hide in reef clefts. *Prionocidaris baculosa* is found throughout the whole Indo-Pacific to depths of 200 m. The length of primary spines is about 7 cm with a thickness of 5 mm, sometimes thorns cover the surface. From these three species, primary spines (= radioles) were removed from the specimens kept in the experimental aquaria. Where fully grown spines were not available, dried and cleaned spines were imported from a shell company (Shell Horizon, USA). Later on the fresh spines were dried for several hours and H_2O_2 was used to remove muscle fibres at the base.

2.1.1 X-ray Computer Tomography

The experiments with spines were conducted in a CT (TomoScope) at a local company (Hema-CT, Schönaich) with a resolution of 1024 x 1024 pixels. Exposure duration at each step during rotation was 250ms. Each sample was scanned for 6 h and their images were saved in bmp-format.

2.2 Methods

The CT image sets were transformed into three dimensional objects by the software VGStudio Max (Version 1.2.1). This software system converts image data sets (pixels of two dimensional images) to three dimensional images (volumetric pixel in three dimensional images), where also the grey values of the images can be classified (Figure 1). The density of material is displayed in a gradient from dark to white. A low density appears in a dark colour,

high density is displayed in a white colour. Adobe Photoshop Extended was used to optimize these images.

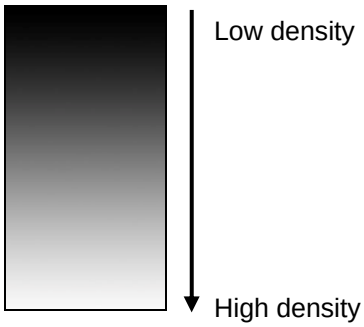

Figure 1: Progression of grey values: This mask is used to describe the density of the material. Dark means very porous, whereas white (= bright) shows a more or less solid structure

3. Results

3.1 *Heterocentrotus mammillatus*

The microstructure of *Heterocentrotus mammillatus* is of special interest for two reasons. Firstly, with regard to the growth rings which are present in its spines, and secondly their massive size. Spines were taken from the aboral and oral side of the test (Figure 2 - 4). The overall sizes of the growth rings in *Heterocentrotus mammillatus* range from around 100 µm wide near the base and rise to about 130 µm near the tip.

3.1.1 *Heterocentrotus mammillatus*: Aboral spine

In Figure 2, a spine from the aboral side of *Heterocentrotus mammillatus* (length 88 mm) in longitudinal view & section (A & B) with detailed cross-sections each of around 10 mm diameter from the base (C), the shaft (D) and the tip (E) is shown. Figure 2A shows the surface of the spine with some irregularities (dents) probably caused by earlier spine damaging in the aquaria or during transport. The wave-like structures covering the surface are artefacts caused by the rendering process of the CT.

Figure 2B shows an opened up spine. Due to the software calibration, the stereom of the medulla and the radiating layer are not visible. The dense white areas are the growth rings. Several, closely spaced growth rings occur at the base, having flattened tips. In the shaft, the growth rings are more separately from one another and their tips are more peaked. In the upper part of the shaft (near the tip of the spine), some rings lie either close together or seem to emerge out of another ring. The small white lobule-like objects which can be found throughout the spine in Figure 2B might represent densely packed areas. At the base of the

spine, the growth rings are more frequent than in the rest of the spine. A large longitudinal growth is observed in the shaft, except in the upper part, where the growth rings are closer together. The change in the form of the growth rings can also be seen in 2C (from nearly oval), via triangular (2D) to triangular & compressed (2E). In Figure 2C the radiating layer is visible as a greyish area but individual pores cannot be seen.

In Figure 2D and 2E the cross-section depicts the spine near the tips of the growth rings. This induces to triangular forms in the innermost growth rings. Some of the growth rings in 2D & E bear thickened blob-like structures in the growth rings. These seem to be denser stereom parts than the rest of the growth rings, probably caused by earlier damaging or regeneration processes. The CT images show that the medulla and the radiating layer differ in their densities of the stereom which is shown by different grey scales (Figure 2C-E).

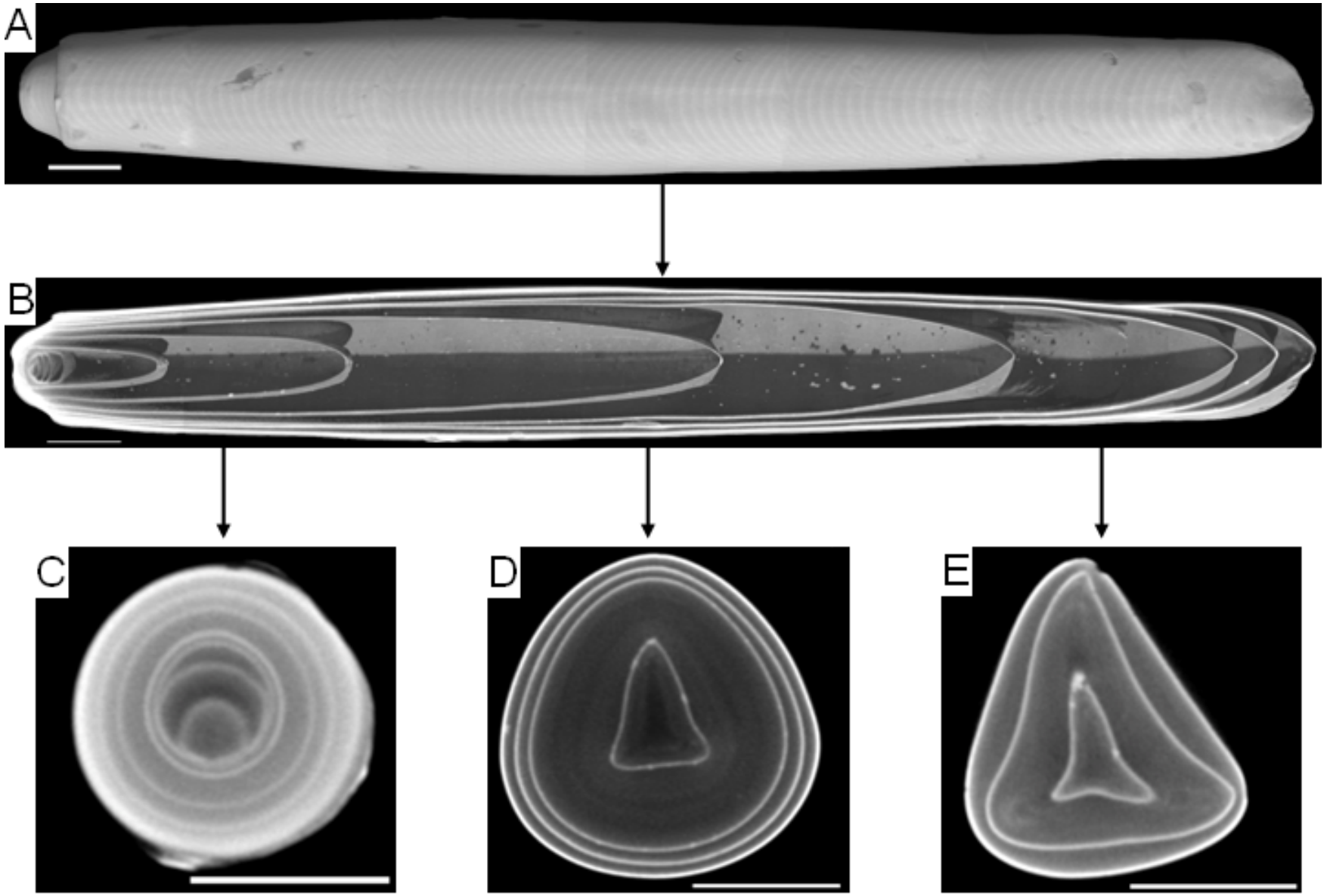

Figure 2: Aboral spine of *Heterocentrotus mammillatus* in different views: Three dimensional longitudinal view (A & B), two dimensional cross-sections of the lower shaft (C), middle shaft (D) and tip (E). The spine from the outer side to the centre is separated in growth rings that disrupt the radiating layer and medulla. The spine is covered by an epidermis. (scale bar= 5 mm)

Figure 3 presents a *Heterocentrotus mammillatus* spine in longitudinal view, including a diagonal basal section of the base (A) and a detailed view of the upper shaft including the tip (B). The middle part of the shaft is not shown. The surface of the spine shows again wave-like structures which are artefacts of the rendering process (Figure 3A). The growth rings are clearly visible and disrupt the medulla. At the base, the growth rings are frequent, however, their incidence decreases in the direction of the tip (also seen in Figure 2). Due to the software calibration, the medulla at the base is partly not visible. The medulla is positioned in the middle of the spine and is shown in agglomerated blob-like forms. The radiating layer itself is not shown.

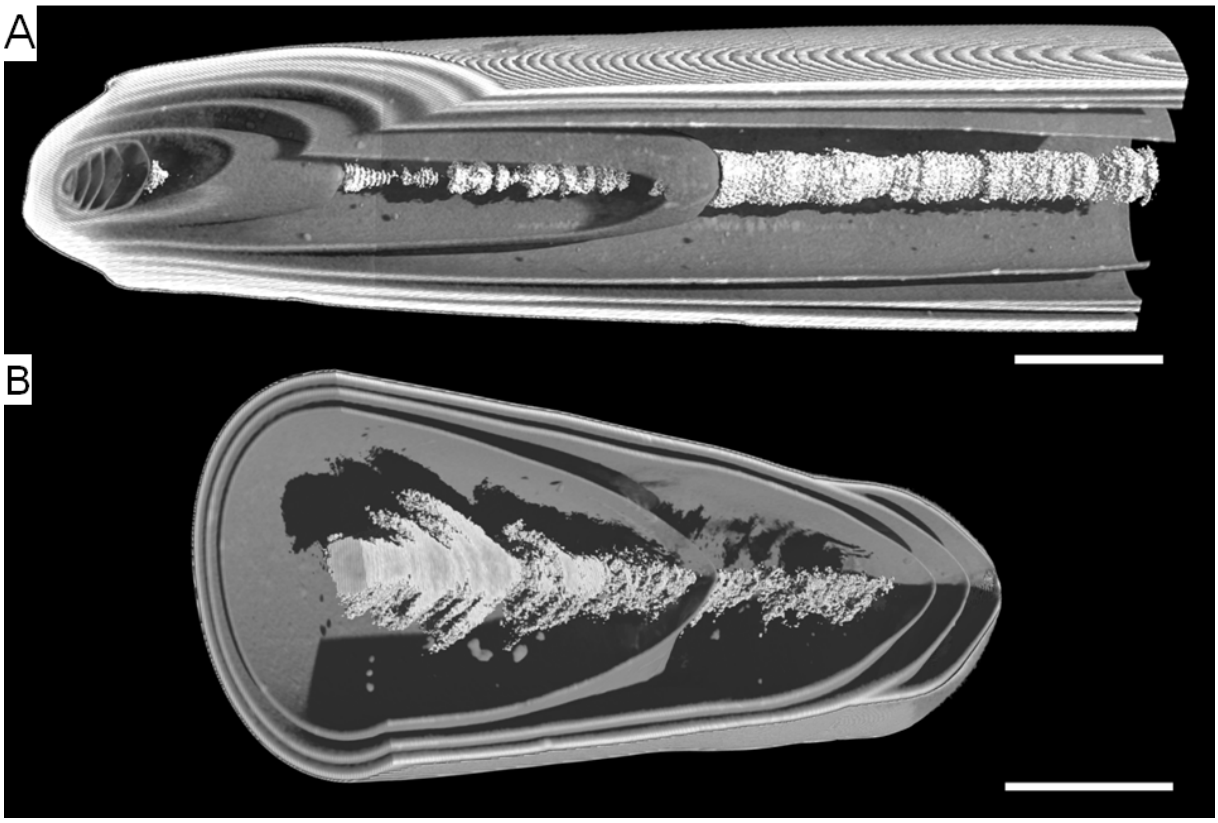

Figure 3: 3D - longitudinal section of a *Heterocentrotus mammillatus* spine: A) Diagonal basal section of the base and parts of the shaft. B) Upper part of the shaft including the tip. The spine from the outer side to the centre is separated in growth rings that disrupt the radiating layer and the medulla. The spine is covered by an epidermis (scale bar = 5 mm)

3.1.2 *Heterocentrotus mammillatus*: Oral spine

Figure 4 shows a spine of *Heterocentrotus mammillatus* (length 25 mm) from the oral side in longitudinal section as a three (A) and two- dimensional view (B) with detailed cross-sections (4 mm diameter) from the base (C), the shaft (D) and the tip (E). The spine shows several growth rings, however, the medulla and the radiating layer are not shown in Figure 4A. A detailed separation of the medulla and the radiating layer is not possible as the grey scaling is almost similar in that area (Figure 4B). The growth rings at the base have flattened tips (Figure 4A & B). This feature was also recognized by observation of spine growth of juvenile specimen in the testing aquaria. The number of rings cannot be count in detail as sometimes they were fused. The extension of the medulla is not clearly visible. Some of the growth rings outgrow another growth ring (Figure 4A & B). Whether or not this observation is regular or an abnormality needs further verification. The form of the growth rings changes from the beginning of the shaft from a round form to triquetrous near the tip. A detailed view of the growth rings is possible, showing a parallel arrangement of distinct struts separated by small spaces (Figure 4D & E). The CT images show that the medulla is loose (due to the dark colour) and that the growth rings are compact or dense (as displayed by the brighter, white colour). The stereom of radiating layer has different densities depending on the position inside the spine.

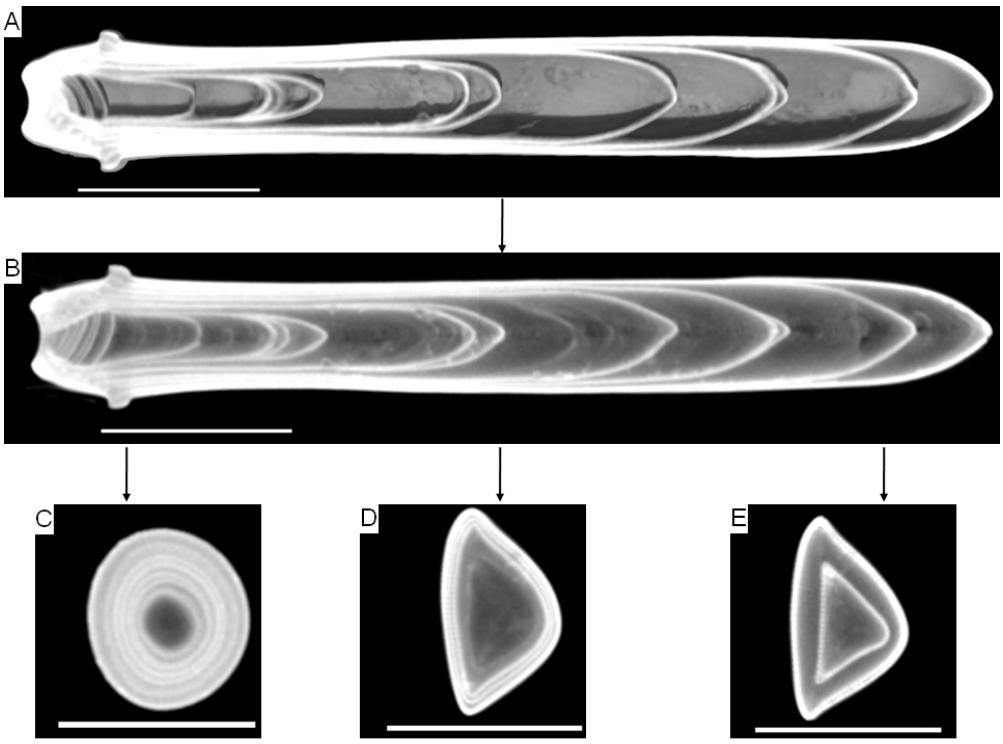

Figure 4: Oral spine of *Heterocentrotus mammillatus* in different views: 3D- longitudinal view (A), two dimensional longitudinal view (B) and cross-sections of the base (C), middle shaft (D) and the tip (E). The spine from the outer side to the centre is separated in the cortex, radiating layer and medulla. The spine is covered by an epidermis (scale bar = 5 mm)

3.2 *Phyllacanthus imperialis*

Spines from *Phyllacanthus imperialis* were investigated for comparison, as their size and thickness are similar to those of *Heterocentrotus mammillatus*. Spines were taken from the aboral and oral side of the test of this sea urchin (Figure 5 & 6).

3.2.1 *Phyllacanthus imperialis*: Aboral spine

Figure 5 shows a spine from the aboral side of *Phyllacanthus imperialis* (length 81 mm) with a longitudinal view (A), longitudinal section (B) and detailed cross-sections (5 mm diameter) from the base (C), the shaft (D) and the tip (E). The rough surface structure in Figure 5A shows fine striations and bosses or thorns, which cover most of the spine (except the collar) as well as encrustations. In the upper area of the shaft the encrustation is damaged. The tip of the spine is flattened. The collar is smooth and has the same size as in spines from the oral side. The wave-like structure is an artefact because of the rendering. The longitudinal section in 5B shows the sectioned spine. The cortex is displayed as a thick white area on the outer side of the spine. The base and the collar are more light grey, compared to the medulla or radiating layer of the spine, demonstrating that the density is different between them. The radiating layer is an undefined dark grey area which ends at the medulla. Due to the calibration the medulla is removed, but some agglomerated blob-like forms occur. The interface between radiating layer and medulla at the tip shows a crenulated form with ups and downs of a solid structure. The cortex is followed by the radiating layer ending at the medulla which is seen as a dark area (Figure 5C). Layered arrangements are visible in the shaft (Figure 5D). Whether this is caused by the software or is due to growth processes of the spine has to be verified by further investigations. The cortex is bright white with some irregularities on the outer side. The tip in Figure 5E has a thick imperforate cortex, followed by the radiating layer and the medulla. An interesting structure (marked with an X) which was also present in 5B might represent the outer surface of the radiating layer towards the medulla. Whether or not these forms are visible because of translucence or an exposure of the border of the radiating layer to the medulla is not clear. In general, the cortex has a compact arrangement represent by its white colour. The radiating layer differs in its density from the medulla as evidenced by different grey scales. The stereom of the medulla is more porous than other parts of the spine (e.g. cortex) as evidenced by the dark colour of that area in the Figure 5C.

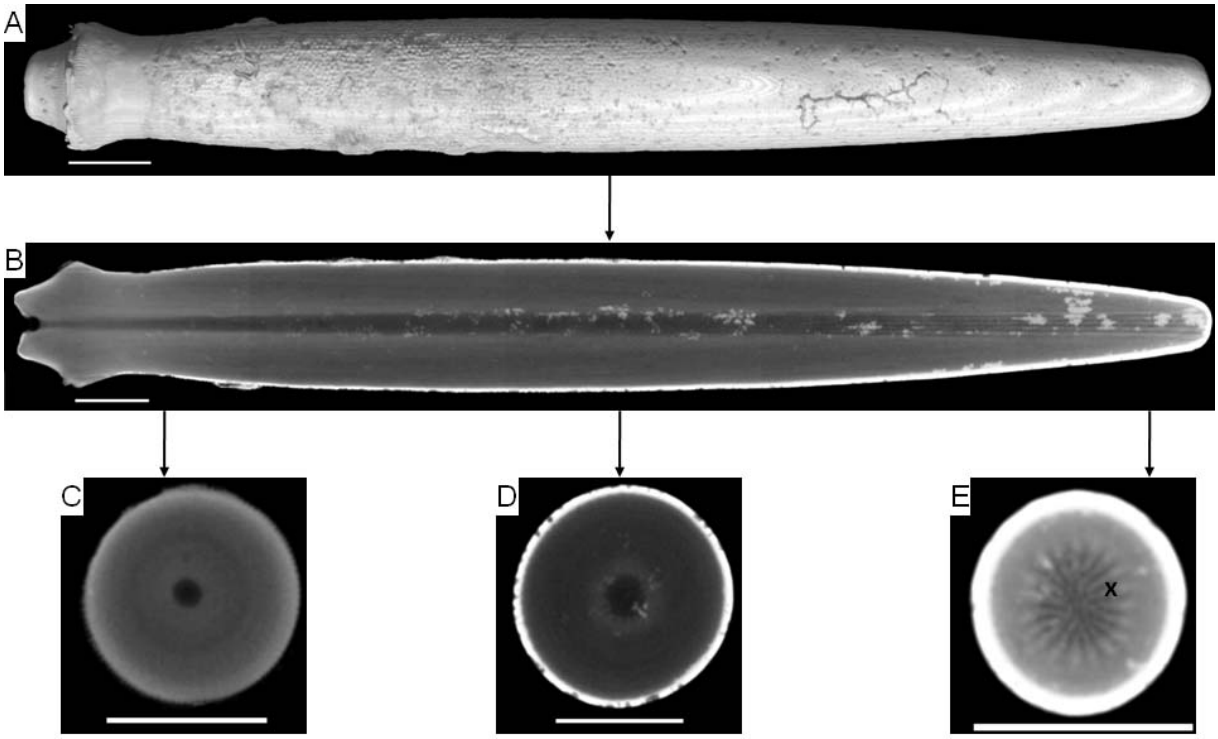

Figure 5: Aboral spine of *Phyllacanthus imperialis* in different views: 3D- longitudinal view (A) two dimensional longitudinal view (B) and cross-sections of lower shaft (C) middle shaft (D) and tip (E). The spine from the outer side to the centre is separated in the cortex, which can be covered by encrustations, radiating layer and medulla (X = specific structure; scale bar = 5 mm)

3.2.2 *Phyllacanthus imperialis*: Oral spine

Figure 6 shows a spine from the oral side of *Phyllacanthus imperialis* (length 25 mm) in longitudinal view & section (6A & B) with detailed cross-sections each of around 5 mm diameter from the base (5C), the shaft (6D) and the tip (6E). The collar is smooth and shows some wave-like structures on the surface, which are artefacts from the rendering of the software (6A). The rest of the shaft bears small indistinct, close series of granules, ending at the tip in a crown-like form. The thickness of these granules increases in the direction of the tip, and similarly with the spaces in between them. The surface of the cortex is encrusted by several organisms. The cortex thickness in Figure 6B enlarges from the base to the tip of the spine. The radiating layer follows as a greyish area, aside the medulla (which is not visible). Several blob-like forms occur. Whether or not they are artefacts or areas with a large density is not clear. Two interesting lines are visible near the milled ring which silhouettes against other parts of the spine (6B) (marked with an X). These could be earlier stages of spine growth, but this cannot be verified at this stage of the investigation. These line- or ring form is also visible in cross-section (6C). In general, the stereom of radiating layer is visible as a greyish area which cannot be further classified. The medulla is present as a black area in the middle of the spine. Figure 6D shows the cortex with some irregular crenulations. The

medulla is enlarged compared to 6C. Figure 6E shows a thick cortex and also struts, which alternate with spaces. More internally, these struts are also visible (marked with an X). It has to be clarified if these struts are a show through from the outer surface or an exposure of the border of the radiating layer towards the medulla.

Figure 6: Oral spine of *Phyllacanthus imperialis* in different views: 3D- longitudinal (A), two dimensional longitudinal section (B) and cross-sections of the lower shaft (C), middle shaft (D) and tip (E). The spine from the outer side to the centre is separated in the cortex, which can be covered by encrustations, radiating layer and medulla (X = ring-like structure; scale bar = 5 mm)

3.3 Prionocidaris baculosa

An aboral spine of *Prionocidaris baculosa* is shown in Figure 7, including longitudinal view (A), longitudinal section (B) and detailed cross-sections (C - E) with a total length of 50 mm. In Figure 7A, the surface of a single spine is shown, with a smooth base and the shaft, (except the collar) it shows a regular ornamentation in form of crenulated structures (bosses or thorns regularly spaced in relation to each other) in rows towards the tip. The cortex is injured at the tip, as parts are broken off (A). The surface is not encrusted as an epidermis is still present. The cortex is visible as a wide white area (7B). The detailed stereom is not visible in the spine. The radiating layer is marked with different grey scales. In the middle, only a small part of the medulla is shown as a black area. Some white blob-like structures are present in the radiating layer. In Figure 7B, two greyish lines appear which start at the base in direction of the tip. These structures are also visible in cross-section in 7C & D. The function of these lines remains unclear. Figure 7C shows the cross-section of the collar with several bright white blob-like forms in the cortex, which represent denser parts of the stereom, probably caused by earlier regeneration processes in the cortex. Towards the medulla, ring-like structures occur and disrupt the radiating layer. Whether or not this is due to the software or due to growth processes is not clear. In Figure 7D, the cortex is shown with regular crenulations which have rounded tips. The disruption of the radiating layer by these ring-like structures also occurs in Figure 7D. The medulla is very porously packed in contrast to the radiating layer and the cortex.

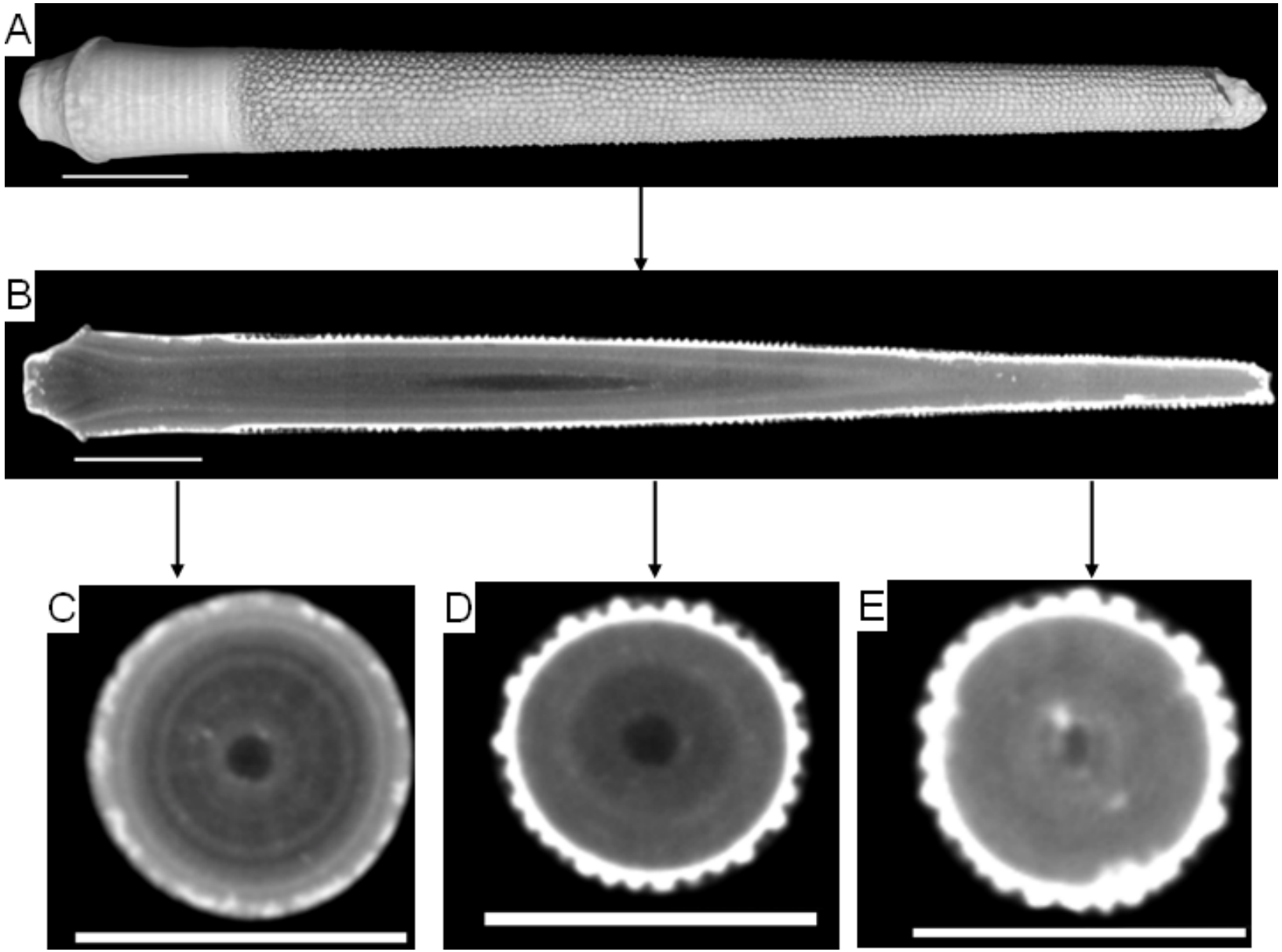

Figure 7: Aboral spine of *Prionocidaris baculosa* in different views: 3D longitudinal view (A), two dimensional longitudinal v view (B) and cross-sections of the lower haft (C), the middle shaft (D) and the tip (E). The pine from the outer side to the centre is separated in the cortex, radiating layer and medulla (scale bar (A - D) = 5 mm; scale bar (E) = 3 mm)

4. Discussion

The investigations of spines of *Heterocentrotus mammillatus*, *Phyllacanthus imperialis* and *Prionocidaris baculosa* with computer tomography displayed several interesting structures and features.

The figures have shown that the density of the stereom is higher in areas which have a light grey (white) scale (e.g. cortex or growth rings) as compared to other areas (e. g. medulla or radiating layer), where the colour turns more into a darker grey. The characterization of the density of a structure is a helpful method to describe investigated objects (see also Stock & Veis 2003). Stock & Veis (2003) also postulated that the lighter the colour in the image, then the higher was the attenuation of the x-ray signal, leading to the conclusion that the density of the material there is higher than in other parts. The medulla as a black area, demonstrates that there is a very loose structure, which can be verified with SEM images (chapter 2), where only a fine meshwork of stereom is found. Unfortunately, the entire extension of the medulla in length and width cannot be seen in Figure 2, thus problems with the calibration cannot be excluded as an explanation. The magnifications available in the CT were not high enough to display structural differences of the stereom in the spines, such as galleried or labyrinthic. The maximum magnification was around 20 µm and so most of the pores could not be displayed in detail as they had an average diameter below that amount.

Some artefacts (such as the wave structures on the surface of *Heterocentrotus mammillatus* in Figure 2A) occurred due to the technical procedure as observed by Wevers & de Meester (2000).

Another question whether or not the CT can be used to generate predictions regarding the mechanical behaviour can be answered: as the images show denser and weaker parts of material predictions about a later mechanical behaviour might be made. In compression tests of *Heterocentrotus mammillatus* the area with the growth rings could withstand an impact longer than areas without these thickenings (Presser et al. 2009).

The base and milled ring of *Phyllacanthus imperialis* in Figure 5 show two lines which were silhouetted from the remaining structures. These lines could resemble earlier stages of the spine e.g. which remain after regenerating of a broken off spine fragment, but this assumption needs to be verified with different species. Also in *Prionocidaris baculosa* these silhouetted lines occur. A possible explanation could also be the appearance of growth zones, as silhouetted zones which was reported by Gage (1987, 1991) for plates of *Psammechinus miliaris*.

The key question which arises from this observation is why are there more frequent growth rings at the base than in the shaft and, as a corollary, whether this is a regular feature or an abnormality during growth. The spines of *Heterocentrotus mammillatus* from the oral side (Figure 4) showed more growth rings than on aboral, which was also observed by Dotan & Fishelson (1985). One explanation for this could be the function of these spines. On the oral side they are smaller and used for daily locomotion, as Baumeister & Leinfelder (1998) and Baumeister (1999) showed it for cidaroid sea urchins. So those from oral should bear more structural features such as thickenings and a faster repairing of damages because of the possible higher mechanical stress. This might occur on the oral side more often than in other parts of the specimen. Later on in chapter 4, the possible influence of these rings in the stability of the spine will be tested.

The advantage of growth rings has to be compared to cidaroid spines and their stability in species such as *Phyllacanthus imperialis*, because this specimen also lives in the reef and can hide in reef clefts and has no growth rings but thick primary spines.

The appearance of the growth rings in *Heterocentrotus mammillatus*, and for example in other sea urchins such as *Echinometra mathaei*, but not in *Prionocidaris baculosa*, prompts questions concerning the advantages or disadvantages of such structures which display greater quantities of materials than other parts of the spine (according to the attenuation in CT images). The discussion about these growth rings, e.g. in *Heterocentrotus mammillatus* and other sea urchins has persisted for decades and is focused largely on growth rings as a response to stress, e.g. breakage or regeneration (Ebert 1967, 1985) and growth rings as a typical annual or rather periodic growth marker (see Weber 1969, Pearse & Pearse 1975, Dotan & Fishelson 1985). In which way the growth rings help in preventing the spine of a complete breaking is still in discussion (e.g. by Presser et al. 2009). At this point the precise function of the growth rings remains unclear and no definite or definitive conclusions can be drawn from the results presented here. Moreover, since many species without those rings are observed the evolutionary potential advantages remain unclear.

As the stereom of the spines could not be presented in detail in this survey another method should be used in further analysis. Also the µCT which was used by Stock et al. (2002a, b) and Stock & Veis (2003) in their survey to investigate echinoids teeth and fossils was not good enough to display different stereom types.

One potential novel method, recently used, could be the use of magnetic resonance imaging, which is common in clinical diagnosis and which was already used in several studies of the organ system in echinoids (Ziegler et al. 2008 & 2009, Holland & Ghiselin 2009).

5. Conclusion

- The application of computer tomography is shown to be a useful method to demonstrate successfully the different internal macrostructures (e. g. medulla and radiating layer) of the spines and to describe the different densities of the stereom, depending on the position inside the spine and/or changes in the density of the material due to damages, e.g. caused by predators.

- The CT technique cannot be taken as a further method to classify the stereom types in spines.

- The growth rings may prevent the spine of a complete failure when attacked. It is important to note, however, that not only the spine itself has to withstand forces, but also the surrounding tissues (e.g. muscles) have to be taken into account.

- Computer tomography, in addition to SEM images, can be used to describe internal spine structures of sea urchins by means of different densities of the material.

- The small difference of the grey scale in the radiating layer of the spines leads to the conclusion that the density is not distributed equally within the layer itself.

6. References

Attwood, D. (2006). “Microscopy: nanotomography comes of age.” Nature 442(7103): 642-643.

Baumeister, J. G. (1999). “Vergleich der Funktionsmorphologie und Paläoökologie zweier Rhabdocidariden (Echinodermata: Cidaridae).“ Paläontologische Zeitschrift 73(3): 319-326.

Baumeister, J. G. & Leinfelder, R. R. (1998). “Constructional morphology of three Upper Jurassic echinoids.” Palaeontology 41: 203–219.

Berman, A., Addadi, L., Kvick, A., Leiserowitz, L., Nelson, M. & Weiner, S. (1990). “Intercalation of sea urchin proteins in calcite: study of a crystalline composite material.” Science 250(4981): 664-667.

Betz, O., Wegst, U., Weide, D., Heethoff, M., Helfen, L., Lee, W. K., & Cloetens, P. (2007). “Imaging applications of synchrotron x-ray phase-contrast microtomography in biological morphology and biomaterials science. I. General aspects of the technique and its advantages in the analysis of millimeter-sized arthropod structure.” Journal of Microscopy 227: 51-71.

Crawford, C. R. & King, K. F. (1990). “Computed tomography scanning with simultaneous patient translation.” Medical Physics 17: 967–982.

David, B., Stock, S. R., de Carlo, F., Hétérier, V. & de Ridder, C. (2009). “Microstructures of antarctic cidaroid spines: diversity of shapes and ectosymbiont attachments.” Marine Biology 156: 1559-1572.

Dotan, A. & Fishelson, L. (1985). “Morphology of spines of *Heterocentrotus mammillatus* (Echinodermata: Echinoidae) and its ecological significance.” In: Keegan, B. F. & O`Connor, B. D. S. (Eds.): Echinodermata: Proceedings of the International Echinoderm Conference, Galway September 24.-29.9.1984, A. A. Balkema, Rotterdam: 253-260.

Dotan, A. (1990a). “Population structure of the echinoid *Heterocentrotus mammillatus* (L.) along the littoralzone of south-eastern Sinai.” Coral Reefs 9: 75-80.

Dotan, A. (1990b). “Distribution of regular sea urchins on coral reefs near the south-eastern tip of the Sinai peninsula, Red Sea.” Israel Journal of Zoology 37: 15-29.

Ebert, T. A. (1967). “Growth and repair of spines in the sea urchin *Strongylocentrotus purpuratus* (Stimpson).” Biological Bulletin 133: 141-149.

Ebert, T. A. (1985). “The non-periodic nature of growth rings in echinoid spines.” In Keegan, B. F. & O`Connor, B. D. S. (Eds.): Echinodermata: Proceedings of the International Echinoderm Conference, Galway September 24-29.9.1984. Rotterdam, A. A. Balkema: 261-267.

Ebinger-Rist, N., Peek, C. & Stelzner, J. (2009). “Gräber im virtuellen Flug erfasst. Kann die 3-D Computertomografie bei der Auswertung des frühmittelalterlichen Gräberfeldes von Lauchheim helfen?” Denkmalpflege in Baden-Württemberg 3: 165-170.

Elmoutaouakkil, A., Fuchs, G., Péres, R. & Peyrin, F. (2003). “Three-dimensional quantitative analysis of polymer foams from synchrotron radiation x-ray microtomography.” Journal of Physics D: Applied Physics 36: A37.

Fischer, F., Lim, G. T., Handge, U. A. & Altstadt. V. (2009). “Numerical simulation of mechanical properties of cellular materials using computed tomography analysis.” Journal of Cellular Plastics 45(5): 441-460.

Flohr, T. (2008). “Technische Grundlagen und Anwendungen der Mehrschicht-CT“, In: Brüning, R., Küttner, A. & Flohr, T. (Eds.): Mehrschicht-CT. Springer, Heidelberg: 3-26.

Gage, J. D. (1987). “Growth of the deep-sea irregular sea urchins *Echinosigra phiale* and *Hemiaster expergitus* in the rockall trough (n. e. atlantic ocean).” Marine Biology 96: 19-30.

Gage, J. D. (1991). “Skeletal growth zones as age-markers in the sea urchin *Psammechinus miliaris*.” Marine Biology 110: 217-228.

Gravante, G. & Giordano, P. (2008). “The role of three-dimensional endoluminal ultrasound imaging in the evaluation of anorectal diseases: a review.” Surgical Endoscopy 22(7): 1570-1578.

Holland, N. & Ghiselin, M. (2009). “Magnetic resonance imaging (MRI) has failed to distinguish between smaller gut regions and larger haemal sinuses in sea urchins (Echinodermata: Echinoidea).” BMC Biology 7(1): 39.

Kalender, W. A., Seissler W., Klotz, E. & Vock, P. (1990). “Spiral volumetric CT with single-breathhold technique, continuous transport, and continuous scanner rotation.” Radiology 176(1): 181-183.

Kalender, W. A. (2006). “X-ray computed tomography.” Physics in Medicine and Biology 51: R29-34.

Kim, N., Kim, M., Yun, S. Sohn, S. & Min, J. (1999). “Comparative study of transrectal ultrasonography, pelvic computerized tomography, and magnetic resonance imaging in preoperative staging of rectal cancer.” Diseases of the Colon & Rectum 42(6): 770-775.

Maisey, J. G. (2001). “CT-scan reveals new cranial features in devonian chondrichthyan *Cladodus wildungensis*.” Journal of Vertebrate Paleontology 21(4): 807-810.

Mietchen, D., Keupp, H., Manz, B., & Volke, F. (2005). “Non-invasive diagnostics in fossils - magnetic resonance imaging of pathological belemnites.” Biogeosciences 2: 133-140,

Mietchen, D., Aberhan, M., Manz, B., Hampe, O., Mohr, B., Neumann, C. & Volke, F. (2008). “Three-dimensional magnetic resonance imaging of fossils across taxa.” Biogeosciences 5(1): 25-41.

Pearse, J. S. & Pearse, V. B. (1975). “Growth zones in echinoid skeleton.2 American Zoologist 15: 731-753.

Presser, V., Schultheiß, S., Berthold, C., Nickel, K. G. (2009). “Sea urchin spines as a model-system for permeable, light-weight ceramics with graceful failure behavior. Part I. Mechanical behavior of sea urchin spines under compression.” Journal of Bionic Engineering 6(3): 203 - 213.

Rack, A., Helwig, H.-M., Bütow, A., Rueda, A., Matjašević, B., Helfen, L., Goebbels, J. & Banhart, J. (2009). “Early pore formation in aluminium foams studied by synchrotron-based microtomography and 3-D image analysis.” Acta Materialia 57(16): 4809-4821.

Rahman, I. A., Zamora, S. & Geyer, G. (2009). “The oldest stylophoran echinoderm: a new *Ceratocystis* from the middle cambrian of germany.” Paläontologische Zeitschrift 83 (3): 431-438.

Schuetz, G. M., Zacharopoulou, N. M., Schlattmann, P. & Dewey, M. (2010). "Meta-analysis: noninvasive coronary angiography using computed tomography versus magnetic resonance imaging." Annals of Internal Medicine 152(3): 167-177.

Stach, G. (2006). "Zum Röntgen bitte." Form + Werkzeug 2: 28-29.

Stock, S. R., Barss, J., Dahl, T., Veis, A. & Almer, J. D. (2002a). "X-ray absorption microtomography (microCT) and small beam diffraction mapping of sea urchin teeth." Journal of Structural Biology 139(1): 1 - 12.

Stock, S. R., Barss, J., Dahl, T., Veis, A., Fezzaa, K. & Lee, W. K. (2002b). "Mineral phase microstructure in teeth of the short spined sea urchin (*Lytechinus variegates*) studied with x-ray phase contrast imaging and with absorption microtomography." Advances in X-ray Analysis 45: 133-138.

Stock, S. R. & Veis, A. (2003). "Preliminary microfocus x-ray computed tomography survey of echinoid fossil microstructure." In Mees, F., Swennen, R. van Geet, M. & Jacobs, P. (Eds.): Applications of x-ray computer tomography in the geosciences, Geological Society, London.

Stock, S. R., Ignatiev, K., Veis, A., Almer, J. D. & de Carlo, F. (2004). "Microstructure of sea urchin teeth studied by multiple x-ray modes." In Nebelsick, J. H. & Heinzeller, P. (Eds.): Echinoderms: München, Taylor & Francis, London: 359-364.

Su, X., S. Kamat, S. & Heuer, A. H. (2000). "The structure of sea urchin spines, large biogenic single crystals of calcite." Journal of Materials Science 35: 5545-5551.

Sutton, M. D. (2008). "Tomographic techniques for the study of exceptionally preserved fossils." Proceedings of the Royal Society B: Biological Sciences 275(1643): 1587-1593.

Weber, J. N. (1969). "Origin of concentric banding in the spines of the tropical echinoid *Heterocentrotus.*" Pacific Science 23: 452-466.

Wevers, M. & de Meester, P. (2000). "Microfocus x-ray computer tomography in materials research." 15th World Conference on Nondestructive Testing. Rom, www.ndt.net/article/wcndt00/papers/idn399/idn399.htm.

Xiao, X., de Carlo, F. & Stock, S. R. (2007). “Practical error estimation in zoom-in and truncated tomography reconstructions.” Review of Scientific Instruments 78(6): online source

Ziegler, A. (2008). “Non-invasive imaging and 3D visualization techniques for the study of sea urchin internal anatomy.” PhD thesis, FU Berlin

Ziegler, A., Faber, C., Mueller, S. & Bartolomaeus, T. (2008). “Systematic comparison and reconstruction of sea urchin (Echinoidea) internal anatomy: a novel approach using magnetic resonance imaging.” BMC Biology 6(1): online source

Ziegler, A., Faber, C. & Bartolomaeus, T. (2009). “Comparative morphology of the axial complex and interdependence of internal organ systems in sea urchins (Echinodermata: Echinoidea).” Frontiers in Zoology 6(1): online source

Chapter 4: 3-point-bending-tests of sea urchin spines

Abstract In this chapter, the results of 3-point-bending-tests (commonly used in the evaluation of mechanical properties for industrial products) performed on two tropical sea urchin species (*Heterocentrotus mammillatus* and *Phyllacanthus imperialis*) from the same habitat are described and discussed. The influence of age (juvenile or fully grown) and size is also considered in the evaluation of the spine properties. The analyses and characterization of the internal microstructure of sea urchin spines is based on the idea of a new bio-inspired impact protective system, for example pedestrian safety in the automotive field. In general, the mechanical properties of sea urchins, namely the light weight and stiffness leads to this hypothesis.

1. Introduction

For the investigation of mechanical properties, such as strength and deformation of construction material (e.g. wood, concrete or steel) it is common to perform bending-tests (Kimura & Masumoto 1980, for plastics see Sideridis et al. 1991, Schinker 2001 for very thin material see Fátima Vales Silva et al. 2003, Kobayashi et al. 2005, Cacciafesta et al. 2008 & Fehling et al. 2009).

In general, in 3-point-bending-tests the sample is supported at two outer pins and deformed by driving a single concentrated load into the middle section of the structure. There, the maximum stress appears. During bending, a test object can be divided into areas of tensile stress (elongation), the neutral fibre and compressive stress (reducing). The neutral fibre is the area where material can be saved without reducing or diminishing the load bearing capacity. For decades, scientists have used these tests for evaluating the structural properties of natural hard parts such as shells or bones to compare them with technical samples (Currey 1975 & 1999a, Wagner & Weiner 1992, Reilly & Currey 1999 and Berns et al. 2001). In industrial applications, the general concept criterion is to design the load bearing capacity of a structure with the least amount of material. The amount of material should be the greatest at the highest point of stress, meaning reduced amount of material can be used in the other parts.

Several factors might influence the structural properties of an object (Figure 1). External factors such as wave stress or predator impact can cause stress and strain which influence the object and its structural organization as well as the material properties. These incidents can cause the deformation reaction of the object. From Figure 1 requirements for a

technical product (e.g. material stiffness) can be deduced and also where improvements in material properties could be made, for example in the morphology of an object.

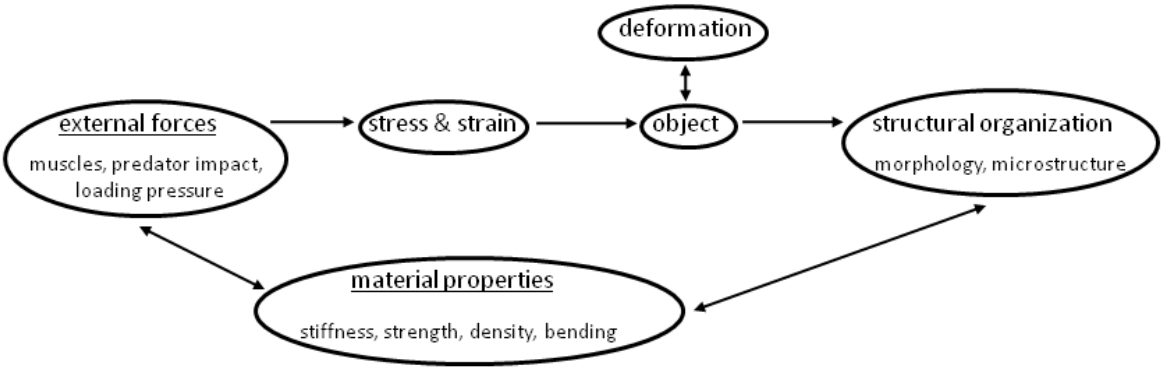

Figure 1: Factors influencing properties of an object (after Rayfield 2007)

In general, in echinoderms and especially sea urchins are of interest due to their mechanical behaviour, lightweight material and internal structure (Hiratzka et al. 1979, Oaki & Imai 2006, Meldrum 2007, Vecchio 2007). Meldrum`s (2007) application ideas deal, for example with the production of crystals based on the regular morphology of the stereom of sea urchins (templating). Denny & Gaylord (1996) focused on the morphological comparison between two sea urchins that live in the same habitat but differ in the morphology of their spines. They investigated *Colobocentrotus atratus* (reduced and flattened aboral spines) and *Echinometra mathaei* (spiky aboral spines). They postulated that not only the reduced spines are an adaption to the high-energy environment of the surf zone, but also the high tenacity and other environmental factors have to be taken into account.

Internally, the spine and the test of a sea urchin persist of porous high-magnesium calcite. The porous arrangement is named stereom and differs depending on the position in the spine or test of a sea urchin. Extensively studies on plate microstructure of sea urchins have been carried out by Smith (1980). Sea urchins use their spines mainly for locomotion and defence. Spine bending can be induced by several factors including predators, wave energy and stress induced during hiding in reef clefts. They are able to abate massive forces (wave-energy, predator impact) by having flexible connections between spines and the test (e.g. Smith et al. 1990).

There have been carried out, however, some investigations regarding the mechanical behaviour especially the crushing and bending behaviour of sea urchin spines, spicules or plates. Weber et al. (1969) compared the crushing strengths of shells with values of several sea urchin spines, such as those of *Heterocentrotus mammillatus* ($48 * 10^3$ N/mm²). Currey (1975) discovered a compressive strength of 50 to 100 MN/ m² for echinoid spines. Emlet

(1982) reported a Young's modulus of 36 $*10^5$ N/mm² for echinoderm larval spicules. Burkhardt et al. (1983) depicted a mean Young's modulus of 50 * 10^3 N/mm² for bending tests of diadematoid spines. Telford (1985) carried out mechanical investigations on the test of several sea urchin species to describe the influence of domes and arches into the mechanical behaviour. Kürmann (1986) discussed the results of hardness experiments from several authors. Su et al. (2000) conducted 4-point-bending-tests with *Heterocentrotus trigonarius* spines flexural strength values of 13 to 41 N/mm². Takemae & Motokawa (2005) investigated the mechanical properties of the catch apparatus. Mannaerts (2007) described the influence of heavy metals to the structural behaviour of spines. A survey with respect to the crushing behaviour of sea urchin spines (e. g. *Heterocentrotus mammillatus* 47 MPa) was carried out by members of the project group (e. g. Presser et al. 2009). Earlier surveys of crushing tests on treated sea urchin spine pieces were carried out by Currey (1965) and Weber et al. (1969).

Application possibilities of the stereom structure are various, based on the references mentioned above, e.g. for automotive processes or for personal security (bullet–proof vests or bicycle helmets). Other applications deal with the replication of the galleried stereom structure of plates to build up a sandwich-like polymer-macroporous copper (Lai et al. 2007). They found out that with implementing the sea urchin stereom structure into the copper material, the mechanical properties can be improved compared to the non-periodic arrangement in the copper.

The idea of stereom structure as an impact protective system has not been taken into account so far. So an investigation was carried out with several bending tests to analyse the spines of different sea urchins.

2. Materials & Methods

2.1 Materials

For the 3-point-bending-tests dried juvenile and fully grown primary spines of *Heterocentrotus mammillatus* and *Phyllacanthus imperialis* were taken (Figure 2). One series of juvenile spines was taken directly of a *Phyllacanthus imperialis* specimen from the aquaria. The other spines were purchased from a local supply company.

Figure 2: Spines of *Heterocentrotus mammillatus* (fully grown (A) & juvenile (B) and *Phyllacanthus imperialis* (fully grown (C) & juvenile (D)): *Heterocentrotus mammillatus* shows a smooth surface, as it is covered by an epidermis. *Phyllacanthus imperialis* lacks an epidermis and bears encrustations by several organisms (scale bar = 5 mm)

2.2 Methods

The material testing machine is shown in Figure 3 (left) (model Zwick Z020, type: BTC-FR020TL.A1K) with which the tests were undertaken. The arrangement of the samples for the 3-point-bending-test was parallel to the c-axis (after Schwickerath & Mokbel 1983) (Figure 3 right). The samples were placed centred in equal distance to the two small brackets (bracket thickness 5 mm). Force was built up with a pin (thickness 5 mm); feed motion was 5 mm/sec. Force (N) as well as deflection (mm) were monitored directly by the program (testXpert V10.0 by Zwick). Further analysis was done with Excel 2007. The general equations are shown in Table 1, additionally the mathematical derivations are described in the supplement to this chapter.

Figure 3: The Zwick material testing machine at the Institute of textile and process engineering (ITV) (left) and a detailed view during a 3-point-bending-test

Table 1: Equations for the bending tests: L = distance space (mm); d = diameter (mm); s = deflection (mm); F = force (N)

equation 1: Second moment of inertia for circular cross-section $I=\frac{\pi \cdot D^4}{64}$
equation 2: Bending strain $\varepsilon=\frac{6 \cdot s \cdot h}{L^2}$
equation 3: Bending stress $\sigma=\frac{M}{W}$
equation 4: bending modul $E=\frac{\Delta\sigma}{\Delta\varepsilon}$

The elasticity of an object is described by the bending modul of elasticity (Young's modulus). It is a measure of the stiffness, defined as the ratio of uniaxial stress over the uniaxial strain. It was extracted from the diagram of the mean values of stress and strain. For comparison to other officially tested products, formulae and arrangements of samples were taken from DIN norms in parts (DIN EN ISO 178 for the 3-point-bending-test). The spine forms were considered as cylinders with equally diameter throughout the spine. Maximum and minimum diameters in the middle of the spine as well as total length of specimen were measured in advance. The mean diameters were then calculated. For statistical reasons, mostly more than 10 spines were taken for each investigated species. After several days of drying the samples, the bending tests were conducted at the Institute of Textile Processing and Technical Engineering (Denkendorf, Germany).

In general, the higher the Young's modulus the stiffer is the material, the lower the value the more flexible (Table 2). From Table 2 the highest values can be seen for glass (up to 81000 N/mm²), the lowest values for conifers (wood). Human bones have a Young's modulus of about 19000 N/mm².

Table 2: Young's moduli of different materials: Comparison between natural and industrial objects (after Burkhardt et al. 1983 & Berns et al. 2001)

material	**Young's modulus** [N/mm²]= [MPa]
conifers	10000
brass	11000
glass	51000-81000
concrete	10000-50000
bones	19000

3. Results

Both juvenile and fully grown spines of the echinoid species *Heterocentrotus mammillatus* and *Phyllacanthus imperialis* were used for the 3-point-bending-test.

3.1 3-point-bending-tests: Juvenile spines of *Heterocentrotus mammillatus*

The spines had mean lengths of 50 mm with mean diameters of 8 mm. A series of 10 juvenile spines of *Heterocentrotus mammillatus* was measured in 3-point-bending-tests (Figure 4). After a continuous force increase the spines broke suddenly. The maximum force was lower than 600 N and a maximum deflection of up to 0.35 mm was observed before the spine breakage. First the values of the samples were equally, when reaching a deflection of about 0.6 mm, the variations became visible between the samples. Also the possible amount of deflection varied. In general, the breakage of spines was mostly perpendicular to the c-axis. From the equations mentioned earlier the stress and strain can be calculated.

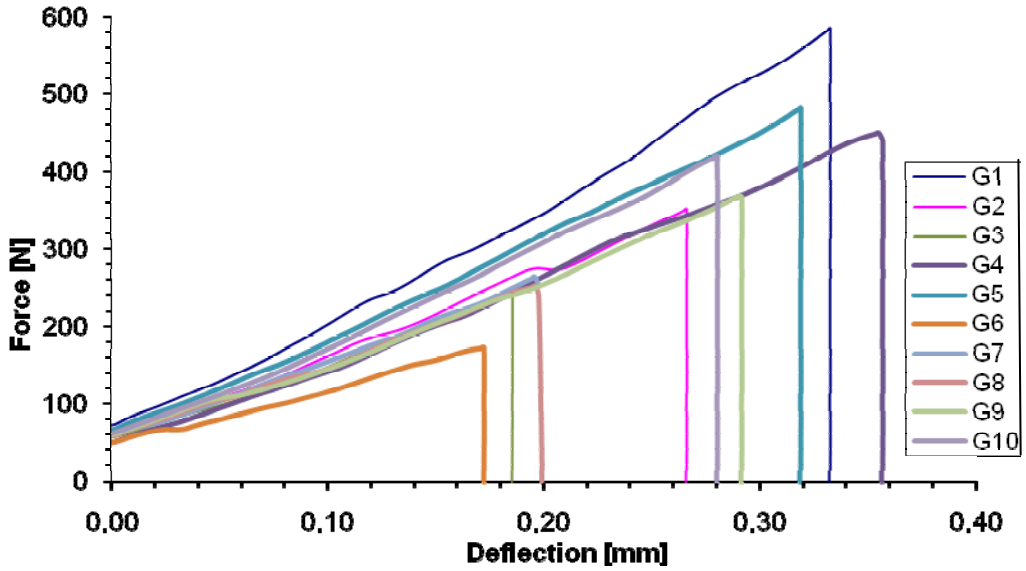

Figure 4: Force-deflection diagram of juvenile *Heterocentrotus mammillatus* spines: The numbers (G1-G10) in the legend are the spine samples. After the highest force loading the spines broke

In Figure 5 the stress-strain diagram of juvenile spines of *Heterocentrotus mammillatus* is shown. The values are also widely distributed here. For example in G1, the highest strain is not synonymous to the highest stress values. The highest stress values, observed in G5 reach only a stress of about 1.7 %. A maximum strain of nearly 2.5% (of the initial position of the spine) can be seen. The maximum stress can reach up to 65 N/mm². The mean calculated bending modulus for juvenile spines is about 2800 MPa.

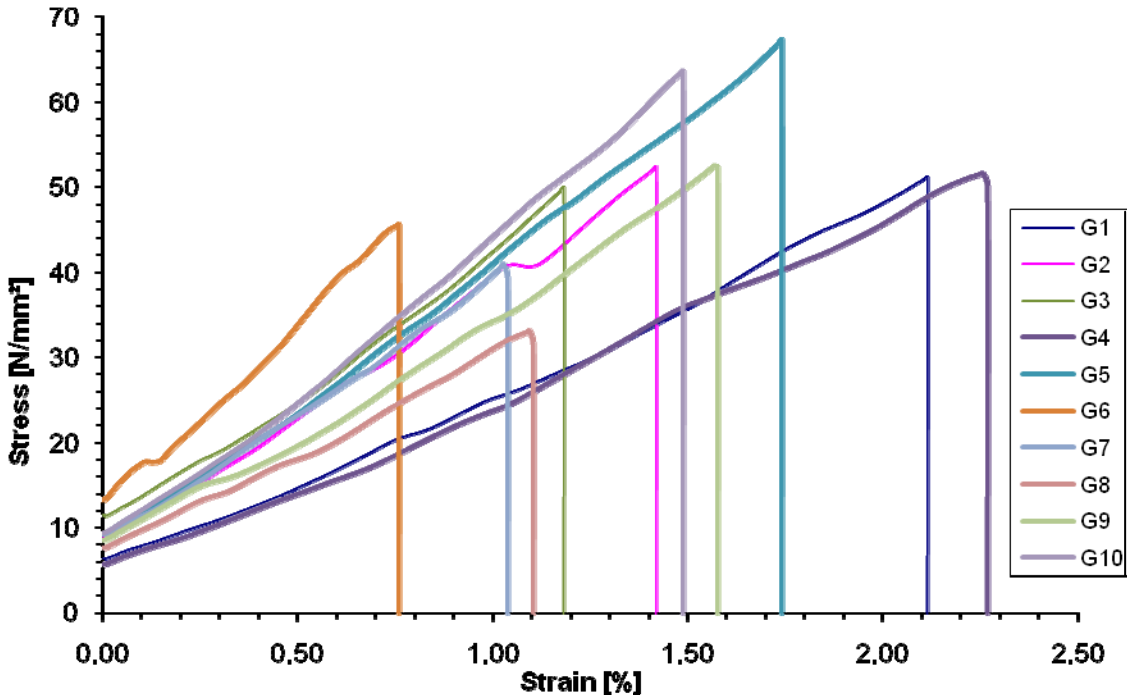

Figure 5: Stress-strain diagram of juvenile *Heterocentrotus mammillatus* spines: The numbers (G1-G10) in the legend are the spine samples. After the highest force loading the spines broke

3.2 3-point-bending-test: Fully grown spines of *Heterocentrotus mammillatus*

The spines had a mean length of 85.7 ± 7.4 mm with a mean diameter of 11.1 ± 0.3 mm. Figure 6 presents The results of fully grown *Heterocentrotus mammillatus* spines (n = 28; A1-C10) in bending tests show a maximum force of 550 to 650 N and a maximum bending of 0.7 mm before breakage. After a straight powering up, most of the samples broke suddenly. Some of the samples show a different behaviour, for example A3, B9 and C2. Whether this is caused by the experimental design or other factors has to be discussed. Compared with the juvenile spines the fully grown spines had larger deflections. The largest deflection (C8) is again not synonymous with the highest force. Highest force was observed in sample (B10) with a deflection of 0.56 mm. The spine breaking was mostly perpendicular to the c-axis.

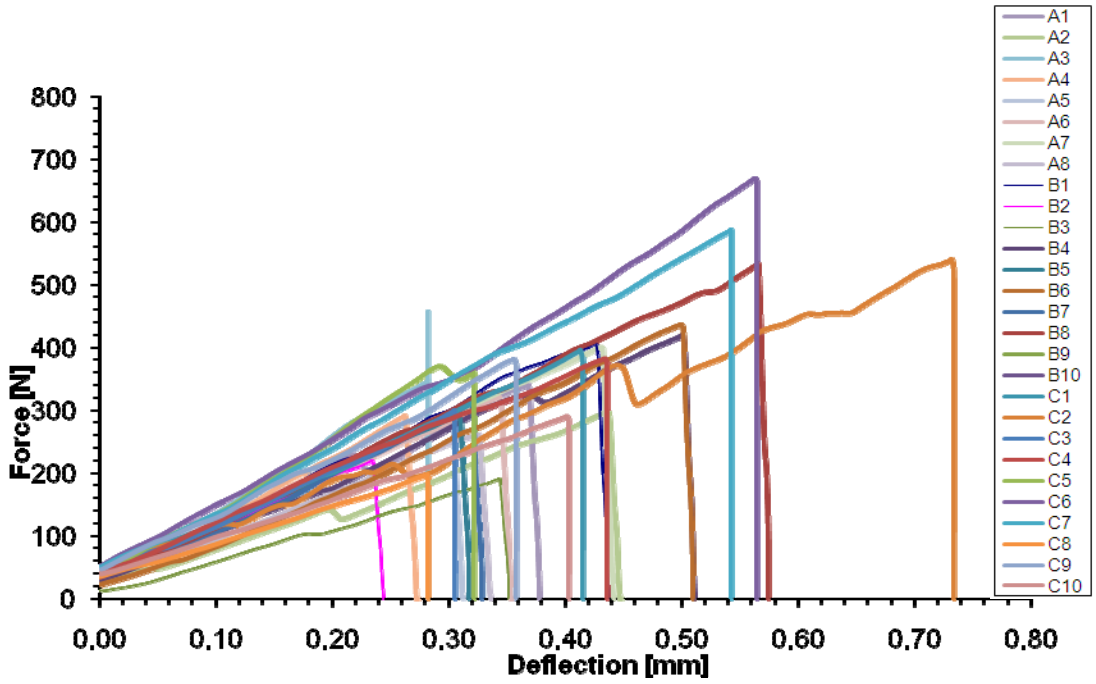

Figure 6: Force-deflection diagram of fully grown *Heterocentrotus mammillatus* spines: The numbers (A1-C10) in the legend are the spine samples. After the highest force loading the spines broke

The values of the sample B9 were excluded in the results of the stress-strain diagram, as the results were not comparable to the rest of the data (Figure 7). A maximum stress between 40 and 50 N/mm² and a minimum of about 23 N/mm² can be observed. The strain does not reach more than 2.3 % of the initial position of the spine. Some of the samples differed in their behaviour from the others, as already mentioned in the force-deflection diagram. The mean bending modulus for fully grown spines is about 2500 MPa.

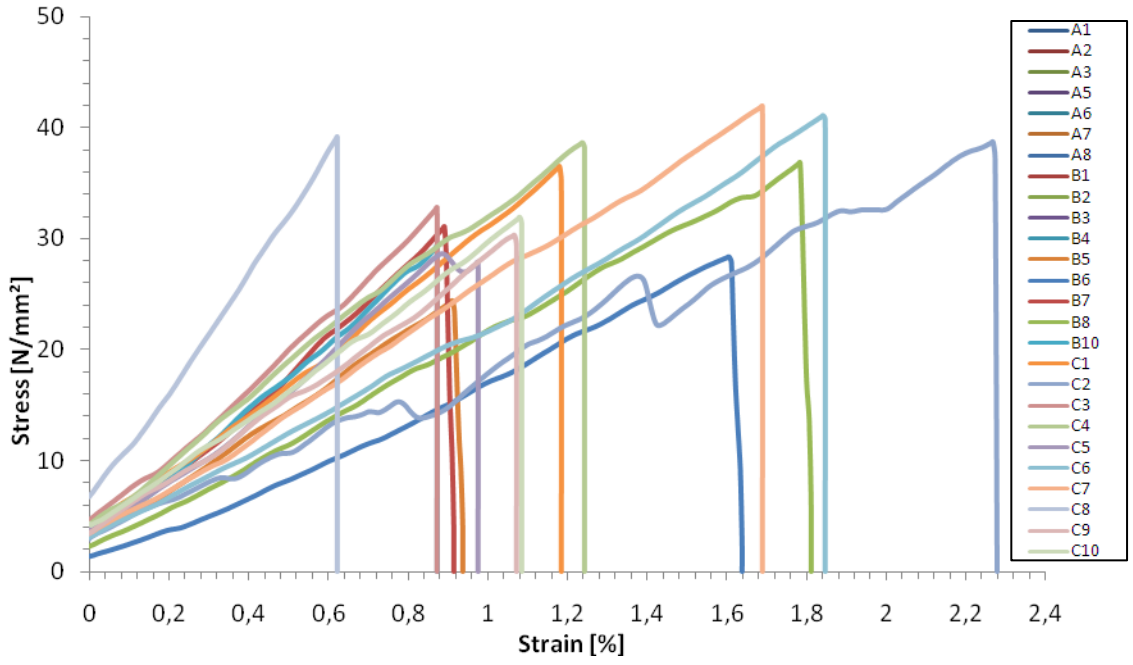

Figure 7: Stress-strain diagram for fully grown *Heterocentrotus mammillatus* spines: The numbers (A1-C10) in the legend are the spine samples. After the highest force loading the spines broke

3.3 3-point-bending-tests: Juvenile spines of *Phyllacanthus imperialis*

A series of nine juvenile spines of *Phyllacanthus imperialis* was measured in 3-point-bending-tests. The spines had mean length of 47.8 ± 6.1 mm and mean diameters of about 5.8 ± 0.3 mm. Figure 8 shows the results in a force-deflection diagram. After a linear force increase all of the spines broke. The different behaviour of sample D1 has to be discussed. The maximum force was around 150 N and a maximum deflection of 0.3 mm was monitored before breakage.

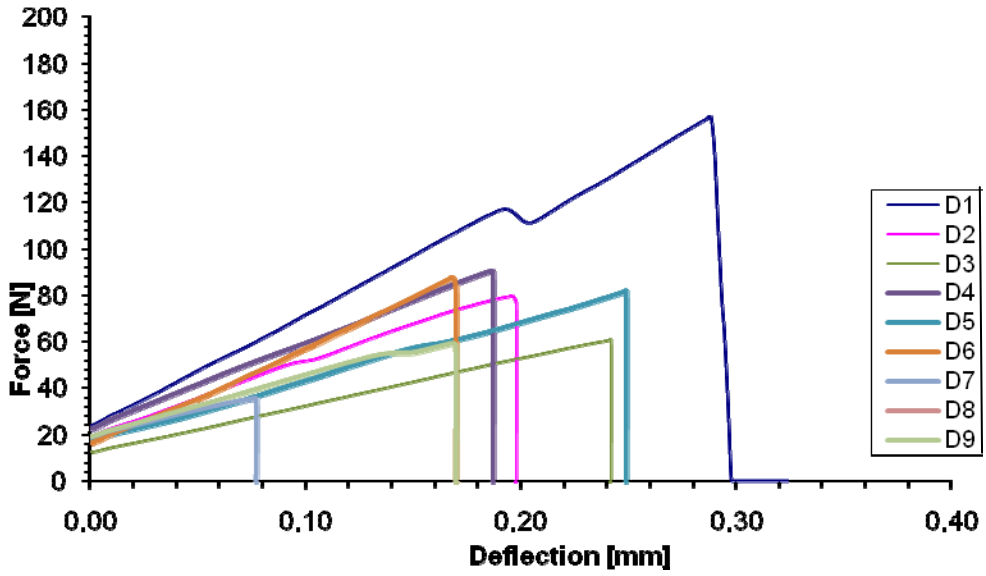

Figure 8: Force-deflection diagram of juvenile *Phyllacanthus imperialis* spines: The numbers (D1-D9) in the legend are the spine samples. After the highest force loading the spines broke

The data of the bending tests are shown as a stress-strain diagram for the juvenile *Phyllacanthus imperialis* spines (Figure 9). The maximum strain was below 1% of the initial position of the spine. A stress value lesser than 40 N/mm² was observed, except for one spine with about 60 N/mm² (D1). Most of the spines showed a linear stress increase and then the spines broke, except three spines (D1, D8 and D9), where shorter slopes occurred before their breakage. The reason for this behaviour has to be discussed. The Young's modulus has a value of about 4100 MPa.

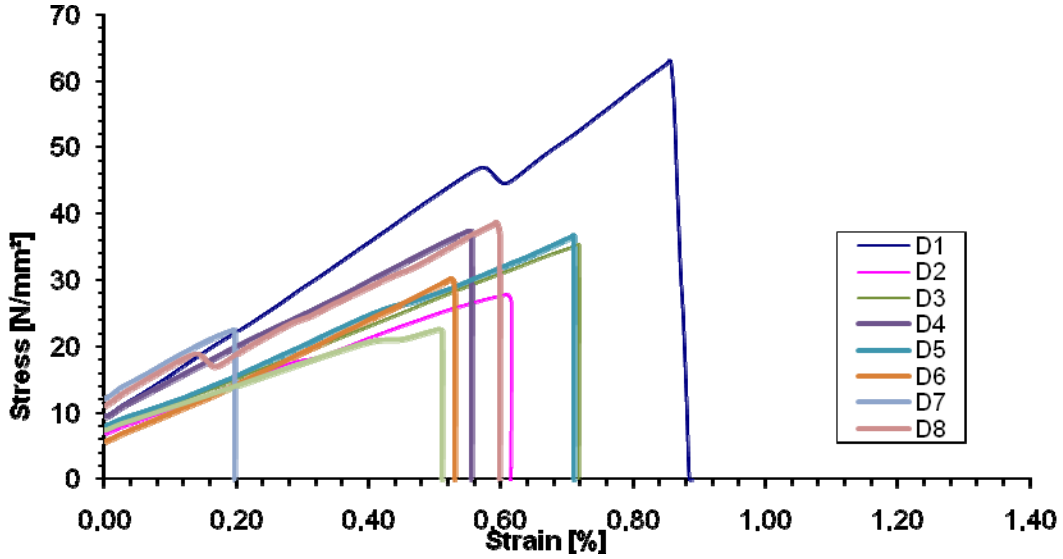

Figure 9: Stress-strain diagram of juvenile *Phyllacanthus imperialis* spines: The numbers (D1-D10) in the legend are the spine samples. After the highest force loading the spines broke

3.4 3-point-bending-test: Fully grown of *Phyllacanthus imperialis*

A series of fully grown of spines of the same species was then investigated. A mean length of 91.8 mm is observed with a mean diameter of 9.1 mm. The test series of *Phyllacanthus imperialis* spines identified forces of up to 450 N and a maximum deflection of around 0.5 mm for big spines before breakdown (Figure 10). Sample E3, E6 - 8 showed a different behaviour with slopes before breakage, which has to be discussed later.

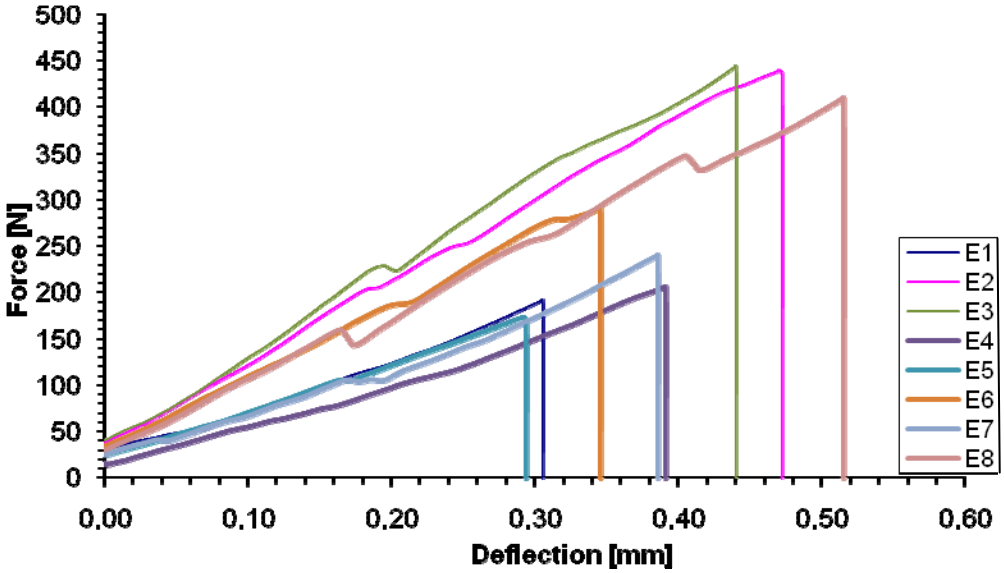

Figure 10: Force deflection diagram of fully grown *Phyllacanthus imperialis* spines: The numbers (E1-E8) in the legend are the spine samples. After the highest force loading the spines broke

The results for stress and strain are shown in the following Figure 11. The effect of a non-linear increase is also observed in this diagram. Nevertheless, the stress reaches maximum values of up to 60 N/mm² and a strain of up to 1.3 % of the initial position of the spine. The different behaviour of E2, E6 - 8 has to be discussed later. Values for the Young's modulus of about 4500 MPa can be observed.

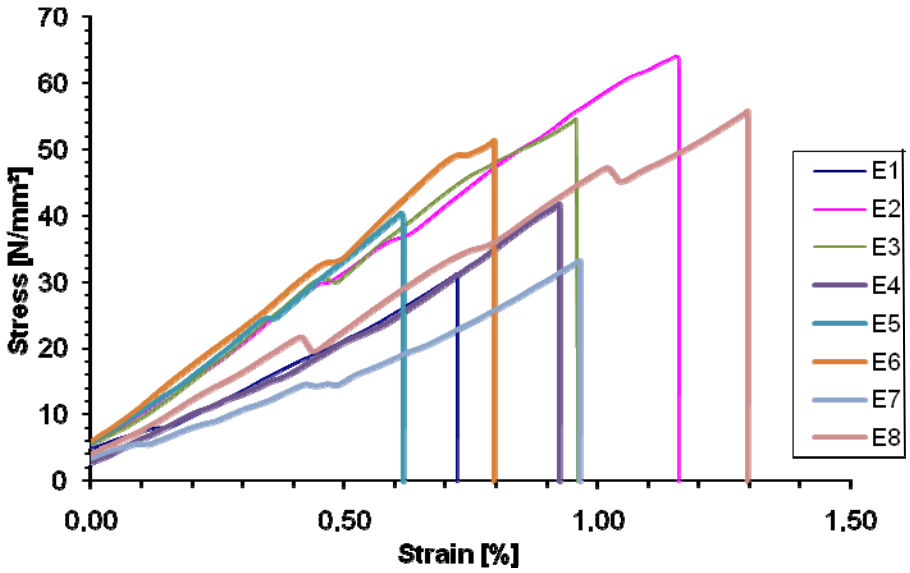

Figure 11: Stress-strain diagram of fully grown *Phyllacanthus imperialis* spines: The numbers (E1-E10) in the legend are the spine samples. After the highest force loading the spines broke

3.5 Values of the bending tests

To summarize the results, the following table (Table 3) shows the mean values of Young's modulus as well as maximum force and stress during the bending tests. As presented in the table above, the Young's modulus of spines are different in 3-point-bending tests with respect to their age and between different species.

Table 3: Summary of the data from the bending tests: Juvenile (juv.) and fully grown (f. g.) spines are compared by 3-point-bending-tests (including their Young's modulus, the mean maximum force and stress)

species	**bending test**	**Young's modulus [MPa]**	**maximum force [N]**	**stress [N/mm²]**
Heterocentrotus mammillatus (juv.)	3-p.	2806.5	358.3	50.8
Heterocentrotus mammillatus (f. g.)	3-p.	2479.8	358.7	29.1
Phyllacanthus imperialis (juv.)	3-p.	4097.1	81.3	34.7
Phyllacanthus imperialis (f. g.)	3-p.	4495.4	299.2	47.1

4. Discussion

Juvenile spines of *Phyllacanthus imperialis* showed a lesser amount of bending and loading capacity than the fully grown ones (see Figure 8 and Figure 10). The juvenile spines of *Phyllacanthus imperialis* compared to those of *Heterocentrotus mammillatus* could withstand lower force than those of *Heterocentrotus mammillatus*. Whether or not these observations are caused by the internal growth rings in *Heterocentrotus mammillatus* or other factors has to be confirmed by later additional compression tests.

Some of the samples differed from the mechanical behaviour which they normally should show (e. g. in Figure 10 and 11). In a bending test the sample should break after a linear force increase. The decrease in the force or stress which was partly observed in some of the might have several reasons. At first the sample might have moved during the testing. A second reason may be that the force pin might have dented some of the internal structure. This can be neglected, however, as none of the spines showed this feature. For the spines of *Phyllacanthus imperialis* the influence of epibenthic growth might be a reason for the behaviour. In general, the bending tests of the sea urchins showed a large variation of values. The main difference to industrial products such as steel is that by working with natural systems it is difficult to get a sufficient large amount of more or less homogeneous samples. Morphological differences in a small number of samples may have a higher impact into the statistical evaluation than with a large number of samples. Despite this fact, general tendencies can be demonstrated.

The investigated spines of the two sea urchins species differed in their internal morphology. Those of *Heterocentrotus mammillatus* have growth rings, which lack in those of *Phyllacanthus imperialis*. The impact of these rings in the stability of the sea urchin spine is still in debate. The discussion about these growth rings, e.g. in *Heterocentrotus mammillatus* and other sea urchins has persisted for decades and is focused largely on growth rings as a response to stress, e.g. breakage or regeneration (Ebert 1967 & 1985) and growth rings as a typical annual or rather periodic growth marker (see Weber 1969, Pearse & Pearse 1975, Dotan & Fishelson 1985, for the tests on deep sea irregular sea urchins Gage 1987). Dotan & Fishelson (1985) observed a continuous growth, although the building of the growth rings was incomplete at that stage.

It should be noted, that the stability of the spines is not only depending on the spine structure itself, but also depends on the structure of the catch apparatus (Strathmann 1981, Motokawa 1982, Castillo et al. 1995 and Takaemae & Motokawa 2005). This catch apparatus,

built up with ligament and muscle fibres connects the spine to the test of the sea urchin. Besides the catch apparatus as an area to reduce the stress impact, echinoderms have developed other mechanisms to avoid longer impacts (e.g. caused by predators) by using the so called autotomy, which is the controlled losing or dropping of appendages or internal organs (Wilkie 2001, Maginnis 2006).

Apart from these results presented here, the natural function of spines also has to be considered including locomotion as well as defence (Baumeister 1999, Stiller 2001). Baumeister & Leinfelder (1998) assumed that the oral spines in recent cidaroids were the (only) ones used for locomotion, reaching conclusions similar to Dotan & Fishelson (1985) for *Heterocentrotus mammillatus* spines.

Burkhardt et al. (1983) postulated that, diadematoid spines are not strained by compression, but by bending. This might be the case for all echinoids as, for example, *Heterocentrotus mammillatus* uses the spines to brace itself into reef clefts. The method used by Burkhardt et al. (1983) was different to that used here. They glued one side of the spine and bent the other.

Berns et al. (2001) showed for cut human femur bones in 3-point-bending-tests a bending strength of around 260 N/mm² and a Young's modulus of 19380 N/mm². The Young's moduli of the species present are in the range of 1000 N/mm² to 4000 N/mm². Nevertheless, the values of *Phyllacanthus imperialis* were almost twice those of *Heterocentrotus mammillatus* in the 3-point-bending-tests.

The 3-point-bending-tests demonstrated a mean bending strength of 50.8 N/mm² for juvenile spines and 29.0 N/mm² for fully grown ones of *Heterocentrotus mammillatus*. In contrast to *Phyllacanthus imperialis* spines, who showed values of 34.7 N/mm² and 47.1 N/mm².

The values of the bending tests of *Heterocentrotus mammillatus* are similar to those of Su et al. (2000), who demonstrated up to 50 N/mm² for the flexural strength of fully grown *Heterocentrotus trigonarius* spines. In the present investigation, it was around 50.8 N/mm² (juvenile) and 29.0 N/mm² (fully grown) for *Heterocentrotus mammillatus* respectively.

The values presented here have to be discussed under the possibility of water pollution and/or stress of the specimens in the aquaria. Pollution can cause a reduction in the concentration of calcite in the skeleton as well as changes in the structural arrangement inside the spines of *Echinus acutus*, which was identified by Mannaerts (2007) who reported Young's moduli of 15.4 GPa for specimens of *Echinus acutus*. In contrast, the present study showed values of the bending moduli of about 2000 to 4000 MPa were observed. Pollution in

Mannaerts (2007) study resulted in a change in the structural arrangements inside the stereom. The problem of pollutants should be excluded in this survey here, as the chemical factors were monitored every week and were corrected (raised or lowered) when necessary. As Ries (2004) showed in an investigation that marine invertebrates (e.g. echinoids and crabs) changes in the Mg/Ca ratio in their skeleton are proportional to the amounts in the seawater in which they grow. This leads to the conclusion that the values which were observed in the present study should be discussed with values in natural environments in later surveys.

The present study suggests that, the bending behaviour of spines is largely affected by environmental factors. Future research should compare the keeping in artificial sea water with natural habitat surveys to detect possible structural arrangement of the stereom in the spines.

In general, bending tests of sea urchin spines are quite rare. Currey (1975), for example, measured the compressive strength of spines. Burkhardt et al. (1983) focused on diadematoid spines and made bending tests in which the spines were glued on one side and bended on the other. They discovered differences in the Young's modulus from fresh (52.1 * 10^3 N/mm²) to dried spines (69.4 kN/mm²). Their values are a thousand larger than the values measured in this investigation. Nevertheless, they had a different test setup and therefore the influence of the glued part has to be taken into account.

A technical material which also has a porous structure is concrete. Reinhardt et al. (2001) reported a Young's modulus of 25.2. GPa for a small concrete steel fibre. So the stiffness is not only depending on the porosity of an object, but also the material itself has to be considered. Kuhn-Spearing et al. (1996) carried out flexural investigations of mollusc shells which had a layered solid aragonite structure. As a result, they reported about 100 MPa in the bending test. This can be compared with the results of the present investigation, e.g. around 50 MPa for juvenile *Phyllacanthus imperialis* spines where different porous layered structures are present. Additionally, Kuhn-Spearing et al. (1996) postulated that a shell has to withstand forces of predators (such as crabs) as well as tidal zone impacts (such as waves) in the magnitude of 800 N. The fact that spines of sea urchins can withstand such forces is confirmed with the bending tests presented here.

The material in the investigations presented here can be seen as brittle, whereas most of the material used in building is solid, e.g. steel. The results presented here can be compared with values of other bending tests, such as those of Reilley & Currey (1999). They reported in 4-point-bending tests of equine bones values of 200 MPa (bending module) which is almost in the same magnitude as the results present here of the spines 3-point-bending tests (e.g. *Heterocentrotus mammillatus*) and the bone material has equal internal porous structure.

In summary, the bending tests of the sea urchin spines are the basis for the later impact protective system. In the context of other tests, such as compression tests which have been undertaken by Presser et al. (2009), there is a high potential that the sea urchin stereom can be used as a model for future bio-inspired products.

5. Conclusion

- *Phyllacanthus imperialis* showed a higher Young's modulus in the 3-point-bending-tests, compared with *Heterocentrotus mammillatus*. This finding was independent of position of the spine and spine size.

- The results presented here provide a basis for the interpretation of the stability of spines. Nevertheless other depending factors, such as the catch apparatus, its muscular fibres and their reaction time need to be taken into account (Motokawa 1982, Castillo et al. 1995, Currey 1999b, Diab & Gilly 1984, Takemae & Motokawa 2005).

- For further evaluation of the mechanical properties of spines, more bending tests have to be carried out, for example in-situ observations in a reef-system. In addition, indenter surveys at different positions in the spine should be evaluated to simulate natural predator-prey situations. These laboratory tests can then be compared with outdoor experiments. Also the use of finite element method or computer-aided-design should be discussed to characterize the areas of stress inside the spine, which is in preparation by the project partners.

- As seen for the spines, the influence of the stereom structure has to be considered. The values (e.g. in Figure 5) vary widely. Whether this occurs because of environmental impacts (for example different habitats or feeding strategies), the different growth process of specimen, surface effects (including encrustation and disruption of the original surface structure) or other matters has to be investigated further. Also the different shapes (e.g. round with nodules or elongated) with partly spiky tips might have an impact in the mechanical behaviour.

- The mechanical diversity shown with the bending tests may also be attributed to material and structural properties of the echinoderm calcite. The internal medulla is the same in the species but the radiating layer varies within the selected species (see chapter 2 for further explanations).

- This present large investigation provided fundamental basic information about the bending behaviour of selected sea urchin spine and showed the principal application possibility for a new product.

6. References

Baumeister, J. G. & R. R. Leinfelder, R. R. (1998). "Constructional morphology of three upper jurassic echinoids." Palaeontology 41: 203-219.

Baumeister, J. (1999). "Vergleich der Funktionsmorphologie und Paläoökologie zweier Rhabdocidariden (Echinodermata: Cidaridae)." Paläontologische Zeitschrift 73(3): 319-326.

Berns, T., Hofmann, C. & Gotzen, L. (2001). "Festigkeitsuntersuchungen an Pins aus humaner Femurkortikalis." Der Unfallchirurg 104(1): 64-68.

Burkhardt, A., Hansmann, W., Märkel, K. & Niemann, H. J. (1983). "Mechanical design in spines of diadematoid echinoids (echinodermata, echinoidea)." Zoomorphology 102: 189-203.

Bhushan, B. (2009). "Biomimetics." Philosophical Transactions of the Royal Society of London A 367: 1443-1444.

Cacciafesta, V., Sfondrini, M. F., Lena, A., Scribante, A., Vallittu, P. K. & Lassila, L. V. (2008). "Force levels of fiber-reinforced composites and orthodontic stainless steel wires: A 3-point bending test." American Journal of Orthodontics and Dentofacial Orthopedics 133(3): 410-413.

Castillo, J. del, Smith, D. S., Vidal, A. M. & Sierra, C. (1995). "Catch in the primary spines of the sea urchin *Eucidaris tribuloides*: A brief review and a new interpretation." Biological Bulletin 188: 120-127.

Currey, J. D. (1965). "Anelasticity in bone and echinoderm skeletons." Journal of Experimental Biology 43(2): 279-292.

Currey, J. D. (1975). "A comparison of the strength of echinoderm spines and mollusc shells." Journal of the Marine Biological Association U.K. 55: 419-424.

Currey, J. D. (1999a). "What determines the bending strength of compact bones." Journal of Experimental Biology 202: 2495-2503.

Currey, J. D. (1999b). "The design of mineralised hard tissues for their mechanical functions." Journal of Experimental Biology 202: 3285-3294.

Denny, M. & Gaylord, B. (1996). “Why the urchin lost its spines: hydrodynamic forces and survivorship in the three echinoids.” Journal of Experimental Biology 199: 717-729.

Diab, M. & Gilly, W. F. (1984). “Mechanical properties and control of nonmuscular catch in spine ligaments of the sea urchin, *Strongylocentrotus franciscanus*.” Journal of Experimental Biology 111(1): 155-170.

Dotan, A. & Fishelson, L. (1985). “Morphology of spines of *Heterocentrotus mammillatus* (Echinodermata: Echinoidae) and its ecological significance.” In: O`Connor, B. F. & Keegan, B. D. S. (Eds.): Echinodermata: Proceedings of the International Echinoderm Conference, Galway September 24-29.9.1984. Rotterdam, A. A. Balkema**:** 253-260.

Ebert, T. A. (1967). “Growth and repair of spines in the sea urchin *Strongylocentrotus purpuratus* (Stimpson).” Biological Bulletin 133: 141-149.

Ebert, T. A. (1985). “The non-periodic nature of growth rings in echinoid spines.” In: O`Connor, B. F. & Keegan, B. D. S. (Eds.): Echinodermata: Proceedings of the International Echinoderm Conference, Galway September 24-29.9.1984. Rotterdam, A. A. Balkema: 261-267.

Emlet, R. (1982). “Echinoderm calcite: A mechanical analysis from larval spicules.” Biological Bulletin 163: 264-275.

Fátima Vales Silva, M., Hancock, P. & Nicholls, J. R. (2003). “An improved three-point bending method by nanoindentation.” Surface and Coatings Technology 169-170: 748-752.

Fehling, E., Leutbecher, T. & Röder, F.-K. (2009). “Zur Druck-Zug-Festigkeit von Stahlbeton und stahlfaserverstärktem Stahlbeton.” Beton- und Stahlbetonbau 104(8): 471-484.

Gage, J. D. (1987). “Growth of the deep-sea irregular sea urchins *Echinosigra phiale* and *Hemiaster expergitus* in the rockall trough (n.e. atlantic ocean).” Marine Biology 96: 19-30.

Hiratzka, L. F., Goeken, J. A., White, R. A. & Whright, C. B. (1979). “In vivo comparison of replamineform, silastic and bioelectric polyurethane arterial grafts.” Archives of Surgery 114(6): 698-702.

Kimura, H. & Masumoto, T. (1980). “Deformation and fracture of an amorphous Pd---Cu---Si alloy in V-notch bending tests I: Model mechanics of inhomogeneous plastic flow in non-strain hardening solid.” Acta Metallurgica 28(12): 1663-1675.

Kobayashi, S., Demura, M., Kishida, K. & Hirano, T. (2005). “Tensile and bending deformation of Ni_3Al heavily cold-rolled foil.” Intermetallics 13(6): 608-614.

Kuhn-Spearing, L. T., Kessler, H., Chateau, E., Ballarini, R., Heuer, A. H. & Spearing, S. M. (1996). “Fracture mechanisms of the *Strombus gigas* conch shell: implications for the design of brittle laminates.” Journal of Materials Science 31(24): 6583-6594.

Kürmann, H. (1986). “Zum Bruch-, Härte- und Temperverhalten natürlicher Mg-Calcite: Stacheln, Coronarplatten und Zähne von Echiniden.” Bochumer geologische und geotechnische Arbeiten 23: 1-64.

Lai, M., Kulak, A. N., Law, D., Zhang, Z., Meldrum, F. C. & Riley, D. J. (2007). “Profiting from nature: macroporous copper with superior mechanical properties.” Chemical Communications 34: 3547-3549.

Maginnis, T. L. (2006). “The costs of autotomy and regeneration in animals: a review and framework for future research.” Behavioral Ecology 17(5): 857-872.

Mannaerts, G. (2007). “Effets des métaux lourds sur la morphologie et la mécanique des piquants de l’échinide *Echinus acutus*.” Diploma thesis, Faculty of Science, Université libre de Bruxelles.

Meldrum, F. C. (2007). “Bio-Casting: biomineralized skeletons as templates for macroporous structures.” In: Behren, P. & Bäuerlein, E. (Eds.): Handbook of Biomineralization, Wiley, Weinheim: 289-309.

Motokawa, T. (1982). “Rapid change in mechanical properties of echinoderm connective tissues caused by coelomic fluid.” Comparative Biochemistry and Physiology 73C: 223-229.

Oaki, Y. & Imai, H. (2006). “Nanoengineering in echinoderms: The emergence of morphology from nanobricks.” Small 2(1): 66-70.

Pearse, J. S. & Pearse, V. B. (1975). “Growth zones in echinoid skeleton.” American Zoologist 15: 731-753.

Presser, V., Schultheiß, S., Berthold, C., Nickel, K. G. (2009). “Sea urchin spines as a model-system for permeable, light-weight ceramics with graceful failure behavior. Part I. Mechanical behavior of sea urchin spines under compression.” Journal of Bionic Engineering 6(3): 203 - 213.

Rayfield, E. J. (2007). “Finite element analysis and understanding the biomechanics and evolution of living and fossil organisms.” Annual Review of Earth and Planetary Sciences 35: 541-576.

Reilly, G. C. & Currey, J. D. (1999). “The development of microcracking and failure in bone depends on the loading mode to which it is adapted.” Journal of Experimental Biology 202: 543-552.

Reinhardt, H. W., Grosse, C. U. & Weiler, B. (2001). “Material characterization of steel fibre reinforced concrete using neutron CT, ultrasound and quantitative acoustic emission techniques.” NDT.net 6(5): online.

Ries, J. B. (2004). “Effect of ambient Mg/Ca ratio on Mg fractionation in calcareous marine invertebrates: A record of the oceanic Mg/Ca ratio over the phanerozoic.” Geology 32(11): 981-984.

Schwickerath, H. & Mokbel, M. A. (1983): “Grundlagen zur Prüfung des Verbundes Metall-Keramik.” Deutsche Zahnärztliche Zeitschrift 38: 949-952.

Schinker, A. S. (2001). “Vergleich der Verbundfestigkeit unterschiedlicher Verblendkunststoffe auf verschiedenen Legierungen im Drei-Punkt-Biegeversuch.” PhD thesis, Dentistry, Oral and Maxillofacial Surgery, University of Gießen.

Sideridis, E., Ashton, J. N. & Kitching, R. (1991). “Measurement of the interlaminar shear strength of glass-reinforced plastics of different construction using the off-axis four-point bending test.” Composite Structures 18(2): 139-161.

Smith, A. B. (1980). “Stereom microstructure of the echinoid test.” Special Papers in Palaeontology 25: 1-83.

Smith, D. S., Castillo, J. del, Morales, M. & Luke, B. (1990). “The attachment of collagenous ligament to stereom in primary spines of the sea-urchin, *Eucidaris tribuloides*.” Tissue and Cell 22(2): 157-176.

Stiller, F. (2001). “Echinoid spines from the anisian (middle triassic) of Qingyan, south-western china.” Palaeontology 44(3): 529-551.

Strathmann, R. R. (1981). “The role of spines in preventing structural damage to echinoid tests.” Paleobiology 7(3): 400-406.

Su, X., Kamat, S. & Heuer, A. H. (2000). “The structure of sea urchin spines, large biogenic single crystals of calcite.” Journal of Materials Science 35: 5545-5551.

Takemae, N. & Motokawa, T. (2005). “Mechanical properties of the isolated catch apparatus of the sea urchin spine joint: muscle fibers do not contribute to passive stiffness changes.” Biological Bulletin 208: 29-35.

Telford, M. (1985). “Domes, arches and urchins: the skeletal architecture of echinoids (echinodermata).” Zoomorphology 105: 114-124.

Wagner, H. D. & Weiner, S. (1992). “On the relationship between the microstructure of bone and its mechanical stiffness.” Journal of Biomechanics 25(11): 1311-1320.

Weber, J. N., Greer, R., Voight, B., White, E. & Roy, R. (1969). “Unusual strength properties of echinoderm calcite related structure.” Journal of Ultrastructure Research 26: 355-366.

Wilkie, I. C. (2001). “Autotomy as a prelude to regeneration in echinoderms.” Microscopy Research and Technique 55: 369-396.

Vecchio, K. S., Zhang, X., Massie, J. B., Wang, M. & Kim, C. W. (2007). “Conversion of sea urchin spines to Mg-substituted tricalcium phosphate for bone impants.” Acta Biomaterialia 3: 785-793.

7. Supplement: Mathematical derivation of equations for the bending tests

Second moment of inertia for circular cross-section area: geometric distribution of material around a neutral axis of bending

$$I=\frac{\pi*D^4}{64}$$

in mm^4
D = diameter

Bending stress: where the force acts over the area

$$\sigma=\frac{M}{W}$$

in N/mm^2

where M is the bending moment for 3 point bending $\frac{F*L}{4}$

and W is the section modulus: $\frac{2*I}{D}$

F = Force
L = distance space

this results in equations for the bending stress in 3-point bending test:

$$\sigma=\frac{F*L*D}{8*I}$$

Bending strain: change in length produced by stress

$$\epsilon=\frac{6*s*h}{L^2}$$

This has to be multiplied by 100 for receiving %; s = deflection; h = diameter; L = distance space

Young's modulus for bending: stiffness of material

$$E=\frac{\Delta\sigma}{\Delta\epsilon}$$

in MPa

where $\Delta\sigma$ is the mean maximum value of the bending stress minus the minimum and $\Delta\varepsilon$ is the mean maximum value for the bending strain minus the minimum

Conclusion & Future prospects

Conclusion

- This PhD thesis as part of a larger interdisciplinary project “New materials for light, permeable impact protective systems: sea urchin as a model” investigated sea urchin spines to give the basis for developing a new bio-inspired (biomimetic) impact protective system.

- With the scanning electron microscopy the ability of describing the stereom structure of selected sea urchin spines was given and different stereom arrangements could be found.

- The presence of galleried stereom in the radiating layer (except for *Heterocentrotus mammillatus*) allows the conclusion to say that this structure is the best solution for that position inside the spine. It should be emphasised that the medulla in all of the spines was always arranged in the same way, supporting the idea that this is the most evolutionary successful structure.

- Nevertheless, the medulla can be seen as the neutral fibre, thus this position is the area where, for material scientists, a lesser amount of material is found. This is important for a later development of a bio-inspired impact protective system.

- The SEM images showed differences in the measurements from oral to aboral spines, supporting the idea of more stable spines on oral than on the aboral side.

- The tips of *Heterocentrotus mammillatus* spines showed a fountain-like arrangement of the pores. Whether this is due to the growth process or for a further stabilizing of the structure could not be answered yet.

- In particular, the use of CT showed the different porosity of the stereom inside spines. Although with the CT scans no differentiations of stereom types in detail could be shown, it was a useful method in comparing the extensions of the stereom types, as well as the

extent of the growth rings in spines of *Heterocentrotus mammillatus* and differences within the growth rings.

- The 3-point-bending-tests demonstrated a difference between juvenile and fully grown spines, as well as between the spines of *Heterocentrotus mammillatus* and *Phyllacanthus imperialis*. The stress values differed between the two species, supporting the idea that the differences in internal structure leads to this different mechanical behaviour. Nevertheless, the bending moduli were much lower than those of, for example concrete or bones. The broad range of values in the bending tests may be due to the experimental design or because of the natural variation in the samples. The investigations can be seen as a fundamental basis for the developing of a new bio-inspired impact protective system.

Future prospects

The microstructure of spines (the stereom) could be applied for a wide range of usages, for example impact protective systems like security parts in automobiles, component materials, metallic foams or bullet-proof vests. Following the goals of material scientists, less material and higher stability could be achieved with the use of such internal arrangements. It is worth mentioning, that this structure has already been used in scientific applications such as construction engineering, macroporous copper and polymer replicas (Hasenpusch 2000, Lai et al. 2007 and Meldrum 2007).

Until now, it is not fully understood to what extent the implementation of the stereom structure in, for example, bicycle helmets would increase protection. Nevertheless, as presented by Weiner et al. (2000), Chen (2005) and Chen et al. (2007) there is a high potential for incorporating stereom-like structures into technical products.

This project was a first step to a successful characterization of the stereom of sea urchin spines in order to give the basis for further extensive application work and some of the results have been published recently by Nickel et al. (2009) and Presser et al. (2009).

References

Chen, L. I. (2005). “A bioinspired micro-composite structure.” PhD thesis, Department of Civil Engineering, Case Western Reserve University, Cleveland.

Chen, L. I., Ballarini, R. Kahn, H. & Heuer, A. H. (2007). “A bioinspired micro-composite structure,” Journal of Materials Research 22(1): 124-131.

Hasenpusch, W. (2000). “Die Stachel der Griffelseeigel.” Mikrokosmos 89(1): 23 - 27.

Lai, M., Kulak, A. N., Law, D., Zhang, Z., Meldrum, F. C. & Riley, D. J. (2007). “Profiting from nature: macroporous copper with superior mechanical properties.” Chemical Communications (Cambridge, United Kingdom) 34: 3547-3549.

Meldrum, F. (2007). “Bio-Casting: biomineralized skeletons as templates for macroporous structures.” In: Behrens, P. & E. Bäuerlein, E. (Eds.): Handbook of Biomineralization, Weinheim, WILEY-VCH: 289-309.

Presser, V., Schultheiß, S., Berthold, C., Nickel, K. G. (2009). “Sea urchin spines as a model-system for permeable, light-weight ceramics with graceful failure behavior. Part I. Mechanical behavior of sea urchin spines under compression.” Journal of Bionic Engineering 6(3): 203 - 213.

Nickel, K.G., Presser, V., Schultheiß, S., Berthold, C., Kohler, C., Nebelsick, J. H., Grossmann, N., Stegmaier, T., Finckh, H. & Vohrer, A. (2009). “Seeigelstachel als Modell für stoffdurchlässige Einschlagschutzsysteme.” In: Kesel, A. B. & Zehren, D. (Eds.): Bionik-Patente aus der Natur, Bionik-Innovations-Centrum Bremen, Bremen: 26-36.

Weiner, S., Addadi, L. & Wagner, H. D. (2000). “Materials design in biology.” Materials Science and Engineering C 11(1): 1 - 8.

Summary

This PhD thesis as part of the greater interdisciplinary project “New materials for light, permeable impact protective systems: sea urchin as a model” investigated several sea urchin spines (*Heterocentrotus mammillatus*, *Echinometra mathaei*, *Eucidaris metularia*, *Phyllacanthus imperialis*, *Plococidaris verticillata*, *Prionocidaris baculosa*) in detail by means of morphological analyses (including scanning electron microscopy (SEM), critical point drying and computer tomography (CT)) and additionally mechanical consideration in 3-point-bending-tests to develop the basis for a new bio-inspired (biomimetic) impact protective system. The motivation was due to the long evolutionary history of echinoderms (including sea urchins) as well as the light weight of spines as they are built up of magnesium calcite in a porous manner. The investigated species were kept in several fully equipped sea water aquaria with tropical conditions over the whole period of the investigations.

For the first time, a large survey to describe the stereom structure of spines was carried out. The SEM study showed that the innermost area (the medulla) is laminar in all the spines. The radiating layer is galleried, except in *Heterocentrotus mammillatus* and *Echinometra mathaei* where it was labyrinthic. The cortex or the growth rings are microperforate. The pore and trabeculae diameter of medulla and radiating layer were compared, also with respect to difference between juvenile and fully grown spines. The pore diameter in medulla differs from that in the radiating layer but no trend-setting could be found. Juvenile spines of *Heterocentrotus mammillatus* showed lower values of pore diameter than the fully grown ones.

Due to the CT scans, it was possible to give assumptions for the bending behaviour of spines with respect to the density of the material and its thickness. Additionally three dimensional images were performed to show the internal arrangement of the spines. CT scans, daily used in clinical diagnosis, could be used as an addiction to SEM images in order to characterize the stereom structure in spines. The CT scans, however, could not display the different stereom types in detail. The investigations of spines of *Heterocentrotus mammillatus*, *Phyllacanthus imperialis* and *Prionocidaris baculosa* with computer tomography displayed several structures. Spines of *Heterocentrotus mammillatus* showed growth rings in contrast to spines of the cidaroids which were also under investigation. The function of these rings, e. g. as mechanical stabilizer is discussed.

The bending behaviour of juvenile and fully grown spines of *Heterocentrotus mammillatus* and *Phyllacanthus imperialis* was analysed by 3-point-bending tests.

Differences occurred between and within the two species. The force loading was lower in fully grown *Phyllacanthus imperialis* spines than in the juvenile ones. Spines of *Heterocentrotus mammillatus* could withstand the same force but differed in the stress-strain analyses.

The use of the stereom for impact protective systems has never been investigated in detail thus far. The arrangement of the stereom inside spines may be innovative for several applications. The possibilities for use in technical fields are various and range from copper plates based on the stereom structure to bio-inspired ideas for new pedestrian safeties in car development. These investigations provided here will serve as a basis for further investigations.

Zusammenfassung

Die Doktorarbeit, als Teil des interdisziplinären Projekts „Neue Materialien für leichte, stoffdurchlässige Einschlagschutzsysteme: Seeigel als Modell" behandelte die Analyse der Mikrostrukturen von verschiedenen Seeigelstacheln (*Heterocentrotus mammillatus*, *Echinometra mathaei*, *Eucidaris metularia*, *Phyllacanthus imperialis*, *Plococidaris verticillata*, *Prionocidaris baculosa*) mittels Rasterelektronenmikroskopie, Kritischer Punkt Trocknung, Computertomografie und 3-Punkt-Biegeversuchen. Dieses bionische Projekt hatte zum Ziel, aus dem Projekterkenntnissen die Basis für einen neuartigen Einschlagschutz zu entwickeln. Echinodermen und im speziellen Seeigel sind interessant, da sie zum einen seit mehreren hundert Millionen Jahren evolutionär erfolgreich sind und beispielsweise dass die Stacheln aus einen besonders leichten Material bestehen (Magnesiumcalcit). Für die Versuche wurden die verschiedenen Seeigel unter simulierten tropischen Bedingungen in Meerwasseraquarien gehalten und bei Bedarf einzelne Stacheln entnommen.

Zum ersten Mal wurde eine umfangreiche Studie über die Stereomstrukturen innerhalb der Seeigelstachel durchgeführt. Die REM-Studien zeigten, dass der innerste Bereich der Stacheln (die Medulla) laminar in allen Stacheln ist, während die umlaufende Schicht (radiating layer) gallerieartige Anordnung besitzt. Außer bei *Heterocentrotus mammillatus* und *Echinometra mathaei* Stacheln, diese zeigten sich labyrinthisch.

Die Ergebnisse aus den CT Aufnahmen ergaben, dass die Medulla in den Stacheln ein offen-poröses Stereom darstellt und dass der Cortex bspw. bei *Phyllacanthus imperialis* ein dichtes Stereom ist. Der Cortex bzw. die Wachstumsringe zeigten eine mikroperforierte Anordnung des Stereoms. Der Poren- und Trabeculaedurchmesser der Medulla und der umlaufenden Schicht wurde zwischen verschiedenen Arten verglichen, ebenso zwischen jungen und ausgewachsenen Stacheln innerhalb einer Spezies. Der Porendurchmesser unterschied sich zwischen Medulla und der umlaufenden Schicht, aber ein genereller Trend konnte nicht aufgezeigt werden. Junge Stacheln von *Heterocentrotus mammillatus* zeigten kleinere Porendurchmesser als die ausgewachsenen Stacheln.

Aufgrund der CT-Aufnahmen war es möglich, Vermutungen bezüglich des Biegeverhaltens von Stacheln zu geben, auch im Hinblick auf die Porosität und Dicke des Stereoms.

Mit den 3D-Aufnahmen konnte die innere Struktur der Stacheln gedeutet werden. Computertomografie, die täglich Einsatz in der klinischen Diagnostik findet, konnte als Zusatz zu REM-Aufnahmen benutzt werden um die interne Stachelstruktur zu beschreiben. Jedoch war es nicht möglich die einzelnen Stereomtypen zu unterscheiden. Die CT-

Aufnahmen von *Heterocentrotus mammillatus*, *Phyllacanthus imperialis* und *Prionocidaris baculosa* Stacheln zeigte verschiedene Strukturen. Die Dichte und Ausdehnung der Wachstumsringe in Stacheln von *Heterocentrotus mammillatus* wurde beschrieben. Das Biegeverhalten von jungen und ausgewachsenen Stacheln von *Heterocentrotus mammillatus* und *Phyllacanthus imperialis* wurde in 3-Punkt-Biegeversuchen analysiert. Unterschiede traten zum einen innerhalb der Arten und zwischen diesen auf. Die Kraftaufnahme durch ausgewachsene *Phyllacanthus imperialis* Stachel war niedriger als die der jungen Stacheln. Grundsätzlich traten keine Unterschiede in der Kraftaufnahme bei Stacheln von *Heterocentrotus mammillatus* auf, jedoch im Spannungs-Dehnungsdiagramm.

Die Anwendungsmöglichkeiten der Stereomstruktur im technischen Bereich kann als vielfältig eingestuft werden und diese werden bereits in neuartigen Kupferplatten eingesetzt. Die Untersuchungen des Seeigelstereoms und dessen Klassifizierung werden zukünftig als Grundlage zur Entwicklung eines neuartigen Aufprallschutzsystems im Automobilbau dienen.

Danksagung

Mein Dank gilt allen Personen, die mir bei der Erstellung dieser Arbeit direkt oder indirekt geholfen und mir in den vergangenen Jahren zur Seite gestanden haben.

Meinem Doktorvater Herrn Prof. Dr. James Nebelsick danke ich für die Vergabe und engagierte Betreuung dieser Promotion. Ein großes Dankeschön auch für die konstruktiven Anmerkungen und fachlichen Diskussionen.

Mein Dank gilt auch der Baden-Württemberg Stiftung, durch deren Finanzierung dieses Projekt erst möglich wurde.

Herrn Prof. Dr. Oliver Betz danke ich für die Bereitschaft das Zweitgutachten für diese Arbeit zu erstellen.

Wolfgang Gerber für das Fotografieren der Stacheln und die Aufsichten auf die Seeigelkörper.

Für die Übernahme der Meerwassertiere am Ende des Projekts möchte ich der IG Meerwasser von Herrn Thomas Musch (Tübingen) danken. Ebenso Frau Isabel Koch und Herrn Alex Mendoza von der Wilhelma (Stuttgart).

Im besonderen Maße bedanken möchte ich mich bei Herrn Dipl. Ing. (MSc.) Achim Vohrer für die Einführung und Hilfestellung in die 3-Punkt-Biegeversuche sowie für die Nutzung der Prüfgeräte am ITV, ebenso für Bilder der Prüfmaschine und des Versuchsaufbaus.

Hugo Rieger möchte ich danken für die Unterstützung in der Interpretation der Ergebnisse der Biegeversuche.

Für die Unterstützung bei den REM-Aufnahmen im Institut für Geowissenschaften der Universität Tübingen möchte ich Hartmut Schultz (ebenso für das Bild des Elektronenmikroskops) und Peter Fittkau sehr herzlich danken.

Indra Gill-Kopp und Per Jeisecke für die Herstellung der Proben zur Rasterelektronenmikroskopie.

Jürgen Berger (MPI) für die kritische Punkt Trocknung und Hilfe beim REM.

Sebastian Schmelzle (Institut für Evolution und Ökologie, Universität Tübingen) für die Hilfe bei der Erstellung der 3D-Aufnahmen aus den CT Daten.

Herzlich bedanken möchte ich mich an dieser Stelle bei Maren, meiner Frau, die mir während der Zeit immer zur Seite stand.

Jane Nagle und David Dunn möchte ich danken für die Unterstützung in der Korrektur der englischen Texte.

Nicht zuletzt gilt ein ganz besonderer und herzlicher Dank meiner Familie, die mich in jeder Hinsicht stets unterstützt haben.